

2013

AN EXPERIMENTAL INVESTIGATION INTO THE EFFECTS OF BIODIESEL BLENDS ON PARTICULATE MATTER OXIDATION IN A CATALYZED PARTICULATE FILTER DURING ACTIVE REGENERATION

James Pidgeon
Michigan Technological University

Follow this and additional works at: <https://digitalcommons.mtu.edu/etds>

 Part of the [Mechanical Engineering Commons](#)

Copyright 2013 James Pidgeon

Recommended Citation

Pidgeon, James, "AN EXPERIMENTAL INVESTIGATION INTO THE EFFECTS OF BIODIESEL BLENDS ON PARTICULATE MATTER OXIDATION IN A CATALYZED PARTICULATE FILTER DURING ACTIVE REGENERATION", Master's Thesis, Michigan Technological University, 2013.
<https://doi.org/10.37099/mtu.dc.etds/483>

Follow this and additional works at: <https://digitalcommons.mtu.edu/etds>

 Part of the [Mechanical Engineering Commons](#)

AN EXPERIMENTAL INVESTIGATION INTO THE EFFECTS OF BIODIESEL
BLENDS ON PARTICULATE MATTER OXIDATION IN A CATALYZED
PARTICULATE FILTER DURING ACTIVE REGENERATION

By

James M. Pidgeon

A THESIS

Submitted in partial fulfillment of the requirements for the degree of

MASTER OF SCIENCE

In Mechanical Engineering

MICHIGAN TECHNOLOGICAL UNIVERSITY

2013

© 2013 James M. Pidgeon

This thesis has been approved in partial fulfillment of the requirements for the Degree of MASTER OF SCIENCE in Mechanical Engineering.

Department of Mechanical Engineering – Engineering Mechanics

Thesis Co-Advisor: *Dr. Jeff Naber*

Thesis Co-Advisor: *Dr. John Johnson*

Committee Member: *Dr. Jason Keith*

Department Chair: *William W. Predebon*

Table of Contents

List of Figures	6
List of Tables	12
Acknowledgements.....	14
List of Abbreviations	15
Abstract	16
Chapter 1 Introduction	18
1.1 Introduction	19
1.2 Research Goal and Objectives.....	20
1.3 Outline of Thesis.....	21
Chapter 2 Background and Literature Review	23
2.1 ULSD and Biodiesel Emissions	23
2.2 PM Oxidation	27
2.2.1 Introduction	27
2.2.2 Reactor PM Oxidation Studies	29
2.3 Active Regeneration	30
2.4 Downstream PM Concentration Sensor.....	32
2.5 Summary.....	34
Chapter 3 Experimental Setup and Test Procedures	36
3.1 Engine and Dynamometer.....	36
3.2 Fuel Properties	37
3.3 Aftertreatment System	38
3.4 Test Cell Setup	38
3.4.1 Data Acquisition System.....	39
3.4.2 Temperature Measurements	40
3.4.3 Pressure Measurements	42
3.4.4 Air and Fuel Flow Measurements	42
3.4.5 Gaseous Emissions Measurements.....	42
3.4.6 PM Concentration Measurements.....	43
3.4.7 Particle Size Distribution Measurements	43
3.4.8 CPF PM Mass Retained Measurements	44
3.5 Experimental DCPF PM Concentration Sensor	48
3.5.1 PM Conductivity Study	48
3.5.2 Sensor Loading Study	49

3.6 Active Regeneration Test Procedure	49
3.6.1 Pre-test Preparation Phase	52
3.6.2 CPF Clean Out Phase	54
3.6.3 Stage 1 Loading Phase.....	54
3.6.4 Stage 2 Loading Phase.....	56
3.6.5 Active Regeneration Phase	58
3.6.6 Stage 3 Loading Phase.....	60
3.6.7 Stage 4 Loading Phase.....	62
3.7 Active Regeneration Test Matrix.....	63
3.8 PM Reaction Rate Calculation Method	66
3.9 Activation Energy Determination Method.....	67
3.10 CPF Resistance Calculation Method	68
Chapter 4 Experimental Results.....	74
4.1 Data Integrity Analysis for Modeling	74
4.2 Active Regeneration	78
4.2.1 Gaseous Emissions	83
4.2.2 CPF Pressure Drop Profile	87
4.2.3 Particle Size Distribution	90
4.2.4 CPF Temperature Gradients	91
4.2.5 PM Reaction Rate	95
4.2.6 Activation Energy Determination	97
4.2.7 Regeneration Efficiency of Fuel Dosing	99
4.2.8 In-cylinder and Post-turbo Dosing Methods.....	103
Chapter 5 Conclusions and Recommendations.....	104
5.1 Conclusions.....	104
5.2 Recommendations.....	105
References	106
Appendix A Biodiesel Blend Molecular Formula Calculations	109
Appendix B Dilution Ratio Calculation Method	112
Appendix C PSD Data Correction Method	114
Appendix D CPF Mass Measurement Procedure.....	116
Appendix E Stage 1 Loading PM Mass Balance Calculations (by Kiran Premchand [19])	118
Appendix F PM Sample Preparation Procedure.....	122
Appendix G Auxiliary Fuel Dosing Injector Calibration Procedure	123

Appendix H Data Integrity Analysis for Modeling	125
Appendix I Stage 2 Loading	172
Appendix J Stage 4 Loading.....	178
Appendix K CPF Mass Balance.....	184
Appendix L Doser Flow Rate Comparison.....	189
Appendix M Gaseous Emissions Summary	191
Appendix N Engine Air Flow Rate and CPF Pressure Drop Profile	194
Appendix O Regeneration Efficiency of Fuel Dosing Calculation Method	204
Appendix P CPF Pressure Drop Comparison between National Instruments (NI) LabVIEW and CalTerm	207
Appendix Q Permission to Use Copyrighted Material.....	223

List of Figures

Figure 2.1: DOC Conversion Efficiencies for Various Gaseous Species [6]	25
Figure 2.2: Example of CPF Wall Flow Substrate Structure.....	25
Figure 2.3: Relative Change of NO _x Emissions with SME Biodiesel Blends Compared to ULSD [7]	26
Figure 2.4: Relative Change of TPM Emissions with SME Biodiesel Blends Compared to ULSD [7]	26
Figure 2.5: Passive Oxidation CPF PM Reaction Rate vs. 1000/Average CPF Temperature (Kelvin) [11]	28
Figure 2.6: Soot Reactivity Measured During Temperature Ramps [13].....	30
Figure 2.7: Efficiency of PM Oxidation as a Function of Average CPF Temperature (T _R) [1]	32
Figure 2.8: Signal Characteristics of the Resistive Particulate Matter Sensor and Images Showing PM Deposition on Electrodes [5], Copyright © SAE International, Reprinted with permission	33
Figure 3.1 Test Cell Schematic for 2007 Cummins ISL	39
Figure 3.2 DOC Thermocouple Layout	41
Figure 3.3 CPF Thermocouple Layout	41
Figure 3.4: Overview of the ISL Active Regeneration Test Procedure.....	45
Figure 3.5: Pre-test Preparation Phase Gaseous Emissions Sampling Strategy	53
Figure 3.6: Gaseous Emissions Sampling Strategy for Stage 2 Loading Phase	57
Figure 3.7: Gaseous Emissions and PSD Sampling Strategy for Active Regeneration Phase	60
Figure 3.8: B20-1 Experimental CPF Flow Resistance (subplot 1), Exhaust Viscosity and CPF Average Temperature (subplot 2), Exhaust Mass Flow Rate (subplot 3), and CPF Pressure Drop Profile (subplot 4).	72
Figure 4.1: Pre-test Phase for Active Regeneration Average Engine-Out PM Concentrations in Chronological Order	82
Figure 4.2: ULSD-3 DCPF HC Measurement during Active Regeneration (In-cylinder Dosing Case)	84
Figure 4.3: Comparison of CPF Pressure Drop for ULSD-4, B10-1, and B20-5, all at Nominal 525°C CPF Inlet Temperature using In-Cylinder Dosing	88
Figure 4.4: 525°C CPF Inlet Temperature B20 and ULSD Tests using In-cylinder and Exhaust Dosing	90

Figure 4.5: Averaged Particle Size Distribution by Particle Numbers by Fuel Type during Active Regeneration sampled DDOC and DCPF	91
Figure 4.6: Radial Temperature Gradients at Four Axial Locations (Distance from CPF Inlet) during ULSD-4 Active Regeneration (525°C CPF Inlet Temperature Target, In-Cylinder Dosing)	93
Figure 4.7: Average-radial Axial Temperature Gradients during Active Regeneration with In-cylinder Dosing	95
Figure 4.8: Optimized Results with All Tests Included in the Optimization.....	98
Figure 4.9: Grams of PM Oxidized per Equivalent Gallon of Fuel Injected during Dosing as a Function of Average CPF Temperature Including Data from Austin [1]	100
Figure 4.10: Grams of PM Oxidized per Equivalent Gallon of Fuel Injected during Dosing as a Function of Average CPF Temperature Including Data from Austin [1] Normalized by Exhaust Volumetric Flow Rate Ratio.....	102
Figure B1: Copper Dilution Line Connected from the Heated Filter to the Dilution Box Outlet.....	112
Figure B2: PSD Sample Line Connected to the DDOC Gaseous Emissions Port.....	113
Figure D1: Cummins 2007 ISL After-treatment System.....	116
Figure E1: A typical ISL AR experiment showing a) DOC and CPF pressure drops, b) Exhaust mass flow rate and c) CPF inlet temperature.....	118
Figure G1: Example Auxiliary Doser Injector Calibration Curve with ULSD	124
Figure H1: Air Flow Rate and CPF Pressure Drop for Run 2 (B20-2)	126
Figure H2: Air Flow Rate and CPF Pressure Drop Profile for Run 3 (B20-5).....	126
Figure H3: CPF Pressure Drop Profile for Run 11 (B10-2) Measured by NI DAQ System and CalTerm Engine Management Software.....	128
Figure H4: Air Flow Rate and CPF Pressure Drop Profile for Run 2 (B20-2).....	129
Figure H5: Stage 2 Loading PM Concentration and Percent Oxidation for All Tests	130
Figure H6: Active Regeneration PM Oxidation for All Tests	133
Figure H7: Run 1 (B20-1) Experimental CPF Flow Resistance (subplot 1), Exhaust Viscosity and CPF Average Temperature (subplot 2), Exhaust Mass Flow Rate (subplot 3), and CPF Pressure Drop Profile (subplot 4).....	134
Figure H8: Run 1 (B20-1) NI and Corrected CalTerm Pressure Drop Profiles Including Linear Fit of NI Stage 1 and Stage 2 Loading and Pressure Drop Offset	140
Figure H9: Run 1 (B20-1) Corrected and Experimental CPF Flow Resistance (subplot 1), Exhaust Viscosity and CPF Average Temperature (subplot 2), Corrected and	

Corrected Experimental Exhaust Mass Flow Rate (subplot 3), Corrected and Experimental CPF Pressure Drop Profile (subplot 4)	143
Figure H10: Run 1 (B20-1) CF	146
Figure H11: Run 1 (B20-1) Corrected and Experimental CPF Flow Resistance (subplot 1), Exhaust Viscosity and CPF Average Temperature (subplot 2), Experimental and Corrected Experimental Exhaust Mass Flow Rate (subplot 3), Corrected and Experimental CPF Pressure Drop Profile (subplot 4)	148
Figure H12: Run 2 (B20-2) Corrected and Experimental CPF Flow Resistance (subplot 1), Exhaust Viscosity and CPF Average Temperature (subplot 2), Experimental and Corrected Experimental Exhaust Mass Flow Rate (subplot 3), Corrected and Experimental CPF Pressure Drop Profile (subplot 4)	149
Figure H13: Run 3 (B20-5) Corrected and Experimental CPF Flow Resistance (subplot 1), Exhaust Viscosity and CPF Average Temperature (subplot 2), Experimental and Corrected Experimental Exhaust Mass Flow Rate (subplot 3), Corrected and Experimental CPF Pressure Drop Profile (subplot 4)	150
Figure H14: Run 4 (ULSD-3) Corrected and Experimental CPF Flow Resistance (subplot 1), Exhaust Viscosity and CPF Average Temperature (subplot 2), Experimental and Corrected Experimental Exhaust Mass Flow Rate (subplot 3), Corrected and Experimental CPF Pressure Drop Profile (subplot 4)	151
Figure H15: Run 5 (ULSD-4) Corrected and Experimental CPF Flow Resistance (subplot 1), Exhaust Viscosity and CPF Average Temperature (subplot 2), Experimental and Corrected Experimental Exhaust Mass Flow Rate (subplot 3), Corrected and Experimental CPF Pressure Drop Profile (subplot 4)	152
Figure H16: Run 6 (ULSD-5) Corrected and Experimental CPF Flow Resistance (subplot 1), Exhaust Viscosity and CPF Average Temperature (subplot 2), Exp. and Crrctd. Exp. Exhaust Mass Flow Rate (subplot 3), Corrected and Experimental CPF Pressure Drop Profile (subplot 4).....	153
Figure H17: Run 7 (ULSD-6) Corrected and Experimental CPF Flow Resistance (subplot 1), Exhaust Viscosity and CPF Average Temperature (subplot 2), Experimental and Corrected Experimental Exhaust Mass Flow Rate (subplot 3), Corrected and Experimental CPF Pressure Drop Profile (subplot 4)	154
Figure H18: Run 8 (B20-6) Corrected and Experimental CPF Flow Resistance (subplot 1), Exhaust Viscosity and CPF Average Temperature (subplot 2), Experimental and	

Corrected Experimental Exhaust Mass Flow Rate (subplot 3), Corrected and Experimental CPF Pressure Drop Profile (subplot 4)	155
Figure H19: Run 9 (B20-4) Corrected and Experimental CPF Flow Resistance (subplot 1), Exhaust Viscosity and CPF Average Temperature (subplot 2), Experimental and Corrected Experimental Exhaust Mass Flow Rate (subplot 3), Corrected and Experimental CPF Pressure Drop Profile (subplot 4)	156
Figure H20: Run 10 (B10-1) Corrected and Experimental CPF Flow Resistance (subplot 1), Exhaust Viscosity and CPF Average Temperature (subplot 2), Experimental and Corrected Experimental Exhaust Mass Flow Rate (subplot 3), Corrected and Experimental CPF Pressure Drop Profile (subplot 4)	157
Figure H21: Run 11 (B10-2) Corrected and Experimental CPF Flow Resistance (subplot 1), Exhaust Viscosity and CPF Average Temperature (subplot 2), Experimental and Corrected Experimental Exhaust Mass Flow Rate (subplot 3), Corrected and Experimental CPF Pressure Drop Profile (subplot 4)	158
Figure H22: Run 12 (B10-3) Corrected and Experimental CPF Flow Resistance (subplot 1), Exhaust Viscosity and CPF Average Temperature (subplot 2), Experimental and Corrected Experimental Exhaust Mass Flow Rate (subplot 3), Corrected and Experimental CPF Pressure Drop Profile (subplot 4)	159
Figure H23: Run 13 (ULSD-1) Corrected and Experimental CPF Flow Resistance (subplot 1), Exhaust Viscosity and CPF Average Temperature (subplot 2), Experimental and Corrected Experimental Exhaust Mass Flow Rate (subplot 3), Corrected and Experimental CPF Pressure Drop Profile (subplot 4)	160
Figure H24: Run 14 (ULSD-8) Corrected and Experimental CPF Flow Resistance (subplot 1), Exhaust Viscosity and CPF Average Temperature (subplot 2), Experimental and Corrected Experimental Exhaust Mass Flow Rate (subplot 3), Corrected and Experimental CPF Pressure Drop Profile (subplot 4)	161
Figure H25: Run 15 (ULSD-9) Corrected and Experimental CPF Flow Resistance (subplot 1), Exhaust Viscosity and CPF Average Temperature (subplot 2), Experimental and Corrected Experimental Exhaust Mass Flow Rate (subplot 3), Corrected and Experimental CPF Pressure Drop Profile (subplot 4)	162
Figure H26: Run 16 (B10-4) Corrected and Experimental CPF Flow Resistance (subplot 1), Exhaust Viscosity and CPF Average Temperature (subplot 2), Experimental and Corrected Experimental Exhaust Mass Flow Rate (subplot 3), Corrected and Experimental CPF Pressure Drop Profile (subplot 4)	163

Figure H27: Run 17 (ULSD-7R) Corrected and Experimental CPF Flow Resistance (subplot 1), Exhaust Viscosity and CPF Average Temperature (subplot 2), Exp. and Crrctd. Exp. Exhaust Mass Flow Rate (subplot 3), Corrected and Experimental CPF Pressure Drop Profile (subplot 4).....	164
Figure H28: Run 18 (ULSD-2R) Corrected and Experimental CPF Flow Resistance (subplot 1), Exhaust Viscosity and CPF Average Temperature (subplot 2), Experimental and Corrected Experimental Exhaust Mass Flow Rate (subplot 3), Corrected and Experimental CPF Pressure Drop Profile (subplot 4)	165
Figure H29: CF for B20-1, B20-2, B20-5	166
Figure H30: CF for ULSD-3, ULSD-4, ULSD-5.....	167
Figure H31: CF for ULSD-6, B20-6, B20-4	168
Figure H32: CF for B10-1, B10-2, B10-3	169
Figure H33: CF for ULSD-1, ULSD-8, ULSD-9.....	170
Figure H34: CF for B10-4, ULSD-7R, ULSD-2R	171
Figure I1: Average Engine-out Gaseous Emissions during Stage 2 Loading for Each Test Fuel	173
Figure I2: Stage 2 Loading Engine-Out and CPF-out Particle Size Distribution Weighed by Number for ULSD, B10, and B20.....	174
Figure I3: Stage 2 Loading Average Engine-Out PM Concentrations in Chronological Order.....	176
Figure I4: CPF Pressure Drop vs. CPF PM Loading at the Conclusion Stage 2 Loading	177
Figure J1: Average Engine-out Gaseous Emissions during Stage 4 Loading for Each Test Fuel	178
Figure J2: Particle Size Distribution by Particle Numbers Averaged by Fuel Type during Stage 4 Loading sampled DDOC and DCPF	180
Figure J3: CPF Pressure Drop at the Start and Stop of Stage 2 and Stage 4 Loading for all tests.....	181
Figure J4: Stage 2 and Stage 4 Loading Reaction Rate Organized by Run Number	183
Figure N1: B20-1 Air Flow Rate (top) and CPF Pressure Drop Profile (bottom).....	194
Figure N2: B20-2 Air Flow Rate (top) and CPF Pressure Drop Profile (bottom).....	194
Figure N3: B20-5 Air Flow Rate (top) and CPF Pressure Drop Profile (bottom).....	195
Figure N4: ULSD-3 Air Flow Rate (top) and CPF Pressure Drop Profile (bottom) ...	195
Figure N5: ULSD-4 Air Flow Rate (top) and CPF Pressure Drop Profile (bottom) ...	196

Figure N6: ULSD-5 Air Flow Rate (top) and CPF Pressure Drop Profile (bottom) ...	196
Figure N7: ULSD-6 Air Flow Rate (top) and CPF Pressure Drop Profile (bottom) ...	197
Figure N8: B20-6 Air Flow Rate (top) and CPF Pressure Drop Profile (bottom).....	197
Figure N9: B20-4 Air Flow Rate (top) and CPF Pressure Drop Profile (bottom).....	198
Figure N10: B10-1 Air Flow Rate (top) and CPF Pressure Drop Profile (bottom)....	198
Figure N11: B10-2 Air Flow Rate (top) and CPF Pressure Drop Profile (bottom)....	199
Figure N12: B10-3 Air Flow Rate (top) and CPF Pressure Drop Profile (bottom)....	199
Figure N13: ULSD-1 Air Flow Rate (top) and CPF Pressure Drop Profile (bottom)..	200
Figure N14: ULSD-8 Air Flow Rate (top) and CPF Pressure Drop Profile (bottom)..	200
Figure N15: ULSD-9 Air Flow Rate (top) and CPF Pressure Drop Profile (bottom)..	201
Figure N16: B10-4 Air Flow Rate (top) and CPF Pressure Drop Profile (bottom)....	201
Figure N17: ULSD-7R Air Flow Rate (top) and CPF Pressure Drop Profile (bottom)	202
Figure N18: ULSD-2R Air Flow Rate (top) and CPF Pressure Drop Profile (bottom)	202
Figure N19: ULSD-10 Air Flow Rate (top) and CPF Pressure Drop Profile (bottom)	203
Figure O1: Modeled CPF PM Mass Retained in the CPF during Active Regeneration for Test ULSD-5	205
Figure P1: B20-1 CPF Pressure Drop	207
Figure P2: B20-5 CPF Pressure Drop	208
Figure P3: ULSD-3 CPF Pressure Drop	209
Figure P4: ULSD-4 CPF Pressure Drop	210
Figure P5: ULSD-5 CPF Pressure Drop	211
Figure P6: B20-6 CPF Pressure Drop	212
Figure P7: B20-4 CPF Pressure Drop	213
Figure P8: B10-1 CPF Pressure Drop	214
Figure P9: B10-2 CPF Pressure Drop	215
Figure P10: ULSD-1 CPF Pressure Drop	216
Figure P11: ULSD-8 CPF Pressure Drop	217
Figure P12: ULSD-9 CPF Pressure Drop	218
Figure P13: B10-4 CPF Pressure Drop	219
Figure P14: ULSD-7R CPF Pressure Drop	220
Figure P15: ULSD-2R CPF Pressure Drop	221
Figure P16: ULSD-10 CPF Pressure Drop	222

List of Tables

Table 3.1: ISL Engine Specifications	36
Table 3.2 Fuel Properties for Experimental Test Fuels*	37
Table 3.3 DOC and CPF Specifications	38
Table 3.4 Thermocouple Specifications.....	40
Table 3.5: Engine Operating Points for Initial Warm-Up Sequence	53
Table 3.6: Engine Speed and Load for Stage 2 Engine Warm Up	56
Table 3.7: Engine Speed and Load for Stage 4 Engine Warm Up	63
Table 3.8: Active Regeneration Test Matrix.....	65
Table 4.1: Data Integrity Analysis Results	75
Table 4.2: Selected Active Regeneration Test Data	79
Table 4.3: HC Measurements Recorded during Active Regeneration Point Validation	85
Table 4.4: HC, CO, and NO ₂ Conversion Efficiencies for All Tests	86
Table 4.5: Data from Tests Run for Figure 4.3	88
Table 4.6: Average CPF Temperature as a Function of Dosing Method for USLD and B20	94
Table 4.7: Calculated Pre-exponential Factors for all Tests	96
Table 4.8: Calculated Reaction Rate and Pre-exponential Factor Values for All Tests	97
Table 4.9: Optimization Results using All Tests	98
Table A1: B100 Properties from Senda [20].....	109
Table A2: Computed B100 Molecular Components	109
Table A3: H/C and O/C Ratios for B100.....	110
Table A4: Mole Fraction of Biodiesel for B10 and B20 Blends.....	110
Table A5: Calculated Properties for B10 and B20 Biodiesel Blends with ULSD Data	111
Table E1: Symbols	121
Table H1: Experimental Exhaust Mass Flow Rate	136
Table H2: LFE Pressure Drop Corrections	137
Table H3: Exhaust Mass Flow Rate Scaling Factors (SF)	138
Table H4: Stage 1 Loading CPF Pressure Drop Offset Corrections	141
Table H5: Active Regeneration Ramp and Active Regeneration CF	145
Table K1: Stage 1 Loading CPF Mass Balance.....	184
Table K2: Stage 2 Loading CPF Mass Balance.....	185
Table K3: Active Regeneration CPF Mass Balance	186

Table K4: Stage 3 Loading CPF Mass Balance.....	187
Table K5: Stage 4 Loading CPF Mass Balance.....	188
Table L1: DOC Energy Balance Results.....	190
Table M1: Pre-test Preparation Phase Gaseous Emissions.....	191
Table M2: Stage 1 Loading Gaseous Emissions	191
Table M3: Stage 2 Loading Gaseous Emissions	192
Table M4: Active Regeneration Gaseous Emissions	192
Table M5: Stage 3 Loading Gaseous Emissions	193
Table M6: Stage 4 Loading Gaseous Emissions	193
Table O1: Normalized Experimental Data	206

Acknowledgements

There are a number of individuals and organizations who are responsible for my ability to complete the work presented in this thesis. To each and every one of you, I say thank you, as there is no way I could have done it without you.

I would like to thank my advisors, Dr. John Johnson and Dr. Jeff Naber, for granting me the research opportunity within the Heavy Duty Diesel Group at MTU and for the guidance they have provided me throughout the time spent working with them. I would also like to thank Dr. Jason Keith for participating as a member of my thesis defense committee.

I would also like to thank the team members within the Heavy Duty Diesel Group from the past, present, and future that have helped immensely in the pursuit of my Master's degree. I would also like to extend thanks to the staff at MTU whose daily responsibilities helped me in the pursuit of my Master's degree.

I would also like to thank Cummins, Inc. for providing the engine and aftertreatment system used in this study and would like to thank the consulting support of Joe Brault, Krishna Chilumukuru, and Arvind Suresh. Finally, I would like to thank the United States Department of Energy for their financial support under Award Number DE-EE0000204, as this research would not have been possible without it.

This material is based upon work supported by the Department of Energy National Energy Technology Laboratory under Award Number(s) DE-EE0000204. This material was prepared as an account of work sponsored by an agency of the United States Government. Neither the United States Government nor any agency thereof, nor any of their employees, makes any warranty, expressed or implied, or assumed any legal liability or responsibility for the accuracy, completeness, or usefulness of any information, apparatus, product, or process disclosed, or represents that its use would not infringe privately owned rights. Reference herein to any specific commercial product, process, or service by trade name, trademark, manufacturer, or otherwise does not necessarily constitute or imply its endorsement, recommendation, or favoring by the United States Government or any agency thereof. The views and opinions of authors expressed herein do not necessarily state or reflect those of the United States Government or any agency thereof.

List of Abbreviations

1D	1 Dimensional
A	Pre-exponential Factor; sec^{-1}
B10	10% blend of biodiesel with ULSD
B20	20% blend of biodiesel with ULSD
C_{in}	Engine-out PM concentration; mg/scm
CO₂	Carbon Dioxide
CPF	Catalyzed Particulate Filter
DCPF	Downstream CPF
DDOC	Downstream DOC
DOC	Diesel Oxidation Catalyst
E_a	Activation energy; kJ. gmol^{-1}
EGR	Exhaust Gas Recirculation
EPA	Environmental Protection Agency
FBP	Final Boiling Point
FID	Flame Ionization Detector
HC	Hydrocarbons
HHV	Higher Heating Value
IBP	Initial Boiling Point
LFE	Laminar Flow Element
LHV	Lower Heating Value
MTU	Michigan Technological University
NMHC	Non-methane hydrocarbons
NO	Nitric Oxide
NO₂	Nitrogen Dioxide
NO_x	NO+NO ₂
PM	Particulate Matter
Pt	Elemental Platinum
R	Universal gas constant; J. (gmol.K)^{-1}
RR_o	PM reaction rate; sec^{-1}
scm	Standard Cubic Meter
SCR	Selective Catalytic Reduction
SME	Soy Methyl Ester
SOF	Soluble Organic Fraction
TPO	Temperature Programmed Oxidation
U.S.	United States
UDOC	Upstream DOC
ULSD	Ultra Low Sulfur Diesel
ΔP	Pressure drop; kPa

Abstract

Active regeneration experiments were carried out on a production 2007 Cummins 8.9L ISL engine and associated DOC and CPF aftertreatment system. The effects of SME biodiesel blends were investigated in this study in order to determine the PM oxidation kinetics associated with active regeneration, and to determine the effect of biodiesel on them. The experimental data from this study will also be used to calibrate the MTU-1D CPF model. Accurately predicting the PM mass retained in the CPF and the oxidation characteristics will provide the basis for computation in the ECU that will minimize the fuel penalty associated with active regeneration.

An active regeneration test procedure was developed based on previous experimentation at MTU. During each experiment, the PM mass in the CPF is determined by weighing the filter at various phases. In addition, DOC and CPF pressure drop, particle size distribution, gaseous emissions, temperature, and PM concentration data are collected and recorded throughout each experiment. The experiments covered a range of CPF inlet temperatures using ULSD, B10, and B20 blends of biodiesel. The majority of the tests were performed at CPF PM loading of 2.2 g/L with in-cylinder dosing, although 4.1 g/L and a post-turbo dosing injector were also used. The PM oxidation characteristics at different test conditions were studied in order to determine the effects of biodiesel on PM oxidation during active regeneration.

A PM reaction rate calculation method was developed to determine the global activation energy and the corresponding pre-exponential factor for all test fuels. The changing sum of the total flow resistance of the wall, cake, and channels, based on calculating $\Delta P/\mu \cdot \dot{V}$, was also determined as part of the data analysis process in order to check on the integrity of the data and to correct input data to be consistent with the expected trends of the resistance based on the engine conditions used in the test procedure.

It was determined that increasing the percent biodiesel content in the test fuel tends to increase the PM reaction rate and the regeneration efficiency of fuel dosing, i.e., at a constant CPF inlet temperature, B20 test fuel resulted in the highest PM reaction rate and regeneration efficiency of fuel dosing. Increasing the CPF inlet temperature also increases PM reaction rate and regeneration efficiency of fuel dosing. Performing

active regeneration with B20 as opposed to ULSD allows for a lower CPF temperature to be used to reach the same level of regeneration efficiency, or it allows for a shorter regeneration time at a constant CPF temperature, resulting in decreased fuel consumption for the engine during active regeneration in either scenario.

Chapter 1 Introduction

The diesel engine is important to many industries around the world since its introduction over a century ago. The durability, thermal efficiency, and increased torque over spark-ignition engines make diesel engines ideal for stationary power generation, on highway trucks, construction, agriculture, and a multitude of other applications worldwide including light-duty vehicles.

U.S. EPA emissions standards for heavy-duty diesel engines for model year 2007 resulted in many diesel engine equipped vehicles being outfitted with aftertreatment systems. These aftertreatment systems commonly consist of exhaust gas recirculation (EGR) with an oxidation catalyst (diesel oxidation catalyst or DOC) and particulate filter which may be catalyzed (catalyzed particulate filter or CPF) to reduce the tailpipe NO_x and particulate matter (PM) emissions from the engine.

As the filter is loaded with retained PM, active regeneration is periodically required to oxidize the PM in the filter. Active regeneration consists of injecting diesel fuel into the exhaust stream via in-cylinder or post-turbo fuel injection methods, which undergoes exothermal oxidation in the DOC, thereby increasing the exhaust gas temperature into the PM filter, and subsequently regenerating it through thermal oxidation. The fuel injected results in a direct fuel penalty because the injected fuel produces no useful work. In order to maximize the vehicle's fuel efficiency, high fidelity DOC and CPF models need to be developed, allowing the most fuel efficient engine control strategies to be implemented. Along with the emissions regulations, new OBD standards related to aftertreatment system functionality monitoring also need to be met. These OBD standards result in the necessity for sensors to be integrated for purposes such as monitoring the CPF outlet PM concentration to alert when failure exists in CPF PM filtering or when the DOC, CPF, and selective catalytic reduction (SCR) are not functioning and reducing the PM and NO_x emissions according to the OBD standards.

In order to help reduce the United States' dependency on foreign oil, the use of up to 20% blends, by volume, of biodiesel has been approved by most manufacturers. The motivation behind this research is to better understand the active regeneration process with diesel and biodiesel fuels, to aid in the development of the DOC and CPF models and subsequent OBD and engine control strategies. As such, the specific

objectives and an overview of the research described are presented in the following sections.

1.1 Introduction

A 2007 Cummins production aftertreatment system was used in this study consisting of a diesel oxidation catalyst (DOC) and a catalyzed particulate filter (CPF). As the engine out exhaust flows through the DOC channels, and subsequently over the precious metal wash coat within the DOC, the carbon monoxide (CO), hydrocarbons (HC), and nitric oxide (NO) are oxidized via chemical reactions occurring in the DOC.

The DOC also oxidizes the hydrocarbons injected via in-cylinder or post-turbo exhaust dosing during active regeneration, which generates the exothermic oxidation reaction that elevates the temperature of the exhaust before entering the CPF. The exotherm generated by the DOC, dependent upon flow rates of exhaust and fuel, produced CPF inlet temperatures ranging from 475 to 600°C to oxidize the particulate matter (PM) retained within the CPF during active regeneration. Active regeneration is periodically required to decrease the back pressure exerted on the engine which increases with CPF PM loading as well as maintaining save PM levels to avoid excessive temperature which could damage the substrate.

The fuel injected during active regeneration results in an overall fuel consumption penalty because the fuel injected in the exhaust produces no useful work. As such, active regeneration is not the preferred method of PM oxidation within the CPF, but it is a necessity because the engine will not always be operating at conditions that are suitable for passive oxidation of the PM. In order to minimize this fuel penalty, understanding the variables that affect the effectiveness of active regeneration is needed to develop fuel efficient engine operation strategies for active regeneration. These variables include, but are not limited to, CPF inlet temperature, PM loading within the CPF, fuel type, and fuel dosing method. CPF inlet temperatures ranging from 475 to 600°C, 2.2 ± 0.2 g/L CPF PM loading, and two blends of biodiesel were used in this study. Blends of biodiesel with ultra-low sulfur diesel (ULSD) are characterized by their 'B' factor, which represents the volume percent of biodiesel present in the ULSD-biodiesel blend, i.e., 10 and 20% biodiesel blended with ULSD are denoted as B10 and B20, respectively. The different fuels tested in this study were ULSD, B10, and B20.

Biodiesel refers to renewable fuel derived from vegetable oil, animal fat, or waste cooking oil and consists of the methyl esters of fatty acids, which is typically used with ULSD to produce various blends of biodiesel [3]. Most manufacturers state that no modifications to the engine are necessary if 20 volume percent or less is blended with ULSD, as long as the fuel meets the requirements stated in ASTM D7467 [4].

Increasing the CPF inlet temperature during active regeneration increases the PM reaction rate. Also, the reaction rate increases with increasing the percent biodiesel in the test fuels as observed by Austin [1]. Austin [1] concluded that at a constant target CPF inlet temperature, as the percent biodiesel increases, the amount of PM oxidized per gallon of dosing fuel used increases as well. At a constant level of PM oxidized per gallon of dosing fuel used, increasing the percent biodiesel decreases the required CPF inlet temperature.

Increasingly stringent regulations related to monitoring of the functionality of the CPF are going into effect as part of new OBD requirements for the model year 2013 [5]. In order to fulfill the requirements for monitoring CPF functionality, new sensors are required that directly measures the PM emissions after the CPF outlet, as well as survives the high temperatures (over 600°C) seen after the CPF (i.e., during active regeneration). These new sensors are required because the PM concentration detection limits required for the new OBD legislation cannot be determined by the other sensors currently in use.

This work is part of a DOE project and the results will also be published in a 2013 SAE paper [2] currently in review.

1.2 Research Goal and Objectives

The goal of this research was to further refine the active regeneration test procedure developed by Austin [1] on the Cummins ISM engine and to quantify active regeneration as conducted on a 2007 Cummins ISL engine operated on ULSD and 10 and 20% blends of methyl-ester biodiesel fuels. In order to achieve this goal, quantification of the effects of CPF PM loading, CPF temperature, dosing method (in-cylinder or post-turbo dosing injection methods), and fuel type was required using the collected experimental data. The objectives used to accomplish the goal were as follows:

1. Conduct a literature review on past PM thermal oxidation studies and relate this to the current studies,
2. Develop an improved procedure to collect high quality data that can support the active regeneration experimental analysis and modeling efforts,
3. Develop a method to calculate the PM reaction rate through the entire active regeneration period based on CPF PM loading and CPF temperature,
4. Determine the effects of CPF temperature, biodiesel blended fuels, and dosing method on the PM oxidation in the CPF during active regeneration including fitting the PM reaction rate to an Arrhenius model and optimization of rate parameters (A and E_a) for each test fuel,
5. Analyze the total of the filter wall, cake, and channel resistances by calculating $\Delta P/(\mu \cdot \dot{V})$ during the entire active regeneration test procedure.

High quality experimental data is vital to accomplishing this goal, and as such, a consistent experimental procedure throughout every test was developed and used which limits the variations between individual tests.

Along with the experimental portion of the research, a modeling effort is proceeding in parallel which uses the experimentally collected active regeneration data for calibration of a 1D CPF computer simulation (the MTU-1D CPF model). As stated above, the modeling effort is proceeding in parallel with the experimental work to develop and calibrate the MTU-1D CPF model. As thus an objective of this research with respect to the modeling effort was to assist in data compilation and explanation. Gaseous emissions, exhaust flow rate, CPF PM loading, engine-out and CPF-out PM concentration, and temperature data has been compiled and processed for each phase of each active regeneration experiment performed on the 2007 Cummins ISL engine. The calibration of the MTU-1D CPF model is underway and will be used to determine and model the PM oxidation kinetics within the CPF during active regeneration under each set of experimental conditions.

1.3 Outline of Thesis

This chapter provides a brief overview of the material included in this study. The introduction section has provided an overview of the aftertreatment system and PM oxidation via active regeneration. Quantifying the effects of biodiesel blends as

compared to ULSD on PM oxidation during active regeneration is the primary goal of this study. The six more specific objectives have been described.

Chapter 2 is devoted to providing background information as well as a synopsis of the literature that has already been published relative to the research goal in this study. Literature from past research projects at Michigan Technological University as well as technical papers published by various organizations relative to this study are summarized in this chapter.

Chapter 3 describes the test cell and data acquisition instruments used to gather temperature, pressure, gaseous concentrations, PM concentrations, and other types of data vital for reaching the research goals and objectives. The engine, aftertreatment system, and dynamometer specifications are presented as well as the overall active regeneration test procedure and active regeneration test matrix.

Chapter 4 begins with the experimental results from active regeneration tests performed in this study. Data from active regeneration pertaining to PM reaction rate and fuel efficiency of PM oxidation is presented along with temperature, gaseous and PM concentrations, and other data. The effects of biodiesel blends on these data are also presented.

Chapter 5 presents a summary, conclusions from this study, and recommendations for future research. Appendices detailing various aspects of this study are also presented following Chapter 5.

Chapter 2 Background and Literature Review

This chapter focuses on the published literature pertaining to the research goals of this thesis. First, papers are reviewed about ULSD and biodiesel emissions related to diesel engines. In this section, emissions regulations are presented along with changes to engine emissions when changing from ULSD to biodiesel blended fuel. Next, mechanisms for PM oxidation are presented, where the findings are based off reactor data from past PM oxidation experimentation. The PM oxidation review leads into the next section, where the results of active regeneration experimentation are reviewed. Finally, a section devoted to PM concentration sensor technology is presented.

2.1 ULSD and Biodiesel Emissions

The diesel engine has been in a state of constant development for the past 75 years. One of the reasons it has seen this effort is its ability to provide reliable power for many applications, at a higher thermal efficiency than the gasoline fueled spark ignition engines. During the past 40 years, the United States EPA regulations regarding the tailpipe emissions of PM and gaseous species of CO, HC, and NO_x, have become more restrictive. Beginning in 2007, the PM emissions regulations were such that manufacturers had to use DOC and CPF aftertreatment devices to reduce the engine-out PM emissions to the levels required by the EPA. In 2010, the EPA heavy duty diesel emissions are regulated to 0.2 g/bhp-h for NO_x, 0.14 g/bhp-h for NMHC, 15.5 g/bhp-h for CO, and 0.01 g/bhp-h for PM which has been in effect since 2007. The DOC provides for the oxidation of NO to NO₂ which then increases the passive NO₂ assisted oxidation of PM in the CPF and its second function is to oxidize the injected hydrocarbons for periodic active regeneration of the retained PM in the CPF.

In the design of a diesel engine, there is a direct tradeoff between PM and NO_x engine-out emissions. Depending on the aftertreatment system components being used, one can tune an engine to produce little PM with elevated NO_x levels (useful when utilizing NO_x reduction aftertreatment technology) or produce more PM with reduced NO_x levels. The approach of using high engine out NO_x levels and a NO_x aftertreatment system allows the reduction of fuel consumption for the engine. Increasing NO_x and decreasing PM emissions results in increased engine efficiency with decreased power and vice versa. The use of a CPF is primarily responsible for

retaining and oxidizing the PM emitted from the engine. The DOC-CPF is the aftertreatment system used in this study. Complete understanding of the loading and oxidation of the PM retained within the CPF allows for the most fuel efficient engine tuning and control strategies to be used.

The DOC serves two purposes; first, it is a flow through chemical reactor which oxidizes CO, HC, and NO emissions into CO₂, NO₂, H₂O, N₂ and O₂. NO emissions are oxidized to NO₂, which is the primary component responsible for the passive oxidation of PM within the CPF. Second, the DOC is used for oxidizing excess HCs injected into the exhaust stream to produce the exotherm required for active regeneration of the PM within the CPF. The concept of active regeneration will be discussed later. Figure 2.1 depicts the conversion of NO to NO₂, as well as the oxidation of HC and CO gaseous species at various temperatures [6].

The most common CPF is a wall flow filter that retains the majority (up to 97%) of PM emissions from the diesel engine. The term wall flow comes from the fact that every other channel in the substrate is blocked, so that the exhaust flows down the inlet channel, through the wall of the substrate, and out the outlet channel. The flow through the substrate wall is where the filtration of PM from the exhaust stream is accomplished. Figure 2.2 depicts the characteristics of a wall flow CPF substrate. The filter undergoes active regeneration to reduce the PM mass, and subsequently, the back pressure on the engine, after an amount of PM, such as 4 g/L, is retained in the filter. The PM is oxidized using passive or active regeneration, as mentioned previously, with active regeneration being the focus of this study.

The use of biodiesel is occurring more as the need for reducing the dependence on petroleum based fuel increases. Biodiesel is the name given to fuels derived from the esterification of renewable oils, fats, and fatty acids as described in Austin [1], and is manufactured from plant oils, recycled cooking grease and oil, or animal fats. As of today, most major engine manufacturers have approved the use of 20% biodiesel blends in their engines as long as the fuel meets the requirements stated in ASTM D7467 [4].

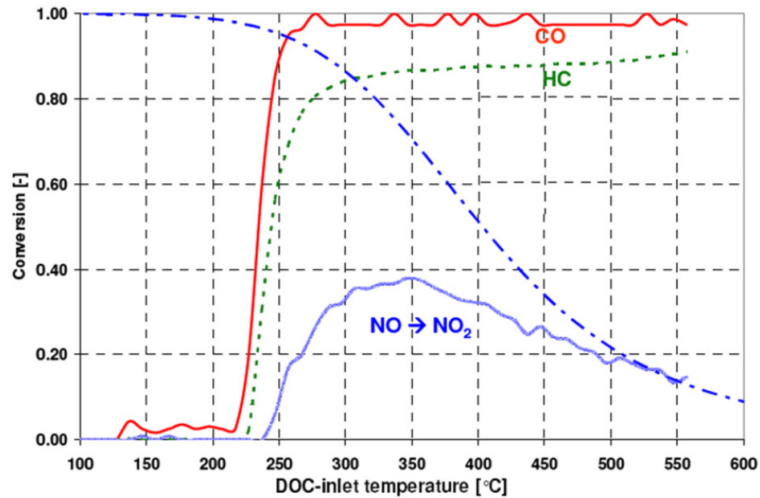


Figure 2.1: DOC Conversion Efficiencies for Various Gaseous Species [6]

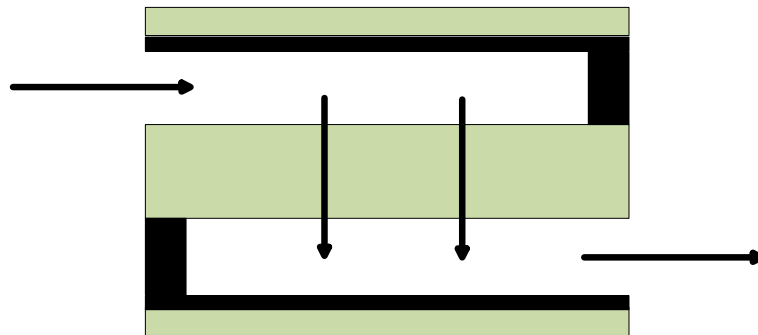


Figure 2.2: Example of CPF Wall Flow Substrate Structure

The effect of biodiesel on engine emissions is such that, in general, HC, CO, and PM emissions are reduced, while NO_x emissions are slightly elevated or reduced, depending on the fuel blend and engine control strategy. A study by Poitras et al. [7] reported that with biodiesel fuels, NO_x levels were increased at high engine loads but were decreased at low engine loads, with increasing biodiesel concentrations in the test fuel. The maximum reported increase and decrease was 7.3 and 25%, respectively, using B100. No significant changes in the NO₂ concentrations were reported, regardless of biodiesel blend used. Figure 2.3, from Poitras et al. [7], depicts the relative change of engine-out NO_x emissions across 3 test modes with varying blends of soy methyl ester (SME) biodiesel. NO_x emissions increased and decreased based on the test mode and fuel blend being used, with no apparent pattern being visible. The largest changes were seen with B50 and B100 blends.

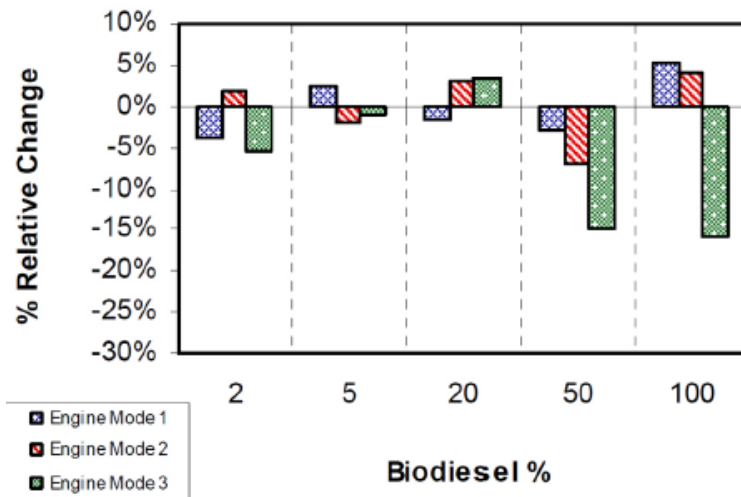


Figure 2.3: Relative Change of NO_x Emissions with SME Biodiesel Blends Compared to ULSD [7]

A study by Kawano et al. [8] on the exhaust characteristics of commercial vehicles fueled with biodiesel confirms those effects. This is partially due to the oxygen in the fuel, where more combustion sites are present in the combustion chamber, reducing the total engine-out emissions due to increased combustion efficiency. A study by Parihar et al. [9] described a reduction of PM mass emissions for 20% biodiesel blends for the complete particulate size range measured.

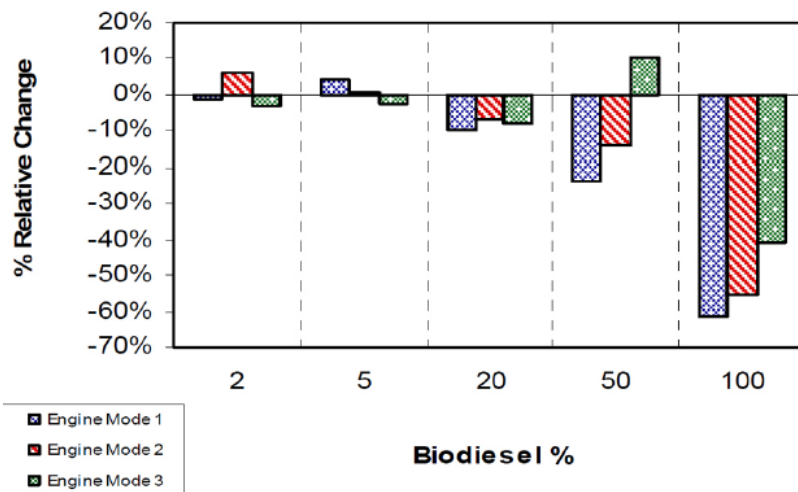


Figure 2.4: Relative Change of TPM Emissions with SME Biodiesel Blends Compared to ULSD [7]

Poitras et al. [7] also reported lower PM emissions with increasing biodiesel blends, even though the NO_x emission results were mixed. Total PM (TPM) emissions decreased 24 and 62% for B50 and B100 SME biodiesel, respectively, when compared to ULSD, with the results shown in Figure 2.4.

In general, the use of biodiesel blends results in a decrease of PM emissions, while some experiments resulted in a decrease of NO_x emissions and an increase of NO_x emissions in other experiments. Eckerle et al. [10] reported that the higher cetane number associated with biodiesel blends causes an increased ignition delay, which leads to higher NO_x emissions at low load conditions due to increased diffusion combustion within the combustion chamber. Other factors which can influence the NO_x emissions from an engine fueled with biodiesel is the fuel flow rate. Since biodiesel has a lower energy content than ULSD, more fuel is required to produce the same power. Since the fuel flow rate is commonly used to estimate the torque output of the engine, the control strategy determines that the engine is operating at a different load point and may adjust parameters such as fuel injection timing and duration, boost pressure, or exhaust gas recirculation (EGR) rate to maintain the desired power output of the engine, which leads to NO_x emission variability.

2.2 PM Oxidation

2.2.1 Introduction

The CPF collects approximately 97% of the engine out PM, on a mass basis, from the exhaust stream before exiting the tailpipe. As PM accumulates in the CPF, a cake layer of PM builds up on the substrate walls, which serves as a secondary filtering medium, removing up to 95% of the PM before reaching the substrate wall which has approximately 50% filtration efficiency.

As the PM is retained in the CPF, the back pressure on the engine gradually increases, which gradually decreases fuel efficiency. Periodically, the PM needs to be oxidized with active regeneration from the CPF to reduce this back pressure. The PM within the CPF is oxidized in one of two ways;

1. Passive oxidation – using the engine-out NO_x concentrations and exhaust temperature with a DOC to produce NO₂, which oxidizes the PM within the CPF.

2. Active regeneration – using fuel injected either in-cylinder or post-turbo and a DOC to elevate exhaust temperatures entering the CPF, which oxidized the PM within the CPF.

For passive oxidation there are no direct fuel penalties, because the engine operating conditions and DOC are what cause the oxidation of the PM within the CPF. Experimentation by Shiel [11] showed passive oxidation to be an effective oxidation technique with exhaust temperatures ranging from 250 to 400°C (corresponding to 1.38 and 1.91 on the horizontal axis in Figure 2.5), where the engine speed and load combinations, along with the DOC, were responsible for the NO₂ production and subsequent PM oxidation within the CPF. Another benefit of passive oxidation is that the PM does not require any contact with the catalyst coating on the CPF substrate; the gaseous NO₂ and temperatures in the exhaust stream passing through the PM cake layer is all that is required for PM oxidation to occur.

Active regeneration is the least desirable method of PM oxidation because of the direct fuel penalty associated with injecting fuel into the exhaust stream, usually diesel fuel from the engine’s fuel system. Understanding the factors that affect PM oxidation during active regeneration is important because the most fuel efficient active regeneration control strategies can be produced once a complete understanding of PM oxidation characteristics is determined.

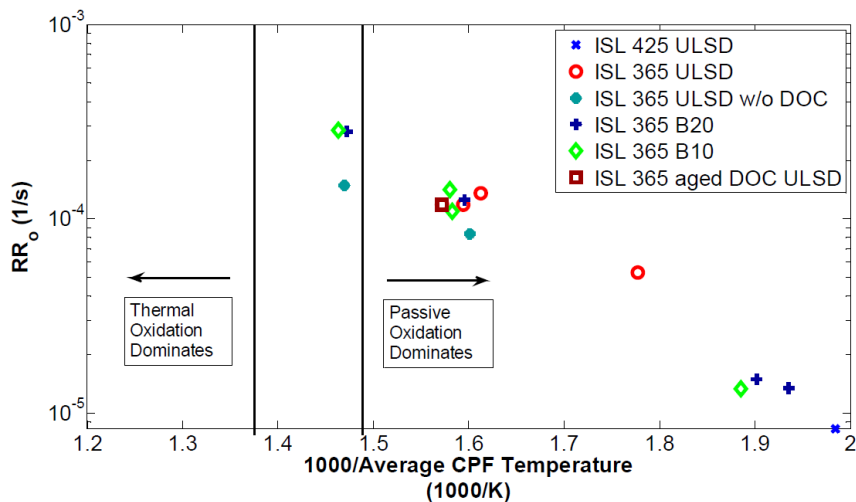


Figure 2.5: Passive Oxidation CPF PM Reaction Rate vs. 1000/Average CPF Temperature (Kelvin) [11]

2.2.2 Reactor PM Oxidation Studies

There are many factors that influence the oxidation of PM within the CPF during active regeneration, such as temperature, filter substrates, catalyst coatings, and many others. In a study by Yezerets et al. [12], carbon black and diesel PM oxidation characteristics were examined. They concluded that diesel PM oxidation was enhanced with the addition of up to 10% water within the reactor while the carbon black was not affected. It is stated that the presence of water does not change the nature of the oxidation process, but enhances the probability of the reaction event, due to the increase in pre-exponential factor of the Arrhenius equation that was observed. With the presence of water, the activation energy for diesel PM remained in the range of 95 ± 3 kJ/gmol and 105 ± 3 kJ/gmol for the carbon black.

In another study by Yezerets et al. [13], un-catalyzed isothermal, temperature programmed oxidation (TPO), and serial TPO experiments on two samples of PM that were obtained from different engines and duty cycles were conducted. This was done in order to evaluate the possible variations in soot reactivity based on PM origin. As such, the samples were found to contain different amounts of the soluble organic fraction (SOF) and ash. It was observed that the kinetic parameters describing PM oxidation are rapidly changing during the first 10-25% of PM oxidation, and that this phenomenon is not related to temperature. It was found that the activation energy changes from 45-65 kJ/gmol for the initial PM oxidation to 125-145 kJ/gmol for the remainder. Yezerets et al. [13] determined that the linearity of the Arrhenius curves produced from PM oxidation after the initial 25% was excellent between 330 and 610°C, as shown in Figure 2.6, where the oxidation rate constant (k) is plotted against $1000/\text{temperature}$. Realizing this, they were able to determine the kinetic parameters of PM oxidation by O_2 with high confidence. It was also concluded that the PM oxidation was uniform after the initial 25% was oxidized. The activation energy for the two PM samples were determined to be 126 ± 3 kJ/gmol and 146 ± 3 kJ/gmol, with a difference of 30°C in light-off temperature. These activation energies were calculated following SOF desorption and oxidative pre-treatment.

In a study by Oki et al. [14], PM emitted from a diesel fired lamp was used in the visualization experimentation. They concluded that the activation energy for the PM trapped on an un-catalyzed DPF membrane resulted in activation energies between 110 and 180 kJ/gmol.

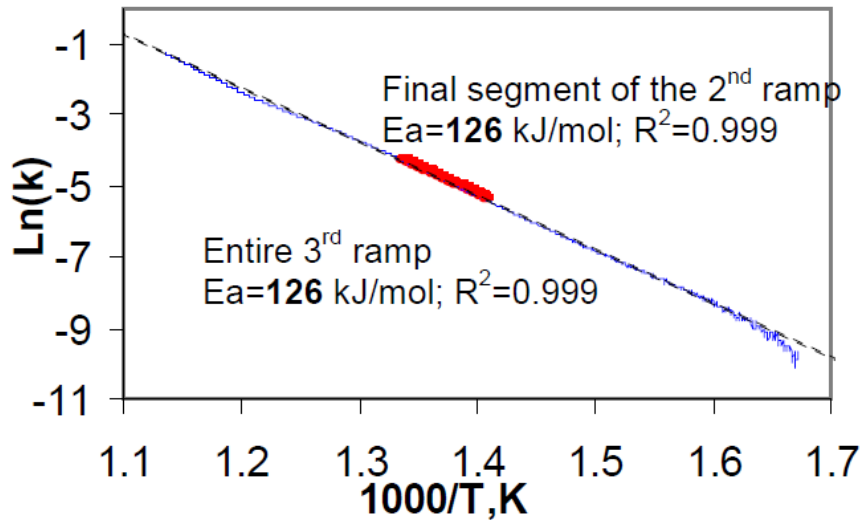


Figure 2.6: Soot Reactivity Measured During Temperature Ramps [13]

2.3 Active Regeneration

Active regeneration of the PM within the CPF results in a direct fuel penalty because the fuel is injected either late in the cylinder or directly into the exhaust downstream of the turbocharger. The fuel injected produces no useful work for the engine, resulting in decreased fuel efficiency. The main benefit of active over passive oxidation is the rate at which PM is oxidized.

As stated previously, active regeneration is the least desirable PM oxidation method due to the direct penalty associated with injecting diesel fuel into the exhaust gases. The fuel is required for the DOC to oxidize it and to raise the exhaust temperature entering the CPF into the thermal oxidation regime. The thermal oxidation regime is generally said to be at CPF temperatures above 400°C. The DOC is subjected to HC concentrations up to 21,000 ppmC according to Chillumukuru [15], so it is important that the DOC has the capability for oxidizing this concentration of HC. DOC's are commonly coated with a Pt-based catalyst that exhibit HC conversion efficiencies based on exhaust gas temperature.

The point at which 50% HC conversion efficiency is reached is termed the DOC's light-off temperature. Attempting active regeneration below the light off temperature can result in DOC face plugging. Attempting active regeneration below the DOC light-off temperature also results in an overall waste of fuel, due to the reduced HC

conversion efficiency below the light-off point. Injecting fuel below the light off point also requires additional fuel to reach the same CPF inlet exhaust temperature, which is a key factor related to CPF PM oxidation during active regeneration.

CPF inlet temperature is one of the most significant influences on the efficiency of PM oxidation during active regeneration. Lower CPF inlet temperatures require less fuel to achieve, but the regeneration process takes longer to reach the same level of PM oxidation. Experimentation by Austin [1] with B20 resulted in an efficiency of PM oxidation of 40 grams of PM oxidized per gallon of fuel injected at a CPF temperature of 520°C compared to 120 grams of PM oxidized per gallon of fuel injected at a CPF temperature of 575°C, corresponding to a PM oxidation efficiency increase of 200% for a 55°C temperature increase. Figure 2.7 depicts the efficiency of PM oxidation resulting from experimental studies conducted by Austin [1].

Maintaining exhaust flow during active regeneration is also important. Once active regeneration has been initiated, a sudden drop in exhaust flow could lead to an uncontrolled regeneration. An uncontrolled regeneration occurs when the PM within the CPF begins to rapidly oxidize on its own, creating large thermal gradients within the CPF, which have the potential to damage the CPF substrate. This occurred during experimentation by Austin [1] where an uncontrolled regeneration resulted in a cracked CPF. The only noticeable change in performance was decreased PM filtration efficiency, with the crack being discovered after investigation into the CPF performance was carried out.

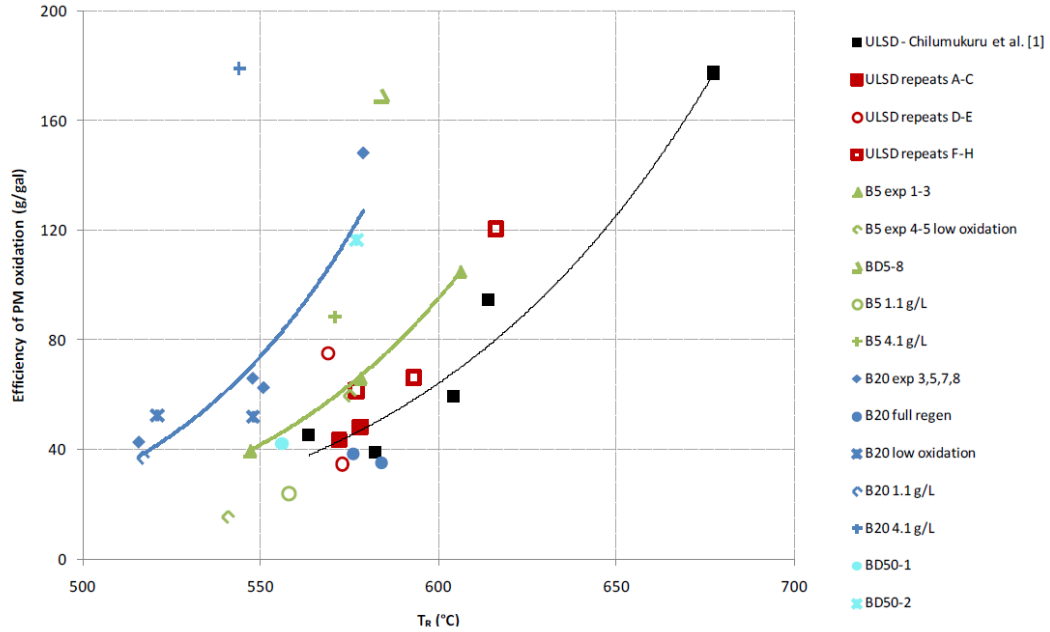


Figure 2.7: Efficiency of PM Oxidation as a Function of Average CPF Temperature (T_R) [1]

2.4 Downstream PM Concentration Sensor

As discussed previously, emissions regulations for the 2007 model year for U.S. heavy duty on-highway diesel engines resulted in diesel engine manufacturers using a DOC and CPF, to meet the PM emission standards. The DOC and CPF remain vital for the reduction of tailpipe PM emissions, but OBD regulations require the monitoring of the functionality of the CPF for the model year 2013 [5]. In order to fulfill the requirements for monitoring CPF functionality, new sensors are required that directly measure the PM emissions after the CPF outlet, as well as survive the harsh environment seen after the CPF (i.e., during active regeneration). These new sensors are required for the new OBD standards since this is the most effective way to sense failed PM filters.

Delphi has begun the development of a downstream PM sensor that uses technology similar to that of Bosch Lambda sensors [5], where the collecting sensing element is based existing multi-layer ceramic sensor technology. According to Ochs et al. [5] and Bender et al. [16], the sensing element is composed of two inter-digitated comb-like electrodes (IDE) with an infinite electrical resistance, an internal heater, and a temperature measuring element.

As PM is deposited on the electrodes, an electrical contact forms between them, and the resistance between electrodes begins to decrease. After a certain amount of PM collection, a pre-defined current threshold is reached, where the heater is activated to heat the electrodes above 600°C, thereby regenerating the sensor. The response time of the sensor is defined as the amount of time between the start of measurement and start of the sensor regeneration. The response time correlates with the exhaust PM concentration; it is the response time that is used to monitor the CPF's functionality within the OBD system. The sensor is connected to a sensor control unit (SCU), which transmits the sensor signal to the engine control unit (ECU) via CAN-bus. According to Ochs et al. [5], the sensor management, regeneration control, signal processing, and sensor signal verification are all controlled by the SCU. Figure 2.8 depicts the sensor functionality as well as PM accumulation on the sensor electrodes as described by Ochs et al. [5]. The blue line represents the sensor current between the electrodes during the PM deposition phase. The images show PM deposition across the electrodes, where the dark areas are the electrodes and the white areas are the isolating aluminum oxide. The left image shows the beginning of the measurement where no connections are formed, and the right image shows the connection between the electrodes by the deposited PM.

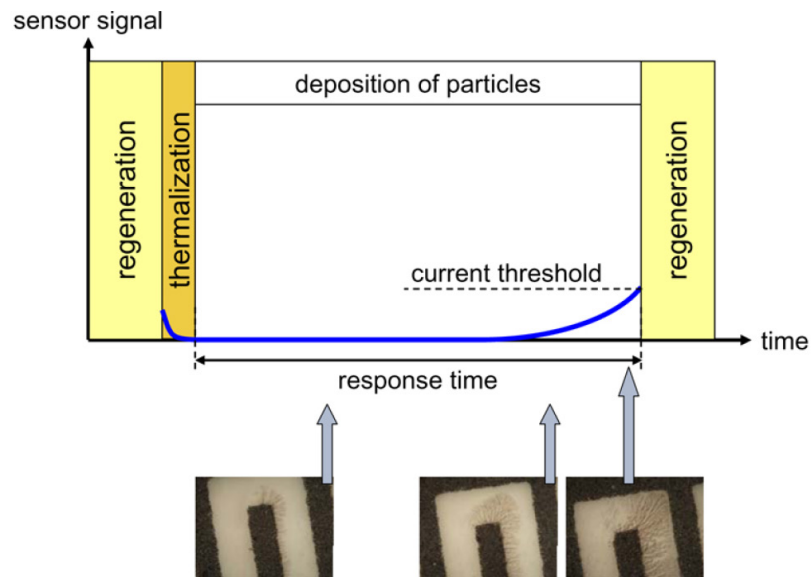


Figure 2.8: Signal Characteristics of the Resistive Particulate Matter Sensor and Images Showing PM Deposition on Electrodes [5], Copyright © SAE International, Reprinted with permission

The CPF OBD model concept utilizes simulated PM mass flow of the engine (available for DPF load calculations) and calculates PM mass flow out of the CPF by utilizing a limit CPF model [5]. The model predicts the expected response time of the sensor and compares it with the actual response time. If the measured response time is greater than the predicted response time, the OBD function declares that the CPF is functioning properly. If the measured response time is lower than the predicted response time, the OBD functions declare that there is a problem with the CPF functionality.

Bender et al. [16] tested six Delphi PM sensors simultaneously, installed at various locations downstream of a CPF in order to assess part-to-part variations and location dependencies over two sets of experiments. The first set utilized a healthy CPF while the second set of experiments utilized simulation of a failed CPF to produce downstream concentration targets of 0.03 g/bhp-hr. It was concluded that there was no obvious location dependency on the sensor output and that the differences in output trends could be related to PM morphology or deposited particle size and that the sensor output voltage should not be used as a direct measure of exhaust PM concentrations. Bender et al. [16] also concluded that the computed PM resistance is inversely proportional to accumulated PM on the sensor, resulting in a diminishing sensor 'gain' with accumulating PM.

2.5 Summary

The diesel engine has been in a state of constant development for the past 50 years, or more, because of its ability to provide reliable power for many applications, at a more efficient level than the gasoline fueled SI engines. Emission standards required for diesel engine equipped vehicles have resulted in the widespread use of DOC and CPF aftertreatment devices to reduce PM emissions. In the world of diesel engine calibration, a direct tradeoff between PM and NO_x emissions is apparent, where decreased NO_x engine-out emissions result in increased engine-out PM emissions and vice versa.

As interest in reducing the dependency on petroleum based fuels has increased, many manufacturers are certifying their engines with use of up to 20% volume blends of biodiesel (B20). In general, the use of biodiesel reduces engine-out HC,

CO, and PM emissions, while NO_x emissions have been shown to increase or decrease, depending on fuel blend and engine control strategy [1, 7, 11].

Since the CPF is able to retain up to 97% of the engine-out PM in the exhaust stream, the back pressure on the engine gradually increases as the filter is loaded over time since the passive oxidation rate is typically not equal to the engine-out PM rate for many applications. Oxidation of the PM by periodic active regeneration within the CPF is necessary to reduce this back pressure.

Passive oxidation utilizes engine-out NO₂ concentrations to oxidize the PM within the CPF gradually with no direct fuel penalty. Active regeneration utilizes excess HC (fuel) injected into the exhaust to drive the temperature of exhaust entering the CPF to levels suitable for thermal PM oxidation. Active regeneration is less desirable because the injection of fuel into the exhaust stream poses a direct fuel penalty, since the fuel being injected produces no useful work. CPF inlet temperature is one of the most significant influences on the efficiency of PM oxidation during passive and active regeneration. Increasing the CPF inlet temperature from 520 to 575°C has shown to increase the PM oxidation efficiency of 200% [1].

With OBD standards in effect for the 2013 model year related to the monitoring of CPF functionality, new sensor technologies are being explored to measure the exhaust PM concentration in the CPF outlet. One such technology is being explored by Delphi where the sensing element is composed of two inter-digitated comb-like electrodes (IDE) with an infinite electrical resistance, an internal heater, and a temperature measuring element [5, 16]. As PM is deposited on the electrodes, an electrical contact forms between them, and the resistance between electrodes begins to decrease. The response time of the sensor is defined as the amount of time between the start of measurement and start of the sensor regeneration, where the response time is used to monitor CPF functionality.

Chapter 3 Experimental Setup and Test Procedures

Eighteen active regeneration experiments using ULSD, B10, and B20 biodiesel blends were conducted on a 2007 Cummins 8.9L 365 HP ISL (ISL 365) and one experiment was conducted on the 425 HP (ISL 425) engine rating. Specifically, ten ULSD, four B10, and five B20 tests were performed between February 2011 and July 2012, with one of the ULSD tests being the one which was performed on the ISL 425. The tests run with ULSD provide baseline data while the data from biodiesel tests allows for the comparison of the PM loading and oxidation characteristics with varying blends of biodiesel.

3.1 Engine and Dynamometer

The specifications for the 2007 Cummins ISL used in this study are shown in Table 3.1. While the ISL 425 was being used during passive oxidation studies by Shiel [11], an active regeneration experiment was performed to determine if any differences were apparent in the PM oxidation characteristics due to the larger turbocharger and the calibration changes in the ECU.

Engine manufacturers often build a base engine and offer a range of power outputs to widen the markets which can utilize the engine for their specific needs. Based on the requirements of the engine, it can be outfitted from a selection of turbochargers and engine calibrations to meet the needs of industries such as mobile power generation, heavy duty trucks of various sizes, buses, and a variety of others.

Table 3.1: ISL Engine Specifications

Model	Cummins ISL - 272 kW (365 HP) and 317 kW (425 HP)*
Year of Manufacture	2007
Cylinders	6, inline
Bore & Stroke	114x144.5 mm
Displacement	8.9L
Aspiration	Turbocharged
Aftercooling	Cummins Charge Air Cooler
Turbocharger	Variable Geometry Turbo (Holset)
Rated Speed and Power	2100 RPM and 272 kW
Peak Torque	1695 Nm @ 1400 RPM
Common Rail Pressure (peak)	160 Mpa
EGR System	Electronically Controlled and Cooled
*Change of turbocharger and ECU	

The engine dynamometer that connects to the 2007 ISL is a Dyne Systems Dynamic unit, model number 8121, wet gap/low inertia eddy current dynamometer. The engine speed and torque were regulated by a Digalog Model 1022A dynamometer controller which can be operated in 'speed' and 'load' control modes. For the active regeneration engine testing, the controller was operated in the 'speed mode' where the controller holds a set speed and the user controls the load by operating the engine's throttle controls.

3.2 Fuel Properties

One batch of each biodiesel blend and two batches of ULSD were used for the active regeneration tests in this study, and samples of the fuels were tested with the results shown in Table 3.2. The hydrogen to carbon (H/C) and oxygen to carbon (O/C) ratios were calculated for each fuel (not included in the fuel analysis) and are also shown in Table 3.2, with the calculation methodology used to determine them in Appendix A.

Table 3.2 Fuel Properties for Experimental Test Fuels*

		ULSD-1	ULSD-2	B10	B20
Sulfur [ppm]		7	12	4	4
Viscosity @ 40°C [cst]		2.290	2.609	2.368	2.533
API Gravity		35.6	33.4	36.5	35.5
Specific Gravity		0.847	0.858	0.842	0.847
Cetane Index		39.83	40.16	45.38	45.52
Distillation	IBP[°C]	168	172	168	168
	FBP[°C]	340	359	343	345
Water [ppm]		92	348	415	553
ICP for Metals [ppm]		<1**	<1**	<1**	<1**
IR for % Biodiesel		0	<0.1	10.1	19.4
Higher Heating Value [MJ/kg]		45.60	45.21	45.09	44.48
Lower Heating Value [MJ/kg]		42.80	42.55	42.47	42.03
H/C		1.833	1.833	1.828	1.826
O/C		-	-	0.01	0.02

** All metal content less than 1 ppm

IBP: Initial Boiling Point

FBP: Final Boiling Point

*Fuel analyzed by Cummins laboratory

Table 3.3 DOC and CPF Specifications

Specification	DOC	CPF
Part #	EPN Q621300 (ISL 365) EPN Q629360-10 (ISL 425)	EPN Q623316
Substrate	Cordierite	Cordierite
Cell Geometry	Square	Square
Diameter [mm]	267	267
Length [mm]	102	305
Total Volume [L]	5.7	17.1
Cell Density [cells/cm ² , cells/in ²]	62, 400	31, 200
Cell Width [mm]	1.09	1.49
Frontal Area [%]	91	69
Channel Wall Thickness [mm]	0.114	0.305
Wall Density [g/cc]	N/A	0.45
Specific Heat [J/kg K]	N/A	891
Thermal Conductivity [W/m K]	N/A	0.84
Porosity [%]	35	52
Mean Pore Size [micron]	N/A	13

3.3 Aftertreatment System

A 2007 Cummins aftertreatment system was used for all active regeneration tests which consisted of a diesel oxidation catalyst (DOC) upstream of a catalyzed particulate filter (CPF). Table 3.3 lists the specifications for the DOC and CPF. After the switch from the ISL 365 to ISL 425, a 2010 Cummins DOC was implemented due to the original DOC being prone to face plugging. No noticeable difference from an active regeneration stand point was noticed with the new DOC, with the exception of the reduced frequency of face plugging.

3.4 Test Cell Setup

The test cell layout can be seen in Figure 3.1, which details the engine, dynamometer, exhaust, instrumentation, and dosing methods that were used in this study. The test cell includes two available exhaust paths for use during testing which provide the ability to start or stop a test phase without adverse effects on the engine or aftertreatment system. The path which bypasses the aftertreatment system is named the baseline while the path which utilizes the aftertreatment system is called the trapline. For startup of the engine and during warm up periods, the exhaust travels through the baseline, allowing the engine to warm up completely before exhaust is allowed to flow through the aftertreatment system, thereby reducing

experimental data variability. Once the engine has stabilized at the desired operating conditions, two pneumatically controlled valves are actuated to divert the exhaust through the trapline. The first valve closes the baseline while the second valve opens the trapline. The instant that the trapline valve is opened marks the beginning of that particular phase in the experiment.

3.4.1 Data Acquisition System

A data acquisition system from National Instruments was used with LabVIEW to monitor and record temperature and pressure data throughout the test cell. Experimental data was recorded at 5Hz for all active regeneration tests conducted in this study. Tests conducted on the 365 and 425 HP rated ISL engines will be referred to as ISL 365 and ISL 425 tests throughout this thesis.

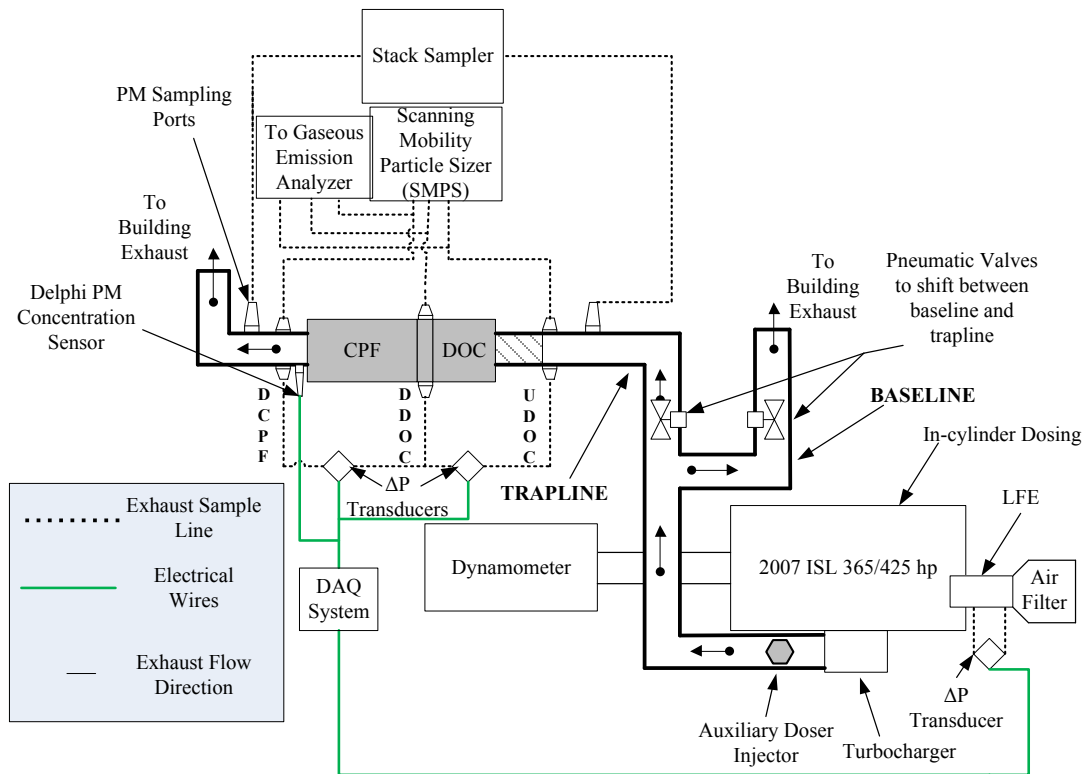


Figure 3.1 Test Cell Schematic for 2007 Cummins ISL

3.4.2 Temperature Measurements

Temperature measurements were recorded using three diameters of ungrounded type K thermocouples, provided by Watlow, located throughout the aftertreatment system. The diameter of thermocouples used depends on the location that the temperature was being recorded. Thermocouple locations, descriptions, and part numbers can be seen in Table 3.4. Gaseous temperatures were measured with 0.125 in. diameter thermocouples. The DOC and CPF required 0.020 and 0.032 in. diameter thermocouples to measure internal substrate temperatures, respectively. The DOC and CPF thermocouple layout can be seen in Figures 3.2 and 3.3, respectively. During the analysis of experimentally collected test data, the average CPF temperature required calculation. The volume averaged CPF temperature was found by applying a weighting factor to certain sets of thermocouples. The weighing factor for C1-C4, C5-C8, C9-C12, and C13-C16 are 0.303, 0.287, 0.197, and 0.213, respectively. The weighting factors were calculated by taking the ratio of the CPF length occupied by each axial set of thermocouples by the overall length of the CPF. For example, for C1-C4, the amount of axial area occupied by them in the CPF is assumed to be 92.5mm. This comes from the addition of the 32mm distance from the inlet to the C1-C4 axial row and the midway distance from C1-C4 to C5-C8 of 60.5mm. This length is then divided by the total length of 305mm to give the 0.303 weighting factor. For the calculations in this study, the volume averaged CPF temperature was calculated using thermocouples C1-C3, C5-C7, C9-C11, C13-C15, or all thermocouples within the CPF except those at the outermost radial location. Hutton [6] further explains the concept of the volume averaged CPF temperature.

Table 3.4 Thermocouple Specifications

Location	Type	Diameter [in]	Length(s) [in]	Watlow P/N	Body Material
DOC	K	0.02	12, 17	AX1078701, PT-227664-001	Inconel
CPF	K	0.032	12, 17	AX1078801, Special Order	Inconel
Engine Exhaust	K	0.125	6	ACGF00Q060U40000	Inconel

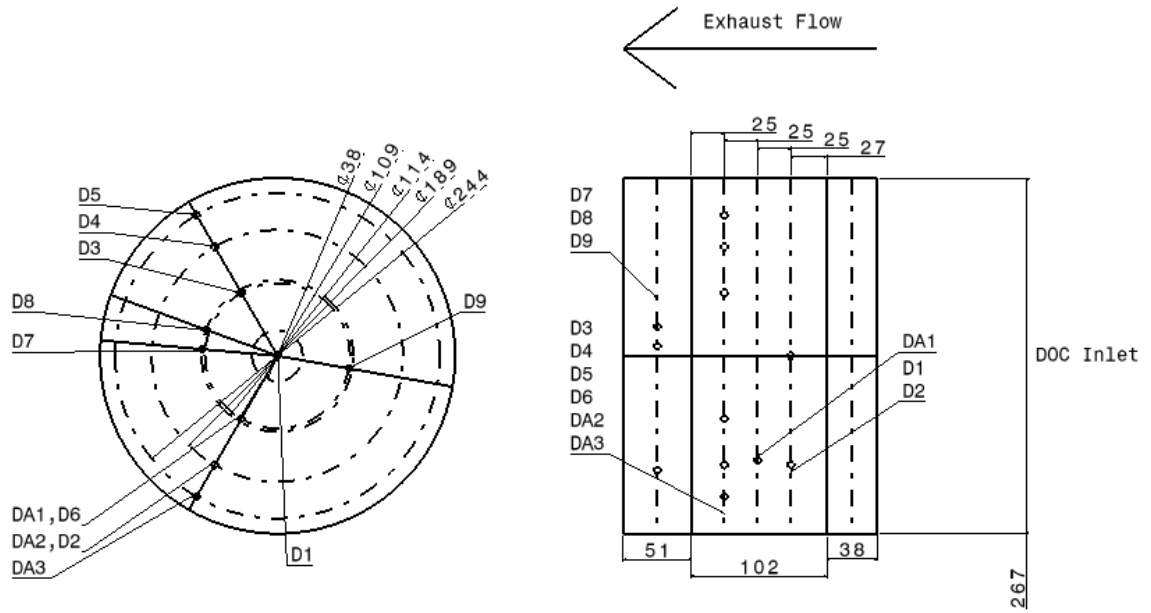


Figure 3.2 DOC Thermocouple Layout

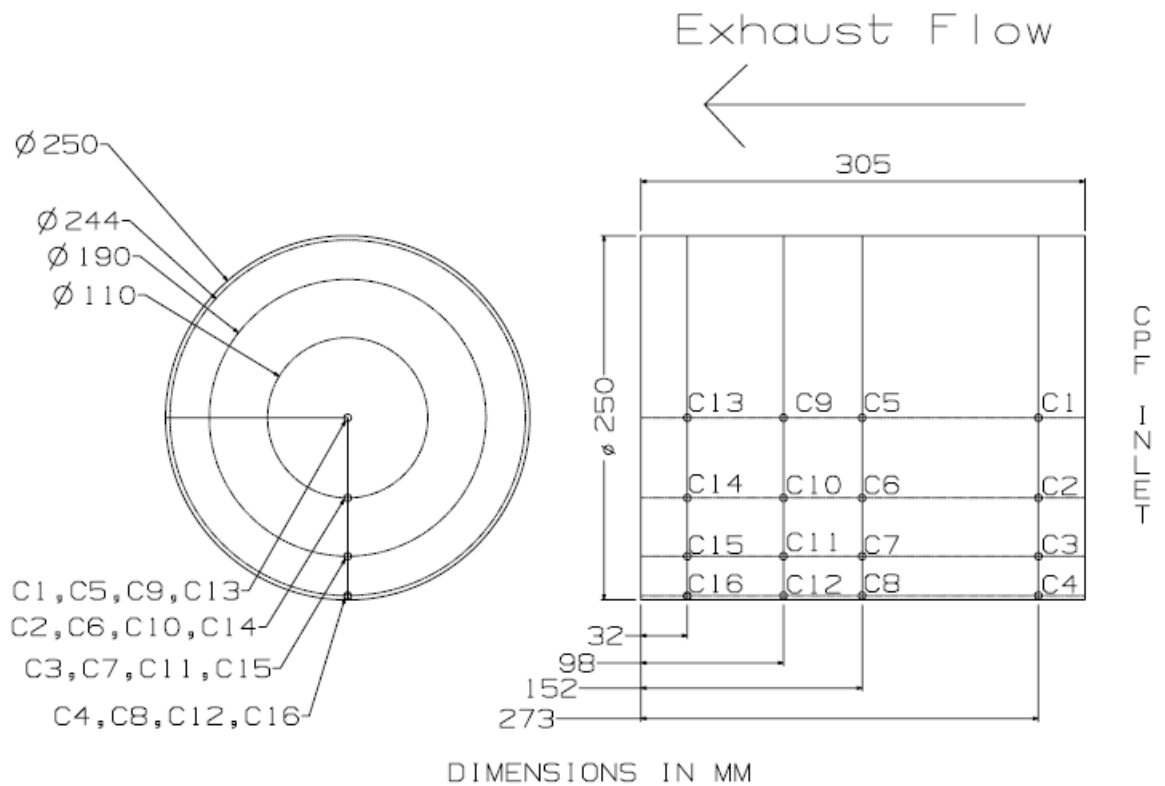


Figure 3.3 CPF Thermocouple Layout

3.4.3 Pressure Measurements

Differential pressure measurements were monitored and recorded on the DOC, CPF, and laminar flow element (LFE). The DOC and CPF differential pressure measurements aid in monitoring the status of the aftertreatment system and are important data for the MTU DOC and CPF modeling studies. The differential pressure across the LFE is used to calculate the air mass flow rate into the engine. The barometric pressure at the LFE is measured by a fourth pressure sensor, with the humidity and test cell temperature being recorded at the LFE as well. These measurements allow for density and viscosity corrections to the air mass flow rate during each test.

3.4.4 Air and Fuel Flow Measurements

A LFE manufactured by Meriam Instruments (Cleveland, OH), was used to determine the air mass flow rate into the engine during each test. The LFE was paired with a 0.5 psig differential pressure transducer to measure the differential pressure across the LFE, which was used to determine the air mass flow rate into the engine. The fuel flow rate was measured by an AVL (Plymouth, MI) fuel mass balance, model number 703G, where the device measures the amount of time it takes for the engine to consume a known mass of fuel (0.4 kg for all tests in this study), and subsequently, the fuel mass flow rate into the engine is known. The total exhaust flow rate is calculated by the summation of the air and fuel mass flow rates determined by the two instruments.

3.4.5 Gaseous Emissions Measurements

Gaseous emissions were measured using an AVL (Plymouth, MI) Pierburg emissions bench, model number AMA 4000. The AMA 4000 emissions bench has the capability to simultaneously measure total hydrocarbons (THC), carbon monoxide (CO), carbon dioxide (CO₂), oxygen (O₂), and can sample either nitric oxides (NO_x) or nitrogen oxide (NO) concentrations in the exhaust. In this study, exhaust NO₂ concentrations were determined by taking the difference between the measured NO_x and NO concentrations at any sampling location. Total gaseous emissions measurements consisted of sampling raw and wet exhaust gas from three locations in the aftertreatment system; upstream of the DOC (UDOC), downstream of the DOC (DDOC), and downstream of the CPF (DCPF), as seen previously in Figure 3.1. After

the exhaust is sampled from any of the three locations, it passes through a heated filter and a sample line maintained at 185°C.

3.4.6 PM Concentration Measurements

Particulate matter (PM) concentrations were obtained using a manual sampling train from Andersen Instruments Inc. (Smyrna, GA). Raw, hot (260-350°C) exhaust gas was drawn through a Pall Corporation (Ann Arbor, MI) type A/E 47mm glass fiber filter. These PM samples were collected multiple times throughout each test, during loading and at the active regeneration engine condition, to determine average exhaust PM concentrations for the various phases of each test. During active regeneration testing, three samples were collected UDOC at the active regeneration engine condition, eight samples were collected UDOC during the loading states, and one sample was collected DCPF during loading as well. All UDOC samples were collected over five minutes, while the DCPF samples were collected over one hour due to the low PM concentrations measured DCPF. The average PM concentrations are used in calculations during post processing of the experimental data. The concentrations are used in the experimental mass balances and as an input for the MTU-1D CPF model. The average engine out PM concentrations are calculated using multiple samples taken during the loading phases and active regeneration engine condition prior to the start of each test. The CPF steady state filtration efficiency was calculated using PM concentrations UDOC and DCPF in conjunction with Eqn. 1; additional information on this process is available in reference [6].

$$\eta_f = \frac{C_{in} - C_{out}}{C_{in}} \cdot 100\% \quad \text{Eqn. 1}$$

η_f = CPF filtration efficiency [%]

C_{in} = CPF inlet PM concentration [mg/scm]

C_{out} = CPF outlet PM concentration [mg/scm]

3.4.7 Particle Size Distribution Measurements

Particle size distribution (PSD) data were collected during the loading and active regeneration portions of the experiments on all experiments when the equipment was in operation. The data were collected using a set of four instruments collectively termed the Scanning Mobility Particle Sizing (SMPS) System, all manufactured by TSI Inc. (Shoreview, MN). The first of the instruments was a mini dilution system which

was manufactured in-house. This dilution system used filtered, compressed air heated to a temperature of 230°C to condition the exhaust gas. The dilution ratios for the active regeneration tests were found to depend on the pressure drop across the aftertreatment components as well as the compressed air pressure. To compensate for these differences, the compressed air pressure was regulated at 30 psig and the dilution ratio was calculated at each engine operating condition used during testing with all test fuels for the post processing of the PSD data. A detailed description of the dilution ratio data collection method can be found in Appendix B.

The sampling locations for PSD measurements were UDOC, DDOC, and DCPF, as shown in Figure 3.1. Filtration efficiency of the CPF was calculated for loading and active regeneration portions of each experiment. The filtration efficiency, η_{filt} , is calculated by using Eqn. 2, and the sum of all the particles from sampling DDOC and DCPF, after corrections to the PSD data have been applied. The PSD Data correction method can be found in Appendix C with the equations and methodology being developed by Hutton [6].

$$\eta_{\text{filt}} = \frac{(\text{DDOC}_{\text{total}} - \text{DCPF}_{\text{total}})}{\text{DDOC}_{\text{total}}} \quad \text{Eqn. 2}$$

The filtration efficiency obtained by PM mass measurements and Eqn. 1 were also calculated to maintain consistency between active regeneration tests conducted on the ISL and tests from references [1, 15].

3.4.8 CPF PM Mass Retained Measurements

The DOC and CPF used in this study are mounted with stainless steel cans which included flanges and clamps allowing for easy removal from the exhaust line during the CPF weighing portion of each experiment. The scale used for measuring the CPF mass at the various times throughout each experiment was an Ohaus Ranger model 35LM with a readability of 0.1g and a repeatability of 0.3g. Experimentation and analysis from Austin [1] showed that the mass of the CPF can be heavily influenced by the temperature at which it is weighed. As a result, care was taken to ensure that the CPF was weighed at approximately the same temperature each time it was weighed in the experiment. In order to ensure that the CPF was weighed at approximately the same temperature, the temperature reading from each thermocouple in the CPF substrate was taken prior to CPF weighing. Individual

thermocouples are measured because the individually measured substrate temperatures can vary widely. For example, measured temperatures within the CPF after a given time with the engine operating at loading conditions (2100 RPM, 195 Nm) can range from 180 to 290°C. Due to these temperature gradients, it is not practical to specify an average CPF temperature at which weighing occurs for each test. Instead, it is preferred that the individual temperature measurements vary by no more than $\pm 15^\circ\text{C}$ for each weighing. The detailed CPF mass measurement procedure can be found in Appendix D.

Active regeneration testing is broken up into eight phases of varying length. Figure 3.4 outlines the various phases for each active regeneration test.

The rate at which PM is deposited within the CPF is assumed to be constant, and for this to hold true, the exhaust mass flow rate, exhaust temperature, engine-out PM concentration, and CPF filtration efficiencies all must be assumed to be constant, or very similar at each phase of active regeneration testing; i.e., average CPF temperatures normally did not fluctuate beyond $\pm 5^\circ\text{C}$ between loading phases in a specific active regeneration test.

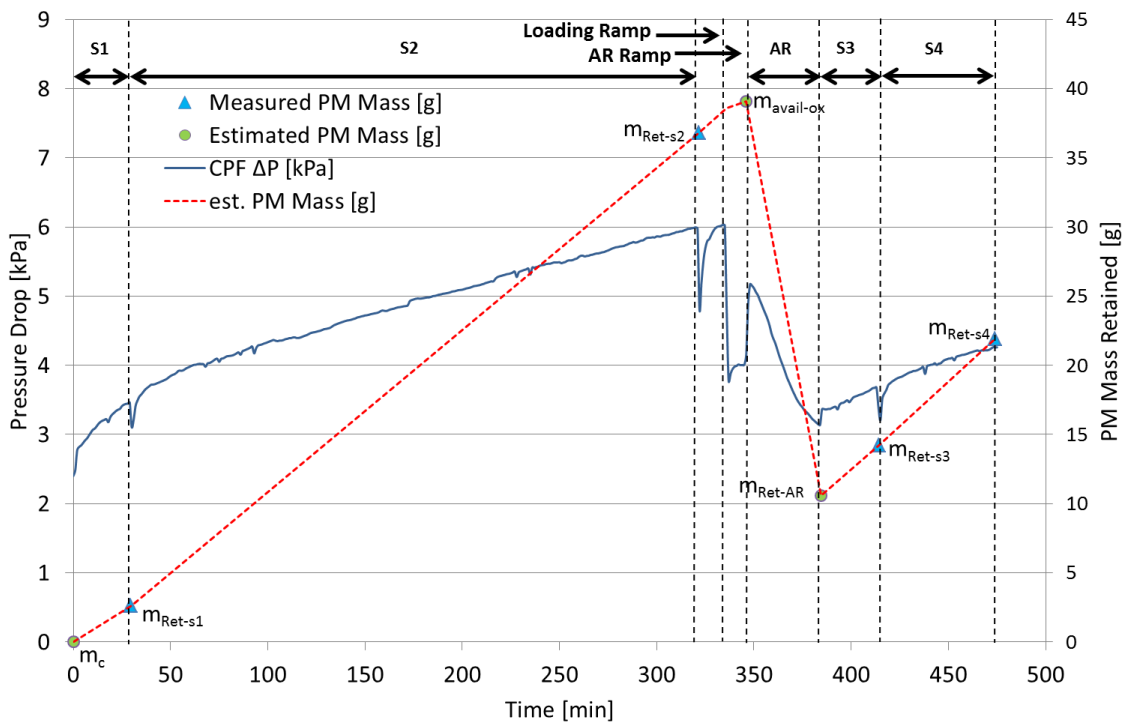


Figure 3.4: Overview of the ISL Active Regeneration Test Procedure

The rate at which PM is deposited within the CPF is assumed to be constant, and for this to hold true, the exhaust mass flow rate, exhaust temperature, engine-out PM concentration, and CPF filtration efficiencies all must be assumed to be constant, or very similar at each phase of active regeneration testing; i.e., average CPF temperatures normally did not fluctuate beyond $\pm 5^{\circ}\text{C}$ between loading phases in a specific active regeneration test.

Shiel [11] conducted an experiment to determine the time required to achieve steady state filtration efficiency following a CPF clean out, measured by the SMPS system. He concluded that the clean CPF filtration efficiency reaches steady state values in a minimal amount of time; therefore, constant filtration efficiency similar to the measured values from Stage 2 loading may be used during Stage 1 loading PM deposition calculations.

For phases of the test where the CPF mass was measured at the beginning and end, such as Stages 2 and 4, the PM mass retained within the CPF is a straight forward calculation. For phases where CPF mass measurements cannot be determined this way, they require separate calculation methodology. The calculation methodology used to determine CPF PM mass retained during Stage 1, Stage 3, loading Ramp, and the Active Regeneration (AR) Ramp phases is detailed below. The calculation methodology assumes that the rate of PM mass deposition during Stage 2 is constant during the loading Ramp (Eqn. 3) and the rate of PM mass deposition during Stage 4 is constant during Stage 3 (Eqn. 4). Eqn. 5 is used to determine the AR Ramp CPF PM mass deposition; due to the nature of the engine operating condition during active regeneration, the CPF is near its balance point. During extended periods of run time at the active regeneration engine condition, the change in the CPF pressure drop was negligible. For this reason, it is assumed that 90% of the engine-out PM is oxidized, 3% is passed through, and the remaining 7% is retained. Eqn. 6 is used to determine the Stage 1 PM mass deposition, with the detailed calculation methodology available in Appendix E.

$$m_{\text{load-ramp}} = \left(\frac{m_{s1} - m_{s2}}{\text{time}_{s2}} \right) \cdot \text{time}_{\text{load-ramp}} \quad \text{Eqn. 3}$$

$m_{\text{load-ramp}}$ = Predicted CPF PM Mass Retained during the Loading Ramp [g]

m_{s1} = Measured CPF mass at the end of Stage 1 loading [g]

m_{s2} = Measured CPF mass at the end of Stage 2 loading [g]

time_{s2} = Time of Stage 2 loading [min]

$\text{time}_{\text{load-ramp}}$ = Time of Loading Ramp [min]

$$m_{\text{add}_s3} = \left(\frac{m_{s3} - m_{s4}}{\text{time}_{s4}} \right) \cdot \text{time}_{s3} \quad \text{Eqn. 4}$$

m_{add_s3} = Predicted CPF PM Mass Retained during Stage 3 loading [g]

m_{s3} = Measured CPF mass at the end of Stage 3 loading [g]

m_{s4} = Measured CPF mass at the end of Stage 4 loading [g]

time_{s3} = Time of Stage 3 loading [min]

time_{s4} = Time of Stage 4 loading [min]

$$m_{\text{AR}_ramp} = m_{\text{in,AR}_ramp} \cdot 0.07 \quad \text{Eqn. 5}$$

m_{AR_ramp} = Predicted CPF PM Mass Retained during AR Ramp [g]

$m_{\text{in,AR}_ramp}$ = PM mass into the CPF during AR Ramp [g]

$$m_{\text{add}_s1} = \eta_{s1} \cdot m_{\text{in},s1} - \left(\eta_{s2} - \frac{m_{s2} - m_{s1}}{m_{\text{in},s2}} \right) \cdot m_{\text{in},s1} \quad \text{Eqn. 6}$$

m_{add_s1} = Predicted CPF PM Mass Retained during Stage 1 loading [g]

η_{s1} = Average CPF filtration efficiency during Stage 1 loading [g]

η_{s2} = Average CPF filtration efficiency during Stage 2 loading [g]

m_{s1} = Measured CPF mass at the end of Stage 1 loading [g]

m_{s2} = Measured CPF mass at the end of Stage 2 loading [g]

$m_{\text{in},s1}$ = PM mass into the CPF during Stage 1 loading [g]

$m_{\text{in},s2}$ = PM mass into the CPF during Stage 2 loading [g]

The MTU-1D CPF model will be used to account for varying exhaust gas concentrations and temperatures recorded during each experiment. Eqn. 3-6 will be used for the mass balances included in this thesis while the MTU modeling team will calibrate the MTU-1D CPF model and use it for determination of the final mass balances. As previously mentioned, the CPF filtration efficiency is determined by physical PM mass measurements upstream and downstream of it. The PM mass into

the CPF is calculated using engine-out PM concentrations and exhaust flow data. The PM mass out of the CPF is calculated for each stage using the measured filtration efficiency. The remainder of the engine-out PM is assumed to be oxidized.

3.5 Experimental DCPF PM Concentration Sensor

A downstream CPF PM concentration sensor manufactured by Delphi (Troy, MI) was installed and evaluated on the ISL 365 engine following the ISL 425-ISL 365 changeover. Regulations related to monitoring the functionality of the CPF is in effect as part of new OBD requirements for the model year 2013 [5], which require the use of sensors to directly measure the PM emitted from the CPF . These sensors are also required to withstand the high temperatures seen at the CPF outlet during active regeneration. These new sensors are required because the concentration detection limits required for the new OBD regulations cannot be determined by other sensors currently in use.

The PM sensor measures the PM resistance in real time. Once a preset threshold for the PM resistance is reached, regeneration of the sensor is performed. The time between regenerations is defined as the sensor's response time. The response time correlates with the exhaust PM concentration; it is the response time that is used to monitor the CPF's functionality within the OBD. The goal is that modeling within the OBD will be used to predict the sensor's response time and compare it with the actual sensor response time. If the measured response time is greater than predicted, the OBD declares that the CPF is functioning normally. If the measured response time is lower than predicted, the OBD declares that there is a problem with the functionality of the CPF.

3.5.1 PM Conductivity Study

The goal of the Delphi sensor testing with respect to the PM conductivity study is to analyze the PM voltage measured by the sensor with ULSD compared to B20 test fuels. Since the sensors are normally operating in extremely low DCPF PM concentrations, the sensor response time can typically be measured in hours or days. In order to effectively study the conductivity of the PM emitted from various test fuels, a CPF with 25% of the inlet channel plugs opened was implemented in the test cell to allow between 2 and 6 (depending on test fuel and test cell conditions) mg/scm of PM to be subjected to the PM sensor.

The CPF modifications were accomplished by milling a pocket with 125 mm diameter and 25 mm depth into the outlet face of the substrate. The visible portion of the outlet face is 250 mm in diameter, so the 125 mm diameter pocket corresponds to 25% of the surface area, thereby producing a CPF with approximately 75% filtration efficiency.

Measuring the changes in PM voltage with respect to time between the two test fuels will determine whether PM conductivity differences between PM emitted from the ISL fueled with ULSD and B20 exists or not.

3.5.2 Sensor Loading Study

Another area of interest with respect to the Delphi DCPF PM sensor is to determine whether sensor PM loading has an effect on the measurement of PM accumulation on the sensor or not.

The first area of interest is whether PM accumulation occurs at an accelerated rate following CPF regeneration or not. Analyzing the PM voltage measured by the sensor before and immediately after CPF regeneration is the preferred method for determining if these differences exist.

The second area of interest is whether PM accumulation rate is affected by PM sensor loading or not. Similarly to the first area of interest, the PM voltage measured by a clean and partially loaded sensor will be analyzed during CPF loading before and immediately after CPF regeneration.

3.6 Active Regeneration Test Procedure

The main objective of the active regeneration testing is to determine the reaction rate of the PM inside the CPF during active regeneration. In order to accomplish this, a combination of CPF modeling paired with several CPF mass measurements are required. CPF models are used in phases where mass measurements are subject to error, i.e., during the temperature stabilization periods before CPF mass measurements which occur after the CPF clean out and active regeneration phases of each experiment.

By using CPF models during the first 30 minutes of the test, following the CPF clean out, the clean weight of the CPF can be calculated without having to measure the

CPF immediately following the CPF clean out when the temperature is elevated, which is where mass measurement error may be introduced. The estimated clean weight of the CPF is used for the remaining calculations to determine the CPF loading and PM reaction rates during the test.

By using CPF models during the pre-active regeneration ramp periods as well as the 30 minutes of operation following active regeneration, the PM loading in the CPF after active regeneration can be determined, allowing for the calculation of the PM reaction rate during active regeneration.

Changes to the active regeneration test procedure on the ISL have been made from the procedure used on the ISM in references [1, 15]. These changes include the pre-dosing ramp at loading conditions for 15 minutes, the pre-active regeneration ramp at active regeneration conditions for 10 minutes, as well as the additional hour of operation at loading conditions following the CPF weighing after active regeneration. Along with the changes to the testing procedure used in references [1, 15], the engine operating condition during active regeneration was changed to allow the use of in-cylinder dosing on the ISL. Experiments from references [1, 15] used an engine operating condition of 2100 RPM and 470 Nm, 40% load, which results in a space velocity (the relation between volumetric flow and the 17.1L aftertreatment volume) that is too high for in-cylinder dosing to raise CPF inlet exhaust temperature to 600°C. Therefore, the engine operating condition chosen for experiments run on the ISL was 1400 RPM and 460 Nm, corresponding to an exhaust flow rate of 8.0 kg/min and a DOC space velocity ranging from 177-180 1/khr, which allows in-cylinder dosing to be used and provides a DOC inlet temperature of $325 \pm 10^\circ\text{C}$, which is above the DOC lightoff point.

Prior to the start of each test, twelve PM sample filters must be prepared at least 24 hours before the test is to begin. The procedure for preparing PM sample filters can be found in Appendix F.

The MTU-1D CPF model should be run to gather base line information for the amount of time the engine is operated in the loading condition to reach a PM loading in the CPF of 2.2 ± 0.2 g/L.

Since time of active regeneration varies depending on the CPF inlet temperature and fuel type being used during any particular test, an active regeneration model

developed by Pidgeon [2] was used to gather base line information for the length of active regeneration required to oxidize 70% of the PM inside the CPF based on experimental test conditions.

The phases of an active regeneration test are:

1. Pre-test preparation: Prior to the CPF cleanout, the engine is operated at the active regeneration engine condition to collect PM samples, since PM samples cannot be collected during active regeneration due to fuel dosing.
2. CPF Clean out: Active regeneration is performed to oxidize the PM inside the CPF to begin with the DOC/CPF in the same state.
3. Stage 1 loading (S1): After the CPF cleanout is complete, the engine is switched to the loading condition for thirty minutes to ensure that the CPF has reached a repeatable temperature for weighing.
4. Stage 2 loading (S2): The engine is operated at the loading condition until a CPF particulate matter (PM) loading of 2.2 ± 0.2 g/L is achieved.
5. Pre-active Regeneration Ramps: The engine is operated at loading conditions for fifteen minutes and the active regeneration condition for ten minutes to stabilize the CPF temperature prior to active regeneration.
6. Active Regeneration (AR): For the active regeneration portion of the experiment, the engine is switched to the active regeneration engine condition.
 - a. Active regeneration can be performed using one of two dosing methods:
 - i. In-cylinder dosing
 - ii. Auxiliary fuel dosing injector; with the injector located downstream of turbocharger.
 - b. The amount of fuel injected (in-cylinder dosing) or the duty cycle of the injector (auxiliary injector) is set to a base value found in the pre-test preparation phase to reach the desired CPF inlet temperature. Once the desired CPF inlet temperature is reached, the amount of fuel being injected is adjusted to maintain the desired CPF inlet temperature within $\pm 10^\circ\text{C}$. After a pre-determined amount of time at the specified CPF inlet temperature or if the slope of the pressure drop

profile across the CPF decreases significantly, the active regeneration portion of the test is stopped and the transition to Stage 3 loading is made. If the slope of the pressure drop profile across the CPF decreases significantly and active regeneration is allowed to continue, there will not be enough PM within the CPF to obtain an accurate mass measurement, due to the mass of PM related to the mass of the CPF (typical PM mass of 2.2 g/L or 37.6 g compared to CPF mass of 17.8+ kg).

7. Stage 3 loading (S3): This follows the active regeneration; the engine is switched back to the loading condition for thirty minutes to ensure that the CPF has reached a repeatable temperature for weighing.
8. Stage 4 loading (S4): The engine is operated at the loading condition for sixty minutes to determine differences in the performance of a clean CPF and a CPF that has been partially regenerated. The experiment is concluded after the CPF weighing following Stage 4 loading has been completed.

3.6.1 Pre-test Preparation Phase

If the auxiliary fuel dosing injector is the method of dosing for the test, calibration of the injector is required prior to the start of this phase. The calibration procedure for the auxiliary dosing injector can be found in Appendix G. The pre-test preparation phase begins by starting the engine and allowing it to reach operating temperatures using the warm-up sequence seen in Table 3.5. During the warm up sequence, the exhaust is allowed to travel through the trapline, and subsequently, through the DOC and CPF to allow them to warm up as well.

After the engine and aftertreatment system are warmed up, the engine is switched to the active regeneration operating point of 1400 RPM and 465 Nm and is allowed to reach steady state.

Once the DOC inlet temperature has stabilized to $325 \pm 10^\circ\text{C}$, gaseous emissions are sampled at all 3 sampling locations (UDOC, DDOC, and DCPF) for 10 minutes. 5 minutes are devoted to NO_x sampling and the remainder is devoted to NO sampling, since they cannot be simultaneously measured on the gaseous emissions analyzer. Figure 3.5 depicts the gaseous emissions sampling strategy for the pre-test preparation phase.

Three engine-out PM samples are also recorded during this phase, because engine-out PM samples cannot be collected during active regeneration. The UDOC gaseous emissions are also used in the post-processing of data because the engine-out gaseous emissions cannot be measured during active regeneration due to possible damage to the analyzer.

Table 3.5: Engine Operating Points for Initial Warm-Up Sequence

Engine Speed [RPM]	Engine Load [Nm]	Time [min]
750	0	1
1200	220	5
1800	220	5
2100	440	5
2100	840	5

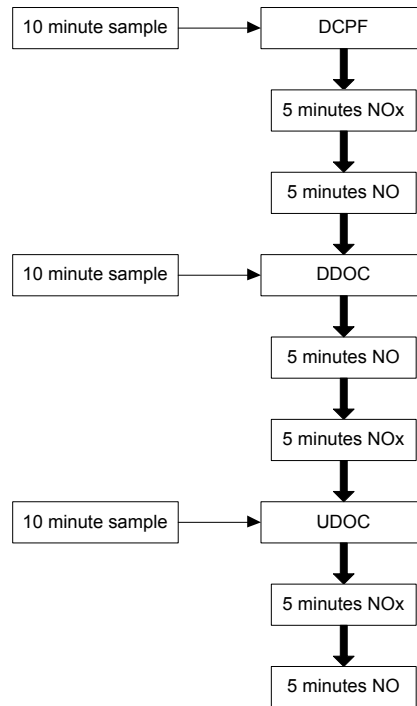


Figure 3.5: Pre-test Preparation Phase Gaseous Emissions Sampling Strategy

Following the completion of the required PM and gaseous emissions measurements, the CPF clean-out phase can begin by initializing fuel dosing and determining the amount of fuel injected that is required to reach the target CPF inlet temperature to be used during the active regeneration phase.

3.6.2 CPF Clean Out Phase

At the completion of the data collection during the pre-test preparation phase, the engine is allowed to continue running at the active regeneration test condition if in-cylinder dosing is to be used, or the engine can be brought to 2100 RPM and 840 Nm if the auxiliary dosing injector is used. If the engine is switched to 2100 RPM and 840 Nm, the DOC inlet exhaust temperature must stabilize to $380 \pm 10^\circ\text{C}$ before proceeding.

Once the desired engine operating point and steady state DOC inlet temperature are reached, dosing is activated and adjusted to reach a CPF inlet temperature of 600°C . After 600°C CPF inlet temperature is achieved, it is maintained for approximately fifteen minutes, ensuring that a constant CPF pressure drop profile is observed. If fifteen minutes passes and the pressure drop profile has not stabilized, the CPF clean out continues until the pressure drop profile is stable for an extended period of time. Once the CPF pressure drop profile is stable, dosing is halted and the CPF pressure drop profile is allowed to stabilize once again, after which the transition to Stage 1 loading is made.

3.6.3 Stage 1 Loading Phase

At the transition to Stage 1 loading, the engine is switched to 2100 RPM and 195 Nm, with a DOC inlet temperature of $265^\circ\text{C} \pm 10^\circ\text{C}$ for Stage 1 loading of the CPF. The engine is allowed to run at the loading condition for approximately thirty minutes to allow the temperature of the CPF to stabilize. By weighing the CPF at a similar temperature during all portions of the test, the buoyancy effect that results from the thermal mass of the CPF is maintained at a constant level. Ultimately, this technique reduces variability between CPF weight measurements from different phases in the experiment.

During Stage 1 loading, gaseous emissions are sampled constantly using the same strategy that was used in the pre-test preparation phase, where samples are taken DCPF, DDOC, and UDOC, in that order.

Exhaust particle size distribution (PSD) samples are also collected DCPF, DDOC, and UDOC. One sample at each location is taken during Stage 1 loading, with each sample being in the range from 20 seconds to 2 minutes in sampling time. The sampling time is set by the user, and can be varied depending on the resolution of data desired. The PSD samples must be taken at a different location than the gaseous emissions to allow each analyzer to receive the full exhaust sample at that location. For example, if gaseous emissions are being sampled DCPF, PSD must be sampled UDOC or DDOC until the DCPF gaseous emissions sampling has been finished.

One PM sample is collected UDOC for five minutes during Stage 1 loading along with the continuous monitoring of temperature, exhaust flow, fuel flow, and pressure drop profiles across the DOC and CPF.

After thirty minutes of Stage 1 loading, the engine out exhaust is switched to the bypass line which diverts the exhaust around the after-treatment system and the engine is shut down. Once the engine is shut down, the aftertreatment system is disassembled to allow the weighing of the CPF. The CPF weighing procedure is explained in detail in Appendix D.

The weighing of the CPF provides for the mass measurement m_{s1} which is used with m_{Ret-S1} to determine the clean weight of the filter (m_c) using Eqn 1. The value m_{Ret-S1} is obtained twice, once prior to the start of the experiment using preliminary test data. This value is used to predict the CPF PM loading during the test.

$$m_c = m_{s1} - m_{Ret-S1} \quad \text{Eqn. 7}$$

m_c = Calculated clean weight of the CPF, [g]

m_{s1} = Measured mass of the CPF after Stage 1 loading, [g]

m_{Ret-S1} = MTU-1D model predicted PM added during Stage 1 loading, [g]

Table 3.6: Engine Speed and Load for Stage 2 Engine Warm Up

Engine Speed [RPM]	Engine Load [Nm]	Time [min]
750	0	1
1200	195	5
1800	195	5
2100	195	5

3.6.4 Stage 2 Loading Phase

After the aftertreatment system is reassembled and installed in the exhaust system, and while the exhaust is still routed through the baseline, the engine is started and brought to idle. Table 3.6 shows the warm up procedure after Stage 1 loading is complete, and warm up is complete when a steady exhaust manifold temperature is achieved.

Once the exhaust manifold temperature has stabilized, the exhaust is switched to the trapline which marks the beginning of Stage 2 loading.

Stage 2 loading takes place at 2100 RPM and 195 Nm, with a DOC inlet temperature of $265^{\circ}\text{C} \pm 10^{\circ}\text{C}$, which is the same operating condition as Stage 1 loading. The time of Stage 2 loading is based on preliminary modeling predictions, and has been shown to vary based upon the engine out PM concentration.

The same measurements and samples that were taken during Stage 1 loading are also taken during Stage 2 loading, but on a more frequent basis.

The strategy for gaseous sampling is modified from Stage 1 loading with initial sampling occurring DDOC. This location was given first priority in order to facilitate the modeling effort as it was deemed important from a modeling perspective to record the CPF inlet concentrations during the start of Stage 2 loading. The second sampling location is DCPF with the final location being UDOC. Gaseous sampling is cycled through these locations during the test with the time at each location split equally dependent upon the length of the test.

Figure 3.6 depicts the gaseous emissions sampling strategy for Stage 2 loading.

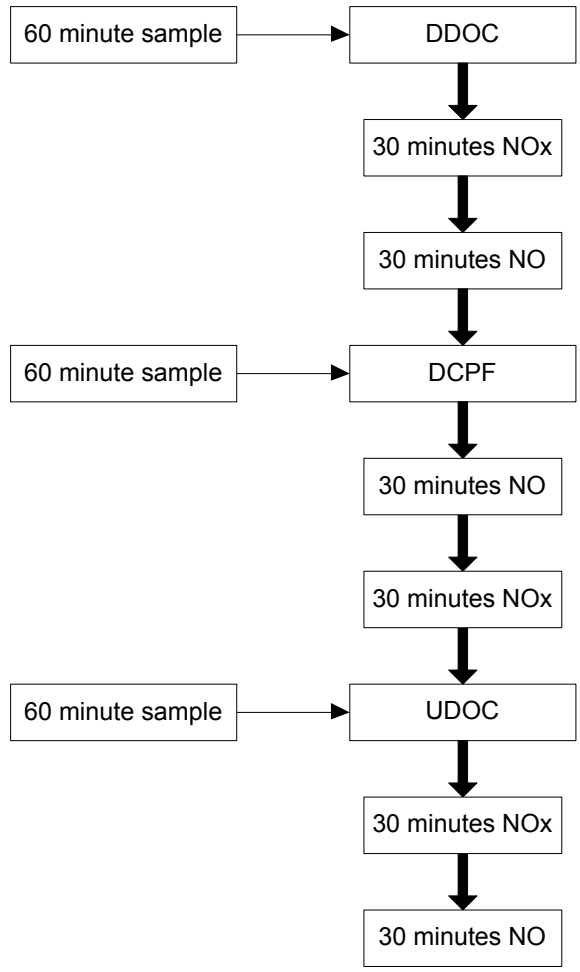


Figure 3.6: Gaseous Emissions Sampling Strategy for Stage 2 Loading Phase

The strategy for PSD sampling is the same as the strategy used for Stage 1 loading, in that PSD samples cannot be taken at the same location as gaseous emissions sampling at the same time.

Four PM samples are collected UDOC and one PM sample is taken DCPF during Stage 2 loading. Only one DCPF PM sample is collected because the PM concentration DCPF is so low that a one hour sample time is required to collect a measurable amount of PM. The sample time for the UDOC PM samples is five minutes, which is the same strategy that was used during Stage 1 loading.

After a predetermined amount of loading time has passed, the exhaust is diverted through the bypass line and the engine is brought to idle and shut down. The after-treatment system is removed from the exhaust system and then disassembled for

CPF weighing. The weighing of the CPF provides for the mass measurement m_{s2} which is used with m_c in Eqn. 8 to determine m_{Ret-s2} , the PM mass retained in the CPF after Stage 2 loading.

$$m_{Ret-s2} = m_{s2} - m_c \quad \text{Eqn. 8}$$

m_{Ret-s2} = Calculated PM mass retained in the CPF at end of Stage 2 loading, [g]

m_{s2} = Measured mass of the CPF at end of Stage 2 loading, [g]

m_c = Calculated clean weight of the CPF, from Eqn. 7, [g]

The PM loading of the filter is verified by using the value m_{Ret-s2} , which is the mass of the accumulated PM in the filter, and dividing this mass value by the volume of the CPF, 17.1 L. If 2.2 ± 0.2 g/L has not been achieved, the after-treatment system must be re-installed in the exhaust system and additional loading will be required.

After verifying that the CPF loading of 2.2 ± 0.2 g/l has been achieved, the after-treatment system is reassembled and reinstalled into the exhaust system and subsequently, Stage 2 loading has been completed.

3.6.5 Active Regeneration Phase

Prior to the start of the Active Regeneration portion of the experiment, the gaseous emissions analyzer bench HC concentration range must be increased in order for the analyzer to accurately measure the increased HC concentrations that are found DDOC during fuel dosing. This is done by selecting the Hydrocarbon tab on screen 2 of the Pierburg bench. Touch the Parameters button, and select Range 4 for the hydrocarbon measurement range. Then span, zero, and adjust the hydrocarbon channel by itself, and confirm that the adjusted hydrocarbon measurement reaches 4200 ppm before finishing the adjust stage; if it does not reach 4200 ppm, re-zero and re-adjust it.

After the after-treatment system has been re-installed, the engine is warmed up in the baseline in the same manner prior to Stage 2 loading. The warm up is complete when a steady state exhaust manifold temperature is achieved.

After a steady exhaust manifold temperature is achieved, the exhaust is switched to the trapline and the aftertreatment system is allowed to warm up at the loading condition for approximately 15 minutes or until the DOC inlet temperature has

stabilized at $265\text{ }^{\circ}\text{C} \pm 10^{\circ}\text{C}$. Once the DOC inlet temperature is stable at the loading condition, the engine is switched to the active regeneration condition, 1400 RPM and 460 Nm, for approximately 10 minutes or until the DOC inlet temperature has stabilized at $325^{\circ}\text{C} \pm 10^{\circ}\text{C}$.

After a steady DOC inlet temperature at the active regeneration engine condition is achieved, fuel dosing is activated by the pre-determined injection method (in-cylinder or auxiliary fuel dosing injector), which marks the start of the Active Regeneration portion of the experiment. A base line length of the Active Regeneration phase for the experiment being conducted was found using the model developed by Pidgeon [2] prior to testing day. The amount of fuel required to be injected to reach the desired CPF inlet temperature was determined during the Pre-test Preparation phase of the test, and is used as the initial fuel injection value at the start of active regeneration. The amount of fuel being injected is adjusted to maintain the desired CPF inlet temperature $\pm 10^{\circ}\text{C}$ for the duration of active regeneration.

Gaseous emissions during active regeneration are collected DDOC for six minutes, with three minutes dedicated to NO_x and three minutes dedicated to NO collection. Gaseous measurements should not be taken UDOC during fuel dosing due to the possibility of damage occurring to the analyzer. For the Active Regeneration phase of the test, it is assumed that the UDOC gaseous concentrations, other than hydrocarbon concentration, remain the same as what was found in the pre-test portion of the experiment.

At the same time that gaseous emissions are being collected, a PSD sample is taken DCPF. If the Active Regeneration portion of the experiment is long enough, gaseous emissions will be sampled for 6 minutes DCPF and a PSD sample will be taken DDOC.

The total gaseous sampling time at each location may need to be adjusted depending on the length of active regeneration.

Figure 3.7 is the visual representation for gaseous and PSD sampling during the active regeneration phase.

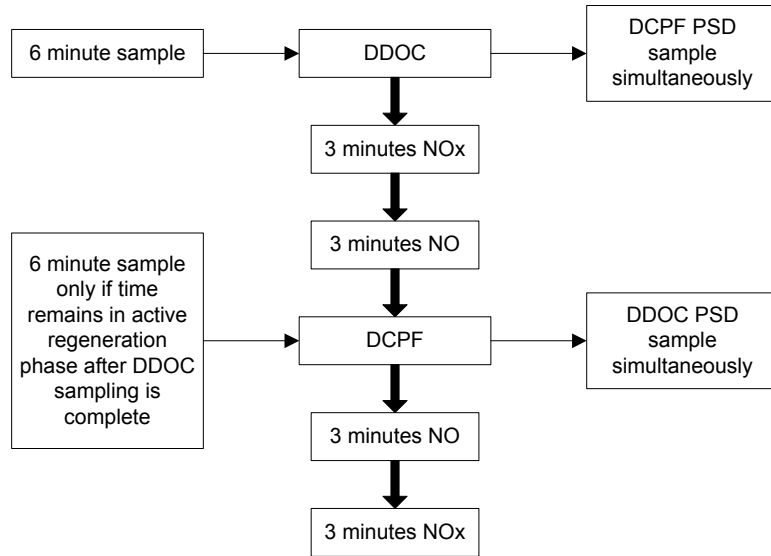


Figure 3.7: Gaseous Emissions and PSD Sampling Strategy for Active Regeneration Phase

After a predetermined amount of time, or if the slope of the pressure drop profile across the CPF decreases significantly, the Active Regeneration phase of the experiment is halted and the transition is made to Stage 3 loading.

3.6.6 Stage 3 Loading Phase

After the Active Regeneration portion of the test is concluded, the transition to Stage 3 loading begins. The engine is brought to the same engine conditions used during Stage 1 and Stage 2 loading, 2100 RPM and 195 Nm, with a DOC inlet temperature of $265^{\circ}\text{C} \pm 10^{\circ}\text{C}$.

The collection of experimental data occurs in the same manner as the Stage 1 loading portion of the experiment, because continuing the sampling of exhaust gases DCPF after active regeneration prevents any false HC concentration readings due to analyzer hang up. Stage 3 loading is thirty minutes long which allows the temperature of the CPF to stabilize to the values that were experienced in Stage 1 and Stage 2 loading, allowing for the best calculation of total PM oxidized during active regeneration.

After thirty minutes of operating in Stage 3 loading, the exhaust is switched to the bypass line and the engine is brought to idle and shut down. The aftertreatment

system is removed from the exhaust system and disassembled for weighing of the CPF.

The weighing of the CPF provides for the mass measurement m_{s3} which is used with m_c in Eqn. 9 to determine the remaining amount of PM mass in the filter (m_{Ret-s3}).

$$m_{Ret-s3} = m_{s3} - m_c \quad \text{Eqn. 9}$$

m_{Ret-s3} = Calculated PM mass retained in the CPF after Stage 3 loading, [g]

m_{s3} = Measured mass of the CPF after Stage 3 loading, [g]

m_c = Calculated clean weight of the CPF, from Eqn. 7, [g]

In order to determine the amount of PM mass present in the filter after the Active Regeneration portion of the experiment, Eqn. 4 is used to calculate the amount of PM mass that is added during Stage 3 loading (m_{add_s3}) which is used with Eqn. 10 to determine the amount of PM present in the filter (m_{Ret-AR}) after the Active Regeneration portion of the experiment.

$$m_{Ret-AR} = m_{Ret-s3} - m_{add_s3} \quad \text{Eqn. 10}$$

m_{Ret-AR} = Calculated PM mass retained in the CPF after Active Regeneration, [g]

m_{Ret-s3} = Measured PM mass retained in the CPF after Stage 3 loading, [g]

m_{add_s3} = Predicted (Eqn. 4) PM mass added to the CPF during Stage 3 loading, [g]

The amount of PM added to the CPF during the 10 minute ramp-up at the active regeneration engine condition can be calculated using the engine out PM concentration (EO_{PM}) and exhaust flow rate (Q_{std}) with Eqn. 11.

$$m_{AR_ramp} = m_{in,AR_ramp} \cdot 0.07 \quad \text{Eqn. 11}$$

m_{AR_ramp} = Predicted CPF PM Mass Retained during AR Ramp [g]

m_{in,AR_ramp} = PM mass into the CPF during AR Ramp [g]

The amount of PM oxidized during active regeneration is calculated using m_{Ret-s2} , m_{Ret-AR} , $m_{AR-ramp}$, and the PM mass added to the CPF during the loading ramp-up time estimated from the MTU-1D CPF model, $m_{load-ramp}$, with Eqn. 12.

$$m_{OX} = m_{Ret-s2} + m_{load-ramp} + m_{AR-ramp} - m_{Ret-AR} \quad \text{Eqn. 12}$$

m_{OX} = Calculated PM mass oxidized in the CPF during Active Regeneration, [g]

m_{Ret-s2} = Calculated PM mass retained in the CPF at end of Stage 2 loading, [g]

$m_{load-ramp}$ = MTU-1D model predicted PM mass added to the CPF during Pre-active Regeneration ramp up at the loading condition, [g]

$m_{AR-ramp}$ = PM mass added to CPF during ramp up at Active Regeneration engine conditions, [g]

m_{Ret-AR} = Calculated PM mass retained in the CPF after Active Regeneration, [g]

After the CPF has been weighed, the after-treatment system is reassembled and installed in the exhaust system in preparation for Stage 4 loading.

3.6.7 Stage 4 Loading Phase

After the after-treatment system is reassembled and installed in the exhaust system, and while the exhaust is still routed through the baseline, the engine is started and brought to idle. Table 3.7 shows the warm up procedure after Stage 3 loading is complete, and warm up is complete when a steady exhaust manifold temperature is achieved.

Once the exhaust manifold temperature has stabilized, the exhaust is switched to the trapline which marks the beginning of Stage 4 loading.

Table 3.7: Engine Speed and Load for Stage 4 Engine Warm Up

Engine Speed [RPM]	Engine Load [Nm]	Time [min]
750	0	1
1200	195	5
1800	195	5
2100	195	5

Stage 4 loading takes place at 2100 RPM and 195 Nm, with a DOC inlet temperature of $265^{\circ}\text{C} \pm 10^{\circ}\text{C}$, which is the same operating condition as the Stage 1, Stage 2, and Stage 3 loading phases. Stage 4 loading is sixty minutes long and allows the behavior of the CPF after a partial regeneration to be explored.

The collection of experimental data occurs in the same manner as the Stage 2 portion of the experiment, with the only differences being that two UDOC PM samples are collected and the total length of Stage 4 loading, which is only 60 minutes.

After sixty minutes of operating in Stage 4 loading, the exhaust is switched to the bypass line and the engine is brought to idle and shut down. The after-treatment system is removed from the exhaust system and disassembled for weighing of the CPF.

The weighing of the CPF provides for the mass measurement m_{s4} which is used with m_c in Eqn. 13 to determine the remaining amount of PM mass in the filter ($m_{\text{Ret-s4}}$).

$$m_{\text{Ret-s4}} = m_{s4} - m_c \quad \text{Eqn. 13}$$

$m_{\text{Ret-s4}}$ = Calculated PM mass retained in the CPF after Stage 4 loading, [g]

m_{s4} = Measured mass of the CPF after Stage 4 loading, [g]

m_c = Calculated clean weight of the CPF, from Eqn. 7, [g]

After the mass retained in the CPF after Stage 4 is determined, the experiment has concluded.

3.7 Active Regeneration Test Matrix

In order to determine the dominant factors affecting the PM oxidation in the CPF during active regeneration, a series of tests were created which cover a range of CPF

inlet temperatures using ULSD, B10, and B20. As well as changes in the test fuel, two higher PM loading cases (4.1 g/L) and exhaust dosing cases were also factored into the test matrix. The engine operating point and percent PM oxidization targets were the constant factors associated with the entire test matrix. Table 3.8 illustrates the active regeneration tests that were completed in this study. The numbers represent the chronological order of the experiments for each fuel (i.e., the blue cell numbered 6 coincides with test B20-6).

3.8 PM Reaction Rate Calculation Method

The method for calculating the reaction rate for active regeneration has been updated since the active regeneration experimentation performed by Austin [1] and Chilumukuru [15] in order to account for varying CPF temperatures. The method utilizes experimentally measured time dependent CPF temperatures, average PM concentrations, and PM loadings at the start and end of the active regeneration portion of the test. The time that fuel dosing was activated is considered the experimental active regeneration period. Conservation of mass in the CPF, with inlet PM concentrations of C_{in} , and an initial PM loading of m_R , results in Eqn. 14, a first order ODE for change in PM mass retained m_R , over time t . It is assumed that everything in Eqn. 14 with the exception of the reaction rate (RRo) is constant, since RRo is temperature dependent, and the average CPF temperature changes with time.

$$\frac{dm}{dt} = \eta_{filt} \cdot C_{in} \cdot Q - m_R \cdot RRo(T) \quad \text{Eqn. 14}$$

Setting $\Delta m = m_R(i) - m_R(i-1)$ and $m_R = m_R(i-1)$ in Eqn. 14, Eqn. 14 can be solved numerically for $m_R(i)$ after substituting $RRo(T) = A \cdot e^{[-Ea/(R \cdot T(i))]}$ which yields Eqn. 15.

$$m_R(i) = \left[\eta_{filt} \cdot C_{in} \cdot Q - m_R(i-1) \cdot A \cdot e^{[-Ea/(R \cdot T(i))]} \right] \cdot \Delta t + m_R(i-1) \quad \text{Eqn. 15}$$

i = Incremental point in time during active regeneration [-]

$m_R(i)$ = PM mass in CPF at time i during active regeneration [g]

$m_R(i-1)$ = PM mass in CPF calculated at time $i-1$ [g]

η_{filt} = CPF filtration efficiency [-]

C_{in} = Engine out PM concentration [g/scm]

Q = Exhaust volumetric flow rate [scm/sec]

A = Pre-exponential factor [1/s]

Ea = Activation energy, 145000 [J/gmol]

R = Universal gas constant, 8.315E-03 [J/(gmol·K)]

$T(i)$ = CPF avg. temperature at time i during AR [K]

Δt = Time step through active regeneration, 1 [sec]

Using Eqn. 15, the PM mass retained within the CPF is calculated at each time step during the active regeneration portion of the experiment. The experimental data from a performed test provides for the length of the active regeneration period along

with the CPF filtration efficiency, engine out PM concentration, exhaust volumetric flow rate, and the average CPF temperature throughout the active regeneration period. The constants in Eqn. 15 are the activation energy (145 kJ/gmol [13]) and the universal gas constant. The pre-exponential factor, A , is fit by iteration until the actual PM mass retained at the end of the active regeneration is matched to the calculated PM mass retained at the end of active regeneration. The iteration is accomplished by comparing the final calculated PM mass retained to the experimental amount of PM mass retained in the CPF after active regeneration. If the calculated ending mass retained is too high (actual PM mass ± 0.1 g), the pre-exponential factor is increased and the calculation runs again. Similarly, if the calculated ending mass retained is too low, the pre-exponential factor is decreased and the calculation runs again. The pre-exponential factor is iterated until the actual PM mass retained ± 0.1 g is matched to the calculated PM mass retained at the end of active regeneration. Once the PM mass retained is within limits, the pre-exponential factor is known.

With the pre-exponential factor known, the average CPF temperature matrix is used as an input to Eqn. 16, which assumes that the activation energy and pre-exponential factor remain constant.

$$RR_o = A \cdot e^{[-E_a/(R \cdot T)]} \quad \text{Eqn. 16}$$

RR_o = reaction rate [1/s]

Using Eqn. 16, the reaction rate is calculated for each time step of the active regeneration portion of the experiment and then reported in matrix form. The reported reaction rate is the calculated value corresponding to the average CPF temperature during active regeneration.

3.9 Activation Energy Determination Method

The experimental data from all ISL 365 runs were used in conjunction with optimization methods, similar to those used by Surenahalli [17], to calculate a single value for the activation energy of each test fuel. The experimental reaction rate, average CPF temperature, and mole fraction of O_2 (YO_2) for each test case is input into the optimization. Upper and lower limits for the activation energy to be used by the optimization are input as well.

The optimization calculates the reaction rates based on the experimental CPF temperature and oxygen concentration from Eqn. 17 and minimizes the difference between the experimental and the optimized reaction rates. The optimization uses the MATLAB® 'fmincon' function to find an activation energy which provides minimal variation in pre-exponential factors and minimizes the cost function. The cost function for the optimization is defined at the percent difference between the experimental and optimized reaction rates, as shown in Eqn. 17.

$$\text{cost} = \sum_{i=0}^n \frac{\text{RR}_{\text{exp}} - \text{RR}_{\text{opt}}}{\text{RR}_{\text{exp}}} \quad \text{Eqn. 17}$$

n = number of tests.

After the cost function has been minimized, the corresponding activation energy is reported along with pre-exponential factors for each test input to the optimization.

3.10 CPF Resistance Calculation Method

In order to determine where any experimental problems occurred during data collection, the total CPF resistance can be calculated and used to determine if data problems occurred during the test. The total hydrodynamic flow resistance of the CPF is expected to increase during loading and decrease during active regeneration followed by an increase during post-loading due to the corresponding changes in the PM retained in the CPF. CPF resistance can be calculated using Eqn. 18 which comes from reference [18] where both sides of the equation represent the sum total of the CPF wall, PM cake, and channel resistances. The mass flow rate of exhaust through the CPF is assumed to be equal to the sum of the mass flow rate of air (measured by the pressure drop across the LFE) and mass flow rate of fuel (measured by the AVL fuel balance) into the engine. The density of the exhaust gas mixture is calculated using the ideal gas equation of state and it is a function of the exhaust pressure and temperature. The dynamic viscosity of the exhaust is calculated by Sutherland's law assuming air as the gas and is a function of temperature. Separate analysis conducted by Premchand [19] has shown that the difference in viscosity between engine exhaust and air is negligible. The weighted CPF average temperature is used in the calculation of CPF resistance on the left side of Eqn. 18 because the weighted

CPF average temperature represents the overall CPF temperature and temperature is the variable that affects the viscosity and density of the exhaust gas.

$$(\Delta P \cdot V_{\text{trap}} \cdot \rho_{\text{exh}}) / (\mu \cdot \dot{m}_{\text{exh}}) = \frac{(\alpha + w_s)^2}{2} \left[\frac{w_s}{k_s \alpha} + \frac{1}{2k_{\text{soot}}} \ln \left(\frac{\alpha}{\alpha - 2w} \right) + \frac{4FL^2}{3} \left(\frac{1}{(\alpha - 2w)^4} + \frac{1}{\alpha^4} \right) \right] \quad \text{Eqn. 18}$$

ΔP = CPF pressure drop [Pa]

V_{trap} = Total volume of the CPF [m³]

ρ_{exh} = Density of exhaust [kg/m³]

$\rho_{\text{exh}} = (\Delta P + P_{\text{barometric}}) / (R \cdot T_{\text{avg}})$

T_{avg} = Weighted average CPF temperature [K]

μ = Exhaust dynamic viscosity [(N·sec)/m²]

\dot{m}_{exh} = Mass flow rate of exhaust [kg/sec]

α = Channel width [m]

w_s = Wall thickness [m]

k_s = Substrate wall permeability [m²]

k_{soot} = Cake layer permeability [m²]

w = Particulate layer thickness [m]

F = Factor = 28.454 [18]

L = Channel length [m]

$(\Delta P \cdot V_{\text{trap}} \cdot \rho_{\text{exh}}) / (\mu \cdot \dot{m}_{\text{exh}})$ = Resistance [-]

The left-hand side of Eqn. 18 includes the CPF pressure drop, total substrate volume, the dynamic viscosity, mass flow rate, pressure, and exhaust temperature of the gas in the CPF, while the right-hand side is the equivalent CPF flow resistance based on dimensions of the substrate channels, channel walls, PM cake layer, and the permeability of the cake layer and the substrate wall. Eqn. 19 [19] describes the change in the substrate wall permeability as a function of the PM mass retained in the substrate wall and resulting change in the porosity and the unit collector diameter. The functions used to describe the change in substrate wall porosity and unit collector diameter are described in detail in reference [19].

$$k_s = k_{s0} \cdot \left(\frac{d_c}{d_{c0}}\right)^2 \cdot \left(\frac{f(\varepsilon)}{f(\varepsilon_0)}\right) \quad \text{Eqn. 19}$$

k_{s0} = Clean substrate wall permeability [m^2]

d_c = Instantaneous diameter of a loaded unit collector [m]

d_{c0} = Diameter of a clean unit collector [m]

ε = Instantaneous substrate wall porosity (= $F(\varepsilon_0$ and $m_{\text{wall}})$) [-]

m_{wall} = Substrate wall PM mass retained

ε_0 = Clean substrate wall porosity [-]

The density of the exhaust is calculated using the ideal gas equation of state ($\rho = P/RT$) where P is equal to the pressure in the exhaust stream defined as the barometric pressure + CPF pressure drop. R is the universal gas constant and T is equal to the weighted average CPF temperature calculated using the methodology described in the Temperature Measurements section of Chapter 3. As previously mentioned, the weighing factor for C1-C4, C5-C8, C9-C12, and C13-C16 are 0.303, 0.287, 0.197, and 0.213, respectively.

The viscosity is also based on the average CPF temperature, and the total CPF flow resistance is evaluated at every time point through the active regeneration experiments. The weighted average CPF temperature is used throughout all the calculations related to the CPF resistance because the weighted average CPF temperature is the best representation of the temperature state of the CPF at any time point of the experiment. The average CPF temperature also produces the best CPF resistance response relative to all other thermocouple measurements and is closely related to the trends seen when analyzing CPF resistance with thermocouple C3, which produced the best resistance trends when calculated using a single thermocouple as the temperature input.

During loading of the CPF, the substrate wall permeability is decreasing and the particulate layer thickness is increasing due to the addition of PM into the substrate wall and PM cake layer, thereby increasing the magnitude of the 1st and 2nd terms of the right-hand side of Eqn. 18 and in turn, increasing the total flow resistance of the CPF.

The opposite is true during regeneration, where the substrate wall permeability increases due to the oxidation of the PM retained in the substrate wall, thereby causing the substrate wall porosity to increase toward the 'clean' substrate value.

The particulate layer thickness decreases as PM retained in the cake layer is oxidized over time, thereby decreasing the magnitude of the 1st and 2nd terms of the right-hand side of Eqn. 18 and in turn, decreasing the total flow resistance of the CPF.

During post loading, the substrate wall permeability is constant (unless the PM cake layer is completely oxidized after active regeneration) and the particulate layer thickness increases because the oxidation rate is less than the PM addition rate from the engine.

The constants in the right-hand side of Eqn. 18 are the cake layer permeability, channel width and length, channel wall thickness, the Fanning friction factor for square channels equal to 28.454 (from reference [18]), and the variables are the substrate permeability and the cake layer thickness. Figure 3.8 graphically displays the raw experimental data pertaining to CPF resistance calculations for test B20-1. Subplot 1 is the calculated CPF resistance over the course of the entire test, subplot 2 is the exhaust viscosity and weighted average CPF temperature, subplot 3 is the exhaust mass flow rate, and subplot 4 is the CPF pressure drop profile.

The vertical drops in resistance at t = 5.8 and 5.9, and the vertical increase at 6.5 hours are not plausible since neither the PM cake layer thickness nor substrate wall permeability can change that rapidly for the given engine conditions of temperature and NO₂ concentration. The only variables that affect the change in CPF flow resistance between consecutive points in time would be the PM cake layer thickness and substrate wall permeability (due to changing PM mass), and at times where these variables are not changed (such as when switching engine conditions as shown at t = 5.8 hours in Figure 3.8), no change in CPF resistance should be present.

In order to correct the vertical shifts in the CPF flow resistance, a correction factor (CF) was applied to the denominator of the left-hand side of Eqn. 18 as indicated in Eqn. 20.

$$\text{Resistance} = \frac{\Delta P \cdot V_t \cdot \rho_{\text{exh}}}{\dot{m} \cdot \mu \cdot \text{CF}} \quad \text{Eqn. 20}$$

CF = Correction factor [fraction]

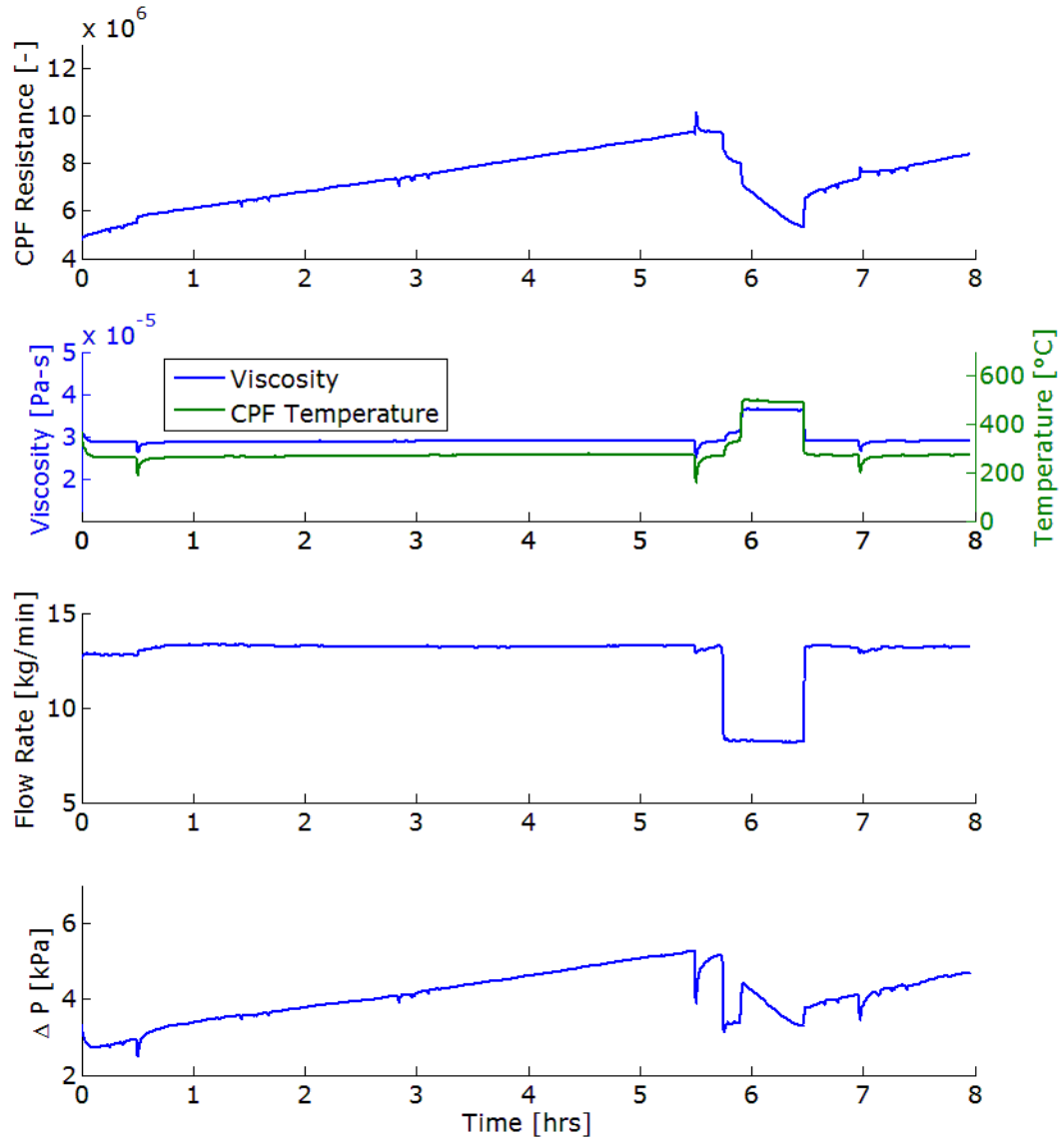


Figure 3.8: B20-1 Experimental CPF Flow Resistance (subplot 1), Exhaust Viscosity and CPF Average Temperature (subplot 2), Exhaust Mass Flow Rate (subplot 3), and CPF Pressure Drop Profile (subplot 4).

The engine-out exhaust mass flow rate is calculated based on a pressure transducer reading on the LFE and is assumed to be equal to the mass flow rate at the CPF inlet. It is believed that the correction factor accounts for PM and temperature maldistribution within the CPF (that may not be accounted for using the weighted average CPF temperature) as well as exhaust flow maldistribution at the CPF inlet. Although it is currently modeled as a constant, the PM cake layer permeability could

also change because of the change in pressure and as a result of the oxidation process during active regeneration, which the correction factor would also account for. The correction factor also compensates for the phasing differences that may be present between the mass flow rate, temperature, or pressure drop signals. The correction factor in Eqn. 20 corrects for the above effects so that a plausible resistance vs. time plot is available to be used with the MTU-1D CPF Model. The specific methodology used to determine CF for every test case can be found in Appendix H along with corrections for DAQ errors involved with the LFE and CPF pressure transducers and exhaust bypass valve leaks.

Chapter 4 Experimental Results

As previously discussed, an active regeneration experiment consists of several phases separated by CPF weighing events; Stage 1 loading, Stage 2 loading, Active Regeneration, Stage 3 loading, and Stage 4 loading are the phases of a typical active regeneration test. The following section details the experimental and modeling results from the Active Regeneration phase after a data integrity analysis of the experimental data that are used in the MTU-1D modeling effort [19]. The complete details of the analysis are in Appendix H.

The results pertaining to Stage 2 and Stage 4 loading, and the effects of biodiesel blends on them can be found in Appendix I and J respectively. The CPF filtration efficiency by mass was determined during Stage 2 loading phases and was determined to be an average of 97%.

4.1 Data Integrity Analysis for Modeling

From a modeling perspective, it is important that the integrity of the experimental data collected during active regeneration testing is good. This is important because inaccuracies with experimental data lead to difficulty in the modeling of the experimental data which can result in inaccurate models. By analyzing a set of key variables throughout the course of each active regeneration test, the integrity of the experimental data to be used in the modeling studies can be determined.

Using all the important variables that affect the model, Table 4.1 was created specifically outlining the specific variables used to analyze the integrity of the experimental data. The table includes simply Pass or Fail conditions for each variable as it relates to each individual test. Green cells indicate that the experimental data met the criterion. Yellow cells indicate that the experimental data can be used for model calibration after data corrections are implemented. The specific data corrections are explained later in this section as well as in Appendix H. Red cells indicate that the experimental data failed one of the criterion and the experimental data needs further analysis. As explained later, the PM concentration data is believed to be the most likely source of error in the experimental data pertaining to Stage 2 PM oxidation after the data corrections were implemented.

Table 4.1: Data Integrity Analysis Results

Run #	Test	Air Flow	CPF Pressure Drop	S2 PM Oxidation	AR PM Oxidation	Overall
1	B20 1	Pass	Pass	Pass	Pass	Pass
2	B20 2	Pass	Pass	Pass	Pass	Pass
3	B20 5	Fail	Fail	Pass	Fail	Pass
4	ULSD 3	Fail	Fail	Fail	Pass	Fail
5	ULSD 4	Fail	Fail	Pass	Pass	Pass
6	ULSD 5	Fail	Fail	Pass	Pass	Pass
7	ULSD 6	Pass	Pass	Pass	Pass	Pass
8	B20 6	Pass	Pass	Pass	Pass	Pass
9	B20 4	Pass	Pass	Fail	Pass	Fail
10	B10 1	Pass	Pass	Pass	Pass	Pass
11	B10 2	Pass	Pass	Pass	Pass	Pass
12	B10 3	Pass	Pass	Fail	Pass	Fail
13	ULSD 1	Fail	Pass	Pass	Pass	Pass
14	ULSD 8	Fail	Pass	Pass	Pass	Pass
15	ULSD 9	Fail	Pass	Pass	Pass	Pass
16	B10 4	Pass	Pass	Pass	Pass	Pass
17	ULSD 7R	Pass	Pass	Fail	Pass	Fail
18	ULSD 2R	Pass	Pass	Pass	Pass	Pass
19	ULSD 10	Pass	Pass	Fail	Pass	Fail

The variables included in Table 4.1 are:

- Air Flow: Pass condition given if there are no significant errors in air flow rate into the engine at constant engine operating conditions. Fail conditions were the result of DAQ system error related to pressure transducer measurements for Stage 1 loading. The steady state exhaust flow rate was corrected for Stage 1 and other test phases in order for the experimental data to be suitable for modeling.
- CPF Pressure Drop: Pass condition given if there are no significant fluctuations in the CPF pressure drop between test phases. Fail conditions could be the result of a sticking bypass line exhaust valve, or DAQ system error related to pressure transducer measurements for any specific test phase. Pass condition exists if CalTerm pressure drop can be used to correct the DAQ system pressure drop. All runs were corrected with the exception of Run 12.
- S2 PM Oxidation: Pass condition given if the S2 loading phase PM oxidation is within $21 \pm 9\%$ of the total PM entering the CPF. Fail conditions are most likely the result of inaccurate PM concentration. Further analysis of the data that affects the the 1D model was carried out and can be seen in Appendix H.
- AR PM Oxidation: Pass condition given if the PM oxidation during active regeneration does not exceed 80% of the total PM mass available for oxidation at the start of active regeneration. Greater than 80% PM oxidation leaves the opportunity for CPF weighing errors due to the small amount of PM within the CPF at the time of weighing for higher levels of PM oxidation.

The tests which failed the air flow criterion were the tests which showed a significant change in experimental flow rate between steady state phases at the same engine operating condition, such as test B20-5, where the air flow rate between Stage 1 and Stage 2 loading was measured 12.7 and 13.2 kg/min, respectively. The flow rate data were corrected based on the analysis in Appendix H. With the corrections implemented, the data can be used for calibration of the MTU-1D CPF model, represented by the color yellow in the 'Air Flow' column of Table 4.1.

Failure of the pressure drop criterion was a result of visible variation in the pressure drop between test phases, such as test B20-5 where the pressure drop at the loading ramp started nearly 1.5 kPa lower than the ending of Stage 2 and suddenly increases midway through. This is characteristic of the exhaust bypass valve sticking open and fully closing during the test, resulting in failure of the pressure drop criterion. The yellow cells marked 'Fail' in the 'CPF Pressure Drop' column of Table 4.1 represent the test cases which experienced a leaking exhaust bypass valve. With the air flow rate corrections implemented, this pressure drop data can be used for calibration of the MTU-1D CPF model, represented by the color yellow.

Test B10-3 was the only test which did not require any Stage 1 CPF pressure drop offset corrections due to DAQ system error with pressure transducer measurements. These data were corrected based on the analysis described in Appendix H and are the yellow cells marked 'Pass' in the 'CPF Pressure Drop' column of Table 4.1.

Failure of the S2 oxidation resulted if the measured PM oxidation during those phases was not between $21 \pm 9\%$. $21 \pm 9\%$ was the expected amount of PM oxidation to occur during loading phases, with variations likely due to PM concentration measurement errors. As detailed in Appendix H, the PM concentration data is the most likely source of error associated with the S2 PM oxidation data.

PM oxidation during active regeneration above 80% can potentially result in CPF weighing errors due to the low levels of PM within the CPF at the time of weighing. Failures are shown by the color red in Table 4.1. The AR PM oxidation during test B20-5 approached 88%; while this is above the 70% target, the CPF mass measurements are believed to be accurate and as such, the test data can be used for calibration of the MTU-1D CPF model.

Overall failure resulted if any given test failed more than the air flow or CPF pressure drop criterion alone, because the air flow can be corrected, as stated previously. For all four test cases in the 'CPF Pressure Drop' column of Table 4.1, the exhaust bypass valve was leaking. The flow rate corrections allow for this pressure drop data to be used for model calibration.

In total, the experimental data from eight tests can be said to be well suited for modeling, where they are shown by the green cells in the 'Overall' column of Table 4.1.

The CPF resistance was calculated for each test case, as described in the CPF Resistance Calculation Method section of Chapter 3 (section 3.10), where the CPF mass flow rate scaling factors (SF), the CPF pressure drop offset corrections, and the correction factor (CF) for active regeneration phases are shown in Tables H3-H5. The un-corrected and corrected experimental data related to CPF resistance for each test case is also shown at the end of Appendix H. The correction methods to be applied to the input data for the MTU-1D CPF model are also given at the end of Appendix H.

The tests which can be used for calibration of the MTU-1D CPF model following the data corrections previously mentioned are shown by the yellow cells in the 'Overall' column of Table 4.1. With the data corrections implemented when necessary, a total of fourteen tests can be used for calibration of the CPF model.

In terms of the active regeneration data analysis, the main variables which are analyzed are the gaseous emissions, CPF pressure drop profile, CPF temperature, CPF mass measurements, active regeneration time, and engine-out PM concentration.

The variables selected for Table 4.2 are the dosing method used during each test, active regeneration time, pre-active regeneration ramp times, DOC inlet temperature, CPF inlet temperature, average CPF temperature, exhaust mass flow rate, estimated dosing flow rate, estimated engine-out HC concentration, engine-out PM concentration, PM mass available for oxidation, and percent of the PM oxidized during active regeneration (which includes the retained PM within the CPF as well as the engine-out PM emitted during the active regeneration process).

4.2 Active Regeneration

The active regeneration of the CPF is the area of interest in this study. The Active Regeneration phase of the experiment is initiated after the CPF loading of 2.2 ± 0.2 (or 4.1 ± 0.2 in two test cases) g/L has been verified at the conclusion of Stage 2 loading. For the testing performed in this study, a range of CPF inlet temperatures from 475 to 600°C using in-cylinder and exhaust dosing methods with ULSD, B10, and B20 were selected for the test matrix to determine which factors affect the PM oxidation within the CPF during active regeneration.

A summary of the most important variables from the active regeneration testing are given in Table 4.2, with the complete mass balances for all phases for each test in Appendix K.

Table 4.2: Selected Active Regeneration Test Data

Variable	Dosing Method	Active Regen Time	Loading Ramp Time	AR Ramp Time	Engine Speed	Engine Load	DOC Inlet Temp.	CPF Inlet Temp.	Average CPF Temp.	Exhaust Mass Flow Rate	Estimated Doser Flow Rate	Estimated Engine Out HC Conc.	Engine Out PM Conc.	PM Mass Available for Oxidation	Percent PM Oxidized
Test/Units	-	Minutes	min	min	RPM	N-m	°C	°C	°C	kg/min	g/sec	ppmC1	mg/scm	g	%
B20 1	in-cyl	34.7	14.9	9.0	1400	460	329	477	474	8.2	0.517	7601	8.3	39.2	53.5
B20 2	in-cyl	38.8	14.3	9.9	1400	460	330	501	508	8.2	0.608	8915	9.9	39.7	78.5
B20 5	in-cyl	19.0	15.0	10.1	1400	460	328	527	534	8.1	0.695	10306	9.9	38.6	87.8
ULSD 3	in-cyl	15.5	15.0	10.8	1400	460	330	524	526	8.0	-	-	22.2	43.8	42.3
ULSD 4	in-cyl	21.0	14.8	10.4	1400	460	334	526	531	7.9	0.648	10124	18.5	47.0	61.0
ULSD 5	in-cyl	21.6	14.5	10.1	1400	460	340	525	529	8.0	0.636	9826	24.3	45.1	62.9
ULSD 6	exhaust	21.5	14.9	9.6	1400	460	334	524	540	8.0	0.667	10303	18.3	45.7	66.8
B20 6	exhaust	15.9	14.6	15.1	1400	460	322	528	540	8.3	0.749	10941	12.9	42.8	78.2
B20 4	in-cyl	21.8	14.6	11.5	1400	460	333	504	506	8.1	0.594	8840	17.8	44.3	71.8
B10 1	in-cyl	25.7	14.8	10.7	1400	460	335	526	534	7.9	0.654	10099	15.1	46.1	75.3
B10 2	in-cyl	18.9	14.7	10.1	1400	460	337	525	531	8.0	0.646	9859	17.4	43.8	75.2
B10 3	in-cyl	22.3	14.3	10.7	1400	460	338	526	531	8.0	0.648	9890	11.2	40.6	67.2
ULSD 1	exhaust	14.6	14.8	10.2	1400	460	336	553	567	8.0	0.759	11724	26.9	48.9	67.5
ULSD 8	in-cyl	19.9	14.8	10.0	1400	460	342	526	539	7.7	0.635	10129	22.5	85.2	51.7
ULSD 9	in-cyl	17.3	14.8	10.3	1400	460	346	550	563	7.9	0.727	11370	21.9	71.4	76.8
B10 4	in-cyl	14.5	14.6	10.6	1400	460	337	550	563	7.9	0.738	11402	15.7	43.8	69.5
ULSD 7R	in-cyl	17.0	14.8	10.3	1400	460	340	550	562	7.7	0.709	11340	25.9	48.4	76.7
ULSD 2R	in-cyl	6.2	14.6	10.1	1400	460	337	604	616	7.7	0.893	14294	19.8	48.3	80.7
ULSD 10	in-cyl	22.4	14.7	9.8	1450	450	345	530	538	8.3	0.663	9895	13.0	41.8	78.5

DOC inlet temperature was a direct measurement from the exhaust pipe located at the DOC inlet cone. Since this is not part of the DOC thermocouple layout (not located in any part of the DOC), it is excluded from Figure 3.2. Each experimentally measured and reported DOC inlet temperature is the result of the average over time of the points during the active regeneration portion of the test, since each temperature is calculated at every time step throughout the experiment during post processing of experimental data.

CPF inlet temperature was defined as the average of D7, D8, and D9 thermocouples, the locations of which can be seen in Figure 3.2.

Average CPF temperature was defined as the weighted average of all thermocouples located in the CPF in Figure 3.3 except the axial set of thermocouples located at the radial edge of the CPF. Thermocouples C1-C3, C5-C7, C9-C11, and C13-C15 carry weighing factors of 0.303, 0.287, 0.197, and 0.213 respectively, due to their axial placement in the CPF substrate. These weighting factors were determined using the methodology described in the Temperature Measurements section of Chapter 3. The locations of these thermocouples was determined based on the method from references [1, 6], in order to allow for the determination of volume averaged CPF temperatures for each experiment.

The engine-out exhaust mass flow rate was calculated using the pressure drop across the laminar flow element (LFE) giving the air flow rate and the fuel flow rate consumed by the engine was calculated using an AVL fuel system. The exhaust mass flow rate is calculated at each time step throughout the experiment and is the result of the summation between the air and fuel mass flow rates. The reported exhaust mass flow rate is the average of all the calculated flow rates throughout each phase of the experiment.

The doser flow rate and engine out HC concentrations represented are the estimated values resulting from a DOC energy balance. There was significant variation in the experimentally determined doser flow rate, and subsequent engine out HC concentrations. A comparison of the experimental vs. estimated doser flow rates can be found in Appendix L. The DOC energy balance was carried out using the methods described in reference [17] in order to estimate the upstream DOC HC concentrations and doser flow rate. The energy balance used the experimentally

measured downstream DOC HC concentrations and the measured temperature rise across the DOC to estimate the amount of HC required at the DOC inlet to produce the observed temperature change. The estimated DOC inlet HC concentrations were then converted back to dosing flow rate in the same manner that is used to calculate upstream DOC hydrocarbon concentrations from the experimental dosing rate (Eqn. 21). The data for estimated doser flow rate is missing for test ULSD-3 because the emissions bench was not operational during this test, which resulted in missing DDOC HC data to be used in the energy balance.

The percent PM oxidized (70% target for all tests) is the calculated amount of PM that was oxidized during the Active Regeneration phase. The total amount of PM available for oxidation is defined as the PM mass within the CPF at the start of active regeneration in addition to the engine-out PM that flows into the CPF during the Active Regeneration phase. The total PM oxidized is calculated based on the CPF mass measurement following Stage 3 loading. Subtracting the estimated PM mass addition during Stage 3 loading from the PM within the CPF at the end of Stage 3 yields the PM mass remaining after active regeneration. Subtracting the mass of PM at the end of active regeneration from the total PM at the start of active regeneration yields the amount of PM mass oxidized during active regeneration. The percent PM oxidized is the percent of the total PM mass available for oxidation that was actually oxidized during the Active Regeneration phase calculated using $\left(\frac{PM \text{ Oxidized during AR}}{Total \text{ PM Available for Oxidation}}\right) \cdot 100$.

In Table 4.2, there are a few items from the experimental results that need to be explained.

Differences in PM concentrations between tests at the same experimental conditions were noticed. For example, the engine-out PM concentration during active regeneration for test B10-2 was 15% higher than test B10-1. Since the absolute humidity was 0.008 and 0.009 kg_{water}/kg_{air} during test B10-2 and B10-1, respectively test cell humidity is not believed to be the cause of these differences.

PM concentrations were also affected by the percent biodiesel in the test fuel, which can be seen in Figure 4.1. In Figure 4.1, the average engine-out PM concentrations measured during the pre-test phase are displayed with error bars representing one standard deviation between all of the PM samples collected during the experiment.

The data is displayed in the order of completion of the tests to see the trends in PM concentration throughout the testing period. The PM concentrations were shown to decrease with increasing concentrations of biodiesel in the test fuel as well as fluctuate due to test cell conditions.

In Figure 4.1, the larger error bars are associated with tests, i.e., Tests 15, 17 and 18, in which individual PM samples may have been damaged during the sampling or weighing processes. These damaged filters introduce error into the filter mass measurements resulting in increased standard deviation of engine-out PM concentration. The damaged filters were subsequently removed from the calculated average engine-out PM concentration reported in the data.

Differences between in-cylinder and exhaust dosing methods regardless of fuel can be seen in the elevated average CPF temperatures during active regeneration. Tests B20-6 and ULSD-6, both of which used exhaust dosing, resulted in an average CPF temperature of 540°C. The comparable B20 (B20-5) and ULSD (ULSD-3, 4, and 5) tests using in-cylinder dosing resulted in an average CPF temperature of 534 and 529°C, respectively, resulting in an average CPF temperature increase of 6°C and 11°C, respectively, when using exhaust dosing.

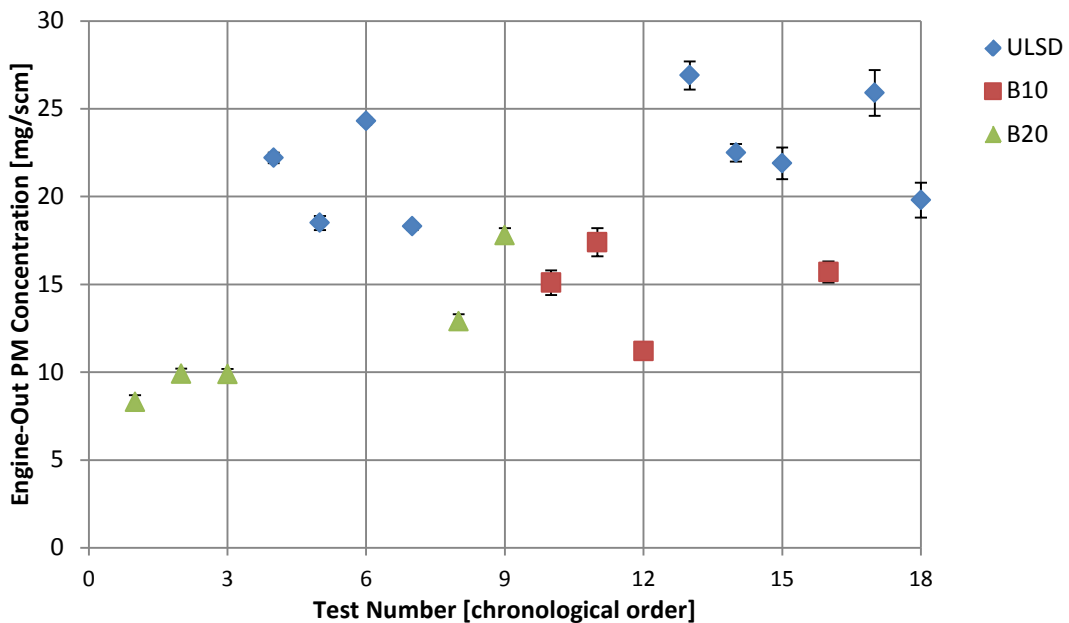


Figure 4.1: Pre-test Phase for Active Regeneration Average Engine-Out PM Concentrations in Chronological Order

4.2.1 Gaseous Emissions

Complete gaseous emissions summaries for all active regeneration experiments can be found in Appendix M. During active regeneration, gaseous emissions are measured DDOC and DCPF only due to the increased HC concentration found UDOC during fuel dosing, regardless of dosing method. The increased HC concentrations found UDOC are out of the range of the gaseous emissions analyzer and could damage it, so the UDOC HC concentrations were calculated using the estimated dosing flow rate and exhaust flow rate with Eqn. 21.

$$Y_{UDOC} = \frac{\frac{\dot{m}_f}{MW_f}}{\frac{\dot{m}_f}{MW_f} + \frac{\dot{m}_{exh}}{MW_{exh}}} \cdot e^6 \quad \text{Eqn. 21}$$

Y_{UDOC} = UDOC HC concentration [ppm C]

\dot{m}_f = Estimated dosing flow rate [g/sec]

\dot{m}_{exh} = Exhaust flow rate [g/sec]

MW_f = Molecular weight of fuel [g/gmol]

MW_{exh} = Molecular weight of exhaust = 28.5 (reference [15]) [g/gmol]

The molecular weight for the B10 and B20 biodiesel blends were calculated based on fuel analysis data from tests performed on ULSD and B100. The molecular weights for ULSD, B10, and B20 were determined to be 166, 168, and 170 g/gmol, respectively, on a C_{12} basis. The computation methodology used to determine the molecular weights can be found in Appendix A.

Eqn. 21 is valid assuming all the dosing fuel was vaporized in the exhaust stream [15]. The other UDOC gaseous emissions were collected and are assumed unchanged from the pre-test phase of each experiment.

Since DDOC HC measurements are taken first during active regeneration, coupled with the length of the active regeneration times, DCPF HC measurements during active regeneration were influenced by HC absorption in the line to the FID when switching sampling locations of high HC concentration to low HC concentration. Figure 4.2 illustrates this graphically, which can be seen since the measured HC concentration never reaches a steady state value during the sample time. The HC concentration shown in Figure 4.2 is the DCPF HC measurement following 6 minutes of sampling HC in the DDOC location during active regeneration.

The data for Figure 4.2 comes from test ULSD-3, but the same trend was present for all fuels. For this reason, the DCPF hydrocarbon concentration found during the active regeneration engine condition validation test was used in calculating CPF hydrocarbon conversion efficiencies. The point validation test was conducted with ULSD before the start of active regeneration testing, in order to map the DOC and CPF inlet temperatures for in-cylinder and exhaust dosing methods across the entire CPF inlet temperature range seen in Table 3.8, the experimental test matrix. Gaseous emissions were collected at all three sampling locations during the entire test, allowing enough time for the values to stabilize. Table 4.3 shows the results of the in-cylinder, 600°C CPF inlet temperature case from the point validation test, which is where the DCPF HC concentration used for conversion efficiency calculations was derived from. The DCPF HC concentration was assumed to remain unchanged across all fuel types for HC conversion efficiency calculations.

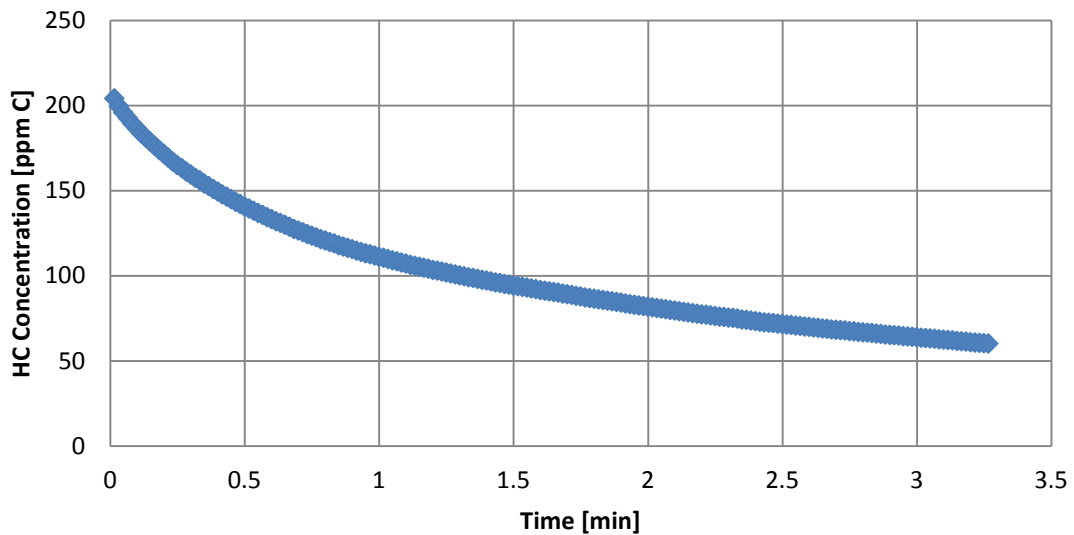


Figure 4.2: ULSD-3 DCPF HC Measurement during Active Regeneration (In-cylinder Dosing Case)

Table 4.3: HC Measurements Recorded during Active Regeneration Point Validation

DOC Inlet Temp	CPF Inlet Temp	CPF Outlet Temp	UDOC HC Conc.	DDOC HC Conc.	DCPF HC Conc.
°C	°C	°C	ppm C	ppm C	ppm C
329	603	609	20829	512	4

Table 4.4 shows the HC, CO, and NO₂ conversion efficiencies across the DOC and CPF during active regeneration for all experiments. A '*' next to the test name indicates a test which used the exhaust dosing method.

The lowest and highest DOC HC conversion efficiencies measured were 94% and 98%, respectively, while the CPF HC conversion efficiency remained between 98 and 99% for all experiments. The lowest and highest DOC CO conversion efficiencies measured were 53% and 96%, respectively. In general, it has been shown that the CO conversion efficiency decreases with increasing CPF inlet temperature due to the chemical reactions occurring within the DOC to oxidize the excess HC. The negative NO₂ conversion across the DOC indicates that NO₂ is being consumed across the DOC, while the positive NO₂ conversion across the CPF indicates that NO₂ is being produced across the CPF, which was observed during all experiments regardless of fuel type. This is the opposite of the trends found in Chilumukuru [15] where NO₂ concentrations across the DOC increased, but decreased across the CPF, indicating net NO₂ consumption in the CPF for PM oxidation.

Table 4.4: HC, CO, and NO₂ Conversion Efficiencies for All Tests

Test	HC Conversion Efficiency [%]		CO Conversion Efficiency [%]		NO ₂ Conversion Efficiency [%]	
	DOC	CPF	DOC	CPF	DOC	CPF
Location						
B20 1	96	98	91	100	-4	26
B20 2	96	99	70	100	-14	26
B20 5	97	99	72	100	-14	18
ULSD 3	-	-	96	100	-10	22
ULSD 4	98	99	91	100	-17	21
ULSD 5	97	99	89	100	-10	22
ULSD 6*	95	99	87	100	-9	22
B20 6*	94	99	77	100	-17	16
B20 4	97	99	83	100	-12	32
B10 1	96	99	83	100	-12	22
B10 2	98	99	83	100	-21	22
B10 3	97	99	85	100	-20	15
ULSD 1*	95	99	83	100	-16	11
ULSD 8	94	99	72	100	-9	14
ULSD 9	94	100	69	100	-19	9
B10 4	96	99	72	100	-17	10
ULSD 7R	96	99	66	100	-6	11
ULSD 2R	97	99	53	100	-4	9
ULSD 10	97	99	77	100	-107	25

* Indicates post-turbo dosing test case

Gaseous emission data during active regeneration from Austin [1] for the ISM engine indicates that some tests resulted in net NO₂ consumption across the CPF while others resulted in NO₂ production, with the same test fuel.

Due to NO₂ production across the CPF for experiments run on the ISL, NO₂ is not believed to be a significant aid for PM oxidation within the CPF at the engine condition selected. NO₂ based oxidation can occur at other engine conditions, which is the main focus in the study by Shiel [11].

HC measurements were unavailable during ULSD-3 due to the flame ionization detector (FID) in the gaseous emissions analyzer experiencing a failure which required repair by AVL.

4.2.2 CPF Pressure Drop Profile

During active regeneration, the pressure drop across the CPF increases upon the start of fuel dosing due to the increase in the temperature of the exhaust, which increases the exhaust actual volumetric flow rate. The actual exhaust volumetric flow rate is given in Eqn. 22 with the equation for calculating density as a function of pressure and temperature in Eqn. 23.

$$\dot{V} = \frac{\dot{m}}{\rho} \quad \text{Eqn. 22}$$

\dot{V} = Actual volumetric flow rate

\dot{m} = Mass Flow Rate [kg/min]

ρ = Density [kg/m³]

$$\rho = \frac{P}{R \cdot T} \quad \text{Eqn. 23}$$

R = Universal gas constant, 8.315E-03 [J/(gmol·K)]

T = CPF weighted avg. temperature [K]

As the active regeneration progresses, PM in the cake and the wall oxidizes, and the pressure drop across the CPF decreases. If the regeneration were allowed to continue for an extended period of time, the pressure drop would asymptotically approach a constant value as the balance point (PM within the CPF is oxidized at the same rate that it is deposited from the engine) is reached.

The pressure drop profile for 525°C CPF inlet temperature runs using ULSD, B10, and B20 with in-cylinder dosing are shown in Figure 4.3. The active regeneration phase during ULSD-4, B10-1, and B20-5 resulted in total PM oxidation of 63%, 77%, and 88%, respectively, as shown in Table 4.5.

In this plot, B10-1 had the longest regeneration, followed by ULSD-4 and B20-5. The amount of time that fuel dosing was activated, and subsequently the active regeneration time, is not an accurate representation of the oxidation rate of PM within the CPF because different amounts of PM were oxidized between all three tests.

Table 4.5: Data from Tests Run for Figure 4.3

Test/Units	AR Time	Average CPF Inlet Temp.	Estimated Doser Flow Rate	CPF Loading Prior to AR	Percent PM Oxidized
	min	°C	g/sec	g/L	%
ULSD 4	21.0	520	0.648	2.6	63
B10 1	25.7	521	0.654	2.5	77
B20 5	19.0	523	0.695	2.2	88

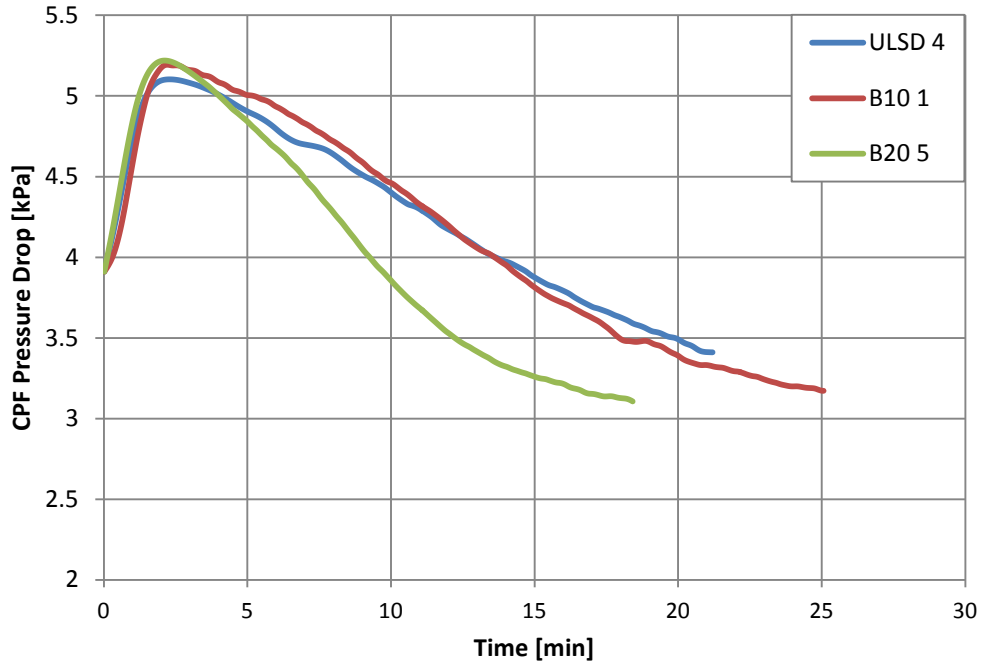


Figure 4.3: Comparison of CPF Pressure Drop for ULSD-4, B10-1, and B20-5, all at Nominal 525°C CPF Inlet Temperature using In-Cylinder Dosing

For tests at the same CPF inlet temperature, prior to the balance point of the CPF, the slope of the pressure drop profile across the CPF is representative of the PM oxidation rate in the wall and cake within the CPF. The balance point of the CPF is defined as the time during active where the CPF pressure drop does not fluctuate and appears as a horizontal time when displayed over time. Keeping this in mind, it can be seen in Figure 4.3 that B20 has the highest PM oxidation rate, followed by B10 and ULSD because the slope of the pressure drop profiles are steepest with B20, followed by B10 and ULSD. The wall pressure drop can have a significant effect on the overall pressure drop even though the mass of PM in the wall is significantly less

than in the cake. Complete pressure drop profiles for all tests can be found in Appendix N.

It can be seen in Figure 4.3 that the peak pressure drop does not occur at the same point for all the tests. This could be due to a number of factors such as PM loading and amount of fuel being dosed during active regeneration, which can be found in Table 4.4. ULSD-4 had the highest PM loading with a dosing rate only slightly higher than that of B10-1, yet the peak pressure drop across the CPF occurred nearly 0.3 kPa lower than the two biodiesel tests. B20-5 had the lowest CPF PM loading with the highest fuel dosing rate while B10-1 had CPF PM loading 0.1 g/L lower than ULSD-4, with the lowest fuel dosing rate, and the peak pressure drop for both tests occurred near 5.3 kPa.

Figure 4.4 shows tests completed with B20 and ULSD at the same CPF inlet temperature (525°C) using in-cylinder and exhaust dosing methods. Blue lines indicate the ULSD tests, with the dashed line representing the exhaust dosing case. The same holds true for the B20 test cases, except the representative lines are orange.

The in-cylinder dosing tests in Figure 4.4 were B20-5 and ULSD-4 while B20-6 and ULSD-6 were the post turbo dosing tests. In both post turbo dosing cases, the peak pressure drop is elevated from the in-cylinder dosing cases. The average CPF temperature was also elevated during these tests, which could account for the differences in the pressure drop peaks because increased temperature results in increased pressure drop due to increased actual exhaust volumetric flow rate. Figure 4.4 also re-iterates the fact that at a constant CPF inlet temperature, PM oxidation with B20 progresses at a significantly faster rate than with ULSD, as shown by the differences in the slope of the pressure drop profile.

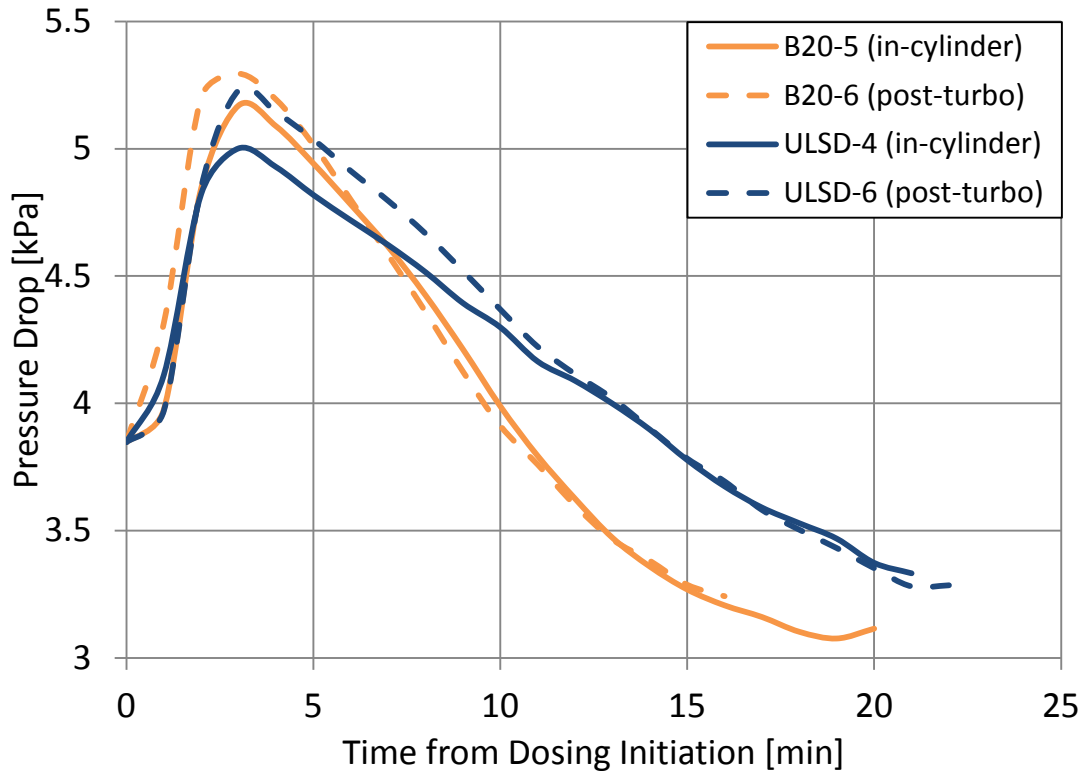


Figure 4.4: 525°C CPF Inlet Temperature B20 and ULSD Tests using In-cylinder and Exhaust Dosing

4.2.3 Particle Size Distribution

Particle size distribution data were collected only DDOC and DCPF during the Active Regeneration phase due to the high levels of hydrocarbons UDIC during fuel dosing which could damage the SMPS system. DDOC and DCPF average particle size distribution data by number of particles, by fuel type can be seen in Figure 4.5. It is believed that a cracked fitting on the SMPS system occurred near the time that test B10-2 was performed, corresponding to run 11 of 19, and as such, only the data collected before this test will be presented.

In Figure 4.5, it can be seen that the number of particles sampled in both locations is greatest with ULSD, followed by B10 and B20, which was expected based on the trends associated with decreasing particle count with increasing percent biodiesel in the test fuel as reported by Austin [1].

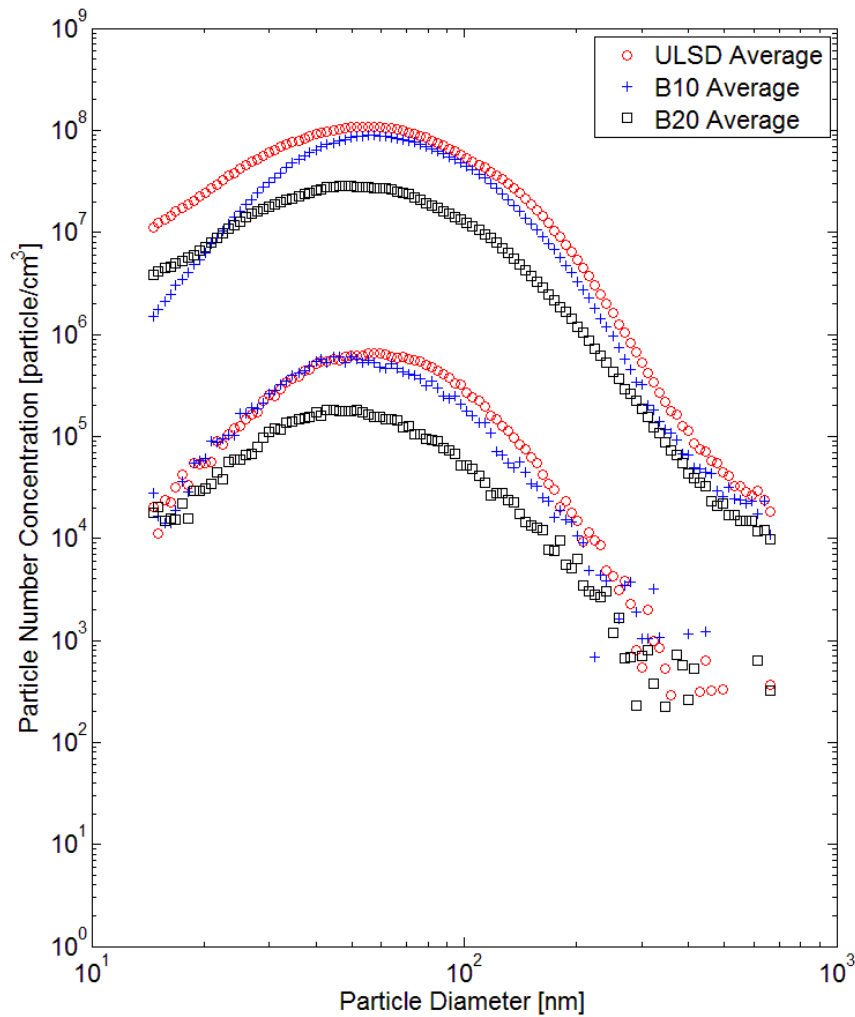


Figure 4.5: Averaged Particle Size Distribution by Particle Numbers by Fuel Type during Active Regeneration sampled DDOC and DCPF

4.2.4 CPF Temperature Gradients

The CPF thermocouple layout, as illustrated in Figure 3.3, is significantly different from the layout by Chilumukuru [15] and Austin [1] because it was not achievable due to physical limitations of the CPF. The modified layout incorporates 4 radial and 4 axial thermocouple placement positions and now includes an axial set of thermocouples located in the center of the CPF. Austin [1] and Chilumukuru [15] did not place any thermocouples in the center of the CPF.

Figure 4.6 represents the radial temperature profiles during active regeneration for each axial set of thermocouples from test ULSD-4 (2.2 g/L and 525°C CPF inlet temperature targets, in-cylinder dosing). The temperatures measured by each thermocouple were averaged for the entire active regeneration portion of the experiment. Figure 4.6 represents the radial temperature gradient at each axial location that thermocouples are located (i.e., the 32mm axial location consists of thermocouples C1, C2, C3, and C4 from Figure 3.3).

As seen in Figure 4.6, as the axial distance from the CPF inlet increases, the temperature measured by the thermocouples in those axial locations increases also. The increase in temperature in the axial direction, from the inlet of the CPF toward the outlet, is the result of hydrocarbon and PM oxidation within the CPF, with the hydrocarbon oxidation being the primary source of energy release according to reference [1]. As the radial distance from the CPF center increases, the temperatures measured by the thermocouples in those locations decreases, which was the same trend in all axial locations in the CPF. For the thermocouples located at 153 and 273 mm from the inlet face, the temperature gradient toward the outer edge of the CPF is greater than the other axial locations. The temperature at the CPF radius was estimated for each case using a 3rd order polynomial fit of the data from all other thermocouple locations and is shown by the red vertical line in Figure 4.6.

The tests which were run with the post turbo dosing injector had elevated CPF temperatures when compared to tests run with in-cylinder dosing at the same test conditions. It can be seen in Table 4.6 that the ULSD and B20 cases had CPF inlet temperatures within 1°C and average CPF temperatures increased by 11 and 6°C, respectively, for the exhaust dosing cases. This could have been caused by the increase in doser flow rate required for post-turbo regeneration to reach the same CPF inlet temperature, allowing more HC to reach the CPF, thereby increasing the exotherm generated during active regeneration. Table 4.6 shows the average CPF temperature for ULSD and B20 in-cylinder dosing compared to post-turbo dosing test conditions.

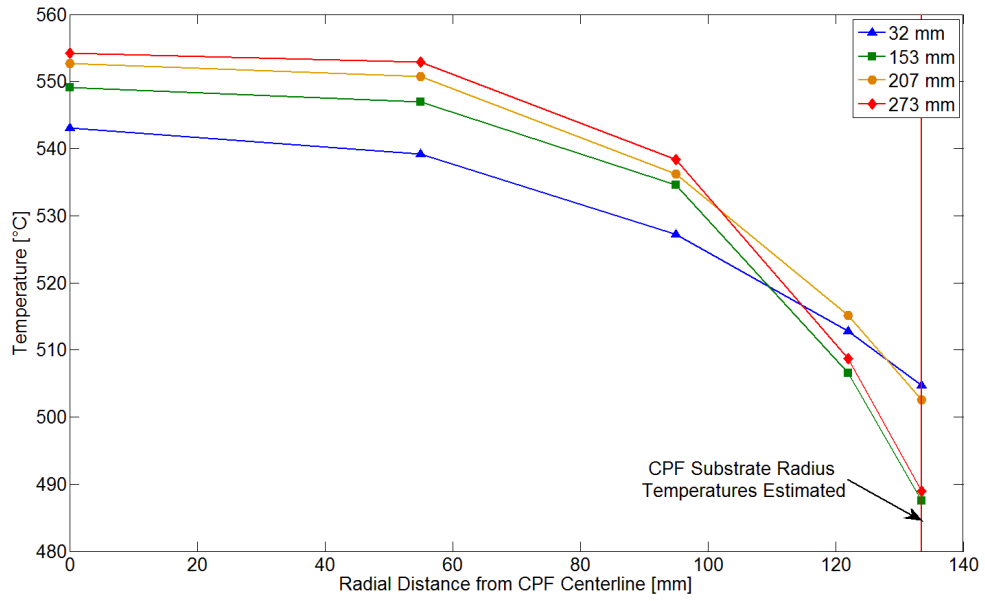


Figure 4.6: Radial Temperature Gradients at Four Axial Locations (Distance from CPF Inlet) during ULSD-4 Active Regeneration (525°C CPF Inlet Temperature Target, In-Cylinder Dosing)

Table 4.6: Average CPF Temperature as a Function of Dosing Method for USLD and B20

Variable	CPF Inlet Temp. [°C]	Average CPF Temp. [°C]
ULSD in-cyl	525	529
ULSD post-turbo	524	540
B20 in-cyl	527	534
B20 post-turbo	528	540

Figure 4.7 illustrates the axial temperature gradients within the CPF during active regeneration. The radial temperature measurements at each axial location were averaged (over the course of the entire active regeneration portion of each experiment) to show the effect of fuel and CPF temperature on the axial temperature gradient. All tests in Figure 4.7 were conducted using in-cylinder dosing.

As shown in Figure 4.7, the effect of fuel type on the axial temperature gradients are minimal, as the temperature gradient lines from tests ULSD-4, B10-1, and B20-5 all lay nearly on top of each other, and since each test had the same CPF inlet temperature target, it can be said that the effects of fuel type on the axial temperature gradients are negligible. As the CPF inlet temperature increases, the temperature change across the CPF also increases, which was expected, because higher HC concentrations required for elevated CPF inlet temperatures lead to higher temperatures in the axial direction from inlet to outlet. Regardless of test fuel type or CPF inlet temperature, the same average-radial temperature change from CPF inlet to outlet was observed at each axial location $\approx 4^{\circ}\text{C}$.

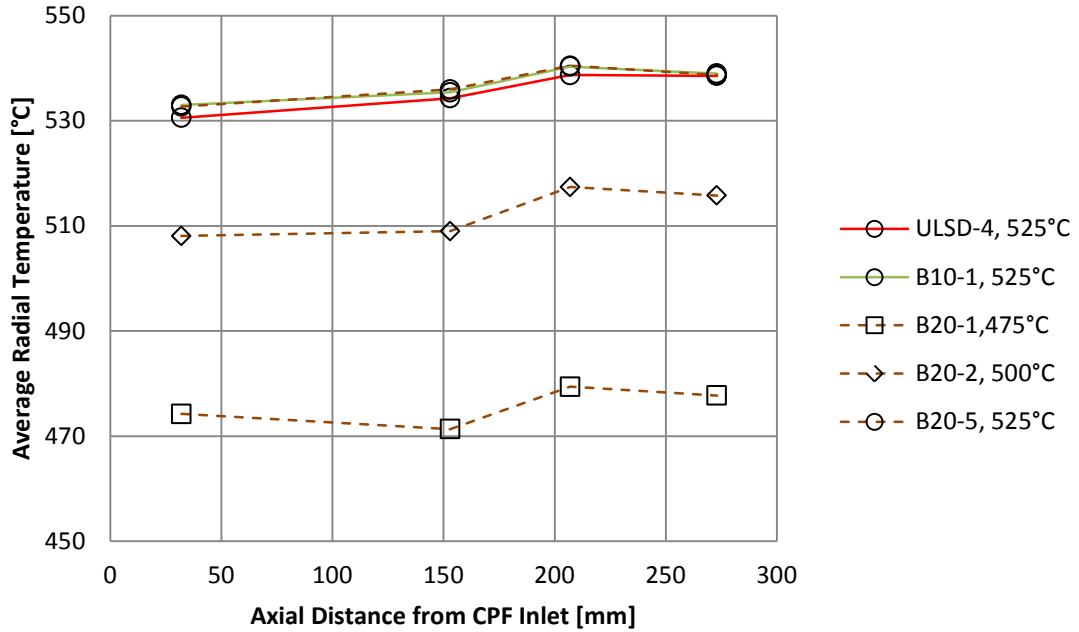


Figure 4.7: Average-radial Axial Temperature Gradients during Active Regeneration with In-cylinder Dosing

4.2.5 PM Reaction Rate

As described in Chapter 3, the PM reaction rate is calculated using a method that is different than what was used by Austin [1] and Chilumukuru [15] in order to account for varying CPF temperatures throughout active regeneration. The first step is using Eqn. 15 to solve for the pre-exponential by iteration until the PM mass within the CPF at the beginning and ending of active regeneration are matched within $\pm 0.1\text{g}$. Table 4.7 is the result of this first step and shows the pre-exponential factors determined for each test case.

Table 4.7: Calculated Pre-exponential Factors for all Tests

Variable	Pre-exponential Factor · 10 ⁶
Abbreviation	A
Test/Units	1/sec
B20 1	5.08
B20 2	3.29
B20 5	4.62
ULSD 3	2.06
ULSD 4	2.04
ULSD 5	2.20
ULSD 6	1.76
B20 6	3.38
B20 4	5.43
B10 1	2.22
B10 2	3.24
B10 3	2.27
ULSD 1	1.46
ULSD 8	1.38
ULSD 9	1.80
B10 4	1.75
ULSD 7R	1.77
ULSD 2R	1.88
ULSD 10	2.71

With the pre-exponential factor known, the average CPF temperature matrix (CPF average temperature calculated at every time point in the experiment) is used as an input to Eqn. 16, which assumes that the activation energy and pre-exponential factor remain constant.

Using Eqn. 16, the reaction rate is calculated for each time step of the active regeneration portion of the experiment and then reported in matrix form. The reported reaction rate is the calculated value corresponding to the average CPF temperature during active regeneration. The calculated reaction rates and corresponding pre-exponential factors for all tests can be seen in Table 4.8.

Table 4.8: Calculated Reaction Rate and Pre-exponential Factor Values for All Tests

Variable	Pre-exponential Factor · 10 ⁶	Reaction Rate	Average CPF Temp.	CPF Inlet O2 Concentration
Abbreviation	A	RRo	T _{CPF_AR_AVG}	YO ₂
Test/Units	1/sec	1/sec	°C	%
B20 1	5.08	4.23E-03	474	8.8
B20 2	3.29	8.29E-03	508	8.0
B20 5	4.62	2.34E-02	534	8.2
ULSD 3	2.06	9.06E-03	526	7.6
ULSD 4	2.04	1.03E-02	531	7.6
ULSD 5	2.20	1.03E-02	529	7.7
ULSD 6	1.76	1.11E-02	540	7.7
B20 6	3.38	2.01E-02	540	8.2
B20 4	5.43	1.25E-02	506	8.3
B10 1	2.22	1.18E-02	534	7.8
B10 2	3.24	1.61E-02	531	7.7
B10 3	2.27	1.12E-02	531	7.8
ULSD 1	1.46	1.96E-02	567	7.2
ULSD 8	1.38	8.37E-03	539	7.8
ULSD 9	1.80	2.18E-02	563	7.3
B10 4	1.75	2.05E-02	563	7.5
ULSD 7R	1.77	2.07E-02	562	7.3
ULSD 2R	1.88	8.28E-02	616	6.9
ULSD 10	2.71	1.47E-02	538	8.5

4.2.6 Activation Energy Determination

All tests were optimized using a range of activation energies of 120-150 kJ/gmol which yielded the results in Table 4.9. In Table 4.9, the reported pre-exponential factors are the result of averaging the pre-exponential factors for each fuel type. The lowest average pre-exponential factor was found with ULSD, while the highest was found with B20, which was expected.

The upper and lower limits for the activation energy were adjusted until the pre-exponential factors reported for each fuel type correlated well with the experimental data. This correlation can be seen in Figure 4.8 where the experimentally determined reaction rate normalized by the molar fraction of oxygen into the CPF is plotted as a function of average CPF temperature in the Arrhenius form.

Table 4.9: Optimization Results using All Tests

Variable	Pre-exponential Factor	Activation Energy
Abbreviation	A	Ea
Fuel/Unit	1/sec	kJ/gmol
ULSD	9.8E+06	139
B10	12.2E+06	
B20	20.1E+06	

A statistical analysis between average pre-exponential factors was done using a two sample t-test in order to determine whether or not the average pre-exponential factors were statistically different between fuel types. It was determined, with 95% confidence, that the average pre-exponential factors were statistically the same for ULSD vs. B10, but were statistically different between ULSD vs. B20 and B10 vs. B20.

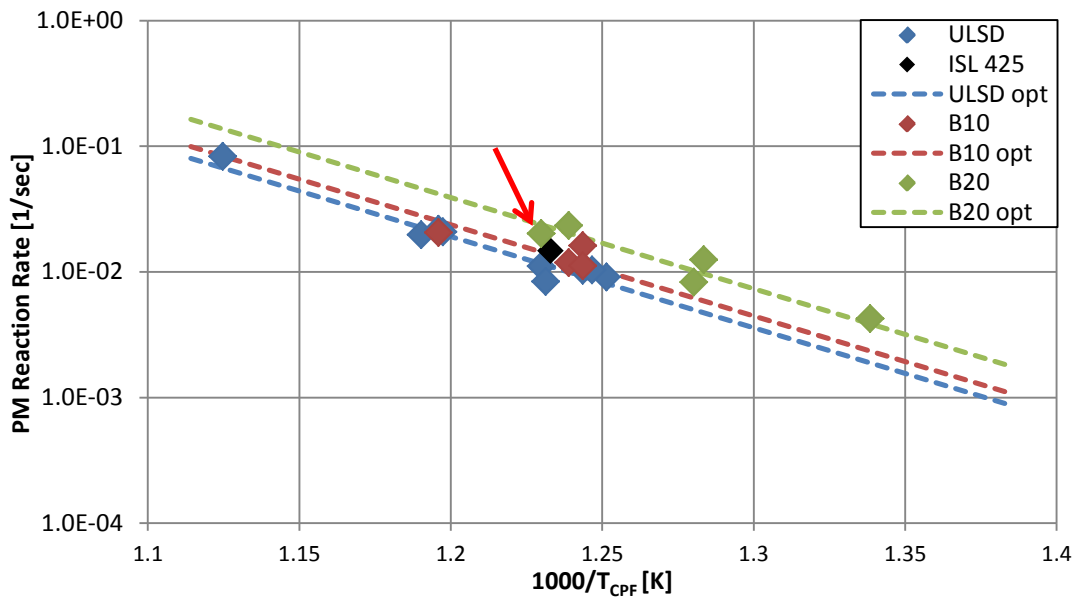


Figure 4.8: Optimized Results with All Tests Included in the Optimization

As can be seen in Figure 4.8, the reaction rate increases with increasing CPF inlet temperature for all experiments run on the 2007 ISL. Reaction rate also increased with an increasing percentage of biodiesel in the test fuel (i.e., B20 had a higher reaction rate than B10, B10 has a higher reaction rate than ULSD, with a constant CPF temperature). These trends were expected and are the same trends seen in the experimental data from Austin [1].

Tests ULSD-6 and B20-6 were conducted using the auxiliary dosing injector located in the exhaust rather than in-cylinder dosing which was used for all other tests. The B20 test utilizing the auxiliary dosing injector in Figure 4.8 has a red arrow marking it, to visualize the shift along the horizontal axis. This shift is a result of the change in average CPF temperature. The average CPF temperature during active regeneration was increased by 6 °C in the B20 case and 11 °C in the ULSD case. ULSD-10, conducted on the ISL 425, is represented by a black marker in Figure 4.12. There is not a significant change in the reaction rate when compared to ISL 365 tests, although more ISL 425 active regeneration tests should be conducted in order to verify this result.

4.2.7 Regeneration Efficiency of Fuel Dosing

Maximizing the fuel efficiency during active regeneration is vital since the highest possible fuel efficiency is desirable for the customer. In order to maximize engine system fuel efficiency, the regeneration efficiency of PM oxidation during fuel dosing needs to be maximized. Regeneration at high temperatures as well as higher biodiesel levels both contributed to a reduced fuel penalty associated with active regeneration due to shorter regeneration times and more efficient PM oxidation, respectively, which is explained later in this section. Some of the data from Austin [1] and the data from this study are displayed in Figure 4.9. Trend lines were incorporated into the plot for each fuel type used (B5 and B20 for the data from Austin [1] and ULSD, B10, and B20 for the data from this study).

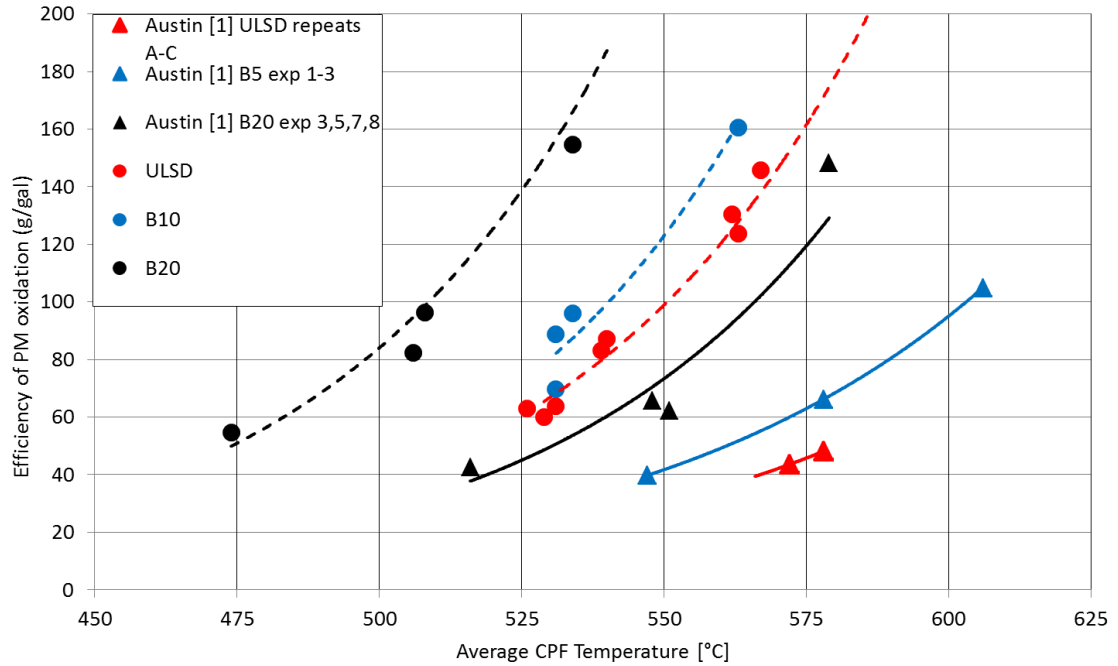


Figure 4.9: Grams of PM Oxidized per Equivalent Gallon of Fuel Injected during Dosing as a Function of Average CPF Temperature Including Data from Austin [1]

It is clearly visible in Figure 4.9 that the data from this study follows the general same trend as the data presented by Austin [1] in that at a constant average CPF temperature, B20 has the highest active regeneration fuel efficiency, and decreases with decreasing test fuel b-factor level. For example, the data from this study suggests that at an average CPF temperature of 525°C, active regeneration with ULSD, B10, and B20 results in 63, 90, and 154 grams of PM oxidized per gallon of dosing fuel used, respectively, coinciding with an increase of 43% from ULSD to B10 and 144% from ULSD to B20.

Another way to interpret the data presented in Figure 4.9 is to look at the equivalent temperatures required to achieve a given PM oxidation/gallon of fuel dosed across all three fuels. For example, active regeneration with ULSD, B10, and B20 near a PM oxidized/fuel dosed value of 80 occurs at 540, 531 and 506°C, respectively. Therefore, as higher blends of biodiesel are used, more PM is oxidized at a given temperature, or a lower CPF temperature is required to achieve the same level of PM

oxidation/fuel dosed. The lower CPF temperature coincides with a lower dosing rate, resulting in increased engine fuel efficiency.

In order to accurately compare the data from Austin [1] and this study, the PM oxidation efficiency data from Austin [1] was normalized by multiplying each data point by the ratio of the standard exhaust volumetric flow rate between the two studies since Austin's [1] engine condition for active regeneration was at a higher flow rate condition than this study. The ratio of the flow rates was $\dot{V}_{GTA} / \dot{V}_{JMP}$ where GTA denotes data from Austin [1] and JMP denotes data from this study. The data following this normalization process can be seen in Figure 4.10.

It can be seen in Figure 4.10 that the data from Austin [1] lies close to the data from this study after the application of the flow rate ratios described above. Since the exhaust flow rate used during active regeneration by Austin [1] was more than twice that which was used during active regeneration in this study, the exhaust volumetric flow rate ratio described above was between 2.0 and 2.3 for every data point from Austin [1].

As a result of the data normalization process, Figure 4.10 shows that the regeneration efficiency for any given temperature is more efficient with a lower exhaust flow rate. The efficiency of PM oxidation from this study was twice that which was reported in the study by Austin [1], regardless of test fuel type. This is due to the approximate 3 times increase in fuel required to raise the exhaust to a given temperature between Austin [1] and this study. At higher exhaust flow rates in the Austin [1] study, more fuel is consumed during active regeneration when compared to lower flow rates in this study due to the required increase in dosing fuel flow rate.

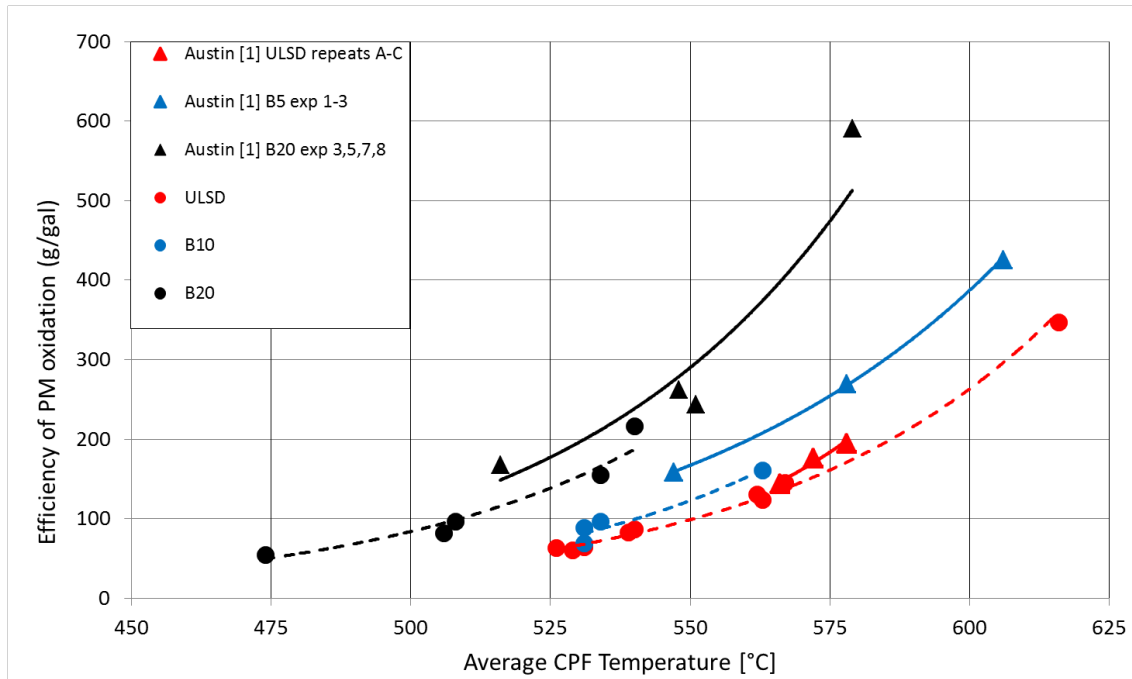


Figure 4.10: Grams of PM Oxidized per Equivalent Gallon of Fuel Injected during Dosing as a Function of Average CPF Temperature Including Data from Austin [1] Normalized by Exhaust Volumetric Flow Rate Ratio

The data from this study differs slightly from the data presented by Austin [1] in that the representative data points in Figure 4.10 are shifted along the CPF temperature axis as well as a slight shift up on the vertical axis for the representative temperature points. This could be possible by a number of factors including the CPF thermocouple layout changes that were explained earlier, differences between the experimental procedures used on the ISM [1, 15] and the ISL, or differences between the ISM and the ISL themselves since the ISM and ISL are two completely different engine platforms. Another possible difference could be related to in-cylinder vs. exhaust dosing methods, as the data in Figure 4.10 from this study was with in-cylinder and exhaust dosing, while data from Austin [1] used the exhaust dosing method only. The exhaust flow rate during active regeneration were much lower on the ISL compared to the ISM [1] in order for in-cylinder dosing to be used to reach a CPF inlet temperature of at least 600°C, which may also have had an effect on the results of the regeneration efficiency of fuel dosing on the ISL.

The analysis methods with respect to the regeneration efficiency of fuel dosing were the same between the ISM and ISL and as such, are not believed to be a

contributing factor in the differences between the data. The differences in engines and active regeneration engine conditions are believed to be the most likely cause for the differences in the experimental data between this study and the data presented by Austin [1].

The calculation and analysis method for determining the data presented in Figures 4.9 and 4.10 is shown in Appendix O.

4.2.8 In-cylinder and Post-turbo Dosing Methods

Tests ULSD-3, ULSD-4, ULSD-5, and ULSD-6 were test cases with experimental CPF inlet temperatures of $525\pm 1^{\circ}\text{C}$ using ULSD. B20-5 and B20-5 were test cases with experimental CPF inlet temperatures of $527\pm 1^{\circ}\text{C}$ using B20. Out of these 6 tests, ULSD-6 and B20-6 were the only test case which used the post-turbo dosing method.

From Table M4, the gaseous emissions summary during active regeneration, it can be seen that the CPF inlet HC concentration was 200-300 ppm higher for the post-turbo dosing case. From Table 4.6, it can be seen that the volume average CPF temperatures were 6°C and 11°C higher for the post-turbo B20 and ULSD tests, respectively. From Figure 4.4, it can be seen that the peak CPF pressure drop during active regeneration was 0.2-0.3 kPa higher for the post-turbo dosing cases with ULSD and B20.

Considering the fact that these tests were conducted at experimental CPF inlet temperatures from $525\text{-}528^{\circ}\text{C}$, it can be said that performing active regeneration with the post-turbo dosing method requires more dosing fuel to achieve the same CPF inlet temperature.

The result is that the DOC HC conversion efficiency is greater with in-cylinder dosing when compared to post-turbo dosing methods, regardless of test fuel type.

Chapter 5 Conclusions and Recommendations

The main goal of this research was to develop an active regeneration test procedure which was suitable for the use of in-cylinder dosing while determining effects of CPF PM loading, CPF temperature, dosing method (in-cylinder or post-turbo dosing injection methods), and fuel on PM oxidation via active regeneration in a CPF. This goal has been met through the completed testing and analysis of the data.

The method for calculating the reaction rate during active regeneration has been modified from Austin [1] and now includes the average CPF temperature at each time step during active regeneration in the calculation of the reaction rate. Changes to the experimental setup (A 2002 Cummins ISM engine was used in [1] while a 2007 Cummins ISL was used in this study) CPF thermocouple layout (and subsequent average CPF temperature calculation) from Austin [1] resulted in a shift in the grams of PM oxidized/gallon of dosing fuel injected data although the trends seen in Austin [1] were also seen in the ISL test data.

5.1 Conclusions

Conclusions from the analysis of the data are as follows.

- A literature review on past research related to PM oxidation during active regeneration and the effects of biodiesel blends on it has been accomplished.
- All experimental data was used in the analysis of PM reaction rate and rate parameter (E_a and A) optimization while 11 total test cases have been deemed suitable for calibration of the MTU-1D CPF Model.
- A method to calculate the PM reaction rate at each time step through the entire active regeneration phase of the experiments has been developed and shows good correlation between experimental test cases.
- The PM reaction rate was shown to increase with increasing test fuel percent biodiesel and CPF inlet temperature and an active regeneration model developed by Pidgeon [2] was used to predict the active regeneration time given a set of experimental test conditions.
- Optimization methods were used to determine a global activation energy of 139 kJ/gmol for all test fuels as well as the pre-exponential factor for each test fuel where B20 was the highest, followed by B10 and ULSD. B20

and ULSD were shown to be statistically different while B10 and ULSD were shown to be statistically similar.

- DOC HC conversion efficiency is increased with in-cylinder compared to post-turbo dosing methods.
- Regeneration efficiency of fuel dosing is increased as exhaust volumetric flow rate is decreased. This is due to the amount of dosing fuel that is required to achieve a given CPF inlet temperature decreases with decreasing flow rate.
- More PM is oxidized per gallon of dosing fuel consumed at a constant CPF temperature with B20 leading to shorter regeneration times and decreased fuel consumption during active regeneration
- A lower temperature is required to achieve the same level of regeneration efficiency of fuel dosing with B20 when compared to B10, and a lower temperature is required with B10 compared to ULSD. A lower CPF temperature requires less dosing fuel to be consumed during dosing, decreasing fuel consumption during active regeneration.
- The CPF resistance was calculated based on experimental data for each test case. LFE and CPF pressure drop offsets were implemented for S1 loading test phases where the measurements were subject to error due to test cell temperature rise. Exhaust flow rate scaling factors were implemented for test phases in which unknown errors with the LFE pressure drop measurements occurred. CF was determined using Eqn. 20 based on a re-constructed, plausible resistance curve, and will be applied to exhaust mass flow rate for simplicity in the input data preparation for the MTU-1D CPF model.

5.2 Recommendations

- Implementation of control of the engine intake air within the test cell would be beneficial to future research that collects data similar to this study because more consistent engine-out PM concentration data could be gathered. Controlling the test cell temperature would be beneficial for more consistent experimental data.

- Complete additional active regeneration tests to cover a more broad range of CPF inlet temperatures with all test fuels used in this study (ULSD, B10, and B20).
- Repeat the tests in which the exhaust bypass line valve was shown to be sticking (Figures P2-P5 corresponding to tests B20-5, ULSD-3, ULSD-4, and ULSD-5).
- Perform additional ULSD tests with the ISL 425 rating to definitively determine whether differences exist, from an active regeneration standpoint, between the two engine ratings.
- Changes to the National Instruments DAQ system to definitely negate the effects of test cell temperature on the pressure transducer readings as shown in Figure P8, where the increase in test cell temperature between the starting points of Stage 1 and Stage 2 loading affected the accuracy of the CPF pressure drop. The pressure drop was affected such that the steady state CPF pressure drop during Stage 1 loading was lower than it should have been, due to errors introduced as a result of the increase in test cell temperature from the first engine start-up to the end of Stage 1.

References

1. Austin G, Naber J, Johnson J, Hutton C, "Effects of Biodiesel Blends on Particulate Matter Oxidation in a Catalyzed Particulate Filter during Active Regeneration," SAE Technical Paper No. 2010-01-0557, 2010.
2. Pidgeon J, Naber J, Johnson J, "An Experimental Investigation into the Effects of Biodiesel Blends on Particulate Matter Oxidation in a Catalyzed Particulate Filter during Active Regeneration", SAE Technical Paper No. 2013-01-0521, 2013, currently under official review.
3. Williams A, McCormick R, Hayes R, Ireland J, Fang H, "Effect of Biodiesel Blends on Diesel Particulate Filter Performance", SAE Technical Paper No. 2006-01-3280, 2006.
4. Morcos M, Ayyappan P, Harris T, "Characterization of DPF Ash for Development of DPF Regeneration Control and Ash Cleaning Requirements", SAE Technical Paper No. 2011-01-1248, 2011.
5. Ochs T, Schittenhelm H, Genssle A, and Kamp B, "Particulate Matter Sensor for On Board Diagnostics (OBD) of Diesel Particulate Filters (DPF)", SAE Technical Paper No. 2010-01-0307, 2010.

6. Hutton C, Johnson J, Naber J, Keith J, "Procedure Development and Experimental Study of Passive Particulate Matter Oxidation in a Diesel Catalyzed Particulate Filter", SAE Technical paper No. 2012-01-0851, 2012.
7. Poitras M, Rosenblatt D, Chan T, and Rideout G, "Impact of Varying Biodiesel Blends on Direct-Injection Light-Duty Diesel Engine Emissions", SAE Technical Paper No. 2012-01-1313, 2012.
8. Kawano D, Mizushima N, Ishii H, Goto Y, and Iwasa K, "Exhaust Emission Characteristics of Commercial Vehicles Fuelled with Biodiesel", SAE Technical Paper No. 2010-01-2276, 2010.
9. Parihar A, Sethi V, Parikh P, Radhakrishna D, Hashmi K, Gupta A, and Dar F, "Physical Characterization of Particulate Emissions from Compression Ignition Engine Operating on Diesel and Biodiesel Fuels", SAE Technical Paper No. 2011-26-0026, 2011.
10. Eckerle W, Lyford-Pike E, Stanton D, LaPointe L, Whitacre S, and Wall J, "Effects of Methyl Ester Biodiesel Blends on NOx Emissions", SAE Technical Paper No. 2008-01-0078, 2008.
11. Shiel K, Naber J, Johnson J, Hutton C, "Catalyzed Particulate Filter Passive Oxidation Study with ULSD and Biodiesel Blended Fuel", SAE Technical Paper No. 2012-01-0831, 2012.
12. Yezerets A, Currier N, Eadler H, Popuri S, Suresh A, "Quantitative Flow-Reactor Study of Diesel Soot Oxidation Process", SAE Technical Paper No. 2002-01-1684, 2002.
13. Yezerets A, Currier N, Eadler H, "Experimental Determination of the Kinetics of Diesel Soot Oxidation by O₂ – Modeling Consequences", SAE Technical Paper No. 2003-01-0833, 2003.
14. Oki H, Karin P, and Hanamura, K, "Visualization of Oxidation of Soot Nanoparticles Trapped on a Diesel Particulate Membrane Filter", SAE Technical Paper No. 2011-01-0602, 2011.
15. Chilumukuru K, Arasappa R, Johnson J, Naber J, "An Experimental Study of Particulate Thermal Oxidation in a Catalyzed Particulate Filter during Active Regeneration", SAE Technical Paper No. 2009-01-1474, 2009.
16. Bender D, Jones J, Harshbarger D, "Analysis of Particulate Matter Sensor Signals", SAE Technical Paper No. 2012-01-0871, 2012.

17. Surenahalli H, Premchand K, Johnson J, Parker G, "Modeling Study of Active Regeneration of a Catalyzed Particulate Filter Using One-Dimensional DOC and CPF Models", SAE Technical Paper No. 2011-01-1242, 2011
18. Konstandopoulos A, Kostoglou M, Skaperdas E, Papaioannou E, Zarvalis D, Kladopoulou E, "Fundamental Study of Diesel Particulate Filters: Transient Loading, Regeneration, and Aging", SAE Technical Paper No. 2000-01-1016, 2000.
19. Premchand K, Johnson J, Yang S, "Development of a 1-D Catalyzed Diesel Particulate Filter Model for Simulation of the Oxidation of Particulate Matter and Gaseous Species during Passive Oxidation and Active Regeneration", SAE Technical Paper No. 2013-01-1574, 2013, currently under review.
20. Senda, J., Okui, N., Suzuki, T., and Fujimoto, H., "Flame Structure and Combustion Characteristics in Diesel Combustion Fueled with Bio-diesel," SAE Technical Paper 2004-01-0084, 2004.
21. Yeliana Y, "Parametric Combustion Modeling for Ethanol-Gasoline Fuelled Spark Ignition Engines", Ph. D. Thesis, Michigan Technological University, 2010.
22. Pinturaud D, Charlet A, Caillol C, Higelin P, Girod P, and Briot A, "Experimental Study of DPF Loading and Incomplete Regeneration", SAE Technical Paper No. 2007-24-0094, 2007.

Appendix A Biodiesel Blend Molecular Formula Calculations

In order to accurately calculate the hydrocarbon concentrations upstream of the DOC during active regeneration, the molecular weight of the fuel being used must be known. Since the molecular weight for the B10 and B20 test fuel was not included in the analysis results, molecular weights based upon the ULSD blended with 10% and 20%, by volume, of B100 required computation. Calculations using ULSD assume that the ULSD empirical formula is $\text{CH}_{1.833}$ (Chilumukuru [15] assumes $\text{C}_{12}\text{H}_{22}$, $\text{H/C} = 1.833$). The density of ULSD comes from the fuel test results presented earlier in this report, and was given as 858 kg/m^3 .

The density and percentages of carbon, hydrogen, and oxygen by mass of waste oil methyl-ester B100 was obtained in Senda [20] and are given below in Table A1.

Table A1: B100 Properties from Senda [20]

Property	Units	Value
Density	$[\text{kg/m}^3]$	888
Carbon	%	77.2
Hydrogen	%	11.7
Oxygen	%	11.1

Using the data from Table A1 in conjunction with Eqn. A1, the moles of each atom in B100 was calculated which are given in Table A2.

$$n_x = \frac{m_x}{MW_x} \quad \text{Eqn. A1}$$

n_x = number of moles of molecule x

m_x = mass percent of molecule x in fraction form (i.e., 0.772, not 77.2)

MW_x = molecular weight of molecule x $[\text{g/gmol}]$

Using the data from A2, the hydrogen/carbon (H/C) and oxygen/carbon (O/C) ratios can be calculated by the division of the two molecules in question. The H/C and O/C ratios for B100 are given in Table A3.

Table A2: Computed B100 Molecular Components

moles Carbon	mol	0.0643
moles Hydrogen	mol	0.1161
moles Oxygen	mol	0.0069

Table A3: H/C and O/C Ratios for B100

Ratio	Value
H/C	1.81
O/C	0.107

Using the H/C and O/C ratios, the empirical formula for B100 can be expressed as $CH_{1.81}O_{0.107}$, subsequently allowing for the calculation of the molecular weight by $(12.01 \cdot 1) + (1.008 \cdot 1.81) + (16.0 \cdot 0.107)$, resulting in a molecular weight of 15.55 g/gmol. The molecular weight for ULSD was calculated similarly using the empirical formula referenced earlier, resulting in 13.85 g/gmol.

Eqn. A2, from Yeliana [21], is used to calculate the mole % of biodiesel in the B10 and B20 blends, which are given in Table A4.

$$\% \text{ mole}_{\text{biodiesel}} = \frac{\% \text{ vol}_{\text{B100}} \cdot \rho_{\text{B100}} / \text{MW}_{\text{B100}}}{\% \text{ vol}_{\text{B100}} \cdot \rho_{\text{B100}} / \text{MW}_{\text{B100}} + (1 - \% \text{ vol}_{\text{B100}}) \cdot \rho_{\text{ULSD}} / \text{MW}_{\text{ULSD}}} \cdot 100 \quad \text{Eqn. A2}$$

$\% \text{ mole}_{\text{biodiesel}}$ = mole fraction of biodiesel in the B10 or B20 blend [%]

$\% \text{ vol}_{\text{B100}}$ = % volume of B100 in the mixture, fraction form

ρ_{B100} = Density of B100 [kg/m^3]

MW_{B100} = Molecular weight of B100 [g/gmol]

ρ_{ULSD} = Density of ULSD [kg/m^3]

MW_{ULSD} = Molecular weight of ULSD [g/gmol]

The empirical formula for the B10 and B20 biodiesel blends can be generally expressed as $(CH_{\beta^*}O_{z^*})_{\alpha^*}$, where α^* , β^* , and z^* are calculated using Eqn. A3, A4, and A5, respectively [21].

Table A4: Mole Fraction of Biodiesel for B10 and B20 Blends

Fuel	Mole Fraction	Unit
B10	9.29	%
B20	18.73	%

$$\alpha^* = (1 - \bar{E}) \cdot \alpha_{ULSD} + [\bar{E}] \cdot \alpha_{B100} \quad \text{Eqn. A3}$$

$$\beta^* = \frac{(1-\bar{E}) \cdot \beta_{ULSD} \cdot \alpha_{ULSD} + [\bar{E}] \cdot z_{B100} \cdot \alpha_{B100}}{(1-\bar{E}) \cdot \alpha_{ULSD} + [\bar{E}] \cdot \alpha_{B100}} \quad \text{Eqn. A4}$$

$$z^* = \frac{(1-\bar{E}) \cdot z_{ULSD} \cdot \alpha_{ULSD} + [\bar{E}] \cdot z_{B100} \cdot \alpha_{B100}}{(1-\bar{E}) \cdot \alpha_{ULSD} + [\bar{E}] \cdot \alpha_{B100}} \quad \text{Eqn. A5}$$

\bar{E} = mole fraction of biodiesel in blend

α = carbon atoms

β = H/C ratio

z = O/C ratio

The calculated values for α^* , β^* , and z^* , the blend empirical formula, and blend molecular weights are given in Table A5 on a C_{12} basis.

Table A5: Calculated Properties for B10 and B20 Biodiesel Blends with ULSD Data

Fuel	α^*	β^*	z^*	Formula	Molecular Weight	H/C	O/C
-	-	-	-	-	[g/gmol]	-	-
B10	1	1.828	0.0099	$CH_{1.828}O_{0.0099}$	168	1.828	0.010
B20	1	1.826	0.0200	$CH_{1.826}O_{0.0200}$	170	1.826	0.020
ULSD	1	1.833	-	$CH_{1.833}$	166	1.833	-

Appendix B Dilution Ratio Calculation Method

The exhaust sampled by the SMPS is diluted with compressed air before PSD data is collected, so determining the dilution ratio for each engine condition, sampling location, and test fuel is important. The dilution ratio is defined as the ratio of CO₂ in the exhaust to the CO₂ after going through the SMPS dilution system, measured by the Pierburg emissions bench. The engine is operated at the condition during which PSD data will be collected. The copper dilution line shown in Figure B1 and is connected from the heated filter to the dilution box outlet as shown. The PSD sample line is then connected to the gaseous emissions port corresponding to the location to be sampled as shown in Figure B2.

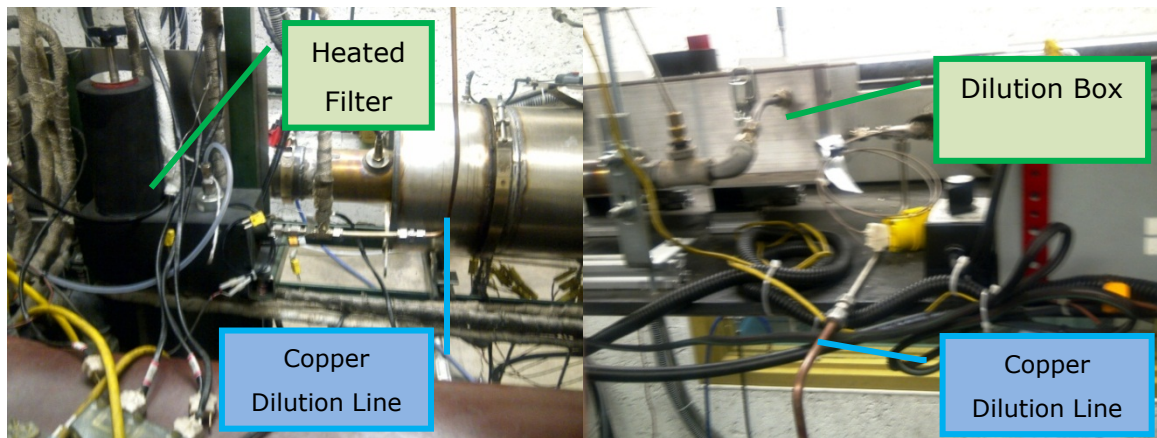


Figure B1: Copper Dilution Line Connected from the Heated Filter to the Dilution Box Outlet

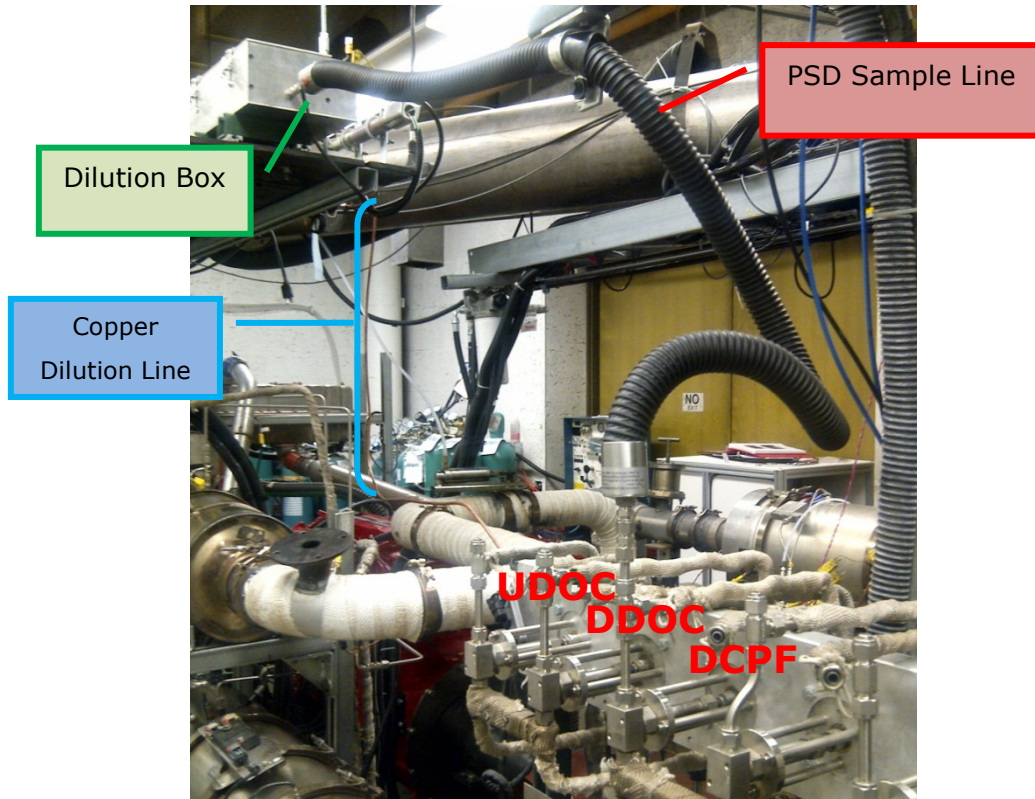


Figure B2: PSD Sample Line Connected to the DDOC Gaseous Emissions Port

With the dilution line and PSD sample line in place emissions data is collected with the Pierburg emissions analyzer. This data collection is performed with the exhaust sample valves for UDOC, DDOC, and DCPF, controlled by LabView, closed for five minutes. The value of CO_2 measured by the Pierburg emissions analyzer at all sampling locations (d_{CO_2}) is used with Eqn. 1 to find the dilution ratio at that point for the engine operating condition being run. The value of CO_2 measured by the Pierburg at all sampling locations during loading and active regeneration is used as a_{CO_2} in Eqn. B1 for each engine condition.

$$\text{Dilution Ratio} = \frac{a_{\text{CO}_2}}{d_{\text{CO}_2}} \quad \text{Eqn. B1}$$

The PSD sample line is then moved to the next point to be tested and emissions data is collected for five minutes as with the prior point. All three points (UDOC, DDOC, and DCPF) are collected in this manner. Every engine operating condition and fuel type during which PSD data is to be collected must have dilution data collected in this way.

Appendix C PSD Data Correction Method

In order to properly report the data collected by the Scanning Mobility Particle Sizing (SMPS) System, corrections to the data collected must be applied. These correction necessities are due to exhaust sample dilution and the particles that are present in the compressed air used in the dilution system.

The total procedure for collecting PSD measurements was originally written by Hutton [6].

1. Prior to measuring PSD data, determine the experimental dilution ratios that are being used at each of the three sample locations, UDOC, DDOC, and DCPF. The dilution ratios were collected at loading and active regeneration engine conditions for each of the three test fuels (ULSD, B10, and B20) in this study.
2. Determine the concentration of particles in the compressed air (C_{CA}) used for the dilution system by measuring the size distribution within the air.
3. Record the PSD data during testing using the dilution system and thermodenuder at all sampling locations when measuring a 'dry' sample. This method allows for consistent conditioning of the sample before measurement
4. After the collection of raw data has been performed, the first step of post processing is accounting for the losses created by the use of the thermodenuder using Eqn C1 and Eqn C2
5. Then finish post processing by taking into account the dilution ratio and number of particles contained in the compressed air using Eqn. C3.

$$TP = A \cdot T + B \cdot D + C \quad \text{Eqn. C1}$$

$$T_{Loss} = 1 - TP \quad \text{Eqn. C2}$$

TP = % of particles passing through thermodenuder [%]

A = -0.0864 [$^{\circ}\text{C}^{-1}$]

B = 0.0108 [nm^{-1}]

C = 91.9

D = Particle diameter [nm]

T_{Loss} = Thermodenuder losses in fraction form

$$C_{\text{exhaust}} = \frac{(D_R+1) \cdot D_{\text{CPC}}}{(1-T_{\text{Loss}})} - D_R \cdot C_{\text{CA}} \quad \text{Eqn. C3}$$

C_{exhaust} = Particle concentration in the exhaust [particle/cm³ or nm³/cm³]

D_R = Dilution ratio

D_{CPC} = Displayed value on CPC counter

T_{Loss} = Thermodenuder losses in fraction form from Eqn. C2

C_{CA} = Concentration of particles in compressed air used for dilution
[particles/cm³ or nm³/cm³]

Appendix D CPF Mass Measurement Procedure

During different portions of the test, the CPF is removed from the aftertreatment system for weighing. The complete aftertreatment assembly is shown in Figure D1. In order to allow for clear communication, the individual parts are listed below and are correlated by number listed on the picture.

1. Inlet Cone
2. Diesel Oxidation Catalyst (DOC)
3. Catalyzed Particulate Filter (CPF)
4. Exit Cone

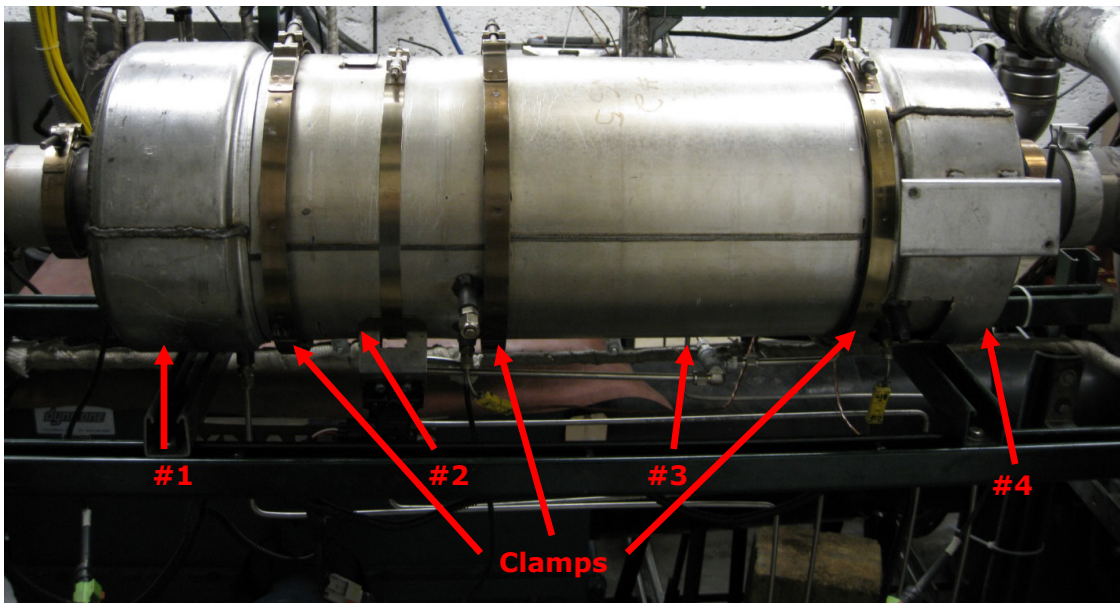


Figure D1: Cummins 2007 ISL After-treatment System

Disassembly and weighing of the CPF takes place a minimum of four times for each of the active regeneration tests. The filter and associated hardware are removed from the system hot, with surface temperatures up to and exceeding 300°C. The weighing is done at elevated temperatures for two main reasons. First, as the CPF cools there is the possibility that the CPF will gain mass due to moisture absorption from the ambient air. Second, it has been shown that the weighing procedure is a dynamic process with the CPF appearing to gain mass as it cools due to the reduction of the buoyancy effect provided by the temperature of the filter. Therefore filter weighing takes place at similar temperatures during the different portions of the test.

A detailed analysis investigating the variability of the mass measurement due to temperature variations is discussed in reference [1].

The weighing procedure is detailed below.

1. The entire after-treatment system, parts 1-4 in Figure D1, are removed from the exhaust system fully assembled.
2. The system is lowered to the ground and rests on Part #4 which then puts the system in a vertical orientation.
3. The clamp between Part #2 and #3 is removed, the DOC and Inlet Cone are then removed as an assembly.
4. A steel cover is placed over the inlet of the CPF and fastened to the filter by the previously removed clamp.
5. The filter is then rotated to rest on the steel cover and the clamp between Part #3 and #4 is removed.
6. The exit cone is then removed and a separate steel cap is placed over the exit of the CPF. This cap is fastened to the filter by the previously removed clamp.
7. The filter is then brought to the scale and temperatures are recorded throughout the filter and caps.
8. The scale is zeroed prior to each mass measurement.
9. A calibration weight is measured to ensure scale accuracy.
10. The CPF is weighed three times, with the temperatures recorded throughout the CPF prior to the first weighing; an average of the mass measurements is then calculated.
11. The actual temperature may vary from day to day somewhat based on ambient temperature. Maintain consistent temperatures between weighing sessions on the same test day. Do not let the individual temperature measurements (at each thermocouple) vary by more than +/- 15° C. The actual separate T/C temperatures can be anywhere from 180° C to 290° C
12. The reassembly process is the reverse of the disassembly process.

Appendix E Stage 1 Loading PM Mass Balance Calculations (by Kiran Premchand [19])

From the ISL AR tests, we do not have measurements of the clean weight of the substrate. Rather, we have 4 other substrate weight measurements:

(M_{S1}), (M_{S2}), (M_{S3}) and (M_{S4}) taken at 4 points in time during each ISL AR test as shown in Figure E1.

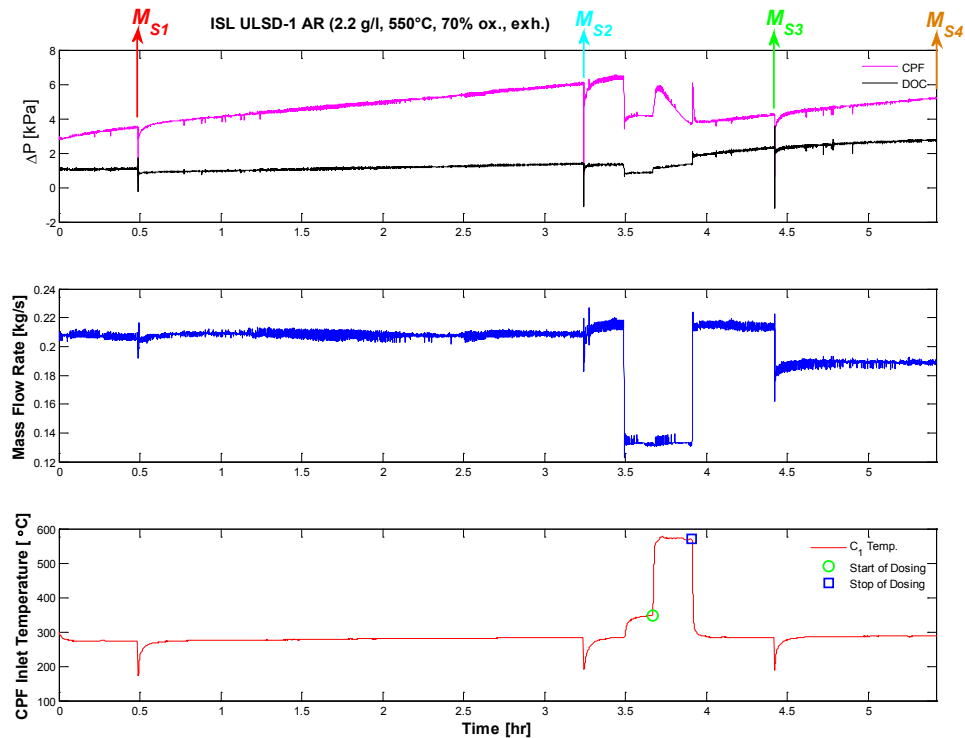


Figure E1: A typical ISL AR experiment showing a) DOC and CPF pressure drops, b) Exhaust mass flow rate and c) CPF inlet temperature

We want to get a good estimate of CPF clean weight (M_{clean}) assuming the following:

The fraction of PM oxidized during Stage-1 loading is equal to the fraction of PM oxidized during Stage-2 loading.

Average filtration efficiency of the CPF during Stage-1 loading and Stage-2 loading are known ($(\bar{\eta}_{S1})$ and $(\bar{\eta}_{S2})$ respectively).

We know the following relations:

$$m_{ret,S1} = M_{S1} - M_{clean} \text{ ----- (1)}$$

$$m_{ret,S2} = M_{S2} - M_{clean} \text{ ----- (2)}$$

$$m_{ret,S3} = M_{S3} - M_{clean} \text{ ----- (3)}$$

$$m_{ret,S4} = M_{S4} - M_{clean} \text{ ----- (4)}$$

Also, from cumulative PM mass balance for Stage-1 and Stage-2 can be mathematically expressed as:

$$m_{in,S1} - m_{ret,S1} - m_{ox,S1} - m_{out,S1} = 0 \text{ ----- [Stage-1] ----- (5)}$$

$$m_{ret,S1} + m_{in,S2} - m_{ret,S2} - m_{ox,S2} - m_{out,S2} = 0 \text{ ----- [Stage-2] ----- (6)}$$

Also, from definition of average filtration efficiencies during Stage-1 and Stage-2,

$$\bar{\eta}_{S1} = \frac{m_{in,S1} - m_{out,S1}}{m_{in,S1}} \text{ ----- (7)}$$

$$\bar{\eta}_{S2} = \frac{m_{in,S2} - m_{out,S2}}{m_{in,S2}} \text{ ----- (8)}$$

From (5) and (1),

$$m_{ret,S1} = m_{in,S1} - m_{ox,S1} - m_{out,S1} = M_{S1} - M_{clean}$$

or

$$(m_{in,S1} - m_{out,S1}) - m_{ox,S1} = M_{S1} - M_{clean} \text{ ----- (9)}$$

Substitute (7) in (9),

$$\bar{\eta}_{S1} m_{in,S1} - m_{ox,S1} = M_{S1} - M_{clean} \text{ ----- (10)}$$

Re-writing (10),

$$M_{clean} = M_{S1} - (\bar{\eta}_{S1} m_{in,S1} - m_{ox,S1}) \text{ ----- (11a)}$$

or

$$M_{clean} = M_{S1} - \bar{\eta}_{S1} m_{in,S1} + m_{ox,S1} \text{ ----- (11b)}$$

or

$$m_{ox,S1} = \bar{\eta}_{S1} m_{in,S1} - (M_{S1} - M_{clean}) \text{ ----- (11c)}$$

From (6), (2) and (1),

$$\begin{aligned}
m_{\text{ox},S2} &= m_{\text{ret},S1} + m_{\text{in},S2} - m_{\text{ret},S2} - m_{\text{out},S2} \\
&= m_{\text{ret},S1} + (m_{\text{in},S2} - m_{\text{out},S2}) - m_{\text{ret},S2} \\
&= m_{\text{ret},S1} + \bar{\eta}_{S2} m_{\text{in},S2} - m_{\text{ret},S2} \\
&= \bar{\eta}_{S2} m_{\text{in},S2} + m_{\text{ret},S1} - m_{\text{ret},S2} \\
&= \bar{\eta}_{S2} m_{\text{in},S2} + (M_{S1} - M_{\text{clean}}) - (M_{S2} - M_{\text{clean}}) \\
&= \bar{\eta}_{S2} m_{\text{in},S2} - (M_{S2} - M_{S1}) \text{-----} (12)
\end{aligned}$$

From (11c),

$$\frac{m_{\text{ox},S1}}{m_{\text{in},S1}} = \bar{\eta}_{S1} - \frac{M_{S1} - M_{\text{clean}}}{m_{\text{in},S1}} \text{-----} (13)$$

And from (12),

$$\frac{m_{\text{ox},S2}}{m_{\text{in},S2}} = \bar{\eta}_{S2} - \frac{M_{S2} - M_{S1}}{m_{\text{in},S2}} \text{-----} (14)$$

So then if we equate the LHS of (13) and (14) [Assumption 1],

$$\begin{aligned}
\bar{\eta}_{S1} - \frac{M_{S1} - M_{\text{clean}}}{m_{\text{in},S1}} &= \bar{\eta}_{S2} - \frac{M_{S2} - M_{S1}}{m_{\text{in},S2}} \\
\frac{M_{S1} - M_{\text{clean}}}{m_{\text{in},S1}} &= \bar{\eta}_{S1} - \left(\bar{\eta}_{S2} - \frac{M_{S2} - M_{S1}}{m_{\text{in},S2}} \right)
\end{aligned}$$

or

$$m_{\text{ret},S1} = M_{S1} - M_{\text{clean}} = \bar{\eta}_{S1} m_{\text{in},S1} - \left(\bar{\eta}_{S2} - \frac{M_{S2} - M_{S1}}{m_{\text{in},S2}} \right) m_{\text{in},S1} \text{-----} (15a)$$

or

$$m_{\text{ret},S1} = \left(m_{\text{in},S1} (\bar{\eta}_{S1} - \bar{\eta}_{S2}) + (M_{S2} - M_{S1}) \frac{m_{\text{in},S1}}{m_{\text{in},S2}} \right) \text{-----} (15b)$$

or

$$M_{\text{clean}} = M_{S1} - \left(\bar{\eta}_{S1} m_{\text{in},S1} - \left(\bar{\eta}_{S2} - \frac{M_{S2} - M_{S1}}{m_{\text{in},S2}} \right) m_{\text{in},S1} \right) \text{-----} (15c)$$

Where:

$$m_{\text{in},S1} = C_{\text{in},S1} \left(\frac{1}{1 \times 10^3} \frac{\text{g}}{\text{mg}} \right) \dot{V}_{S1} t_{S1} \text{ and } m_{\text{in},S2} = C_{\text{in},S2} \left(\frac{1}{1 \times 10^3} \frac{\text{g}}{\text{mg}} \right) \dot{V}_{S2} t_{S2}$$

Table E1: Symbols

Variable	Description	Units
M_{S1}	Substrate weight measurement at the end of Stage-1	[g]
M_{S2}	Substrate weight measurement at the end of Stage-2	[g]
M_{S3}	Substrate weight measurement at the end of Stage-3	[g]
M_{S4}	Substrate weight measurement at the end of Stage-4	[g]
$m_{in,S1}$	PM mass into the CPF during Stage-1	[g]
$m_{in,S2}$	PM mass into the CPF during Stage-2	[g]
$m_{in,S3}$	PM mass into the CPF during Stage-3	[g]
$m_{in,S4}$	PM mass into the CPF during Stage-4	[g]
$m_{out,S1}$	PM mass out of the CPF during Stage-1	[g]
$m_{out,S2}$	PM mass out of the CPF during Stage-2	[g]
$m_{out,S3}$	PM mass out of the CPF during Stage-3	[g]
$m_{out,S4}$	PM mass out of the CPF during Stage-4	[g]
$m_{ret,S1}$	PM mass retained in the CPF at the end of Stage-1	[g]
$m_{ret,S2}$	PM mass retained in the CPF at the end of Stage-2	[g]
$m_{ret,S3}$	PM mass retained in the CPF at the end of Stage-3	[g]
$m_{ret,S4}$	PM mass retained in the CPF at the end of Stage-4	[g]
$m_{ox,S1}$	PM mass oxidized in the CPF during Stage-1	[g]
$m_{ox,S2}$	PM mass oxidized in the CPF during Stage-2	[g]
$m_{ox,S3}$	PM mass oxidized in the CPF during Stage-3	[g]
$m_{ox,S4}$	PM mass oxidized in the CPF during Stage-4	[g]
$\bar{\eta}_{S1}$	Average filtration efficiency of the CPF during Stage-1	[.]
$\bar{\eta}_{S2}$	Average filtration efficiency of the CPF during Stage-2	[.]
$C_{in,S1}$	CPF inlet PM concentration during Stage-1	[mg/std.m ³]
$C_{in,S2}$	CPF inlet PM concentration during Stage-2	[mg/std.m ³]
\dot{V}_{S1}	Volumetric flow rate of exhaust during Stage-1	[std.m ³ /s]
\dot{V}_{S2}	Volumetric flow rate of exhaust during Stage-2	[std.m ³ /s]
t_{S1}	Duration of Stage-1 loading	[s]
t_{S2}	Duration of Stage-2 loading	[s]

Appendix F PM Sample Preparation Procedure

1. Label twelve plastic filter holders (Millipore Catalog Number PDMA04700) with the appropriate test number and filter number (i.e., B20-1-1, B20-1-2, etc.).
2. Place one filter (Pall Corporation P/N 61631) in each filter holder.
3. The oven used for baking filters is located in the MEEM building, room B006 which is also the welding shop. The temperature on the oven is set to 575° F. The oven needs to be turned on and allowed to warm up for one hour prior to baking filters.
4. After the oven has warmed up for one hour, place each filter, without the filter holder, onto the metal baking tray and place the tray in the oven. Leave the filters to bake for 15 minutes.
5. After the filters have baked for 15 minutes, remove them from the oven and place each one in its filter holder
6. Place each filter/filter holder combination, with the lid removed, in the humidity chamber located in the MEEM building, room SB013. The filters must stay in the chamber for 24 hours before weighing. The humidity chamber is maintained at $75 \pm 5\%$ relative humidity.
7. Weigh each filter three times and record their weights, along with two control filters. the control filters are weighed at the time of filter weighing to track the weight change due to humidity changes in the chamber
8. After each filter is weighed three times and recorded, the filters are ready to be removed from the chamber and are prepared for the upcoming test. The filters can stay in the chamber until test day.

Appendix G Auxiliary Fuel Dosing Injector Calibration Procedure

It is important to know the flow rate out of the doser injector during each test. The gaseous concentrations are not measured upstream of the DOC during active regenerations, so the HC concentrations are determined from the flow rate of the injector, fuel properties, and the flow rate of the exhaust. The doser is calibrated before each test to give the most accurate data.

The calibration process is as follows:

1. Disconnect the doser injector from the mount on the exhaust pipe.
2. Connect the doser injector to the doser injector calibration mount.
3. Place the doser, connected to the calibration mount, on top of a 500mL beaker
4. Starting at 10% duty cycle, inject fuel into the beaker until at least 150mL of fuel are collected. For duty cycles over 50%, collect at least 250mL of fuel.
5. Remove the beaker and pour entire contents into 500mL graduated cylinder.
6. Verify that there are no bubbles in the fuel, and then take a reading from the graduated cylinder to determine how much fuel was injected at that duty cycle.
7. Empty contents of the graduated cylinder into fuel tank and move to the next duty cycle, in increments of 10%.
8. Use the LabVIEW data file to determine how long the fuel was injected at each duty cycle, and subsequently, determine the injector flow rate at each duty cycle.

Figure G1 is an example of the calibration curve for the auxiliary doser injector with ULSD.

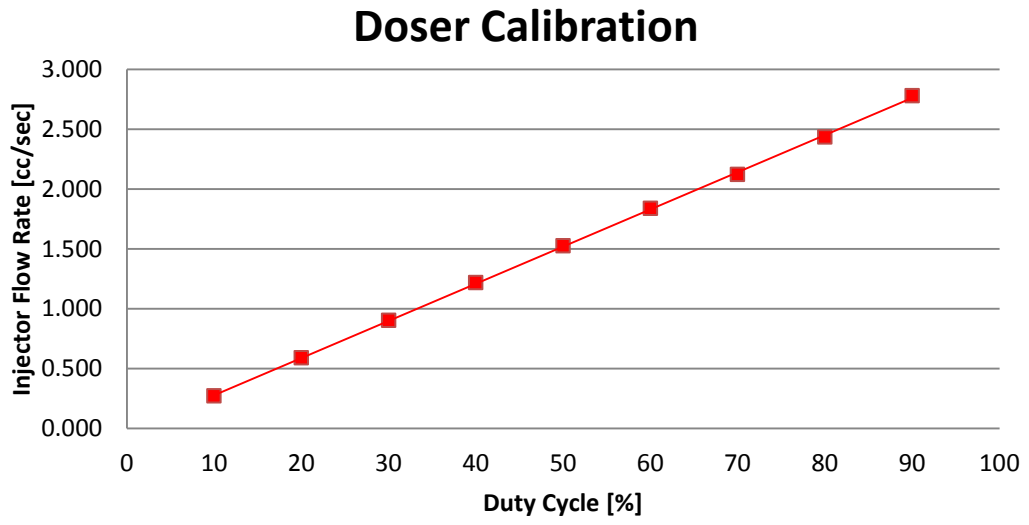


Figure G1: Example Auxiliary Doser Injector Calibration Curve with ULSD

Appendix H Data Integrity Analysis for Modeling

From a modeling and data integrity perspective, it is important that the integrity of the experimental data collected during the active regeneration testing is good. This is important because inaccuracies with experimental data lead to difficulty in the modeling of the experimental data or inaccurate models all together. By analyzing a set of key variables throughout the course of each active regeneration test, the integrity of the experimental data to be used in the modeling studies can be determined. The key variables analyzed in this study include: exhaust flow rate, PM mass balance, CPF pressure drop profile, PM oxidation during loading, and the PM oxidation during active regeneration. Exhaust flow rate inaccuracies may lead to inaccurate PM mass balance, inaccurate PM mass balance can lead to inaccurate PM reaction rate analysis, visible variation in the CPF pressure drop profile at steady state conditions show data acquisition problems or pinpoint possible exhaust flow problems (such as a stuck exhaust diversion valve), and PM oxidation during loading and active regeneration help pinpoint PM concentration data and CPF mass flow rate measurement errors.

Air Flow Rate and CPF Pressure Drop Profile

Analyzing the air flow rate over the course of the entire test is important because errors in air flow rate data can lead to inaccurate CPF pressure drop modeling and PM mass balance results.

If the air flow rate and pressure drop profiles are not in error, the result is what is shown in Figure H1. Figure H1 shows the air flow entering the engine and CPF pressure drop profiles as a function of time for Run 2 (B20-2). It can be seen that the flow rate has two distinct values, corresponding to loading and active regeneration engine conditions. The pressure drop profile should be smooth and continuous through the loading phases, with the only major changes occurring during active regeneration. If the air flow rate and pressure drop profiles appear as shown in Figure H1, it can be said that the data, with respect to these two variables, has the correct trends. If the pressure drop recorded by the NI data acquisition system ΔP sensor shows variation between phases, but the pressure drop recorded by CalTerm ΔP sensor does not, it can be assumed that the data integrity is still good,

but the variations were caused by errors in the data acquisition system itself, and these variations can be corrected prior to modeling and data analysis.

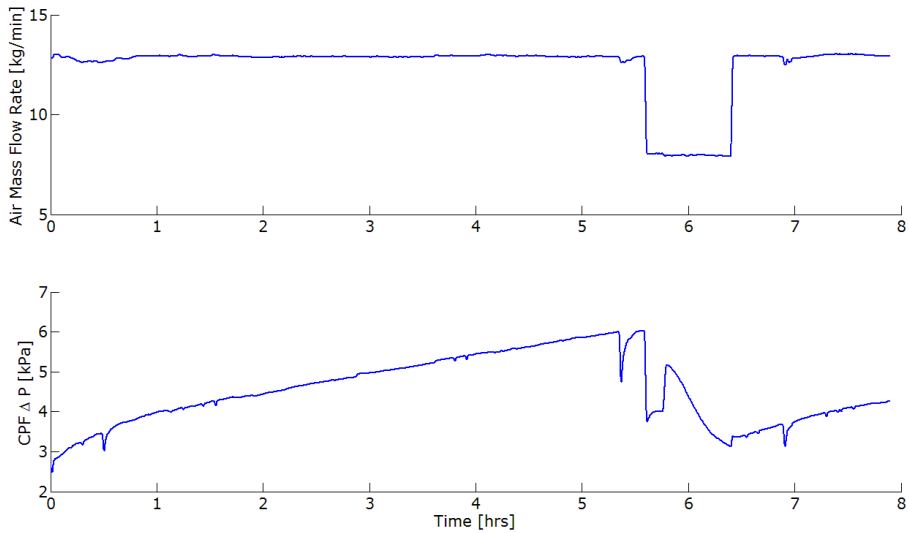


Figure H1: Air Flow Rate and CPF Pressure Drop for Run 2 (B20-2)

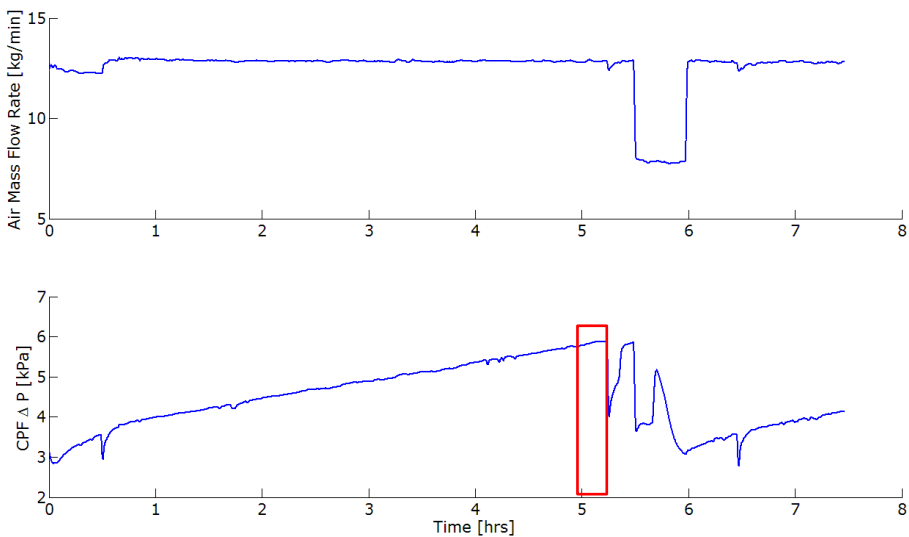


Figure H2: Air Flow Rate and CPF Pressure Drop Profile for Run 3 (B20-5)

The exhaust diversion valve is believed to be the cause for the drops in CPF pressure drop profile during loading ramp shown in Figure H2. Figure H2 is the same type of plot as Figure H1 except that Run 3 (B20-5) is shown. Within the area outlined in red

in Figure H2, at 5.3 hrs, a rapid increase can be seen in the pressure drop profile during the loading ramp phase, prior to active regeneration. This was caused by the exhaust valve in the base line sticking slightly open. The rapid increase of the pressure drop was caused by this valve fully closing upon being struck with a hammer. This stuck valve results in an error in the exhaust flow rate at the CPF inlet i.e., all the engine air flow does not go through the CPF. This requires an air flow rate correction as described later in this section. If the pressure drop profile looks as expected (smooth and steady increase during loading, followed by smooth decrease during active regeneration, and another steady increase during post loading), and the flow rate data looks to be in error, the flow rate can be corrected based on prior test data. This is because the ISL 365 engine is operated at the same conditions during loading (2100 RPM and 195 Nm) and active regeneration (1400 RPM and 460 Nm). Exhaust flow rate is computed based on the pressure drop across the laminar flow element on the engine intake system. One possible error source within the DAQ system is that the pressure transducers, responsible for measuring pressure drop profiles across the LFE, DOC, and CPF, have an offset due to the variation in ambient temperature, resulting in inaccurate Stage 1 pressure drop data.

Another way of determining if the CPF pressure drop measurements are in error is to compare the CPF pressure drop measured by the DAQ system to the CPF pressure drop measured by the engine calibration software. One such comparison can be seen in Figure H3, where the CPF pressure drop, measured by both systems, are displayed together as a function of time for Run 11 (B10-2).

It can be seen that during the Stage 1 loading portion of the experiment, the pressure drop measured by the DAQ system is slightly lower (with respect to Stage 2 loading) than the pressure drop measured by CalTerm. This could be caused by the changing of the zero-pressure point due to the temperature change in the test cell through the end of Stage 1. The decreased pressure drop was not measured by CalTerm, which is why errors with the DAQ system are believed to have been present. With respect to the Stage 1 to Stage 2 vertical shifts in pressure drop across the CPF, the trend in the CalTerm data is assumed to be correct since the test cell temperature does not appear to affect this data as it has shown to affect the data recorded by the NI DAQ system.

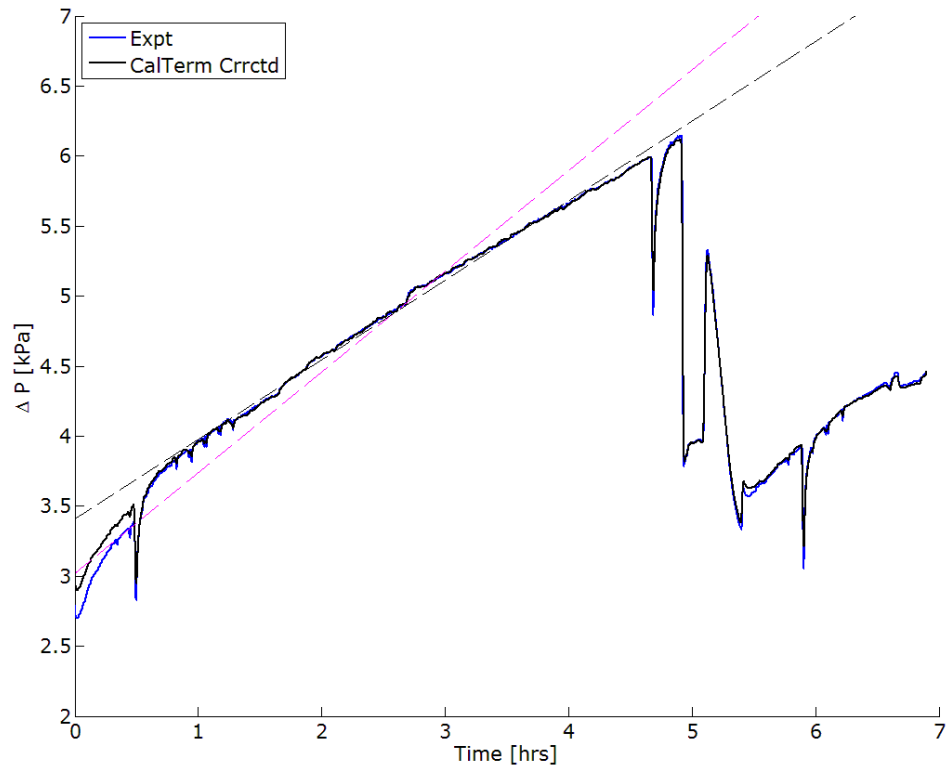


Figure H3: CPF Pressure Drop Profile for Run 11 (B10-2) Measured by NI DAQ System and CalTerm Engine Management Software

If the air flow rate and pressure drop profiles are not in error, the result is similar to which can be seen in Figure H4 which shows the air flow entering the engine and CPF pressure drop profiles as a function of time for Run 2 (B20-2). It can be seen that the flow rate has two distinct values, corresponding to loading and active regeneration engine conditions, as expected. The pressure drop profile is also smooth and continuous through the loading phases, with the only major fluctuations occurring during active regeneration. If the air flow rate and pressure drop profiles appear as shown in Figure H4, it can be said that the data, with respect to these two variables, is good. If the pressure drop profile appears as expected, but there are variations in the measured flow rate, the data remains good because the flow rate data can be corrected.

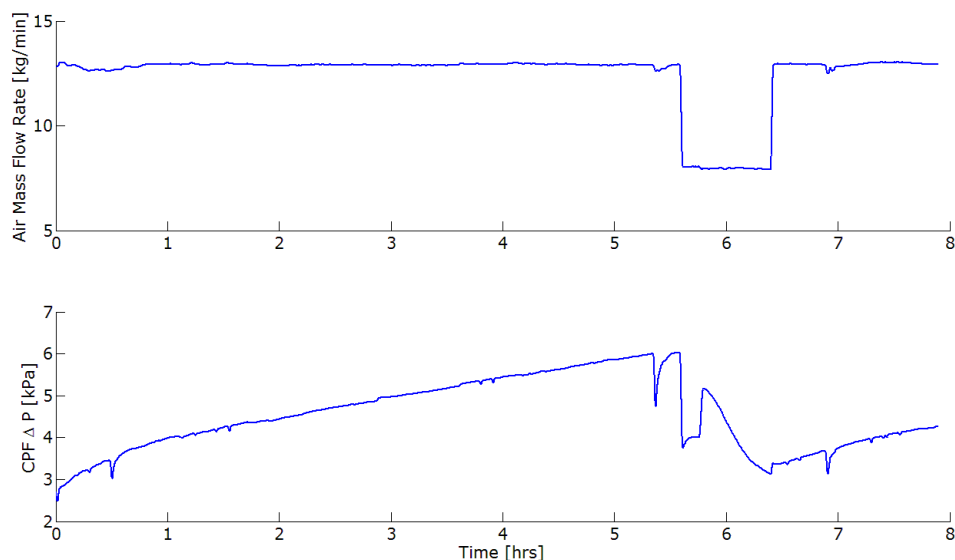


Figure H4: Air Flow Rate and CPF Pressure Drop Profile for Run 2 (B20-2)

The experimentally measured air flow rate and CPF pressure drop profile plots for all tests can be found in Appendix N while the CPF pressure drop comparison between the NI LabVIEW DAQ system and CalTerm for all tests (where CalTerm data was not corrupted) can be found in Appendix P. The CalTerm data in Appendix P was corrected to lie on the data from the NI LabVIEW DAQ system using the calibration equation that was obtained from separate calibration of the CalTerm CPF pressure drop sensor.

Stage 2 Loading PM Mass Balance

The PM mass balance throughout the various phases of each experiment is also important from a modeling and a data analysis point of view because accurate CPF PM mass retained prediction is a vital component to the MTU-1D CPF model. The model relies on accurate flow rate and PM concentration data to accurately predict the amount of PM entering the CPF at any given point during the test. If the flow rate or PM concentration data are in error, the resulting CPF PM mass retained is also in error, resulting in difficulty with model calibration and validation.

The amount of PM oxidized during Stage 2 loading indicates potential irregularities with PM concentration, flow rate, NO₂ concentration, exhaust gas temperature, or CPF weight measurements. During the ISL 365 testing presented in this study, the

mean PM oxidation during Stage 2 loading for all test cases was 21% with a standard deviation of 9%. The test cases outside of this boundary were extreme cases, such as test ULSD-3, where 38% PM oxidation was observed.

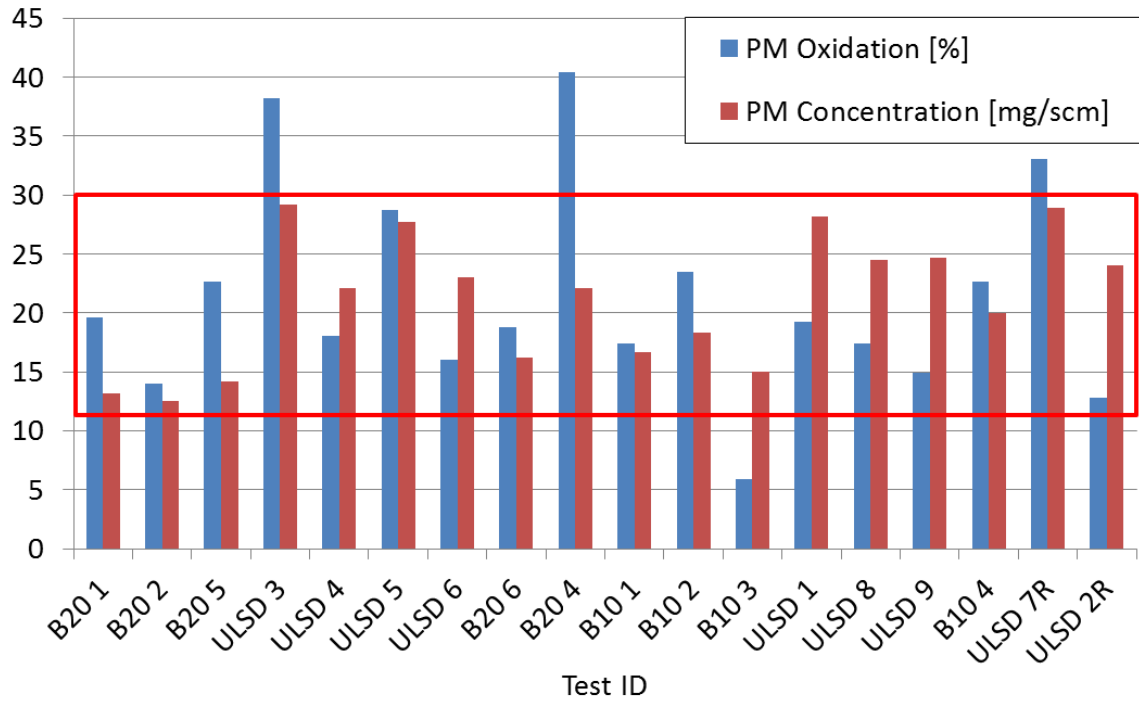


Figure H5: Stage 2 Loading PM Concentration and Percent Oxidation for All Tests

The red rectangle in Figure H5 outlines the $21 \pm 9\%$ bounds for PM oxidation during Stage 2 loading. Since the CPF inlet NO_2 concentrations for all test cases are within 10 ppm of each other, and since the test cases with PM oxidation above 30% did not show elevated CPF inlet NO_2 concentrations, gaseous emission measurement errors are not believed to be a contributing factor to the results shown in Figure H5. Engine-out PM concentration and CPF mass measurement errors have the potential to introduce error into the CPF PM retained calculations, thereby affecting the PM oxidation calculation results.

If the Stage 2 loading PM oxidation falls within the described bounds, the data set is assumed to be good with respect to the Stage 2 loading PM mass balance. PM oxidation for runs ULSD-3, B20-4, B10-3, and ULSD-7R are outside the $21 \pm 9\%$ bounds.

The experimental results from test ULSD-3 show that the PM oxidation during Stage 2 was approaching 40%, which was inconsistent with previous ISL 365 data. In order for the Stage 2 PM oxidation to be reduced, the engine-out PM concentration or CPF mass measurement data is in error. The PM concentration data is the most likely source of error in this case because the CPF mass measurements at the end of Stage 1 and Stage 2 loading were within 3 grams of each other for tests ULSD-3, 4, 5, and 6, which were run within the same two week window. The Stage 2 PM oxidation and engine-out PM concentration data for ULSD-3 and ULSD-5 were elevated compared to ULSD-4 and 6, which can be seen by the blue and red bars in Figure H5. Reducing the experimental engine-out PM concentration by 4 mg/scm reduces the Stage 2 PM oxidation to 30% for ULSD-3, which is within the described boundaries.

The elevated PM oxidation during Stage 2 of test B20-4 is also a function of elevated PM concentration data. The PM concentration for B20-4 was the highest of all the B20 tests, as shown by the red bars in Figure H5. As with ULSD-3, the CPF mass measurements are believed to be accurate. Reducing the engine-out PM concentration by 4 mg/scm reduces the Stage 2 PM oxidation to 30% for B20-4, which is within the described boundaries.

Similarly, the elevated Stage 2 PM oxidation data from ULSD-7R is also a function of elevated PM concentration data as well. The CPF mass measurements at the end of Stage 1 and Stage 2 loading between ULSD-7R and 2R were within 1 gram of each other with the same reported CPF PM loading for each test (2.6 g/L). The PM concentration for ULSD-7R is similar to ULSD-3, where the PM concentrations were among the highest of all the test cases, which can be seen by the red bars in Figure H5. Reducing the engine-out PM concentration by 2 mg/scm reduces the Stage 2 PM oxidation to 29% for ULSD-7R, which is within the described boundaries.

The low amount of PM oxidation reported during Stage 2 of test B10-3 is also a function of inaccurate PM concentration data. The PM concentration from test B10-3 is the lowest of all of the B10 tests, which can be seen by the red bars in Figure H5. When compared to tests B10-1 and 2, the CPF mass measurements at the end of Stage 1 were within 2 grams of each other. The mass measurement at the end of Stage 2 for B10-3 was an average of 7 grams lower than B10-1 and 2, but the CPF PM loading was 0.4 g/L lower, which coincides with a 7 gram reduction in CPF mass.

Raising the engine-out PM concentration by 2 mg/scm raises the Stage 2 PM oxidation to 15%, which is within the described boundaries.

The specific reasoning behind the error associated with the PM concentration data is unknown. It is possible that filter mass errors were introduced by the physical handling of each PM sample. Any addition or loss of mass on the PM sample due to handling directly introduces error into the PM sample mass measurements, which is used directly to determine the mass of PM from a measured volume of exhaust flow.

Active Regeneration PM Mass Balance

For all experiments in this study, the target PM oxidation through active regeneration remained at 70% for a number of reasons. First, the behavior of a clean CPF vs. a partially regenerated CPF is the reason behind the post loading which occurs after regeneration. Second, if all of the PM within the CPF is oxidized, there is a chance that error in the CPF mass measurements could be introduced due to a lack of PM retained within the CPF. For example, with 2.2 g/L PM loading prior to active regeneration, 37.6 g of PM is present in the filter. After 80% PM oxidation occurs during active regeneration, 7.5 g of PM remain, and after 30 minutes of Stage 3 loading, there is typically an additional 5 g of PM deposited, for a total of 12.5 g of PM retained within the CPF.

The CPF itself weighs upwards of 17.5 kg, so the highest amount of PM retained within the CPF at the time of weighing is desirable. The possibility of CPF weighing inaccuracy is increased with increased levels of PM oxidation during active regeneration; therefore, if PM oxidation during active regeneration is between 40 and 80%, it is assumed that the PM mass retained within the CPF can accurately be determined.

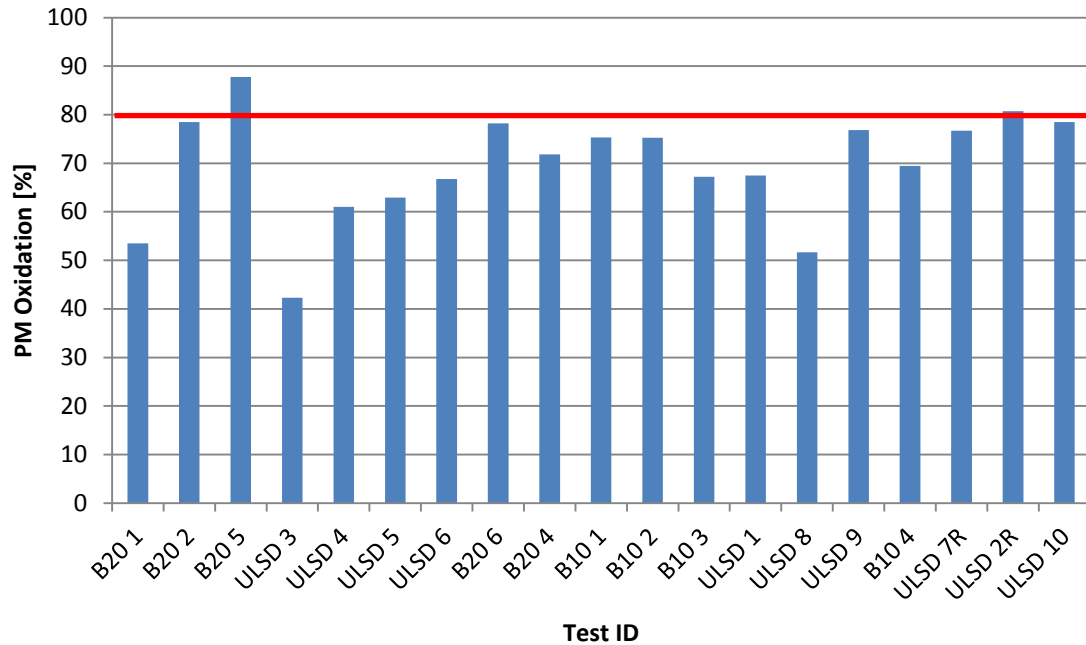


Figure H6: Active Regeneration PM Oxidation for All Tests

Figure H6 shows the amount of PM oxidized for each run through active regeneration, with a red line showing the cutoff point of 80%. The reason low PM oxidation is not considered to invalidate the data is because the PM mass within the CPF at the time of weighing is increased, thereby reducing the possibility of CPF mass measurement errors.

As previously mentioned, 12.5 g of PM is typically retained within the CPF at the time of CPF weighing following Stage 3 loading assuming 80% PM oxidation during active regeneration. With a scale rated for 0.1 g readability and 0.3 g repeatability, 12.5 g of PM can easily be calculated by using CPF mass measurements.

27.6 g of PM is typically retained within the CPF at the time of CPF weighing following Stage 3 loading assuming 40% PM oxidation during active regeneration. With 2.2 g/L equating to 37.6 g of PM, 10 g of PM is oxidized. With the scale ratings described above, 10 g of CPF mass change due to PM oxidation can easily be calculated using CPF mass measurements. For this reason, 40% oxidation is the lower limit that is acceptable to accurately determine the change in CPF mass due to the active regeneration test phase.

CPF Resistance

The CPF flow resistance was calculated for each test case based on the methodology from the CPF Flow Resistance section in Chapter 3 (section 3.10). The first step is to determine the CPF flow resistance based on the raw experimental data as shown in Figure H7.

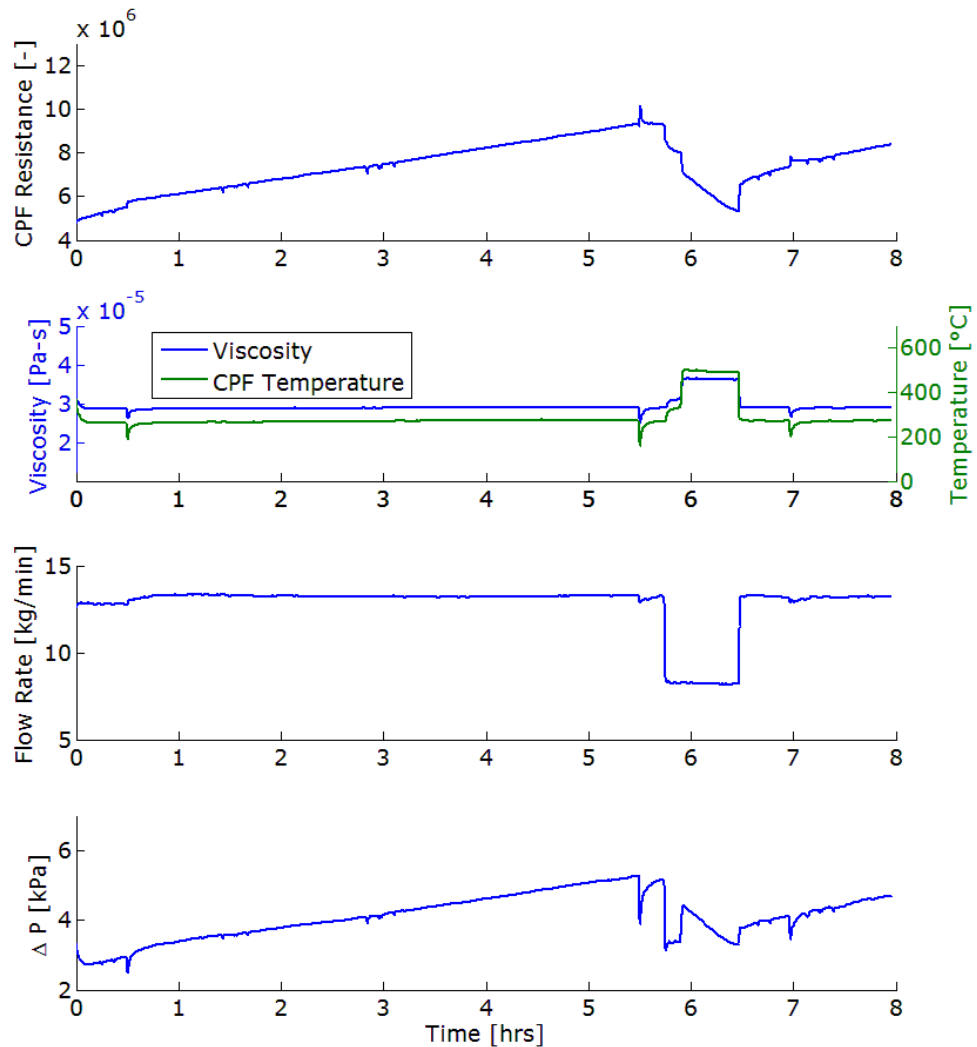


Figure H7: Run 1 (B20-1) Experimental CPF Flow Resistance (subplot 1), Exhaust Viscosity and CPF Average Temperature (subplot 2), Exhaust Mass Flow Rate (subplot 3), and CPF Pressure Drop Profile (subplot 4)

The CPF flow resistance analysis allows for the determination of the correction factor CF (Eqn. 20), during the pre-active regeneration ramp up and active regeneration

test phases, in order to eliminate the upward and downward vertical shifts in CPF resistance that should not be present, as explained earlier in section 3.10. In order to determine CF for each test case, a specific procedure for experimental data corrections need to be utilized. The steps for this procedure are outlined below.

1. Correct the engine-out mass flow rate based upon DAQ system error associated with pressure transducer readings as well as exhaust bypass valve leaks which result in less mass flow rate through the CPF.
2. Correct CPF pressure drop data based on Stage 1 vs. Stage 2 loading CPF pressure drop offset
3. Determine the CF for active regeneration ramp and active regeneration test phases based on a resistance curve without upward and downward vertical shifts as present in Figure H7.

Step 1

LFE pressure drop errors are believed to have been introduced during Stage 1 loading due to the temperature change in the test cell, affecting the calculated engine-out mass flow rate as a result. The increase in test cell temperature during Stage 1 loading is believed to have introduced an error in the DAQ system and its ability to properly read a zero-pressure reading on the pressure transducers. Since the engine-in air flow rate is calculated based on the pressure drop of the LFE, the errors associated with the pressure drop readings affect the exhaust mass flow rate. The pressure transducer on the LFE has a measurement limit of 3.4 kPa. A 20 °F change in test cell temperature can influence the LFE pressure drop by 0.2 kPa, subsequently resulting in a difference in exhaust mass flow rate of 0.3 kg/min (2.4% of a typical average equivalent to 12.7 kg/min).

Table H1 shows the average exhaust mass flow rate for S1, S2, Loading Ramp, S3, and S4 loading phases, for all experiments. The average exhaust mass flow rate for all loading phases was calculated for each experiment and is shown in the 'Loading Average' column of Table H1. The green cells in Table H1 correspond to those tests which are within 5% of the average value for the loading phases of that particular test, because experimental measurements within 5% of one another are acceptable from an experimental data collection standpoint.

Table H1: Experimental Exhaust Mass Flow Rate

Run	Test	Test Phase Exhaust \dot{m} [kg/min]					Loading Average
		S1	S2	LD_RMP	S3	S4	
1	B20 1	12.8	13.3	13.1	13.2	13.2	13.1
2	B20 2	13.0	13.2	13.1	13.2	13.2	13.1
3	B20 5	12.7	13.2	13.0	13.1	13.0	13.0
4	ULSD 3	12.7	12.9	12.8	12.8	13.0	12.8
5	ULSD 4	10.9	12.7	12.5	12.7	12.5	12.6
6	ULSD 5	12.8	12.7	12.8	12.9	12.9	12.8
7	ULSD 6	12.8	12.8	13.0	13.0	12.9	12.9
8	B20 6	12.7	13.0	13.0	13.1	13.0	13.0
9	B20 4	12.8	13.0	13.0	13.0	13.0	13.0
10	B10 1	12.7	12.9	12.8	12.9	12.9	12.8
11	B10 2	12.4	12.8	12.9	13.0	12.9	12.8
12	B10 3	13.0	13.0	12.8	13.0	12.9	12.9
13	ULSD 1	12.4	12.5	12.8	12.8	11.3	12.6
14	ULSD 8	10.7	12.4	12.3	12.5	12.5	12.4
15	ULSD 9	12.4	11.0	12.8	12.6	12.6	12.6
16	B10 4	12.2	12.5	12.3	12.7	12.7	12.5
17	ULSD 7R	12.1	12.5	12.2	12.4	12.3	12.3
18	ULSD 2R	12.1	12.4	12.4	12.4	12.4	12.3

In order to correct for the error in the Stage 1 loading LFE pressure drop, the pressure transducer readings at the beginning and end of Stage 1, when the engine was not running, was analyzed. The difference in the zero-pressure readings between the start and stop of Stage 1 were tabulated, with the results shown in Table H2. The positive Stage 1 LFE pressure drop offset, measured exhaust mass flow rate, the change in the flow rate due to the LFE pressure drop offset, the corrected flow rate, and the percent change in flow rate are shown in Table H2. Only Runs 5 and 14 required a flow rate correction that is large enough to be considered an error not due to experimental variability. They were the only test cases which experienced more than 5% change in the measured exhaust mass flow rate, as compared to the results shown in the S1 column of Table H1.

Table H2: LFE Pressure Drop Corrections

Run	Variable	S1 LFE DP Offset	S1 Measured Exhaust Mass Flow Rate	Flow Rate Change	S1 Corrected Exhaust Mass Flow Rate	Percent Change in Flow Rate
	Test/Units	kPa	kg/min	kg/min	kg/min	%
1	B20 1	0.02	12.8	0.2	13.0	1.7
2	B20 2	0.01	13.0	0.2	13.2	1.4
3	B20 5	0.01	12.7	0.2	12.9	1.5
4	ULSD 3	0.01	12.7	0.1	12.8	0.6
5	ULSD 4	0.11	10.9	1.6	12.5	14.5
6	ULSD 5	0.02	12.8	0.2	13.0	1.7
7	ULSD 6	0.02	12.8	0.3	13.1	2.1
8	B20 6	0.00	12.7	0.1	12.8	0.5
9	B20 4	0.01	12.8	0.1	12.9	0.7
10	B10 1	0.02	12.7	0.3	13.0	2.2
11	B10 2	0.02	12.4	0.2	12.6	1.8
12	B10 3	0.02	13.0	0.2	13.2	1.7
13	ULSD 1	0.01	12.4	0.2	12.6	1.7
14	ULSD 8	0.11	10.7	1.6	12.3	14.9
15	ULSD 9	0.01	12.4	0.2	12.6	1.4
16	B10 4	0.02	12.2	0.2	12.4	1.8
17	ULSD 7R	0.02	12.1	0.2	12.3	1.9
18	ULSD 2R	0.02	12.1	0.2	12.3	1.9

The information from Table H2 was used to determine the exhaust mass flow rate scaling factors (SF) for all phases of each test. The scaling factors (SF) for each test case can be seen in Table H3. The cells which are green in Table H3 correspond to the test phases which did not require any scaling because the experimental flow rates were measured within acceptable experimental variability. The scaling factors shown in Table H3 for S4 and S2 of Runs 14 and 15, respectively, were due to an unknown error source during LFE pressure drop measurements. The scaling factors shown in the 'S1' column of Table H3 for each test was due to the LFE pressure drop corrections from Table H2.

The exhaust flow rate also required scaling factors to be applied where exhaust bypass valve leaks were occurring. A leaking exhaust bypass valve results in decreased pressure drop across the CPF due to a reduction in exhaust flow. The reduction in CPF pressure drop is proportional to the reduction in flow rate. Scaling factors were applied to the exhaust flow rate in the same method which was used to

correct LFE pressure drop measurement errors. For Runs 3, 4, 5, and 6, the bypass exhaust valve was leaking as evidenced by their respective CPF pressure drop profiles, which were shown to be inconsistent with the characteristics associated with CPF PM loading (steady increase in CPF pressure drop at steady state engine conditions) between and/or during test phases.

The exhaust flow rate scaling factors for each test case can be seen in Table H3. The scaling factors (SF) shown in Table H3 account for LFE pressure drop errors as well as exhaust flow rate reduction due to a leaking exhaust bypass valve. As previously mentioned, up to 5% variation was seen within the test phases corresponding to green cells in Table H3, but this range was considered to be due to experimental variability. The MTU-1D CPF model does not have any problems operating with these small variations in experimental data.

Table H3: Exhaust Mass Flow Rate Scaling Factors (SF)

Run	Test	Average Mass Flow Rate Correction by Phase* [-]						
		S1	S2	LD RMP	AR RMP	AR	S3	S4
1	B20 1	1.02						
2	B20 2	1.01						
3	B20 5	1.02		0.92**				
4	ULSD 3	1.01		0.86**	0.86**	0.86**	0.90**	0.90**
5	ULSD 4	1.15	0.95**	0.82**	0.95**	0.95**	0.95**	0.84**
6	ULSD 5	1.02		0.94**				
7	ULSD 6	1.02						
8	B20 6	1.01						
9	B20 4	1.01						
10	B10 1	1.02						
11	B10 2	1.02						
12	B10 3	1.02						
13	ULSD 1	1.02						1.15
14	ULSD 8	1.15						
15	ULSD 9	1.01	1.13					
16	B10 4	1.02						
17	ULSD 7R	1.02						
18	ULSD 2R	1.02						

*Corrects for LFE flow rate measurement and bypass valve errors

** Corrects for bypass valve leaks

The cells within Table H3 which are highlighted green are the test phases which required slight scaling factors greater than 0.95 and less than 1.05 because experimental measurement within 5% of the actual exhaust flow rate is acceptable.

The cells within Table H3 which include a numerical value are the test phases which required SF to compensate for flow rate errors (Runs 5, 13, 14, and 15) and exhaust bypass valve leaks (Runs 3, 4, 5, 6).

In terms of the active regeneration analysis in this study, no experimental data requires alteration due to the exhaust mass flow rate scaling factors (SF). This is because the active regeneration analysis in this study (i.e., PM reaction rate, regeneration efficiency of fuel dosing, etc.) is based off of the CPF mass measurements.

The exhaust flow rate is important from a modeling perspective because the PM flowing into the CPF at any test point is a function of exhaust mass flow rate and engine-out PM concentration. For test cases, such as ULSD-4, the scaling factors should be applied to the MTU-1D CPF Model exhaust mass flow rate input data. For purposes of the analysis of PM oxidation during Stage 2 loading phases, the flow rate data shown in the CPF mass balances for Stage 2 loading (Appendix K) has been updated using the SF · experimental mass flow rate data.

Step 2

As previously stated, it is believed that the test cell temperature rise through the end of Stage 1 loading is negatively affecting the experimental data by introducing error into the CPF and LFE pressure drop measurements. In order to correct the CPF pressure drop data during Stage 1 loading, comparison of the CPF pressure drop recorded by the National Instruments DAQ system and Cummins CalTerm software are compared.

The Cummins CPF pressure drop sensor was calibrated by the Heavy Duty Diesel Group over a pressure range from 0 to 30 kPa. The first step is applying the calibration correction to the CalTerm pressure drop where the experimental readings are $DP_{\text{CPF-Cal}}$ and the corrected readings are DP_{actual} . The calibration curve equation was determined to be $DP_{\text{actual}} [\text{kPa}] = 1.0597 \cdot DP_{\text{CPF-Cal}} [\text{kPa}] + 0.8946$ with an R^2 value of 0.9996 over five data points.

After the CalTerm pressure drop data calibration correction has been applied, the difference between CalTerm and DAQ system pressure drop readings is calculated from the start of Stage 2 through the end of Stage 4 loading. The average of this

difference is applied to the CalTerm data so that the curves lie on each other after Stage 1 loading, with the results for B20-1 visible in Figure H8.

In Figure H8, the blue curve is the experimental CPF pressure drop measured by the DAQ system and the black curve is the corrected CalTerm pressure drop. The correlation between the two signals is good after Stage 2 loading, confirming the hypothesis that the Stage 1 loading pressure drop measurements are subject to error. The red line at the end of Stage 1 loading represents the offset to be applied to the DAQ system pressure drop and is equal to 0.19 kPa for test B20-1.

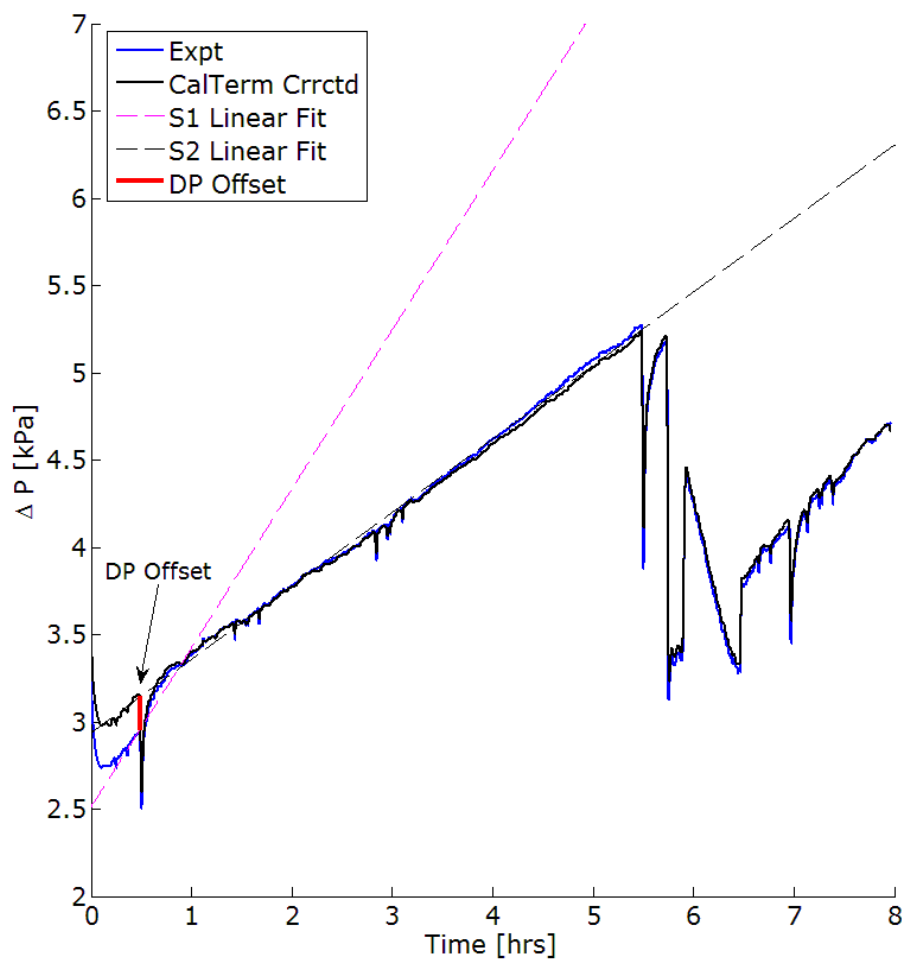


Figure H8: Run 1 (B20-1) NI and Corrected CalTerm Pressure Drop Profiles Including Linear Fit of NI Stage 1 and Stage 2 Loading and Pressure Drop Offset

For tests in which CalTerm data was unavailable, the liner fit curves were employed. The difference in linear fit curves of Stage 1 and Stage 2 loading at $t = 0.5$ hours is assumed to be the offset to be used for that specific test case. The specific values for the Stage 1 loading pressure drop offsets applied to the DAQ system pressure drop profile can be seen in Table H4.

The CPF and LFE pressure drop measurements during Stage 1 were subject to error, as previously explained. The offset corrections for the LFE and CPF pressure transducers can be seen in Table H4. The LFE data presented in the 'S1 LFE DP Offset' column of Table H4 is the same which is presented in the 'S1 LFE DP Offset' column of Table H2. Runs 5 and 14 required the highest LFE pressure drop corrections, which are within 2% of corrections required during S4 and S2 of Runs 13 and 15, respectively.

Table H4: Stage 1 Loading CPF Pressure Drop Offset Corrections

Run	Variable	S1 CPF DP Offset	S1 LFE DP Offset
	Test/Units	kPa	kPa
1	B20 1	0.19	0.02
2	B20 2	0.11	0.01
3	B20 5	0.11	0.01
4	ULSD 3	0.05	0.01
5	ULSD 4	0.34	0.11
6	ULSD 5	0.18	0.02
7	ULSD 6	0.21	0.02
8	B20 6	0.03	0.00
9	B20 4	0.07	0.01
10	B10 1	0.27	0.02
11	B10 2	0.17	0.02
12	B10 3	0.00	0.02
13	ULSD 1	0.17	0.01
14	ULSD 8	0.18	0.11
15	ULSD 9	0.18	0.01
16	B10 4	0.19	0.02
17	ULSD 7R	0.21	0.02
18	ULSD 2R	0.22	0.02

Step 3

Once the CPF pressure drop offset and exhaust flow rate scaling factors were applied, the correction factor (CF) discussed in section 3.10 is determined. First, the CPF resistance is calculated using the CPF pressure drop corrected for offsets and exhaust mass flow rate corrected with the scaling factors. The CPF resistance for test B20-1 is shown in Figure H9. Again, the corrections applied to the data in Figure H9 are only to account for LFE pressure drop measurement error and/or exhaust bypass valve leaks affecting the mass flow rate and pressure drop offset affecting the CPF pressure drop curve.

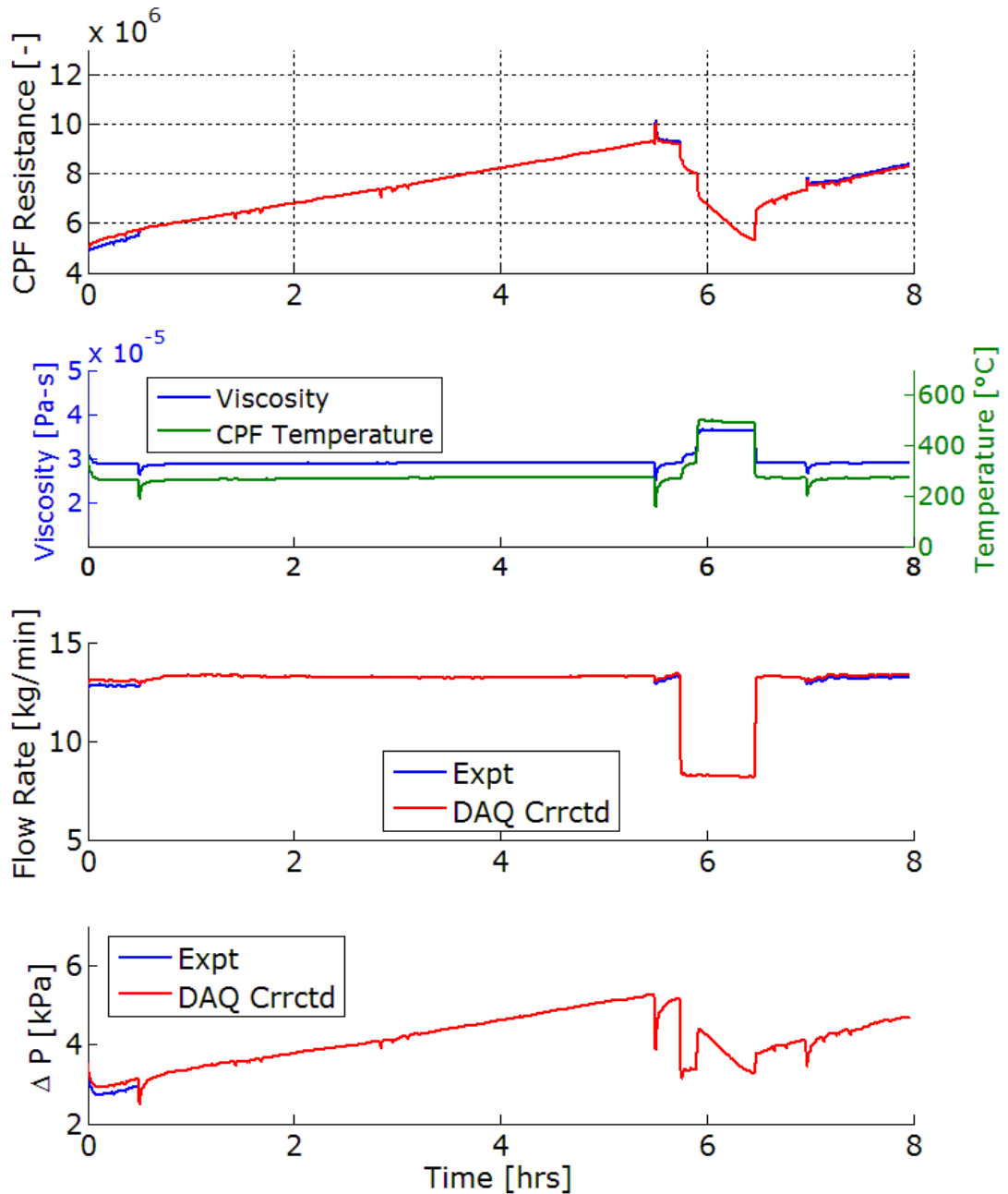


Figure H9: Run 1 (B20-1) Corrected and Experimental CPF Flow Resistance (subplot 1), Exhaust Viscosity and CPF Average Temperature (subplot 2), Corrected and Corrected Experimental Exhaust Mass Flow Rate (subplot 3), Corrected and Experimental CPF Pressure Drop Profile (subplot 4)

In Figure H9, the pressure drop offset during Stage 1 loading of 0.19 kPa was applied.

Next, the graphical input tool within MATLAB is used to re-construct the plausible resistance curve based on the DAQ measurement error corrected CPF pressure drop and exhaust mass flow rates (shown in red on the first subplot in Figure H9). Using this resistance curve from the graphical input, the required CF is determined using the CPF resistance equation, Eqn. 20.

Average values for the corrections (SF) applied to all test phases based on DAQ system measurement errors and/or bypass valve leaks as tabulated in Table H3 are used in the analysis. The active regeneration ramp and active regeneration phase correction factor (CF) is determined using the experimental exhaust mass flow rate (after SF from Table H3 was applied, where required).

The plausible resistance curve is used to calculate a correction factor (CF) for the pre-active regeneration ramp and active regeneration test phases. Eqn. 20 can be re-written to solve for the correction factor, CF, which is shown by Eqn. H1.

$$CF = \frac{\Delta P \cdot V_t \cdot \rho_{exh}}{m \cdot \mu \cdot \text{Resistance}} \quad \text{Eqn.H1}$$

The 'Resistance' variable in Eqn. H1 comes from the re-constructed plausible resistance curve where all other variables used to solve for CF come from the experimental data.

The resulting CF is a scalar multiplier to be applied to the experimental mass flow rate in order to simplify input data preparation for the MTU-1D CPF model. The average CF for pre-active regeneration ramp and active regeneration phases for each experiment can be seen in Table H5.

Table H5: Active Regeneration Ramp and Active Regeneration CF

Run	Test	Correction Factor	
		AR RMP	AR
1	B20 1	0.87	0.77
2	B20 2	0.88	0.74
3	B20 5	0.86	0.72
4	ULSD 3	0.85	0.75
5	ULSD 4	0.93	0.73
6	ULSD 5	0.87	0.76
7	ULSD 6	0.87	0.74
8	B20 6	0.87	0.73
9	B20 4	0.88	0.76
10	B10 1	0.88	0.75
11	B10 2	0.87	0.74
12	B10 3	0.87	0.76
13	ULSD 1	0.89	0.76
14	ULSD 8	0.87	0.75
15	ULSD 9	0.88	0.73
16	B10 4	0.87	0.76
17	ULSD 7R	0.88	0.75
18	ULSD 2R	0.87	0.73
Average		0.87	0.74
Std. Deviation		0.02	0.01

The resulting CF is equal to 1 in all test phases except active regeneration ramp and active regeneration, because CF corrects for possible temperature and PM maldistribution in the CPF, exhaust flow maldistribution at the CPF inlet, and changing cake layer permeability which cannot be quantified from experimental data at this time. It is believed that there are two triggers which drive the need for the correction factor (CF). The first is the switch to the active regeneration engine condition during the AR-ramp test phase. The second is the initiation of active regeneration by fuel dosing because the CF rapidly changes during the first few minutes of temperature increase after dosing has been initiated and PM oxidation has started.

The average CF during the active regeneration ramp and active regeneration phases are 0.87 and 0.74, respectively, with a standard deviation of 0.2 and 0.1, respectively. This shows that the CF likely does not carry an effect of biodiesel blends

or CPF inlet temperature, but is affected by unknown variables that cannot be determined with the experimental data that has been measured.

The CF for test B20-1 is shown below in Figure H10. CF figures for each test can be found at the end of Appendix H in Figures H29-H34.

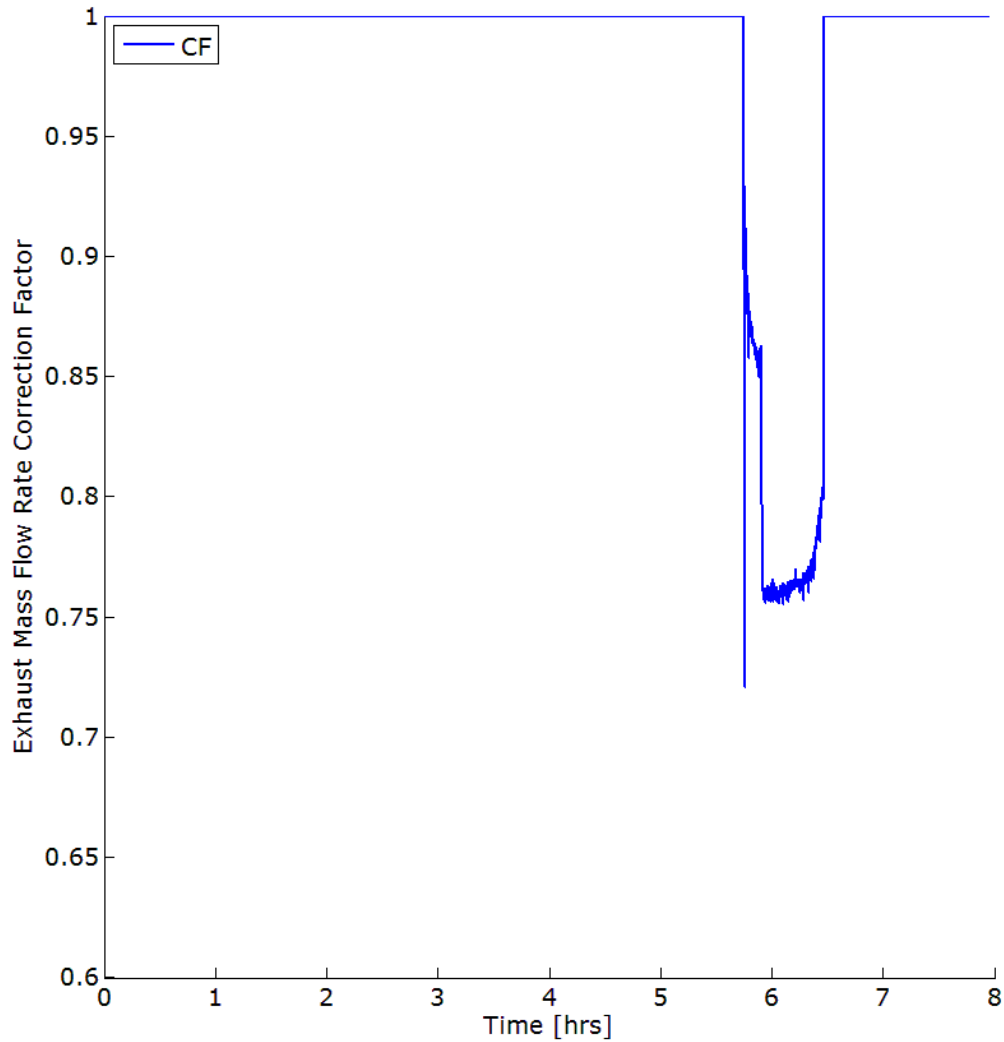


Figure H10: Run 1 (B20-1) CF

In Figure H10, the correction factor (CF) for the active regeneration ramp and active regeneration phases is shown. The CF, as previously described, is 1 for all test phases except the two phases at the active regeneration engine condition.

With the exhaust mass flow rate scaling factors determined and implemented based on DAQ system and measurement error (pressure transducer error and/or exhaust bypass valve leaks), the pressure drop offset corrections applied, and the CF determined for the active regeneration ramp and active regeneration phases, the result is what can be seen in Figure H11. Figure H11 shows the experimental and corrected, continuous CPF flow resistance curve (subplot 1), exhaust temperature and viscosity (subplot 2), the experimental and corrected (corrections from Steps 2 and 3 combined – assuming the CF is applied to the mass flow rate which is the way it is used in the MTU-1D CPF Model) exhaust mass flow rate (subplot 3), and the experimental and corrected CPF pressure drop (subplot 4).

With the pressure drop offset corrections, mass flow rate DAQ and measurement error scaling factors (SF), and the active regeneration ramp and active regeneration correction factors (CF) known, they can be appropriately applied to the experimental exhaust mass flow rate input data for the MTU 1-D CPF model. The corrected resistance plots for all tests, similar to Figure H11, can be found in Figures H12-H28. The plots showing CF for all test cases can be seen in Figures H29-H34.

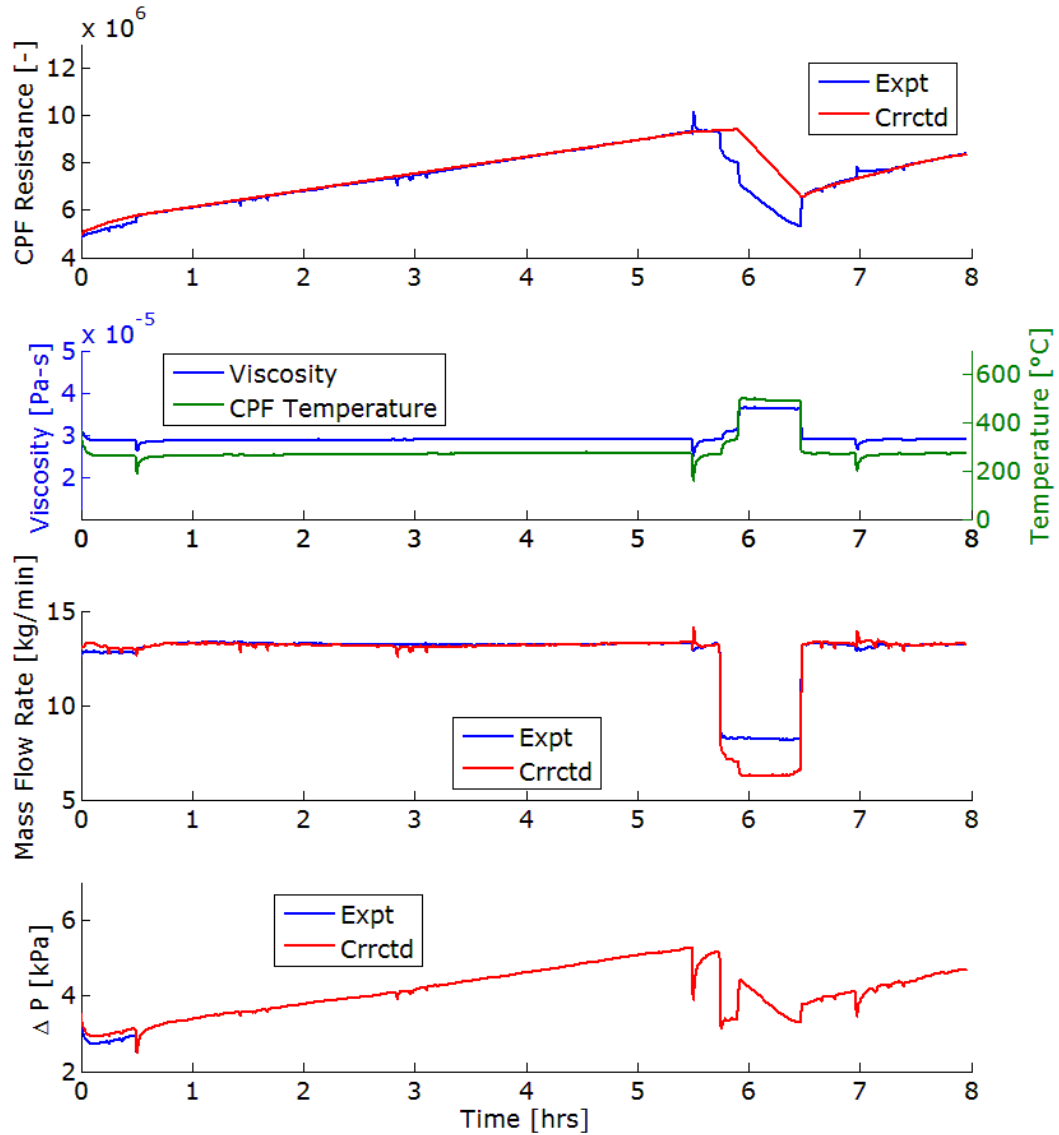


Figure H11: Run 1 (B20-1) Corrected and Experimental CPF Flow Resistance (subplot 1), Exhaust Viscosity and CPF Average Temperature (subplot 2), Experimental and Corrected Experimental Exhaust Mass Flow Rate (subplot 3), Corrected and Experimental CPF Pressure Drop Profile (subplot 4)

In Figure H11, the most significant corrections are the Stage 1 loading CPF pressure drop and mass flow rate, the CF applied to the mass flow rate during the regeneration phases of the experiment, and the temperature stabilization periods of Stage 4 loading and the loading ramp phase.

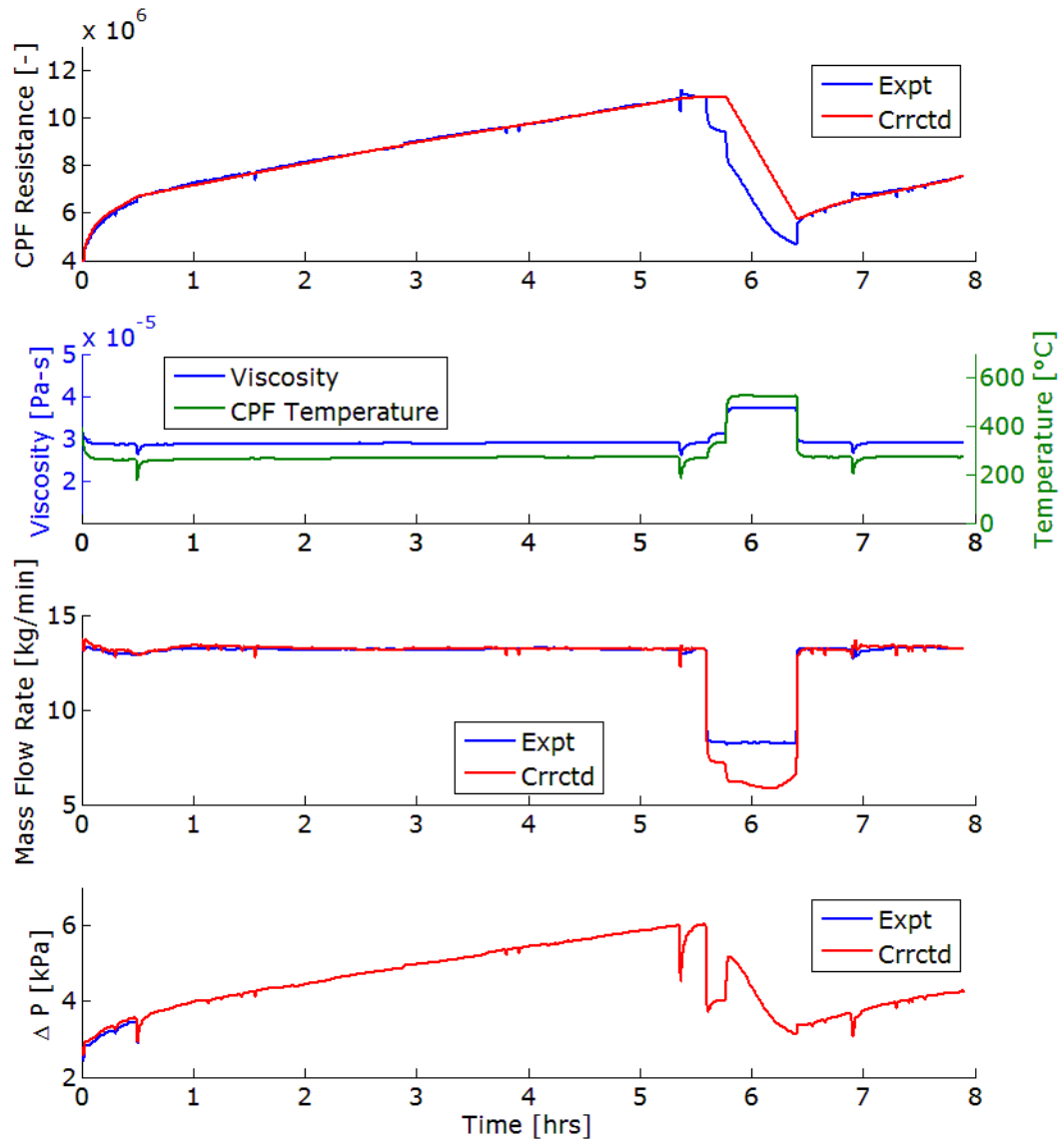


Figure H12: Run 2 (B20-2) Corrected and Experimental CPF Flow Resistance (subplot 1), Exhaust Viscosity and CPF Average Temperature (subplot 2), Experimental and Corrected Experimental Exhaust Mass Flow Rate (subplot 3), Corrected and Experimental CPF Pressure Drop Profile (subplot 4)

In Figure H11, the most significant corrections are the Stage 1 loading CPF pressure drop, the CF applied to the mass flow rate during the regeneration phases of the experiment, and the temperature stabilization period of Stage 4 loading and the loading ramp phase.

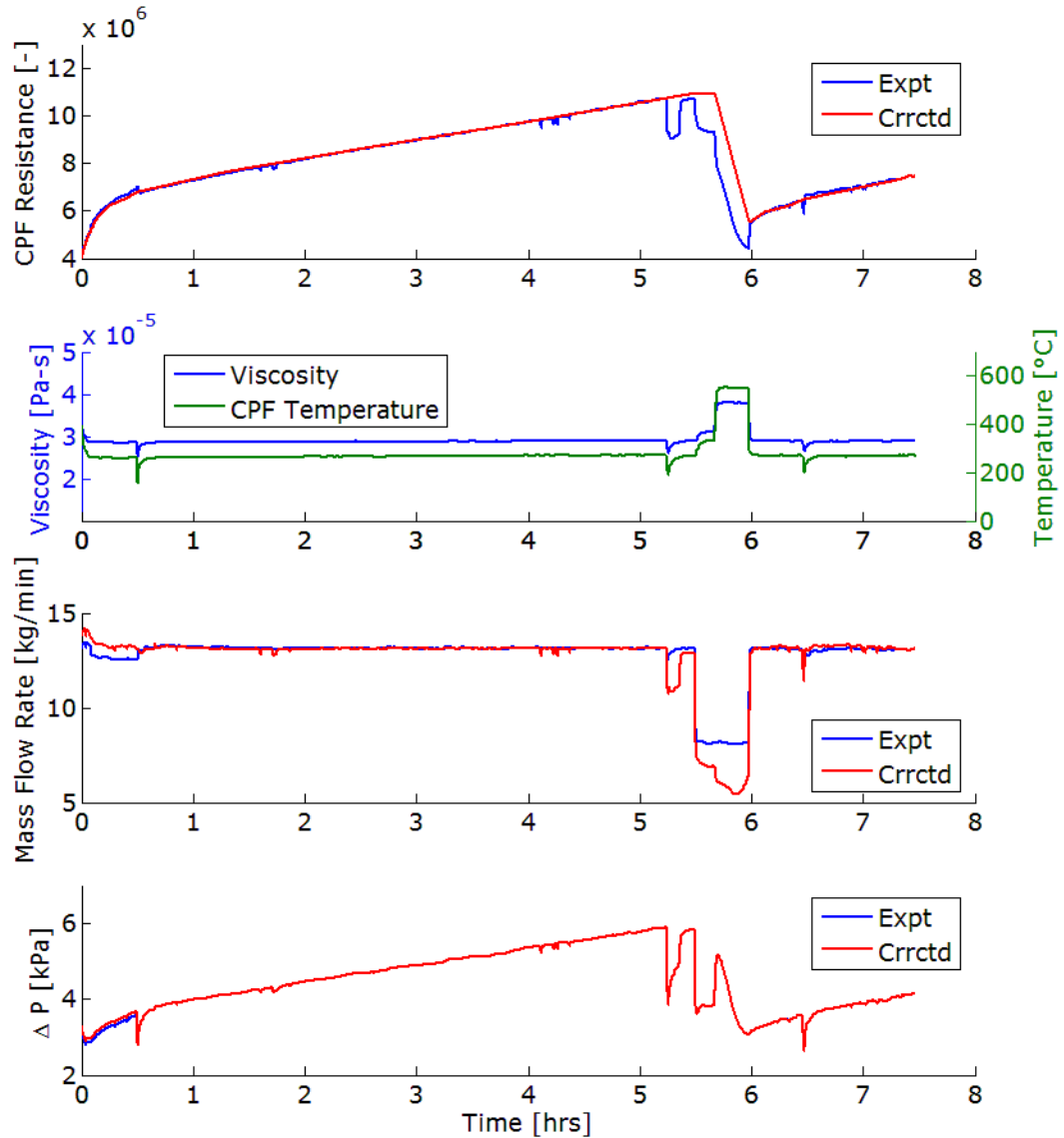


Figure H13: Run 3 (B20-5) Corrected and Experimental CPF Flow Resistance (subplot 1), Exhaust Viscosity and CPF Average Temperature (subplot 2), Experimental and Corrected Experimental Exhaust Mass Flow Rate (subplot 3), Corrected and Experimental CPF Pressure Drop Profile (subplot 4)

In Figure H13, the most significant corrections are the Stage 1 loading CPF pressure drop and mass flow rate, the CF applied to the mass flow rate during the regeneration phases of the experiment, and the temperature stabilization periods of Stage 4 loading.

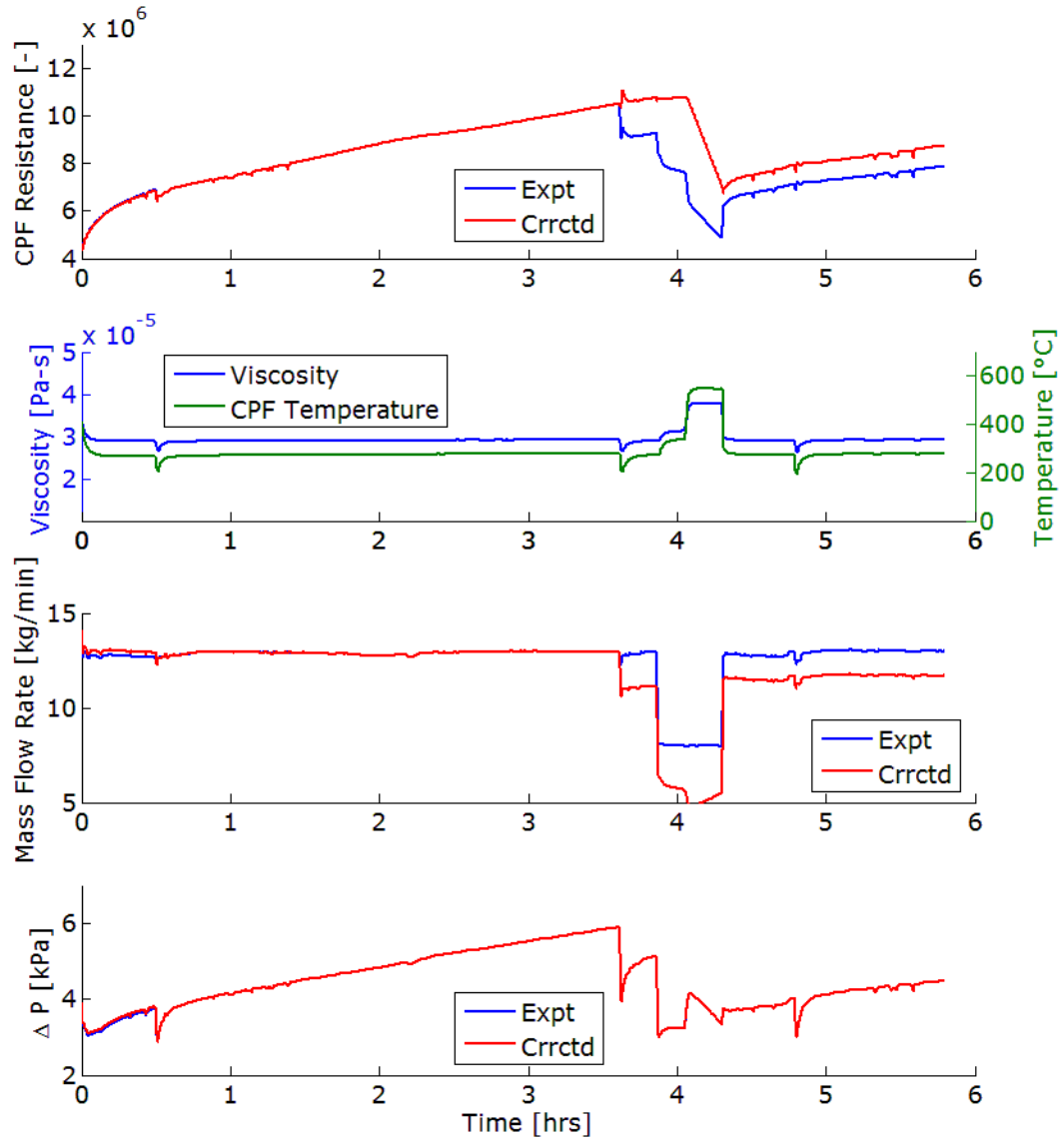


Figure H14: Run 4 (ULSD-3) Corrected and Experimental CPF Flow Resistance (subplot 1), Exhaust Viscosity and CPF Average Temperature (subplot 2), Experimental and Corrected Experimental Exhaust Mass Flow Rate (subplot 3), Corrected and Experimental CPF Pressure Drop Profile (subplot 4)

In Figure H14, the most significant corrections are the Stage 1 loading CPF pressure drop and mass flow rate and the CF applied to the mass flow rate during the regeneration phases of the experiment. The mass flow rate for test phases after Stage 2 loading was adjusted to compensate for a leaking exhaust bypass valve.

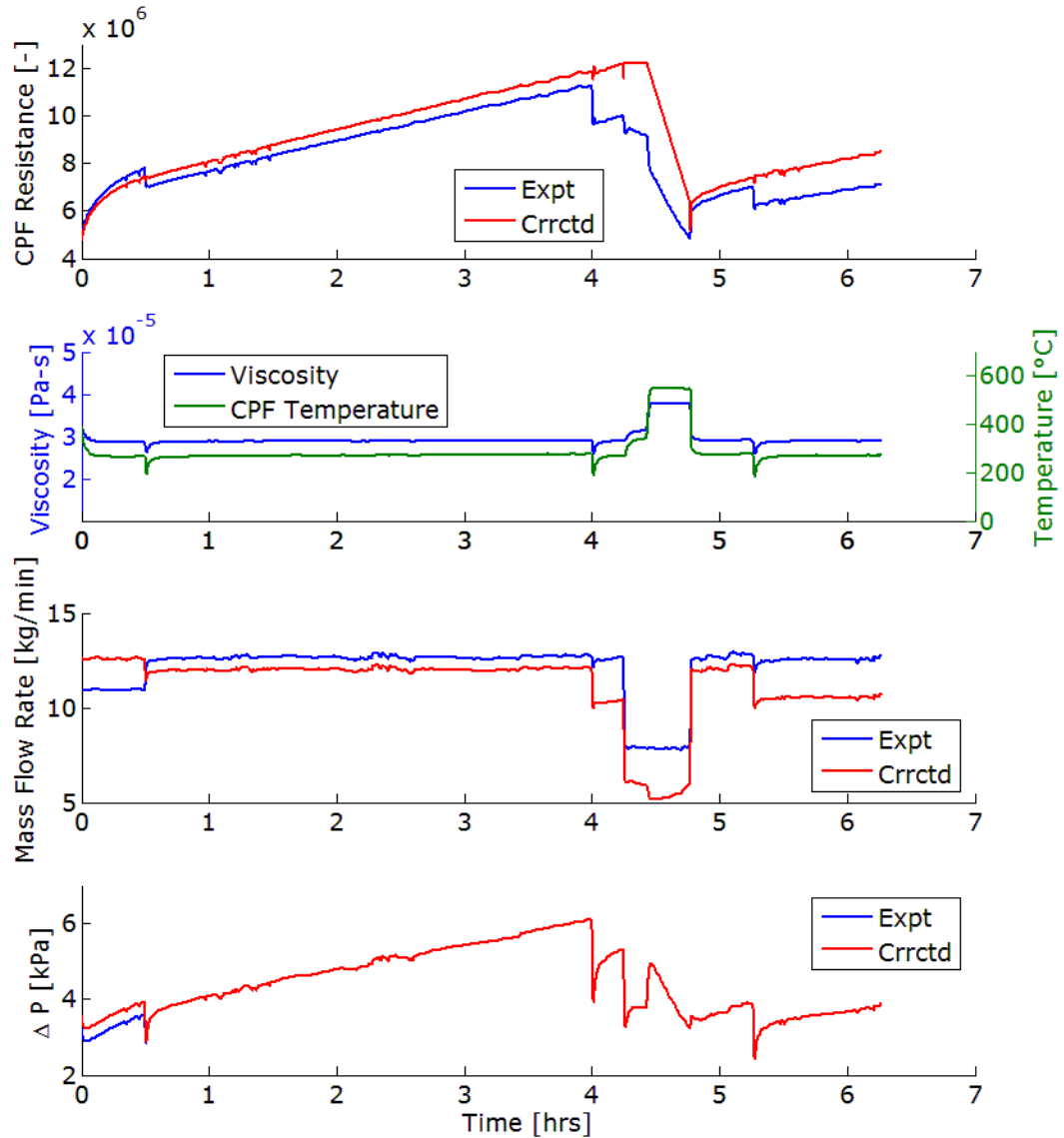


Figure H15: Run 5 (ULSD-4) Corrected and Experimental CPF Flow Resistance (subplot 1), Exhaust Viscosity and CPF Average Temperature (subplot 2), Experimental and Corrected Experimental Exhaust Mass Flow Rate (subplot 3), Corrected and Experimental CPF Pressure Drop Profile (subplot 4)

In Figure H15, the most significant corrections are the Stage 1 loading CPF pressure drop and mass flow rate and the CF applied to the mass flow rate during the regeneration phases of the experiment. The mass flow rate for test phases after Stage 1 loading was adjusted to compensate for a leaking exhaust bypass valve.

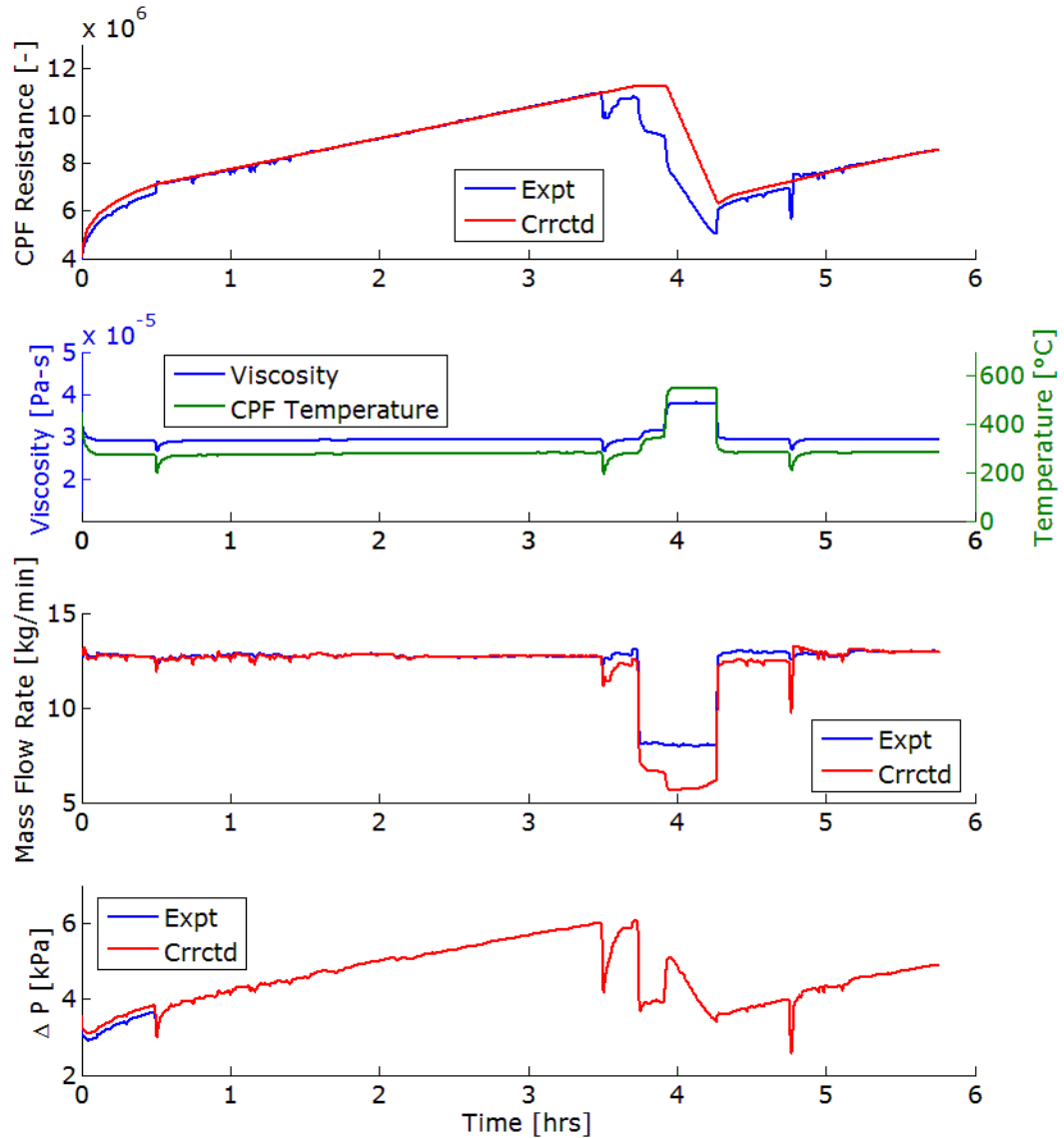


Figure H16: Run 6 (ULSD-5) Corrected and Experimental CPF Flow Resistance (subplot 1), Exhaust Viscosity and CPF Average Temperature (subplot 2), Exp. and Crrctd. Exp. Exhaust Mass Flow Rate (subplot 3), Corrected and Experimental CPF Pressure Drop Profile (subplot 4)

In Figure H16, the most significant corrections are the Stage 1 loading CPF pressure drop, the CF applied to the mass flow rate during the regeneration phases of the experiment, and the temperature stabilization periods of Stage 4 loading. The mass flow rate for the loading ramp and Stage 3 loading phases was adjusted to compensate for a leaking exhaust bypass valve.

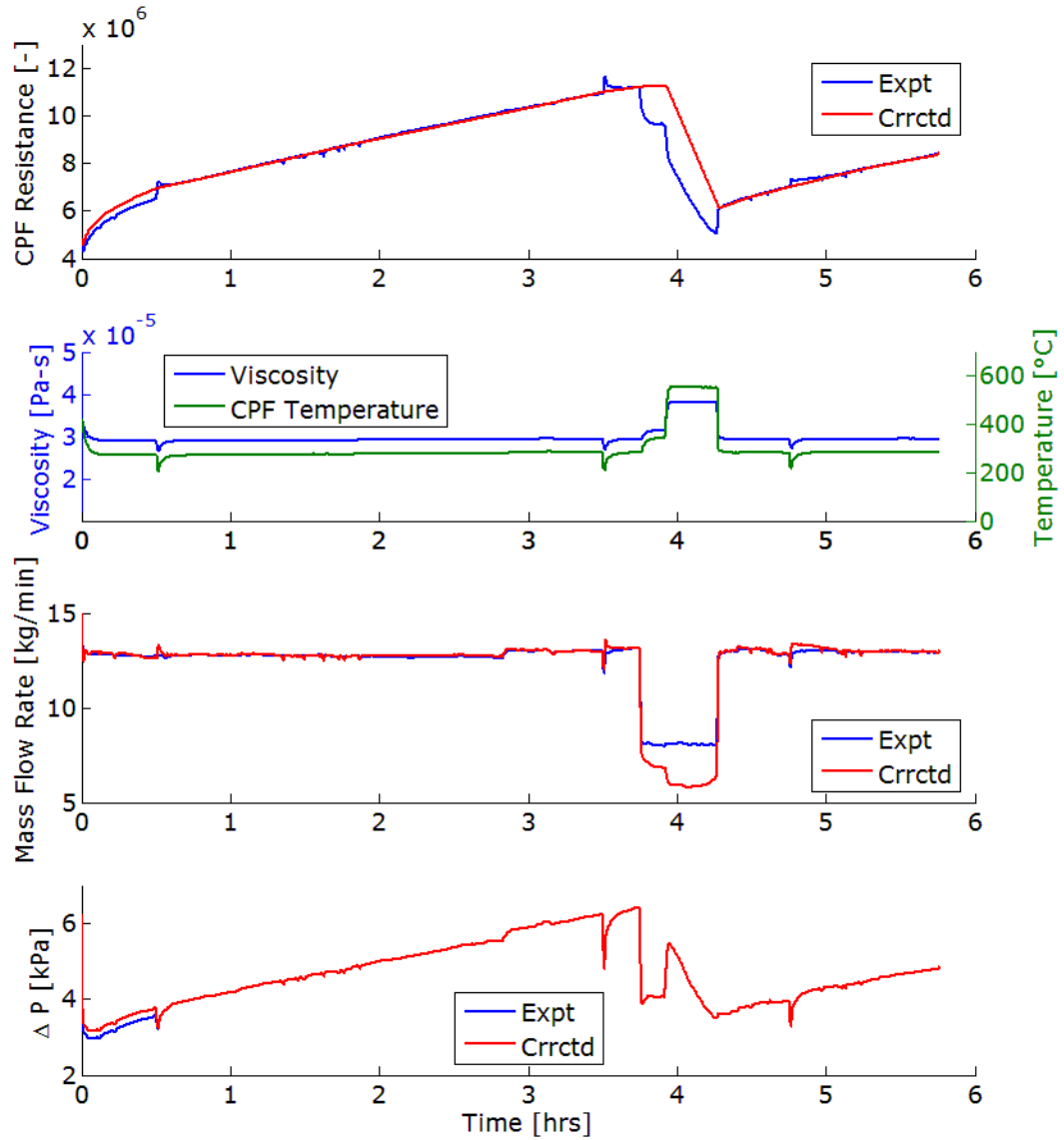


Figure H17: Run 7 (ULSD-6) Corrected and Experimental CPF Flow Resistance (subplot 1), Exhaust Viscosity and CPF Average Temperature (subplot 2), Experimental and Corrected Experimental Exhaust Mass Flow Rate (subplot 3), Corrected and Experimental CPF Pressure Drop Profile (subplot 4)

In Figure H17, the most significant corrections are the Stage 1 loading CPF pressure drop, the CF applied to the mass flow rate during the regeneration phases of the experiment, and the temperature stabilization periods of Stage 2 and Stage 4 loading and the loading ramp phase.

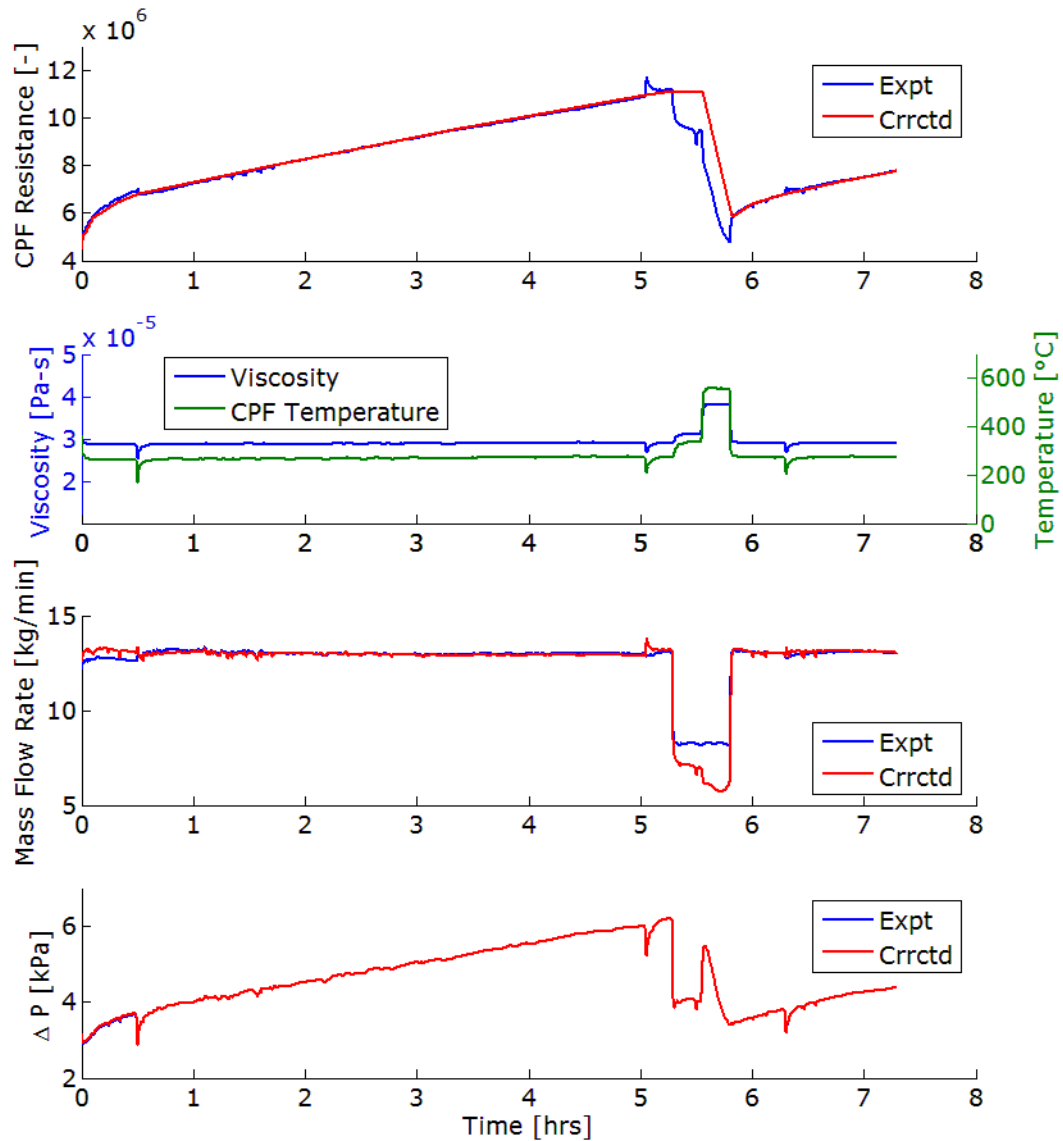


Figure H18: Run 8 (B20-6) Corrected and Experimental CPF Flow Resistance (subplot 1), Exhaust Viscosity and CPF Average Temperature (subplot 2), Experimental and Corrected Experimental Exhaust Mass Flow Rate (subplot 3), Corrected and Experimental CPF Pressure Drop Profile (subplot 4)

In Figure H18, the most significant corrections are the Stage 1 loading CPF pressure drop and mass flow rate, the CF applied to the mass flow rate during the regeneration phases of the experiment, and the temperature stabilization periods of Stage 2 and Stage 4 loading and the loading ramp phase.

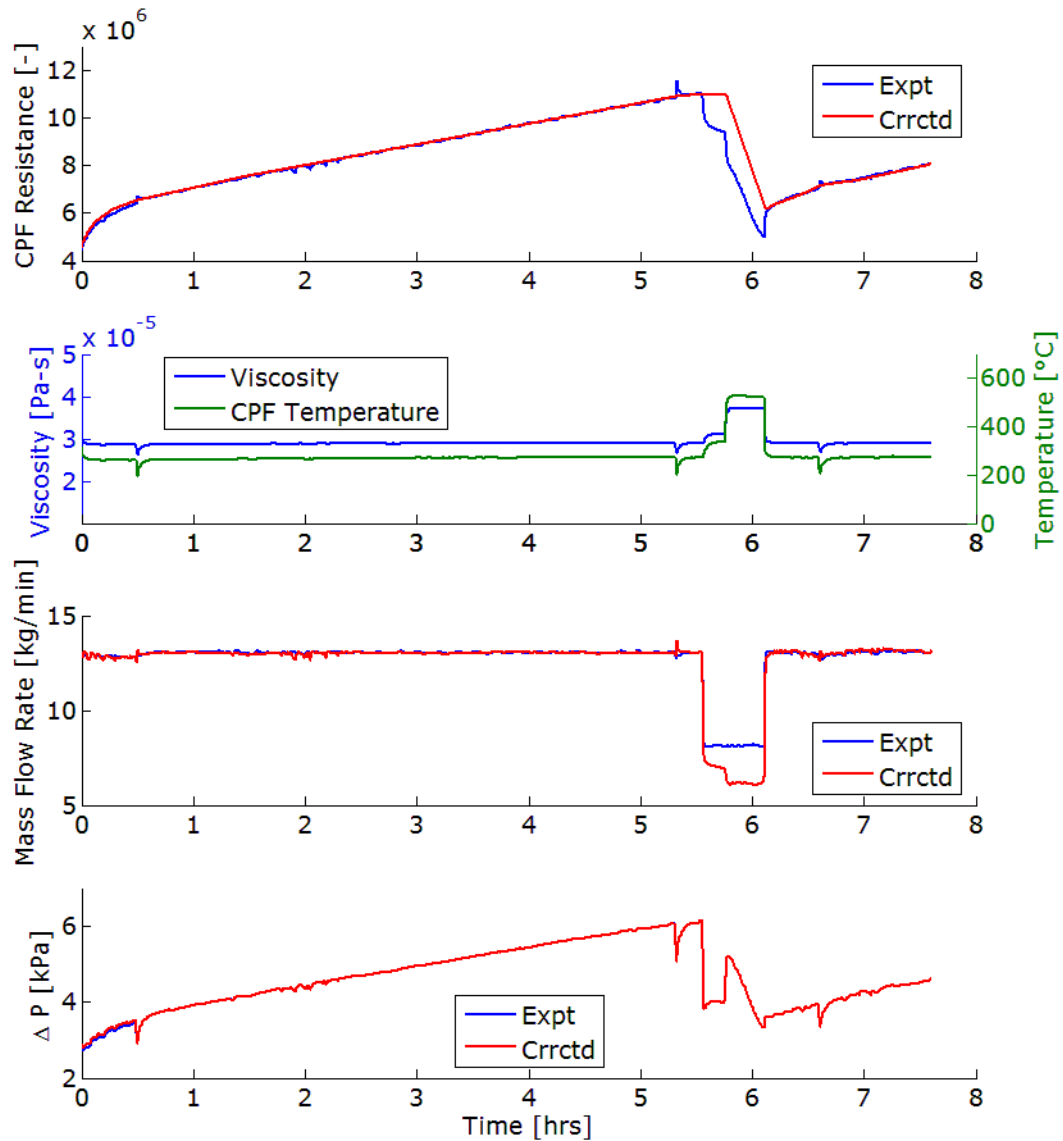


Figure H19: Run 9 (B20-4) Corrected and Experimental CPF Flow Resistance (subplot 1), Exhaust Viscosity and CPF Average Temperature (subplot 2), Experimental and Corrected Experimental Exhaust Mass Flow Rate (subplot 3), Corrected and Experimental CPF Pressure Drop Profile (subplot 4)

In Figure H19, the most significant corrections are the Stage 1 loading CPF pressure drop, the CF applied to the mass flow rate during the regeneration phases of the experiment, and the temperature stabilization periods of Stage 2 and Stage 4 loading and the loading ramp phase.

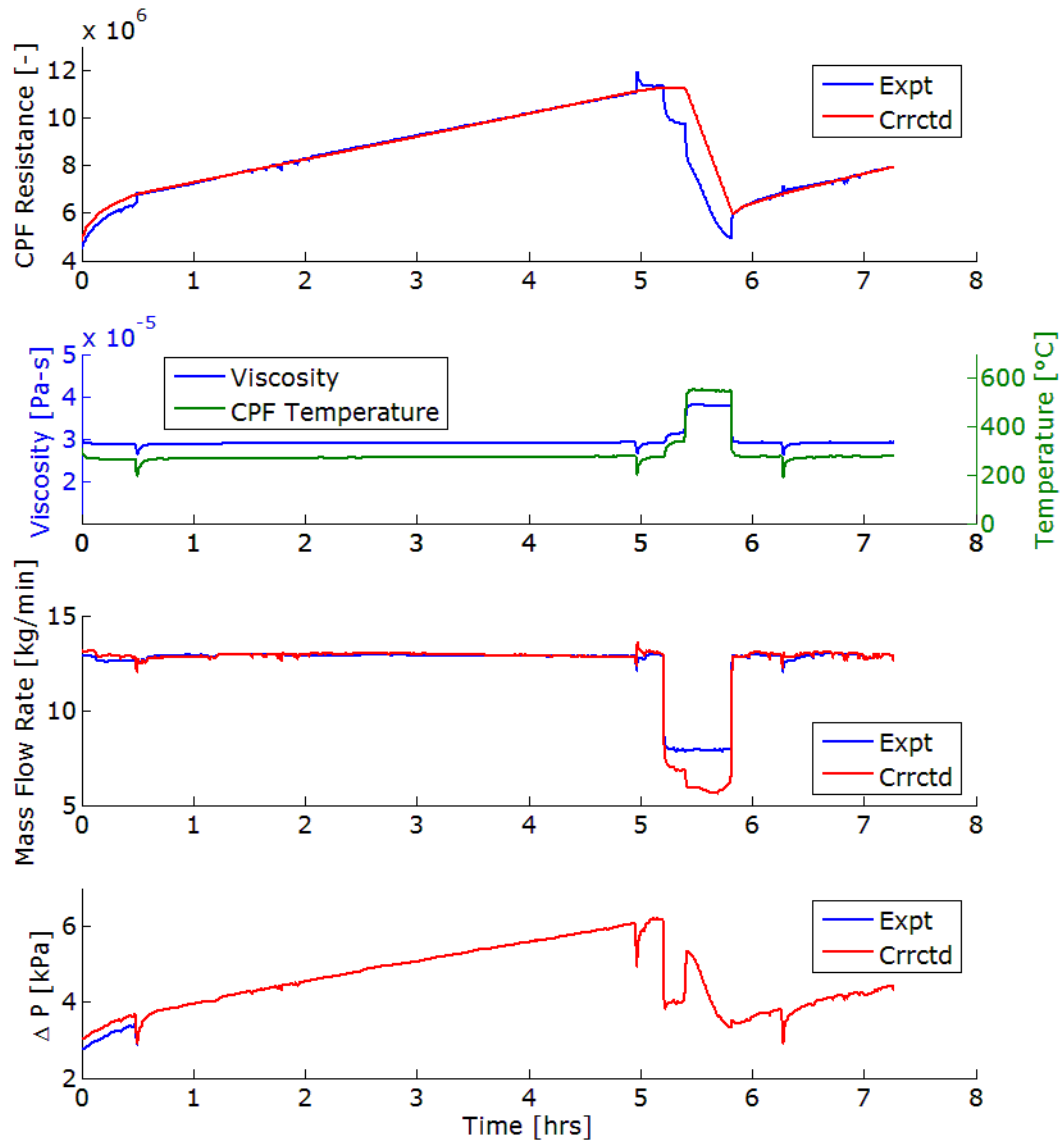


Figure H20: Run 10 (B10-1) Corrected and Experimental CPF Flow Resistance (subplot 1), Exhaust Viscosity and CPF Average Temperature (subplot 2), Experimental and Corrected Experimental Exhaust Mass Flow Rate (subplot 3), Corrected and Experimental CPF Pressure Drop Profile (subplot 4)

In Figure H20, the most significant corrections are the Stage 1 loading CPF pressure drop and mass flow rate, the CF applied to the mass flow rate during the regeneration phases of the experiment, and the temperature stabilization periods of Stage 2 and Stage 4 loading and the loading ramp phase.

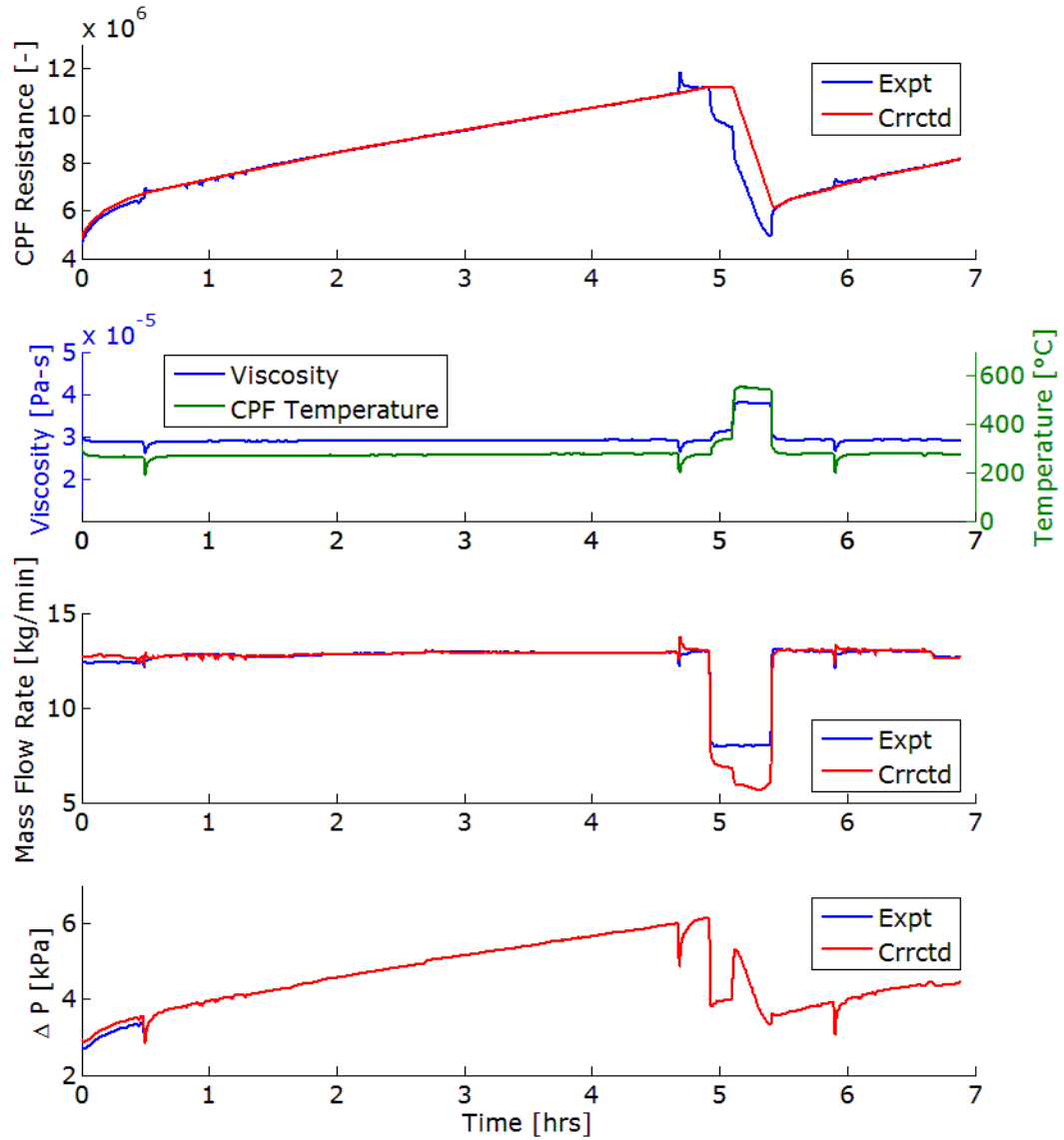


Figure H21: Run 11 (B10-2) Corrected and Experimental CPF Flow Resistance (subplot 1), Exhaust Viscosity and CPF Average Temperature (subplot 2), Experimental and Corrected Experimental Exhaust Mass Flow Rate (subplot 3), Corrected and Experimental CPF Pressure Drop Profile (subplot 4)

In Figure H21, the most significant corrections are the Stage 1 loading CPF pressure drop and mass flow rate, the CF applied to the mass flow rate during the regeneration phases of the experiment, and the temperature stabilization periods of Stage 2 and Stage 4 loading and the loading ramp phase.

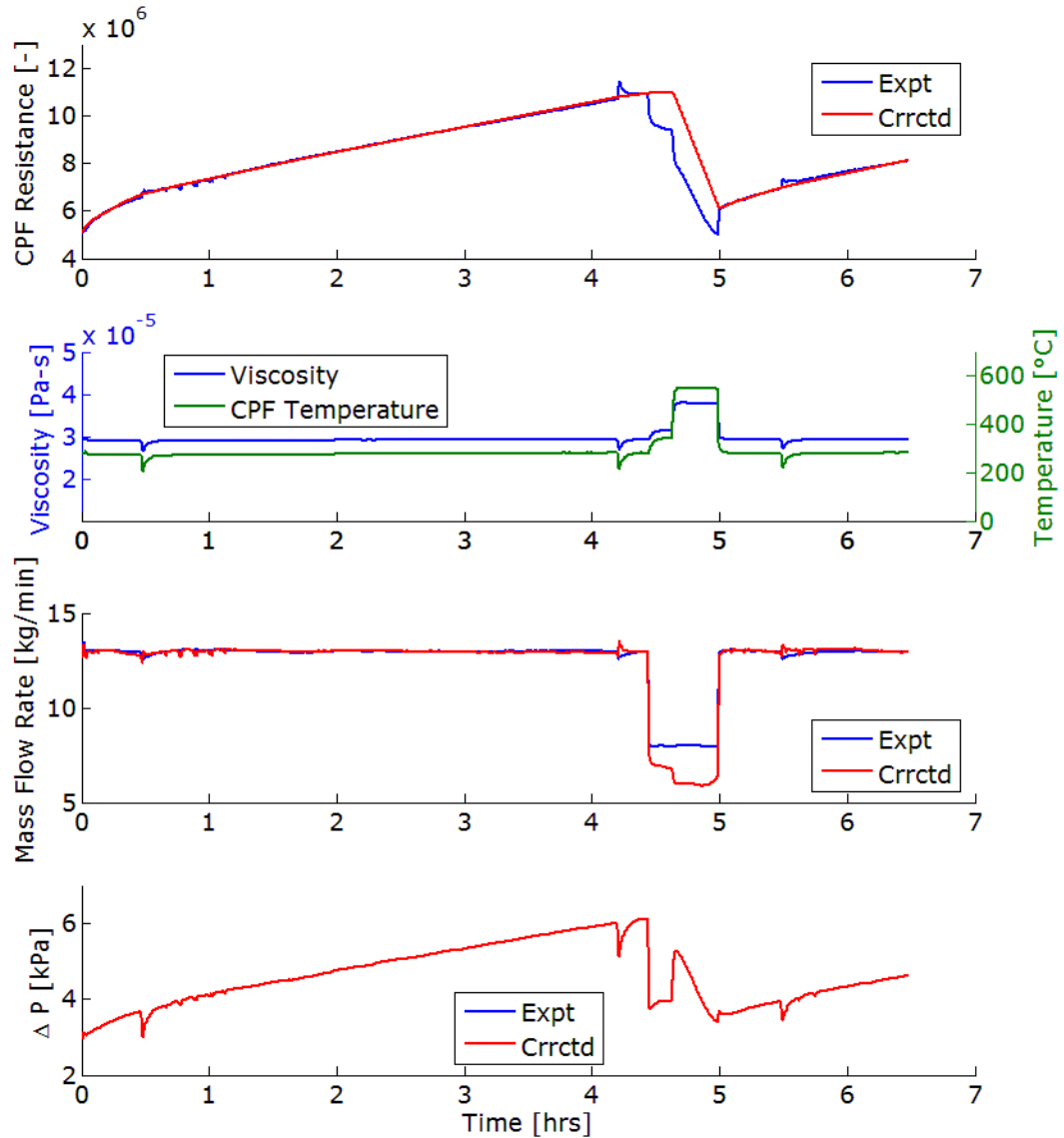


Figure H22: Run 12 (B10-3) Corrected and Experimental CPF Flow Resistance (subplot 1), Exhaust Viscosity and CPF Average Temperature (subplot 2), Experimental and Corrected Experimental Exhaust Mass Flow Rate (subplot 3), Corrected and Experimental CPF Pressure Drop Profile (subplot 4)

In Figure H22, the most significant corrections are the CF applied to the mass flow rate during the regeneration phases of the experiment, and the temperature stabilization periods of Stage 2 and Stage 4 loading and the loading ramp phase.

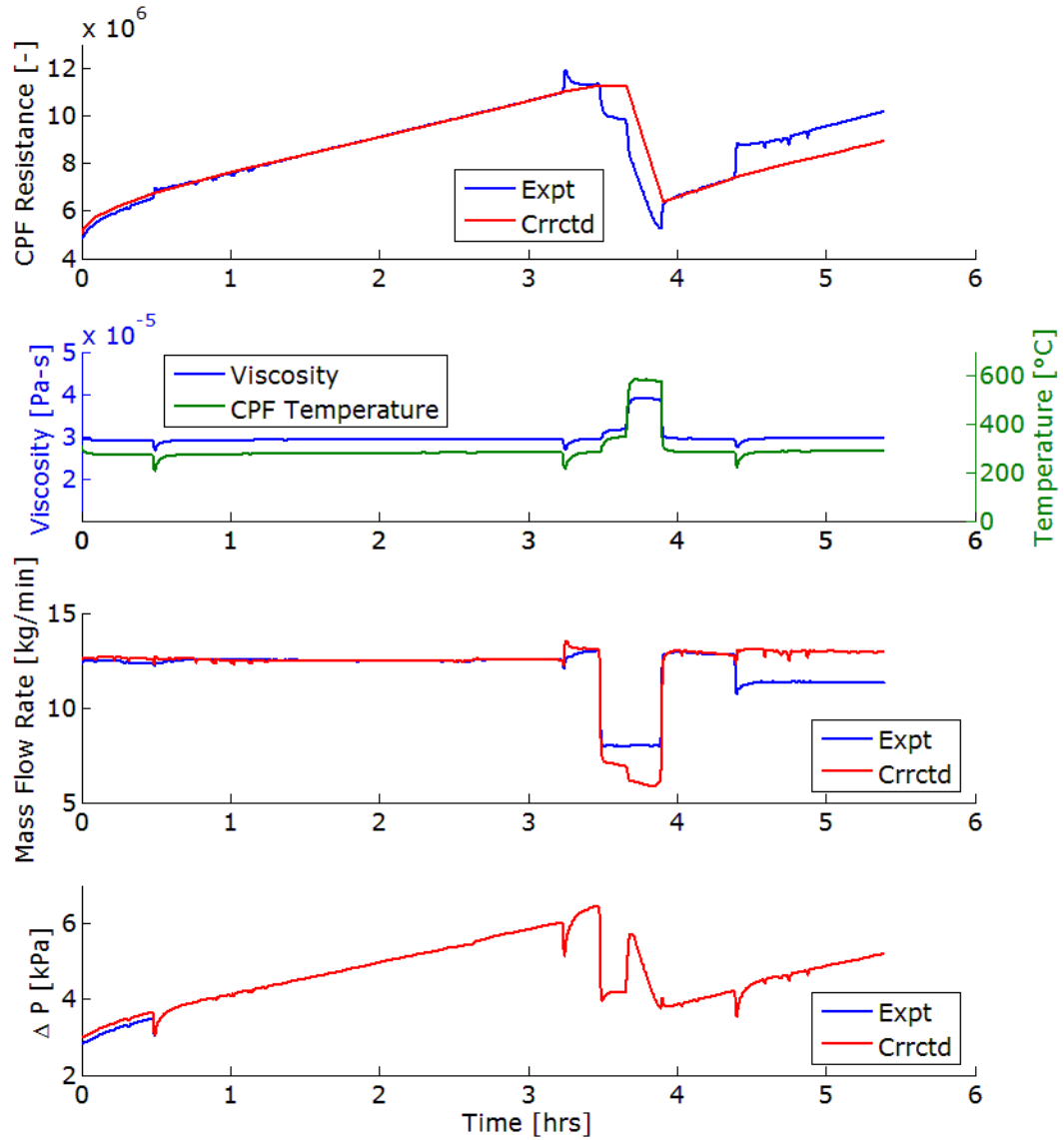


Figure H23: Run 13 (ULSD-1) Corrected and Experimental CPF Flow Resistance (subplot 1), Exhaust Viscosity and CPF Average Temperature (subplot 2), Experimental and Corrected Experimental Exhaust Mass Flow Rate (subplot 3), Corrected and Experimental CPF Pressure Drop Profile (subplot 4)

In Figure H23, the most significant corrections are the Stage 1 loading CPF pressure drop and mass flow rate, the CF applied to the mass flow rate during the regeneration phases of the experiment, and the temperature stabilization periods of Stage 2 and Stage 4 loading and the loading ramp phase.

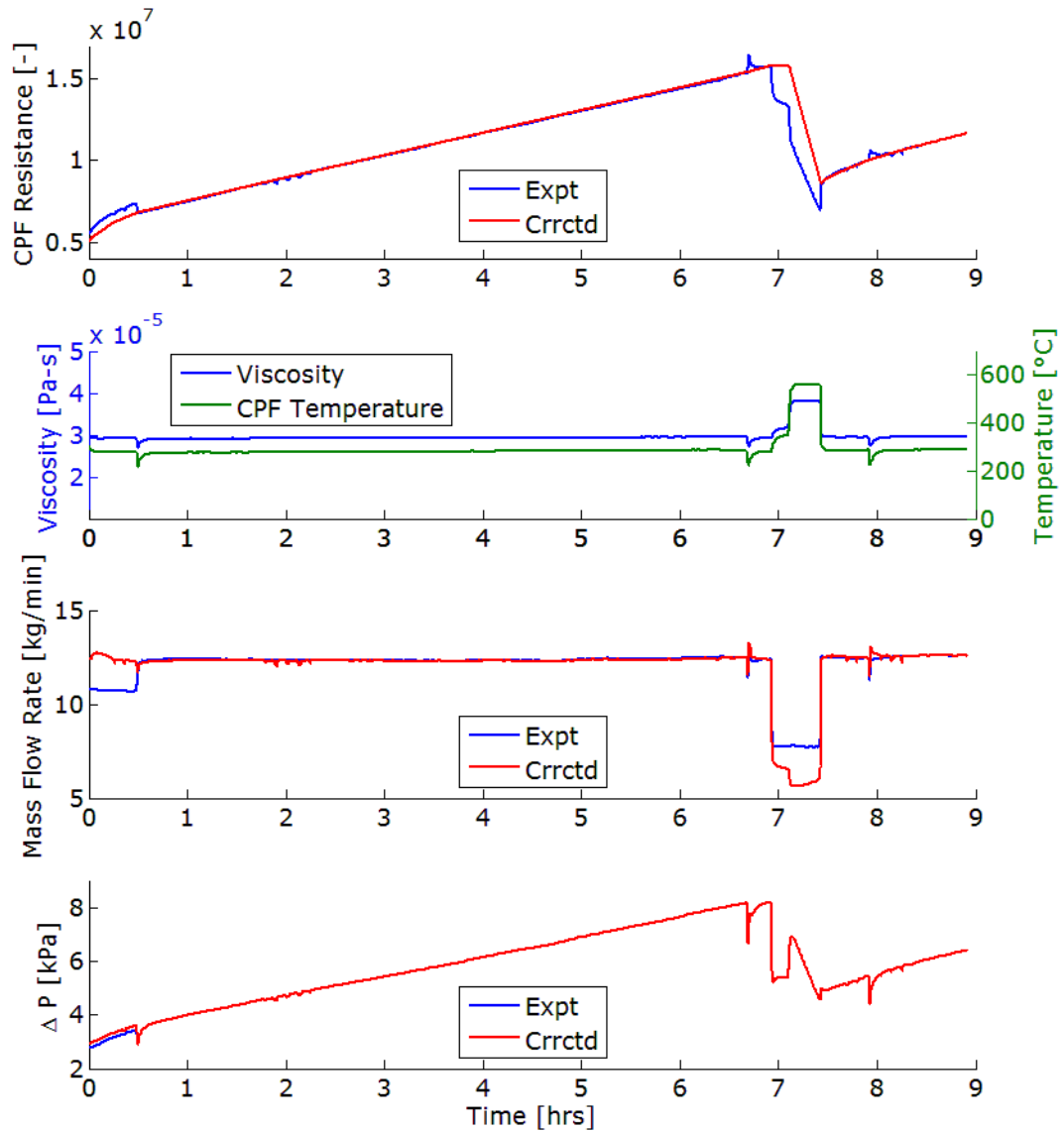


Figure H24: Run 14 (ULSD-8) Corrected and Experimental CPF Flow Resistance (subplot 1), Exhaust Viscosity and CPF Average Temperature (subplot 2), Experimental and Corrected Experimental Exhaust Mass Flow Rate (subplot 3), Corrected and Experimental CPF Pressure Drop Profile (subplot 4)

In Figure H24, the most significant corrections are the Stage 1 loading CPF pressure drop and mass flow rate, the CF applied to the mass flow rate during the regeneration phases of the experiment, and the temperature stabilization periods of Stage 2 and Stage 4 loading and the loading ramp phase.

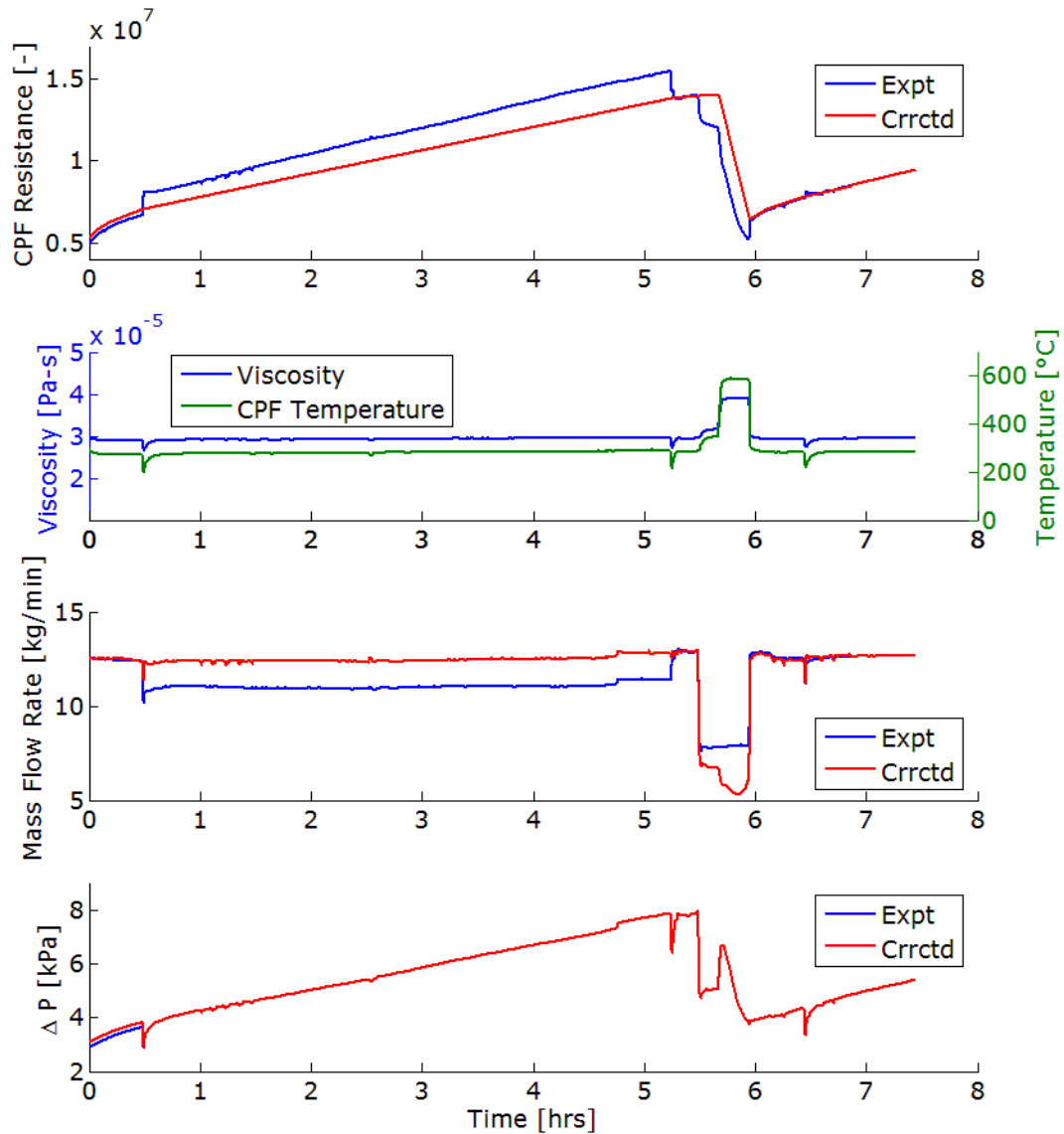


Figure H25: Run 15 (ULSD-9) Corrected and Experimental CPF Flow Resistance (subplot 1), Exhaust Viscosity and CPF Average Temperature (subplot 2), Experimental and Corrected Experimental Exhaust Mass Flow Rate (subplot 3), Corrected and Experimental CPF Pressure Drop Profile (subplot 4)

In Figure H25, the most significant corrections are the Stage 1 loading CPF pressure drop, the Stage 2 mass flow rate due to LFE error, the CF applied to the mass flow rate during the regeneration phases of the experiment, and the temperature stabilization periods of Stage 2 and Stage 4.

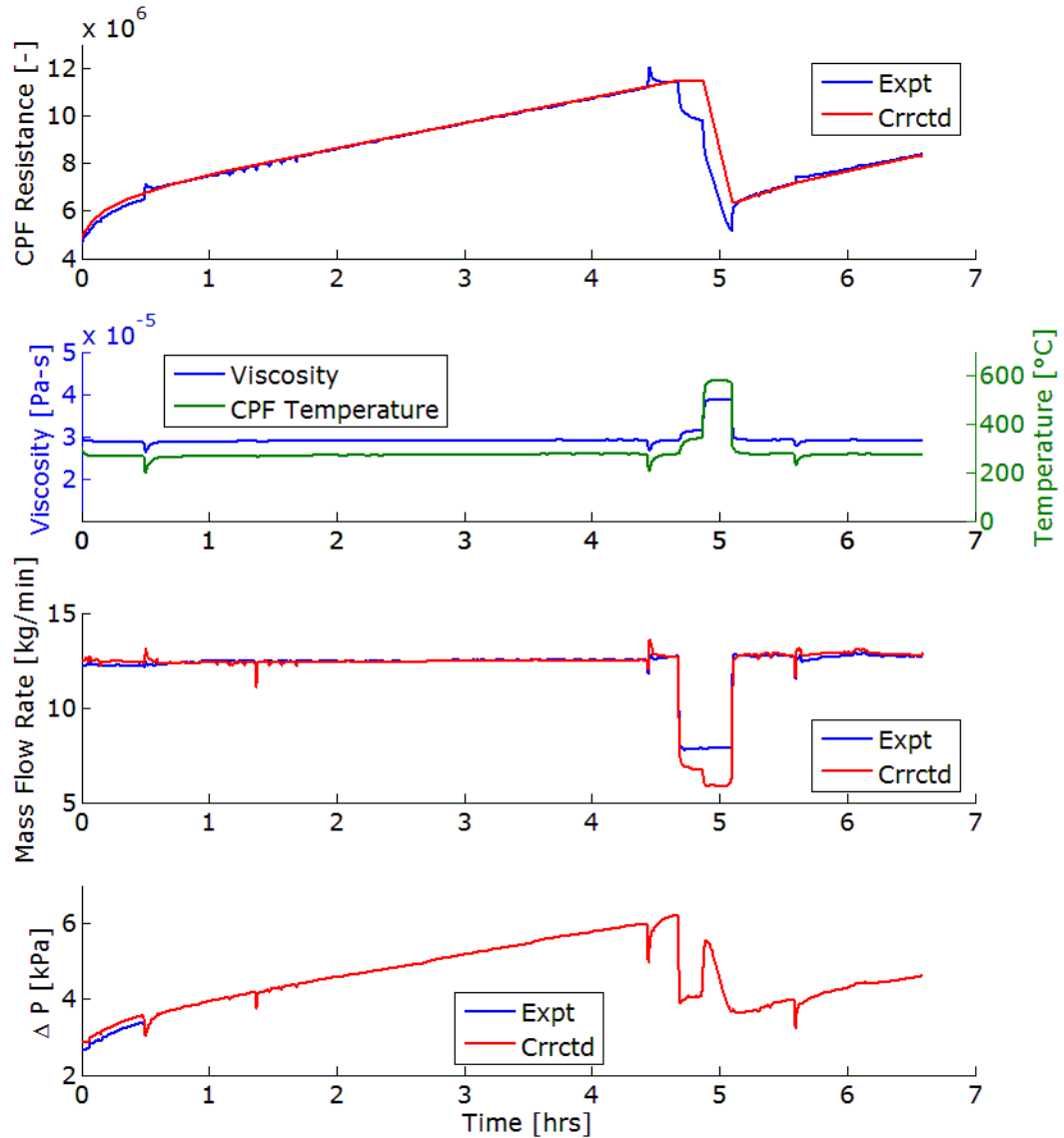


Figure H26: Run 16 (B10-4) Corrected and Experimental CPF Flow Resistance (subplot 1), Exhaust Viscosity and CPF Average Temperature (subplot 2), Experimental and Corrected Experimental Exhaust Mass Flow Rate (subplot 3), Corrected and Experimental CPF Pressure Drop Profile (subplot 4)

In Figure H26, the most significant corrections are the Stage 1 loading CPF pressure drop and mass flow rate, the CF applied to the mass flow rate during the regeneration phases of the experiment, and the temperature stabilization periods of Stage 2 and Stage 4 loading and the loading ramp phase.

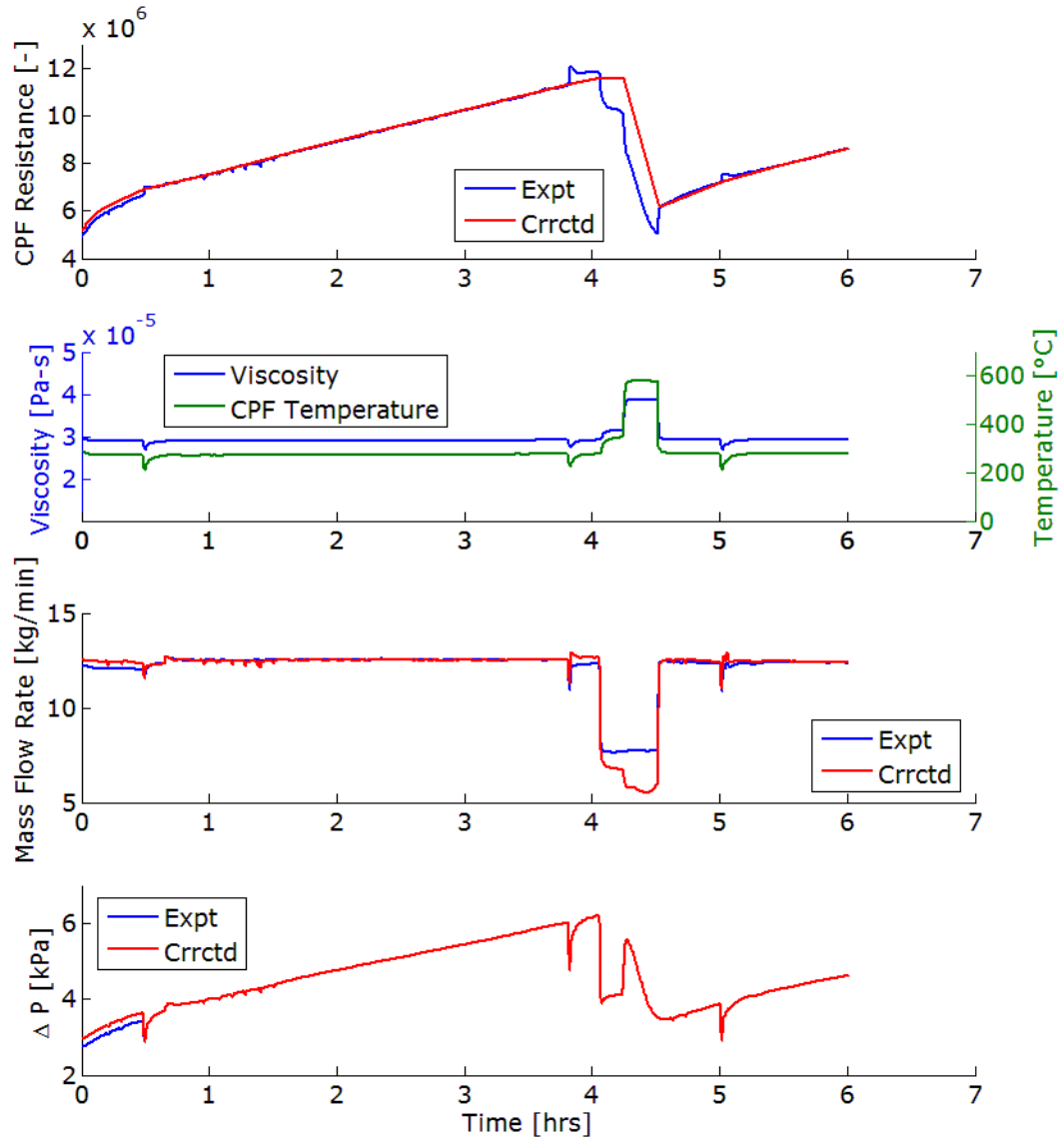


Figure H27: Run 17 (ULSD-7R) Corrected and Experimental CPF Flow Resistance (subplot 1), Exhaust Viscosity and CPF Average Temperature (subplot 2), Exp. and Crrctd. Exp. Exhaust Mass Flow Rate (subplot 3), Corrected and Experimental CPF Pressure Drop Profile (subplot 4)

In Figure H27, the most significant corrections are the Stage 1 loading CPF pressure drop and mass flow rate, the loading ramp mass flow rate due to LFE error, the CF applied to the mass flow rate during the regeneration phases of the experiment, and the temperature stabilization periods of Stage 2 and Stage 4 loading and the loading ramp phase.

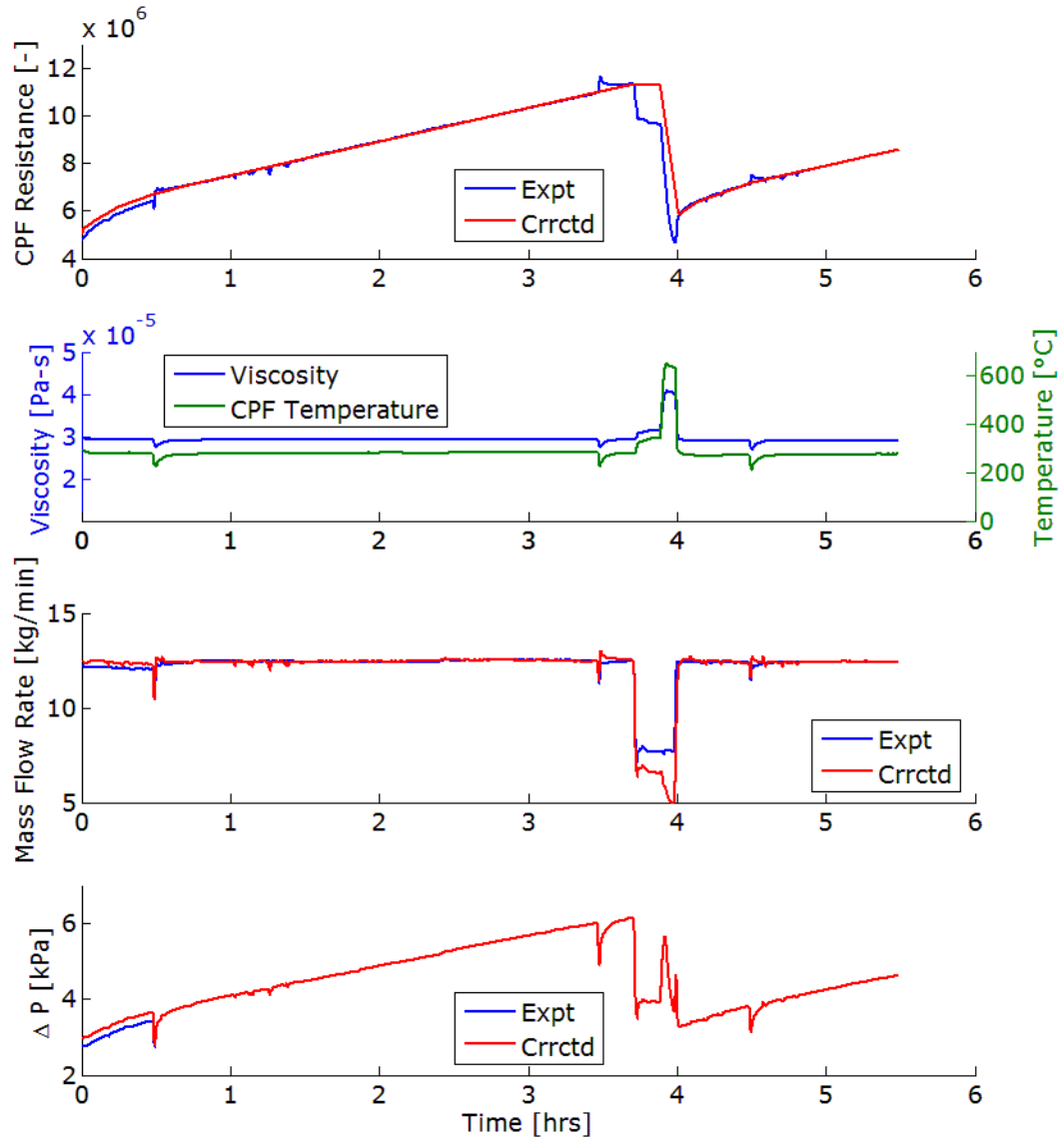


Figure H28: Run 18 (ULSD-2R) Corrected and Experimental CPF Flow Resistance (subplot 1), Exhaust Viscosity and CPF Average Temperature (subplot 2), Experimental and Corrected Experimental Exhaust Mass Flow Rate (subplot 3), Corrected and Experimental CPF Pressure Drop Profile (subplot 4)

In Figure H28, the most significant corrections are the Stage 1 loading CPF pressure drop and mass flow rate, the CF applied to the mass flow rate during the regeneration phases of the experiment, and the temperature stabilization periods of Stage 2 and Stage 4 loading and the loading ramp phase.

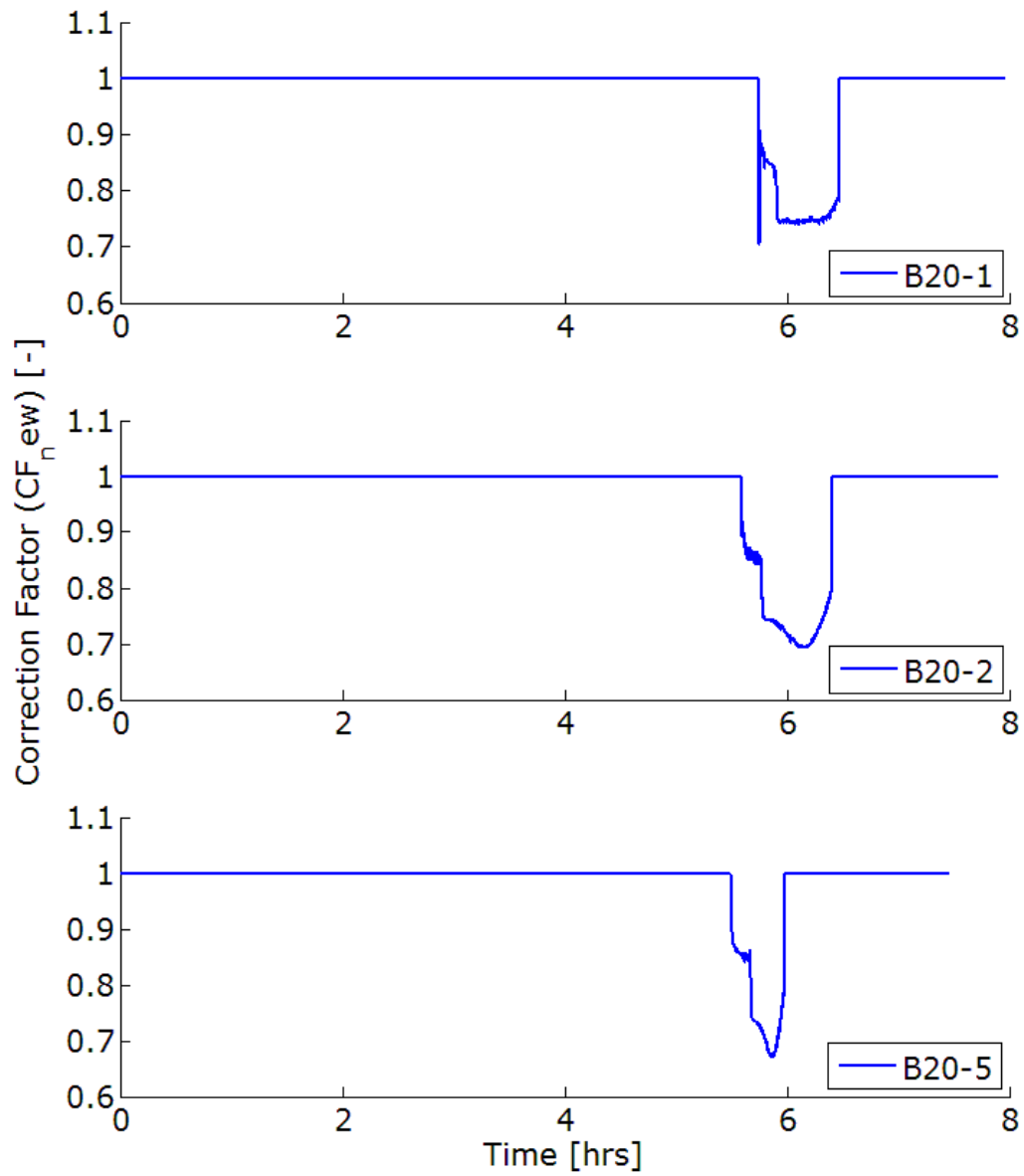


Figure H29: CF for B20-1, B20-2, B20-5

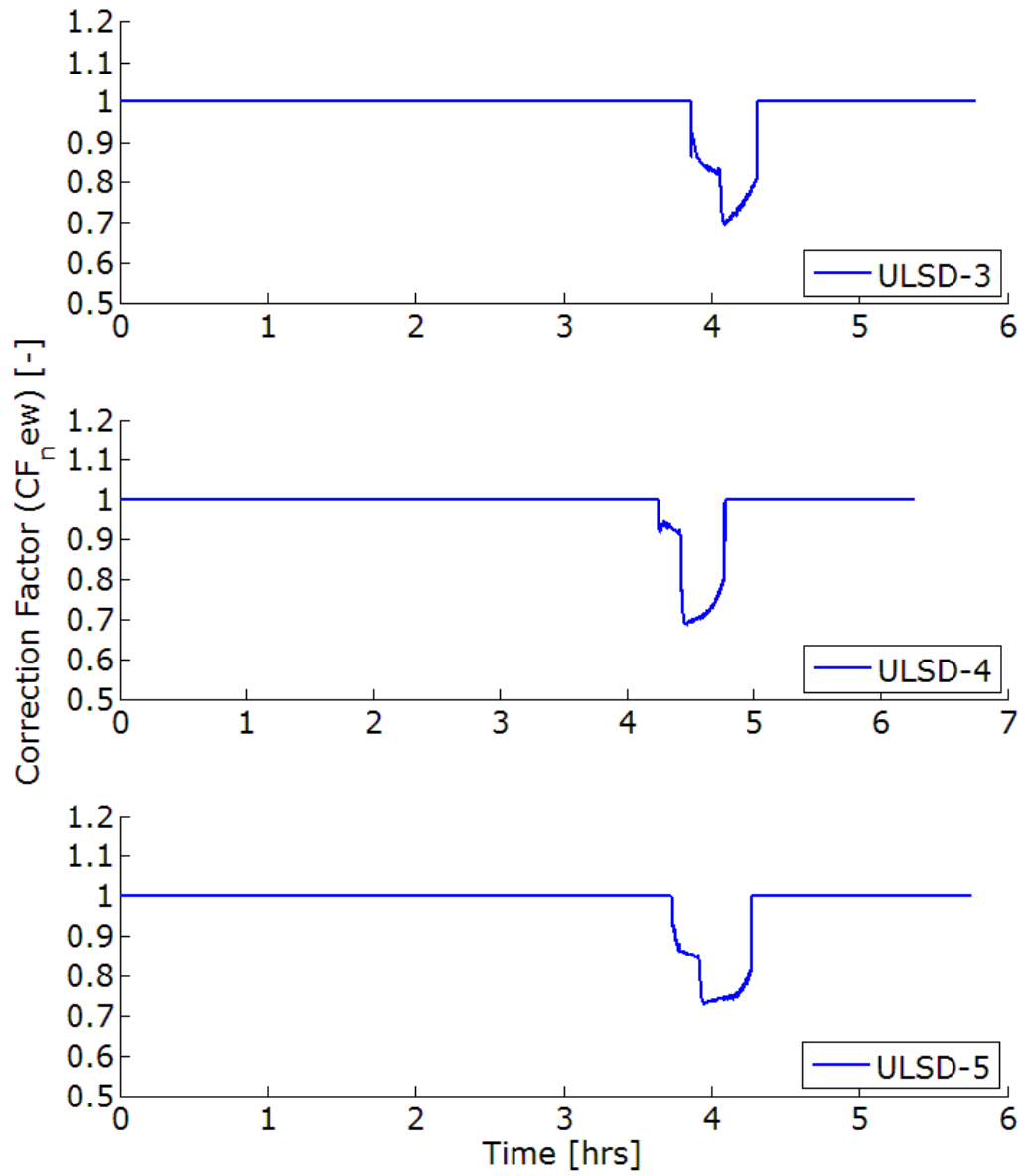


Figure H30: CF for ULSD-3, ULSD-4, ULSD-5

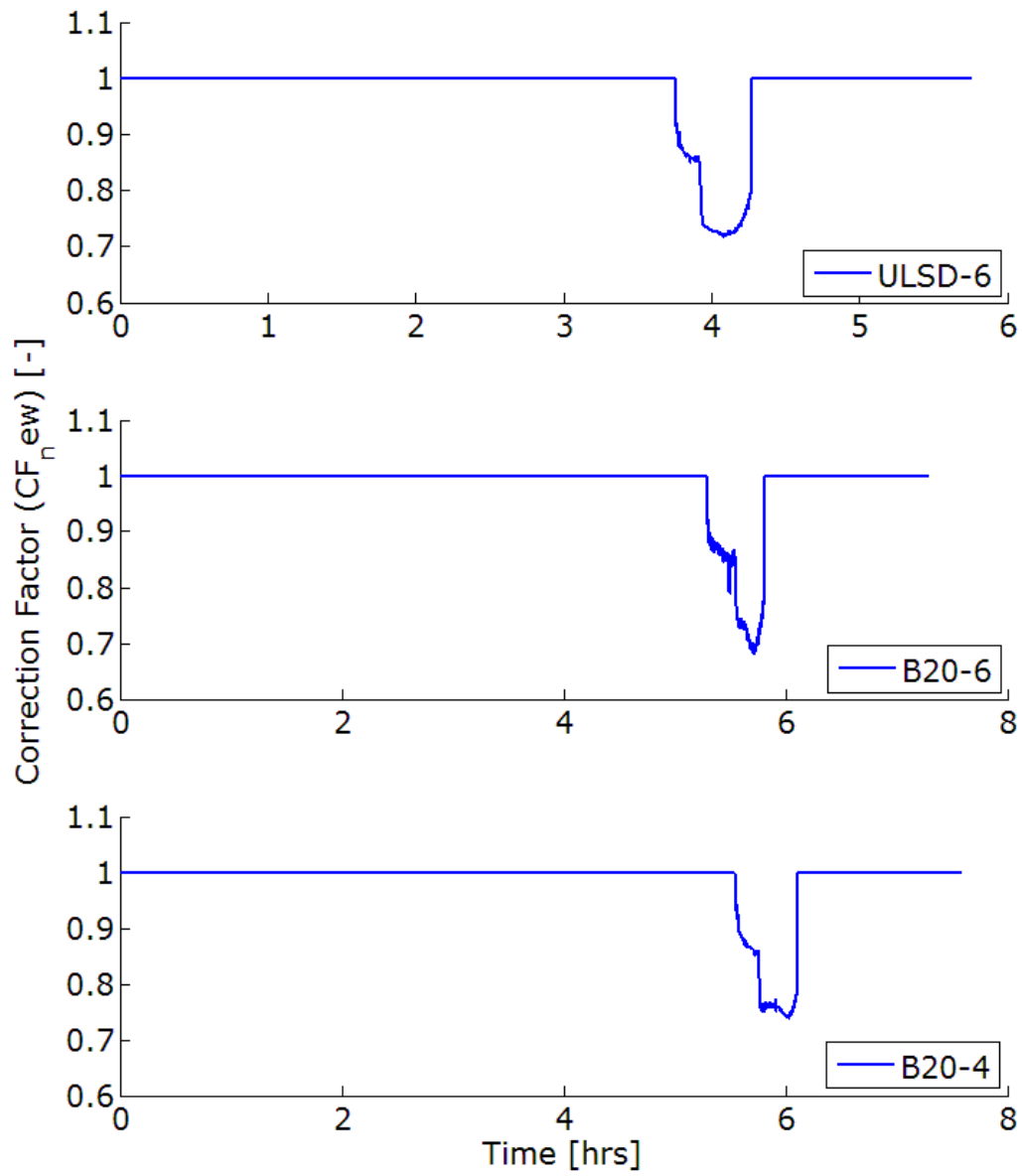


Figure H31: CF for ULSD-6, B20-6, B20-4

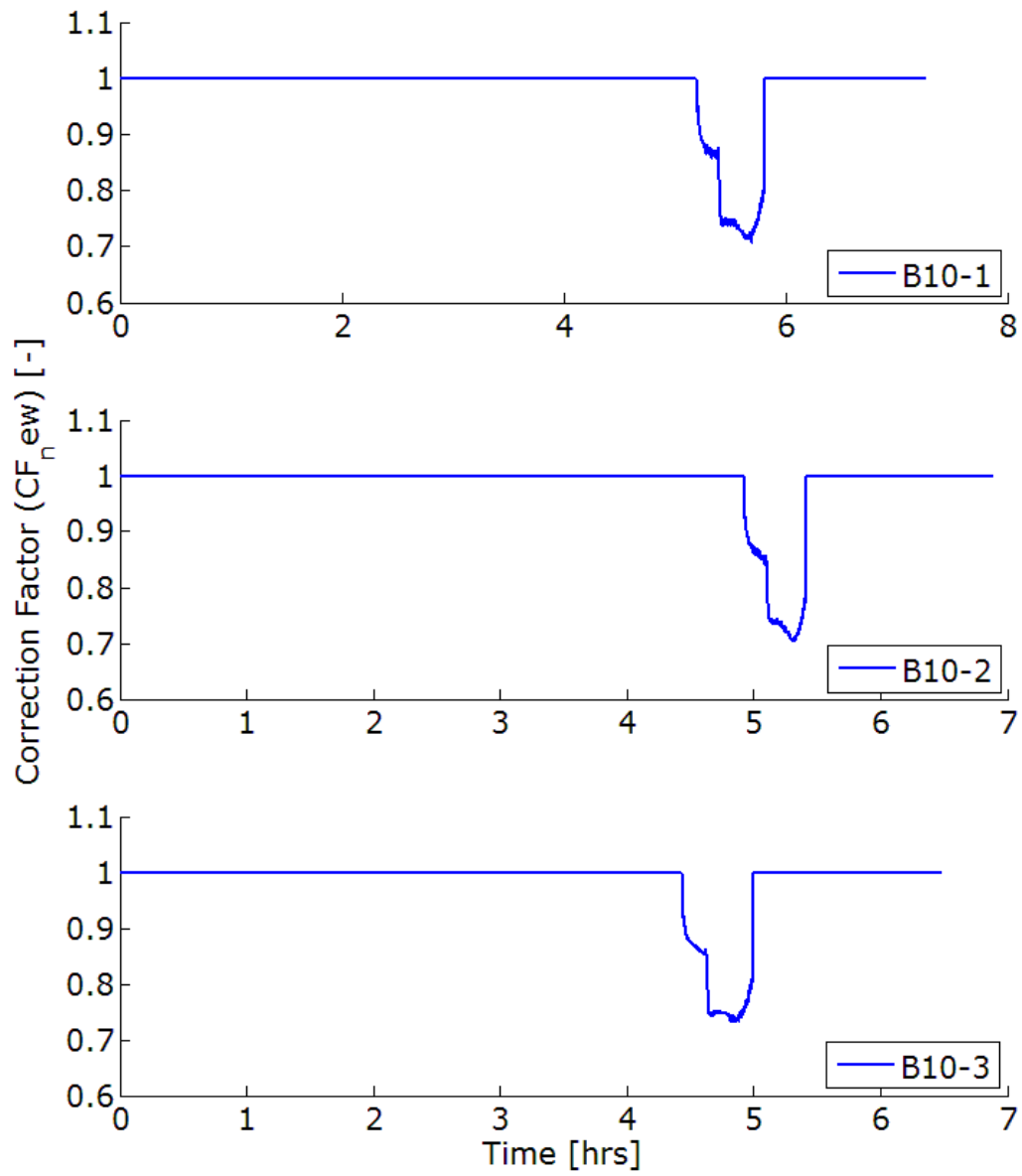


Figure H32: CF for B10-1, B10-2, B10-3

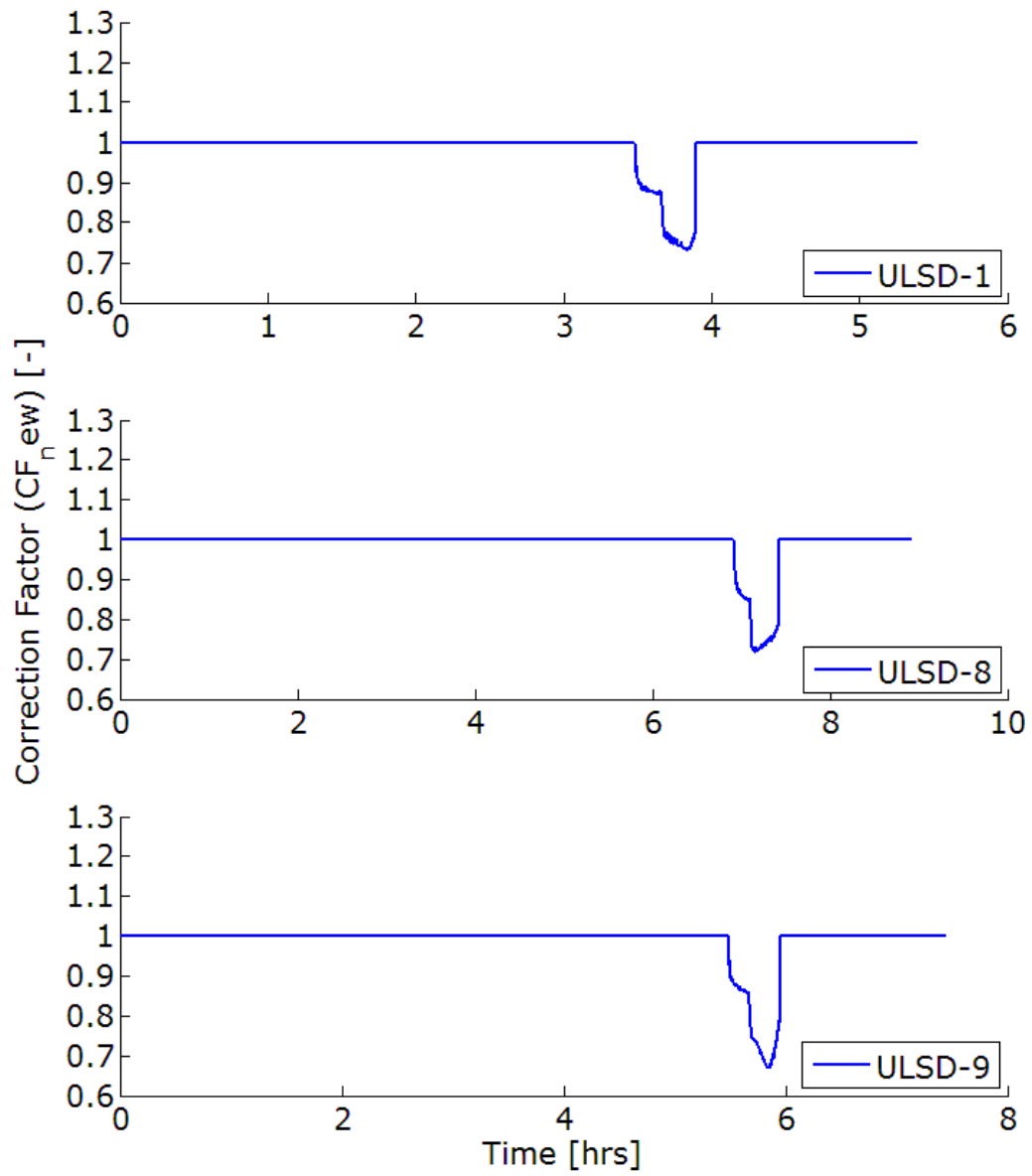


Figure H33: CF for ULSD-1, ULSD-8, ULSD-9

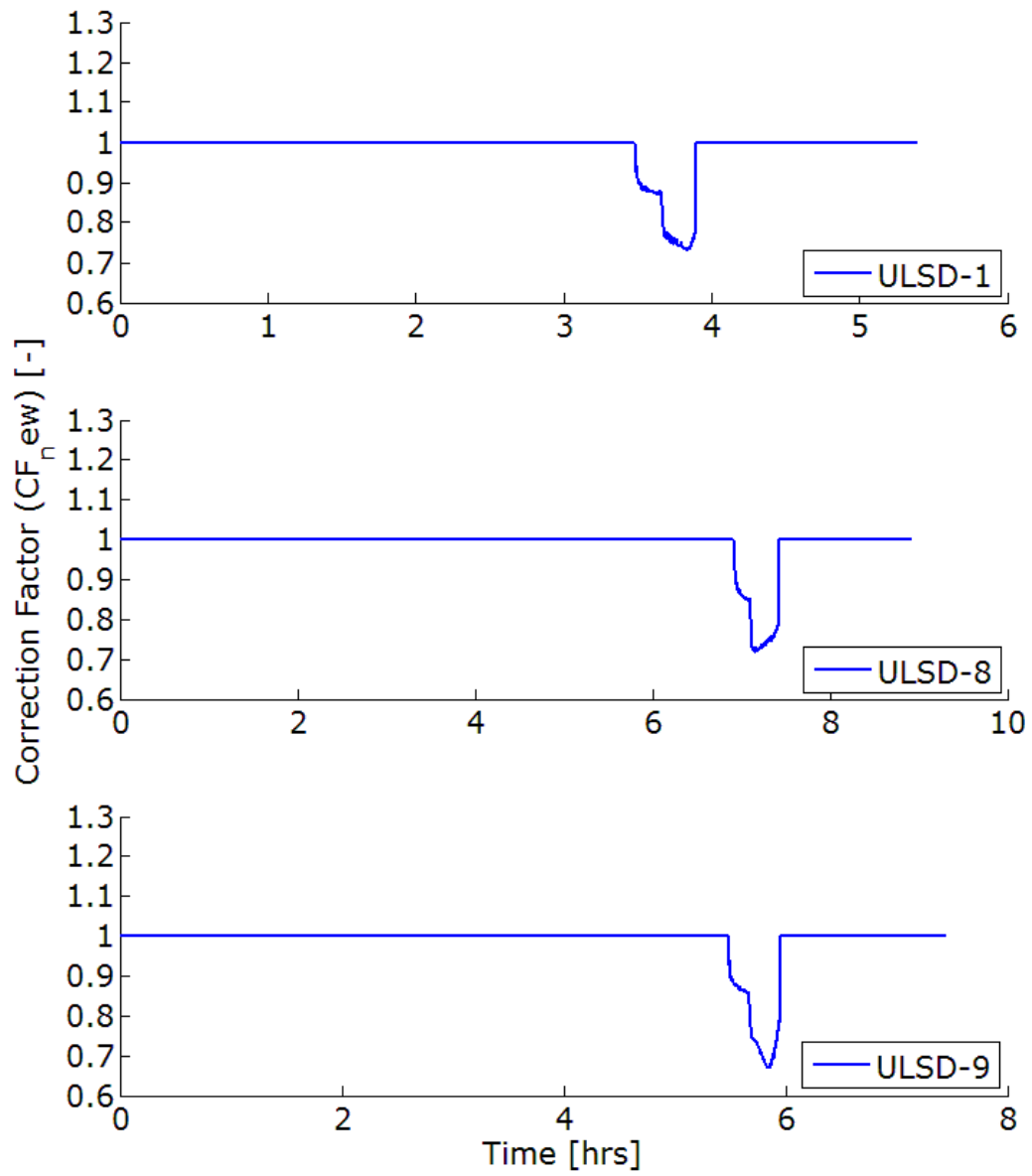


Figure H34: CF for B10-4, ULSD-7R, ULSD-2R

Appendix I Stage 2 Loading

Following the CPF cleanout and subsequent CPF weighing following the Stage 1 loading phase, Stage 2 loading is carried out until the desired amount of PM has been deposited within the CPF. As described in Chapter 3, loading was performed on the ISL 365 at 2100 RPM and 195 Nm and 2090 RPM and 255 Nm on the ISL 425. Throughout Stage 2 loading, gaseous emissions, engine and CPF out PM concentrations, and PSD are measured along with the logging of temperature and pressure drop across the aftertreatment system components.

Gaseous Emissions

Average engine out gaseous emissions during Stage 2 loading are shown in Figure I1. The concentrations were averaged over all ISL 365 runs with the same test fuel type and the error bars shown correspond with ± 1 standard deviation of the average values. As stated in Chapter 3, all gaseous concentrations reported in this study are wet concentrations as measured by the emissions bench.

The engine-out HC concentrations were lower with increasing biodiesel concentrations, but overlapping error bars indicate that the differences between them may be insignificant. Average HC concentrations for ULSD, B10, and B20 were 98, 84, and 70 ppmC, respectively. As previously described, NO_x values have been shown to increase or decrease depending on the fuel type and test conditions. In the case of this study, average engine-out NO_x concentrations were shown to decrease with increasing test fuel biodiesel content, however, overlapping error bars indicate that the differences between them may be negligible, as with the HC concentrations. Austin [1] discusses this in further detail where it was shown that the variation in NO_x concentrations between tests with one test fuel was greater than the variation in concentrations between test utilizing various ULSD and biodiesel blended fuels.

The NO concentrations also followed the trend with respect to variations in the NO_x concentrations, while the NO₂ concentrations were increasing with increased test fuel biodiesel content. The engine-out CO, CO₂, and O₂ concentration differences with respect to the test fuel were negligible. Detailed emissions summaries for Stage 2 and Stage 4 loading as well as active regeneration test phases are available in Appendix M.

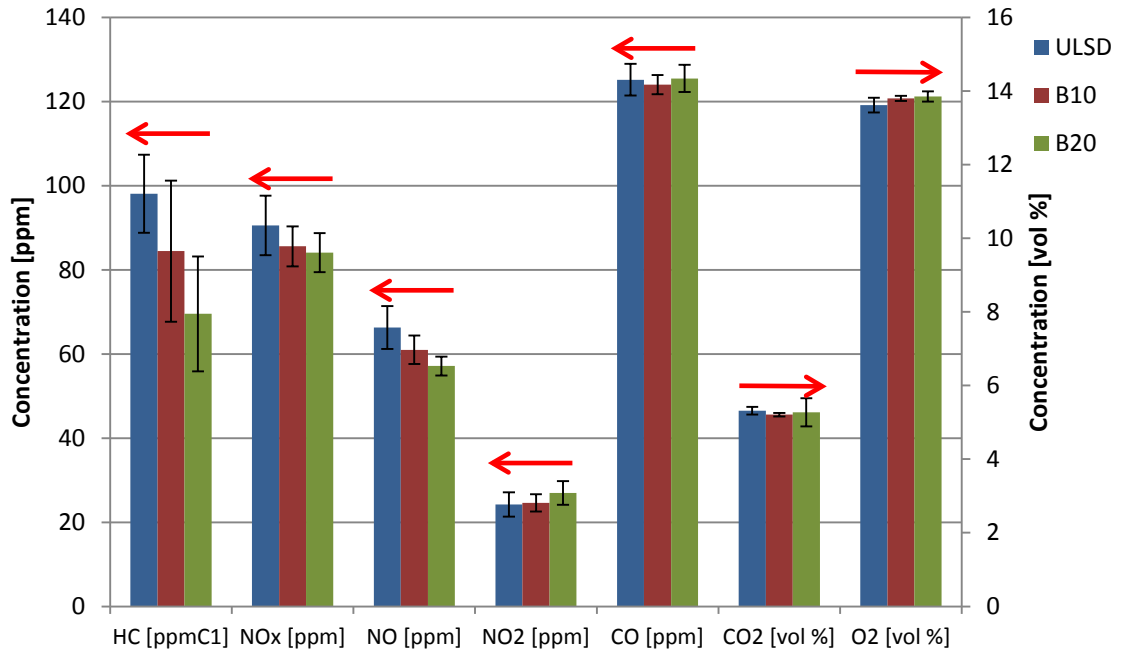


Figure I1: Average Engine-out Gaseous Emissions during Stage 2 Loading for Each Test Fuel

PSD Data

Particle size distribution (PSD) data were collected during active regeneration tests performed, when the SMPS system was operational. The PSD samples were taken from each sampling location (UDOC, DDOC, and DCPF) throughout each phase of testing, with the exception of active regeneration phases. During active regeneration, PSD samples cannot be taken UDOC due to the excess hydrocarbons in the exhaust stream. Therefore, only DDOC and DCPF PSD samples were collected during active regeneration phases. It is believed that a cracked fitting on the SMPS system occurred near the time that test B10-2 was performed, corresponding to run 11 of 19, and as such, only the data collected to this point will be presented.

The data sets obtained with the same test fuel were averaged and the resulting trend for all three test fuels is shown in Figure I2, where the engine-out (UDOC) and CPF-out (DCPF) data are both shown. The data sets at a higher vertical location represent the UDOC samples while the data sets at the lower vertical location represent the DCPF samples. The vertical axis corresponds to the particle number concentration

normalized by bin size within the SMPS system. The peak particle count, for both UDOC and DCPF cases, was shown to be with ULSD, followed by B10 and B20, which were the same trends shown by Austin [1]. Austin [1] reported that as the percent biodiesel in the test fuel increases, the particle count decreases, which is also shown in Figure I2.

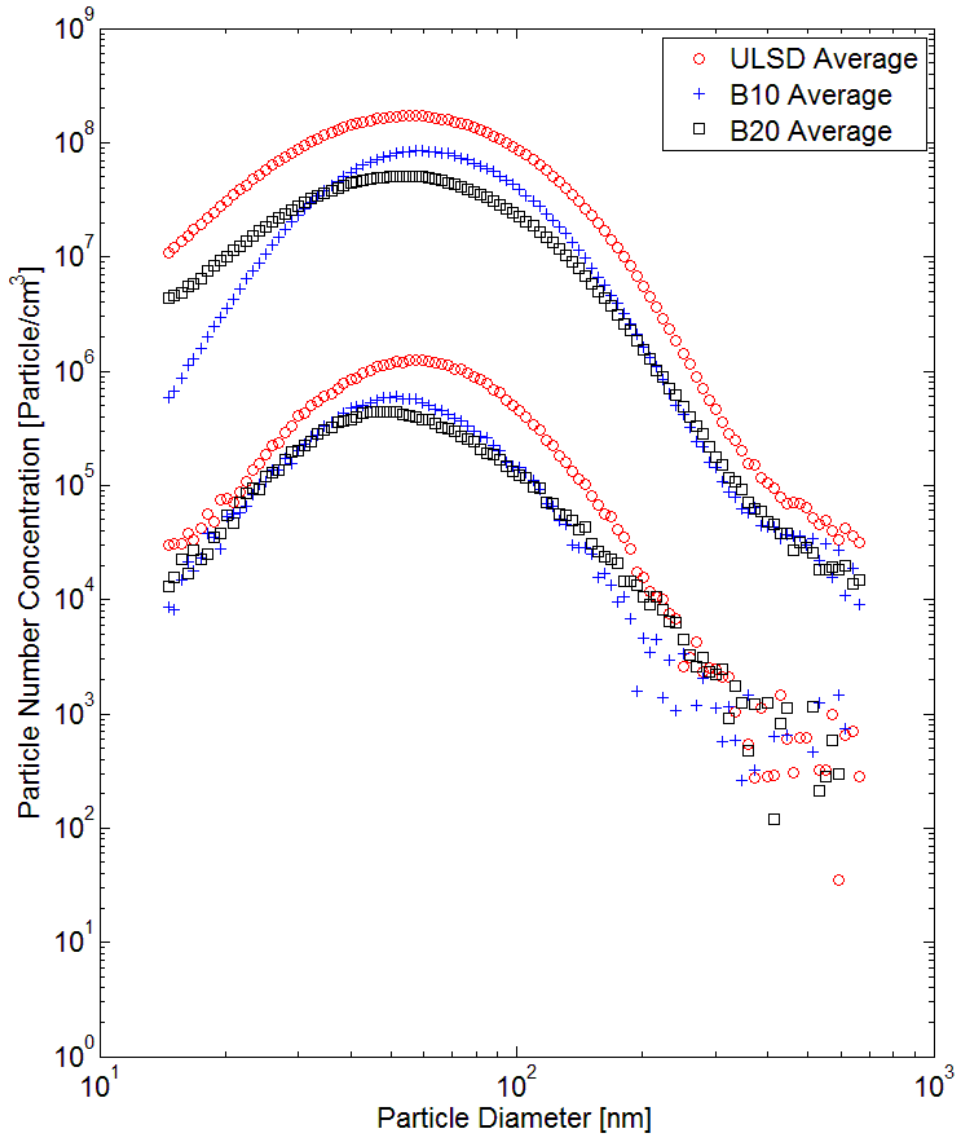


Figure I2: Stage 2 Loading Engine-Out and CPF-out Particle Size Distribution Weighed by Number for ULSD, B10, and B20.

PM Concentration Data

Particulate matter (PM) hot samples were collected at various times throughout each test to determine the exhaust PM concentration. The measured PM concentrations for ULSD, B10, and B20 were between 21.2 and 29.4 mg/scm, 15.7 and 19.0 mg/scm, and 12.7 to 21.6 mg/scm, respectively. Variation between test fuels and between tests with the same fuel was observed and can be seen in Figure I3, where the results are plotted vs. test number to show the trends throughout the testing period. In Figure I3, the PM concentrations measured throughout Stage 2 loading were averaged and the error bars correspond with standard deviations of the samples used to calculate that average. The error bars appear to be hidden for some of the data shown in Figure I3, meaning that the standard deviation between the samples was small and therefore, the samples taken during that test were very consistent. For a small number of tests, not all PM samples were used to calculate the average PM concentration during each test, because damage to the filter can occur during handling resulting with inaccurate filter mass measurements, and subsequently, inaccurate PM concentration data. The tests with large error bars, i.e., Tests 2 and 13 indicate that a PM sample could have been damaged and the associated PM sample was removed from calculation of the average engine-out PM concentration.

In general, it can be seen that the measured engine-out PM concentration was lower with increasing percent biodiesel in the test fuel, which was expected following the work reported in references [1, 6, and 11] because the same trends were shown. Test 9 is one anomaly in the data where the PM concentration measured was significantly higher than Test 8. The specific reason for this is unknown, but it is suspected that the changes in the test cell ambient air temperature and humidity were a factor.

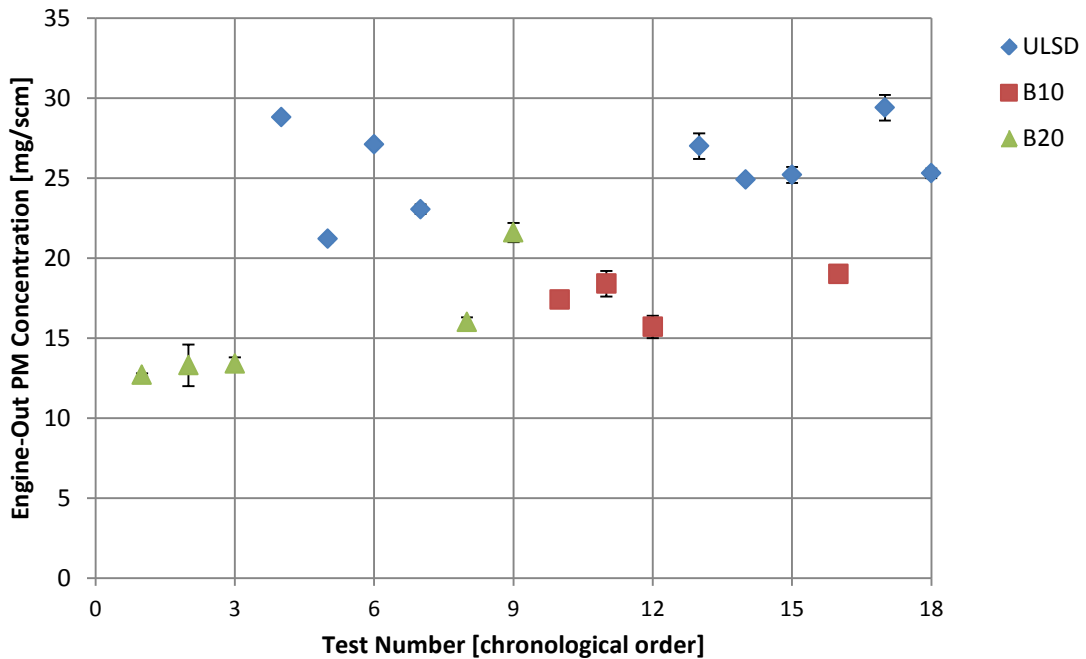


Figure I3: Stage 2 Loading Average Engine-Out PM Concentrations in Chronological Order

The increase in PM concentrations over time, with the same test fuel, suggests that the PM concentration increases with increasing temperature and humidity in the test cell, because testing initiated during the winter with test B20-1. Additional analysis on this phenomenon was carried out and explained in detail by Austin [1].

CPF Pressure Drop Profile

Figure I4 presents the CPF pressure drop vs. the CPF PM loading at the conclusion of Stage 2 loading. It can be seen that a CPF pressure drop of 6 kPa corresponds to 2.2 to 2.5 g/L CPF PM loading. The two tests between 4 and 5 g/L CPF PM loading were the two test cases in which a target CPF PM loading of 4.1 g/L was utilized. One B20 test (circled in blue) shows a CPF pressure drop below the 5.5 kPa threshold that also corresponds to a CPF loading between 2.2 and 2.3 g/L. This is believed to have been caused by a leaking bypass line valve. The valve is intended to seal the bypass line off from any flow while running in the trap line. If this valve sticks, exhaust is able to flow into the bypass line, reducing the total amount of exhaust reaching the aftertreatment system, where a decreased pressure drop is measured.

The ULSD test in the same pressure drop regime (circled in red) is the single test ran on the ISL 425, where a lower CPF pressure drop correlates to the same PM loading as with the ISL 365, which is also reported in Shiel [11].

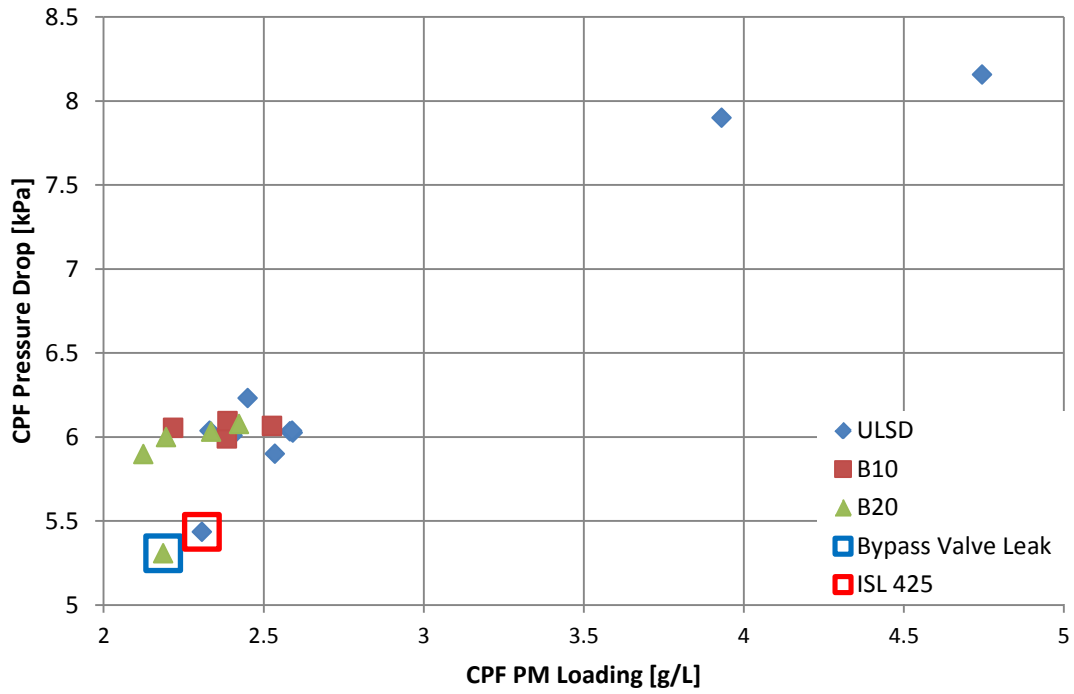


Figure I4: CPF Pressure Drop vs. CPF PM Loading at the Conclusion Stage 2 Loading

Appendix J Stage 4 Loading

Following the CPF weighing at the conclusion of active regeneration, Stage 4 loading is carried out for sixty minutes. As described in Chapter 3, loading was performed on the ISL 365 at 2100 RPM and 195 Nm and 2090 RPM and 255 Nm on the ISL 425. The purpose of Stage 4 loading is to observe changes in the CPF performance related to gaseous emissions and CPF pressure drop after a partial regeneration as opposed to a full regeneration, such as at the beginning of each experiment. Throughout Stage 4 loading, gaseous emissions, engine and CPF out PM concentrations and PSD are measured along with the constant monitoring of temperature and pressure drop across the aftertreatment system components.

Gaseous Emissions

The engine-out gaseous emissions are graphically represented in Figure J1. The average engine-out gaseous emissions are presented with error bars representing the standard deviation resulting from calculating those average values.

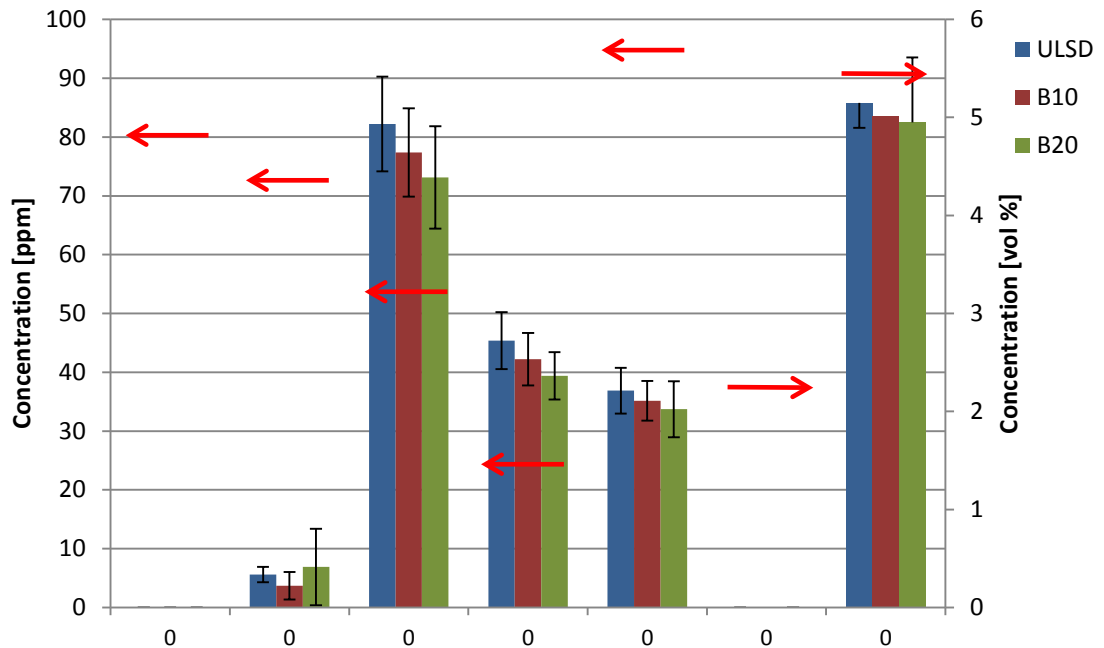


Figure J1: Average Engine-out Gaseous Emissions during Stage 4 Loading for Each Test Fuel

Since Stage 4 loading takes place at the same operating conditions as Stage 2 loading, there are no significant changes in fuel use, gaseous emissions, or PM concentrations between the two. The only significant differences between the gaseous emissions during loading prior to and after active regeneration were seen in the hydrocarbon concentrations measured by the emissions bench. For all tests, the hydrocarbon measurement range had to be increased prior to active regeneration in order to capture the elevated hydrocarbon concentrations DDOC during active regeneration. For some tests, the range was adjusted back to its low level after active regeneration, but for other tests, it was not because this part of the test had not been incorporated into the standard testing procedure, and had been forgotten. Since the high range can read up to 4200 ppmC of hydrocarbons compared to the low range which can only read up to 150 ppmC, the hydrocarbon measurements for the tests where the low range was not used during Stage 4 loading could have been elevated due to such a small fraction of the bench's range being used for actual hydrocarbon measurements. Another factor which could have led to these elevated readings could be attributed to the length of measurement time between Stage 2 and Stage 4 loading. During Stage 2 loading, hydrocarbons are measured in each location (UDOC, DDOC, or DCPF) for an entire hour, where each location is sampled for 20 minutes during Stage 4 loading, which gave the emissions bench more time for the hydrocarbon measurements to stabilize at the low concentrations.

PSD Data

The PSD data collected during Stage 4 loading follows the same trend as Stage 2 loading, as expected, and is shown in Figure J1. The particle count is highest with ULSD, followed by B10 and B20 in both sample locations (UDOC and DCPF) which was expected based on the results reported by Austin [1].

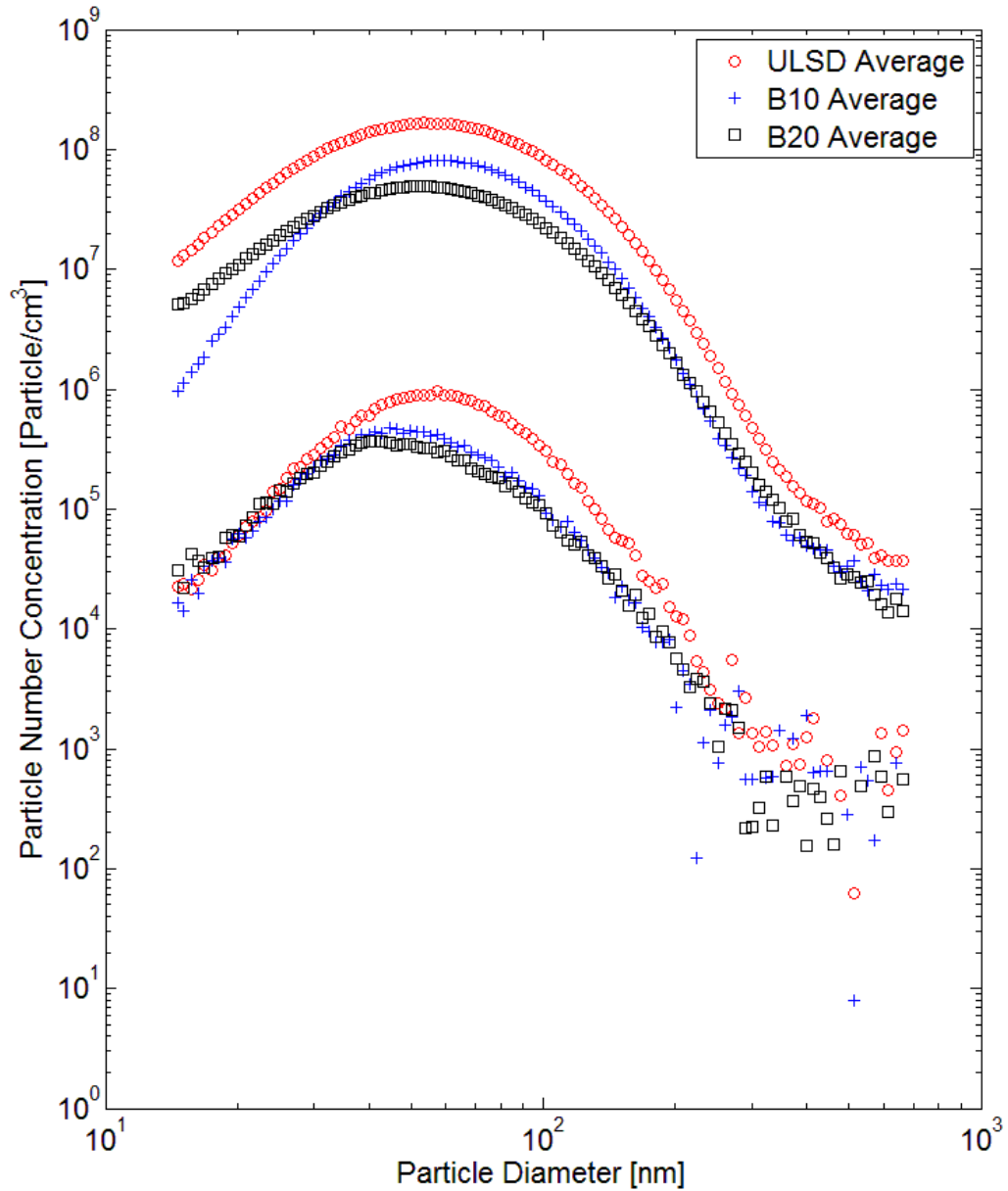


Figure J2: Particle Size Distribution by Particle Numbers Averaged by Fuel Type during Stage 4 Loading sampled DDOC and DCPF

CPF Pressure Drop Profile

One area where visible differences between Stage 2 and Stage 4 loading can be observed is in the pressure drop across the CPF. Figure J3 below displays the

pressure drop and associated CPF PM load for all 2.2 g/L targeted ISL 365 tests, from the beginning and end of Stage 2 and Stage 4 loading phases. The data are categorized by fuel and estimated trend-lines are added to the Stage 2 and Stage 4 data sets.

It can be seen in Figure J3 that the pressure drop between Stage 2 and Stage 4 loading do not match for a given CPF PM loading. For example, following the B20 trend lines, for a given CPF PM load of 20 grams, the pressure drop during Stage 4 loading was about 0.5 kPa lower than during Stage 2 loading.

As the CPF is regenerated, the PM that is in the channel walls is oxidized during active regeneration. A cake layer could still remain present after a partial regeneration, resulting in the PM entering the CPF following regeneration to not reach the wall itself. This occurs because the filtration efficiency of the cake layer is 94% or greater, preventing the PM from reaching the wall of the CPF channels. This results in the wall's porosity being increased from when the wall is loaded with PM, reducing the pressure drop across the CPF [1]. This leads to an increased level of difficulty when relating the total pressure drop of the CPF to the PM mass inside it.

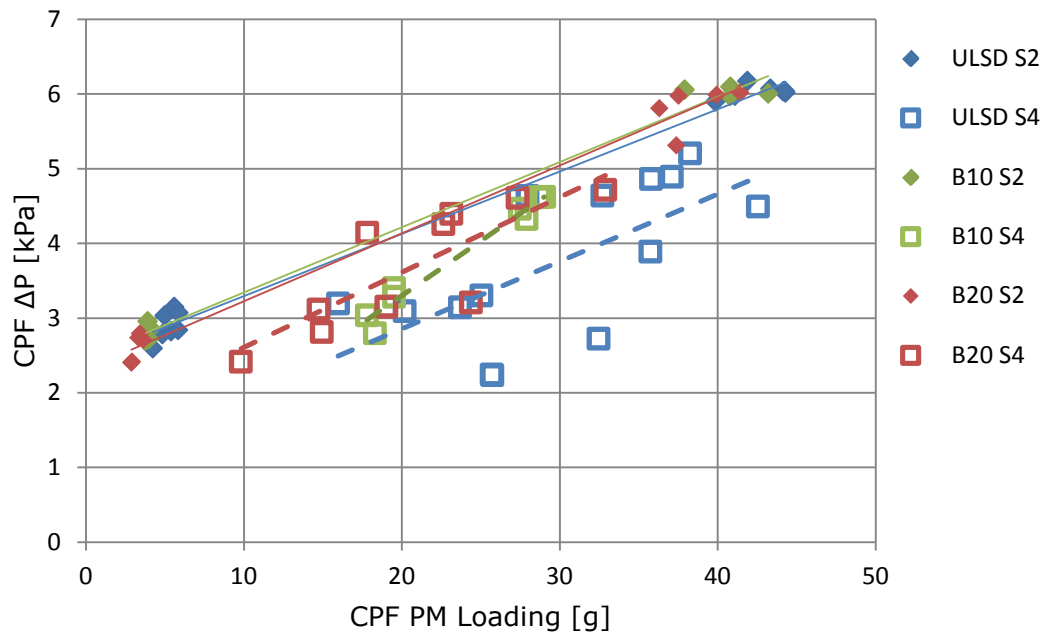


Figure J3: CPF Pressure Drop at the Start and Stop of Stage 2 and Stage 4 Loading for all tests.

One trend in Figure J3 that was noted in Austin [1] is that there is less separation between Stage 2 and Stage 4 loading data sets at lower levels of CPF PM loading. This is possibly due to decreased cake PM layer thickness after active regeneration which possibly could let more PM into the wall. This conclusion is reinforced by the fact that the Stage 2 loading pressure drop vs. CPF PM loading trend lines are nearly identical for all tests.

Loading Reaction Rate

In order to compare the loading characteristics of the CPF between Stage 2 and Stage 4 loading, the reaction rate for each phase was calculated based on the CPF PM mass retained at the beginning and end of each phase. Eqn. J1 is used to calculate the reaction rate.

$$m_{\text{stop}} = \frac{Q_{\text{exh}} \cdot C_{\text{in}} \cdot \eta_f}{RR_o \cdot 1000} [1 - e^{(-RR_o \cdot t_{\text{eff}})}] + m_{\text{start}} \cdot e^{(-RR_o \cdot t_{\text{eff}})} \quad \text{Eqn. J1}$$

RR_o = PM reaction rate [1/sec]

η_f = CPF filtration efficiency [fractional]

C_{in} = Engine-out PM concentration [mg/scm]

Q_{exh} = Exhaust standard volumetric flow rate [scm/sec]

t_{eff} = Time of the phase for which RR_o is being calculated [sec]

m_{stop} = PM mass retained in the CPF at phase end [g]

m_{start} = PM mass retained in the CPF at phase start [g]

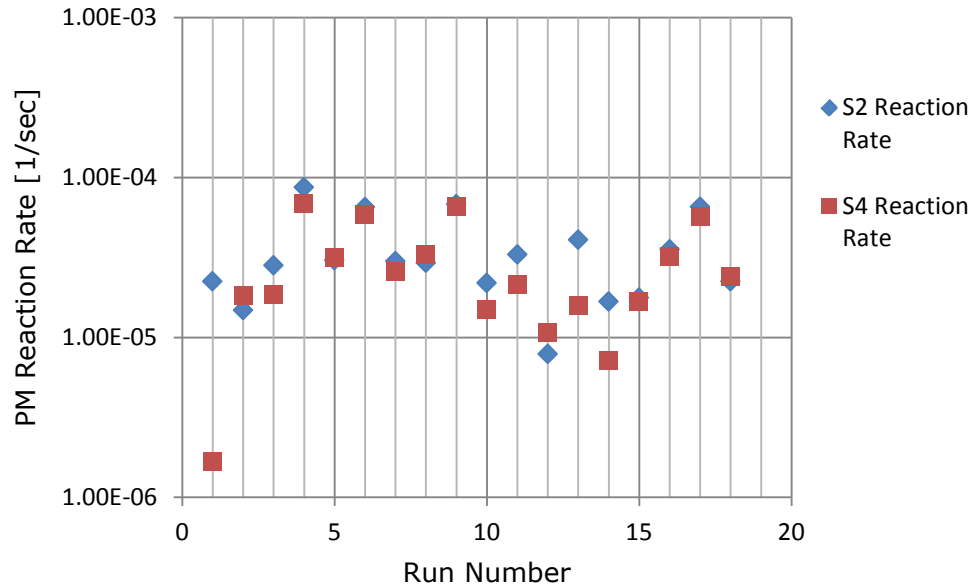


Figure J4: Stage 2 and Stage 4 Loading Reaction Rate Organized by Run Number

All of the variables presented in Eqn. J1 are gathered from the experimental test data with the exception of the reaction rate. The reaction rate is solved iteratively until the calculated PM mass retained within the CPF at the end of the phase is matched. The resulting reaction rate calculations from Stage 2 and Stage 4 loading phases are shown in Figure J4.

It can be seen in Figure J4 that some runs experience similar reaction rates between Stage 2 and Stage 4 loading while some runs are significantly different. The reaction rates which do not match between the two loading phases could be attributed to CPF mass measurement errors volumetric flow rate measurement errors, or PM concentration measurement errors, all of which would be responsible for inaccurate reaction rate data. The PM entering the CPF for any given phase is calculated based on the volumetric flow rate and engine-out PM concentration, which is why errors in these measurements could contribute to the differences in PM reaction rates during Stage 2 and Stage 4 loading. Determining whether the experimental data is valid from a modeling point of view is aided by analyzing the reaction rates between Stage 2 and Stage 4 loading.

Appendix K CPF Mass Balance

Table K1: Stage 1 Loading CPF Mass Balance

Variable	Time	Engine Speed	Engine Load	DOC Inlet Temp.	CPF Inlet Temp.	Exhaust Volumetric Flow Rate	Exhaust Mass Flow Rate	Engine Out PM Conc.	Engine Out PM mass	PM Mass Retained in CPF	CPF Weight	Mass Oxidized	Percent PM Oxidized	CPF Loading
Abbreviation	Minutes	RPM	N-m	°C	°C	Q _{exh} -S1	mdot _{exh} -S1	Cin	mE.O.-S1	mRet-S1	ms1	mOxd-S1	PM% _{oxd} -S1	mcpf-S1
B20 1	29.9	2100	195	261	264	0.180	12.8	12.7	4.1	2.9	17788.1	0.8	19.6	0.2
B20 2	29.9	2100	195	260	264	0.184	13.0	13.3	4.4	3.3	17786.3	0.6	14.0	0.2
B20 5	30.0	2100	195	258	262	0.180	12.7	13.4	4.3	2.9	17776.4	1.0	22.6	0.2
ULSD 3	30.3	2100	195	268	273	0.179	12.7	28.8	9.4	4.9	17778.3	3.6	38.2	0.3
ULSD 4	30.1	2100	195	263	268	0.154	10.9	21.2	5.9	4.2	17777.7	1.1	18.0	0.2
ULSD 5	30.1	2100	195	269	274	0.180	12.8	27.1	8.8	5.4	17778.9	2.5	28.7	0.3
ULSD 6	30.4	2100	195	272	276	0.180	12.8	23.1	7.6	5.6	17780.1	1.2	16.0	0.3
B20 6	29.8	2100	195	258	262	0.179	12.7	16.0	5.1	3.6	17779.4	1.0	18.8	0.2
B20 4	29.6	2100	195	257	260	0.181	12.8	21.6	6.9	3.4	17782.5	2.8	40.4	0.2
B10 1	29.5	2100	195	260	263	0.179	12.7	17.4	5.5	4.0	17786.5	1.0	17.4	0.2
B10 2	29.5	2100	195	258	262	0.175	12.4	18.4	5.7	3.8	17786.5	1.3	23.5	0.2
B10 3	28.4	2100	195	265	268	0.183	13.0	15.7	4.9	4.1	17784.0	0.3	5.9	0.2
ULSD 1	29.2	2100	195	266	270	0.175	12.4	27.0	8.3	5.9	17787.6	1.6	19.3	0.3
ULSD 8	29.5	2100	195	270	274	0.151	10.7	24.9	6.7	4.8	17792.5	1.2	17.4	0.3
ULSD 9	29.3	2100	195	268	271	0.175	12.4	25.2	7.8	5.8	17789.1	1.2	14.9	0.3
B10 4	29.7	2100	195	260	263	0.172	12.2	19.0	5.8	3.9	17792.7	1.3	22.7	0.2
ULSD 7R	29.3	2100	195	265	269	0.170	12.1	29.4	8.8	5.0	17793.1	2.9	33.1	0.3
ULSD 2R	29.3	2100	195	272	276	0.171	12.1	25.3	7.6	5.9	17793.5	1.0	12.9	0.3
ULSD 10	30.0	2090	255	269	275	0.179	12.7	9.4	3.0	3.3	17806.1	-0.6	-20.9	0.2

Table K2: Stage 2 Loading CPF Mass Balance

Variable	Time	Engine Speed	Engine Load	DOC Inlet Temp.	CPF Inlet Temp.	Exhaust Volumetric Flow Rate	Exhaust Mass Flow Rate	Engine Out PM Conc.	Engine Out PM mass	PM Mass Retained in CPF	CPF Weight
Abbreviation	tS2	Minutes	N-m	°C	°C	cm ³ /sec	kg/min	mg/5cm	mE.O.-S2	mRet-S2	ms2
B201	299.9	2100	195	262	262	0.187	13.2	44.4	34.5	17822.6	
B202	291.8	2100	195	259	262	0.186	13.2	40.7	34.2	17820.5	
B205	284.7	2100	195	258	262	0.185	13.2	44.9	33.4	17809.8	
ULSD 3	187.0	2100	195	265	268	0.182	12.9	29.2	59.6	17813.3	
ULSD 4	210.2	2100	195	262	265	0.178	12.7	22.1	49.6	17816.8	
ULSD 5	180.0	2100	195	268	271	0.179	12.7	27.7	53.5	17814.6	
ULSD 6	180.0	2100	195	268	271	0.180	12.8	23.0	44.7	17816.4	
B206	273.0	2100	195	261	261	0.183	13.0	16.2	48.6	17815.7	
B204	289.5	2100	195	262	263	0.184	13.0	22.1	70.6	17820.5	
B101	268.3	2100	195	264	266	0.182	12.9	16.7	48.9	17825.7	
B102	251.3	2100	195	263	266	0.181	12.8	18.3	49.9	17823.5	
B103	223.9	2100	195	268	274	0.183	13.0	15.0	36.9	17817.8	
ULSD 1	165.1	2100	195	269	273	0.176	12.5	28.2	49.2	17825.9	
ULSD 8	371.7	2100	195	272	275	0.174	12.4	24.5	95.1	17868.8	
ULSD 9	285.4	2100	195	273	276	0.175	12.4	24.7	74.0	17850.5	
B104	236.7	2100	195	263	265	0.176	12.5	20.0	50.0	17829.6	
ULSD 7R	199.8	2100	195	265	268	0.176	12.5	28.9	61.0	17832.4	
ULSD 2R	179.1	2100	195	271	274	0.175	12.4	24.0	45.1	17831.9	
ULSD 10	295.0	2090	255	269	273	0.184	13.1	9.4	30.5	17842.2	

Variable	Time	Mass Oxidized	Percent PM Oxidized	CPF Loading	CPF Filtration Efficiency	Test Cell Temp	Relative Humidity	Atmospheric Pressure	Absolute Humidity	Reaction Rate	CPF Loading Rate
Abbreviation	tS2	Minutes	g	PM% oxd-S2	%	°C	Φ	p	ω	RR0	g/min
B201	299.9	8.7	19.6	2.2	97.3%	31.6	7.7	29.5	0.0021997	3.16E-05	0.115038346
B202	291.8	5.7	14.0	2.2	98.2%	31.5	14.2	29.3	0.0021948	2.58E-05	0.117203564
B205	284.7	10.2	22.6	2.1	97.1%	29.6	15.5	29.5	0.0037476	3.85E-05	0.117316473
ULSD 3	187.0	22.8	38.2	2.3	96.9%	37.0	27.4	28.9	0.0098663	1.08E-04	0.187165775
ULSD 4	210.2	8.9	18.0	2.5	96.8%	31.3	20.7	29.4	0.0058629	4.50E-05	0.186013321
ULSD 5	180.0	15.4	28.7	2.4	95.4%	35.4	19.4	29.4	0.0064564	8.36E-05	0.198333333
ULSD 6	180.0	7.2	16.0	2.5	97.2%	34.1	28.9	29.2	0.0092704	5.24E-05	0.201666667
B206	273.0	9.1	18.8	2.3	93.5%	34.3	24.7	29.1	0.0079945	3.66E-05	0.132967033
B204	289.5	28.6	40.4	2.4	94.2%	30.5	31.4	28.8	0.0088118	7.51E-05	0.131260794
B101	268.3	8.5	17.4	2.5	97.5%	31.4	31.6	29.2	0.0090962	3.41E-05	0.146105106
B102	251.3	11.7	23.5	2.4	97.5%	32.9	26.5	29.4	0.0080429	4.68E-05	0.147234381
B103	223.9	2.2	5.9	2.2	97.5%	33.0	26.6	29.2	0.0081624	2.43E-05	0.15096025
ULSD 1	165.1	9.5	19.3	2.6	97.2%	36.7	34.6	29.1	0.0122935	6.48E-05	0.231980618
ULSD 8	371.7	16.6	17.4	4.7	97.7%	26.6	23.4	29.5	0.0052833	2.23E-05	0.20527307
ULSD 9	285.4	11.0	14.9	3.9	97.9%	33.3	27.8	28.8	0.0087600	2.76E-05	0.21513665
B104	236.7	11.3	22.7	2.4	96.5%	29.6	20.1	29.1	0.0053225	4.89E-05	0.155893536
ULSD 7R	199.8	20.2	33.1	2.6	97.5%	31.6	12.4	29.4	0.0035436	8.49E-05	0.196696697
ULSD 2R	179.1	5.8	12.9	2.6	97.9%	31.2	14.2	29.0	0.0040497	4.65E-05	0.21440536
ULSD 10	295.0	-6.4	-20.9	2.3	97.3%	28.0	11.3	29.5	0.0027150	-9.11E-06	0.122360438

Table K3: Active Regeneration CPF Mass Balance

Variable	Dosing Method	Time	Loading Ramp Time	AR Ramp Time	Engine Speed	Engine Load	DOC Inlet Temp.	CPF Inlet Temp.	Average CPF Temp.	Exhaust Volumetric Flow Rate	Exhaust Mass Flow Rate	Doser Flow Rate
Abbreviation	-	Time	min	min	RPM	N-m	°C	°C	°C	scfm/sec	kg/min	g/sec
Test/Units	-	Minutes										
B201	in-cyl	34.7	14.9	9.0	1400	460	329	477	474	0.116	8.2	0.431
B202	in-cyl	38.8	14.3	9.9	1400	460	330	501	508	0.116	8.2	0.633
B205	in-cyl	19.0	15.0	10.1	1400	460	328	527	534	0.115	8.1	0.882
ULSD 3	in-cyl	15.5	15.0	10.8	1400	460	330	524	526	0.113	8.0	0.638
ULSD 4	in-cyl	21.0	14.8	10.4	1400	460	334	526	531	0.111	7.9	0.763
ULSD 5	in-cyl	21.6	14.5	10.1	1400	460	340	525	529	0.113	8.0	0.735
ULSD 6	exhaust	21.5	14.9	9.6	1400	460	334	524	540	0.114	8.0	0.739
B206	exhaust	15.9	14.6	15.1	1400	460	322	528	540	0.116	8.3	0.690
B204	in-cyl	21.8	14.6	11.5	1400	460	333	504	506	0.115	8.1	0.687
B101	in-cyl	25.7	14.8	10.7	1400	460	335	526	534	0.112	7.9	0.730
B102	in-cyl	18.9	14.7	10.1	1400	460	337	525	531	0.113	8.0	0.898
B103	in-cyl	22.3	14.3	10.7	1400	460	338	526	531	0.113	8.0	0.743
ULSD 1	exhaust	14.6	14.8	10.2	1400	460	336	553	567	0.113	8.0	0.819
ULSD 8	in-cyl	19.9	14.8	10.0	1400	460	342	526	539	0.110	7.7	0.744
ULSD 9	in-cyl	17.3	14.8	10.3	1400	460	346	550	563	0.110	7.9	0.899
B104	in-cyl	14.5	14.6	10.6	1400	460	337	550	563	0.111	7.9	0.896
ULSD 7R	in-cyl	17.0	14.8	10.3	1400	460	340	550	562	0.109	7.7	0.830
ULSD 2R	in-cyl	6.2	14.6	10.1	1400	460	337	604	616	0.109	7.7	1.056
ULSD 10	in-cyl	22.4	14.7	9.8	1450	450	345	530	538	0.117	8.3	0.785

Variable	Dosing Method	Doser Flow Rate	Engine Out PM Conc.	Engine Out PM mass	PM Mass Retained in CPF After AR	Loading Ramp PM Deposit	AR Ramp PM Deposit	PM Deposited During AR	PM Mass for Oxidation	Total Mass Oxidized	Percent PM Oxidized	CPF Loading
Abbreviation	-	mdot-dos-AR	Cin-AR	mE.O.-AR	mRet-AR	mload-ramp	mAR-ramp	madd-AR	mAvailable-AR	mOxd-tot-AR	PM% oxd-AR	mcptf-AR
Test/Units	-	g/sec	mg/scm	g	g	g	g	g	g	g	%	g/L
B201	in-cyl	0.431	8.3	2.0	20.2	1.7	0.1	1.9	39.2	21.0	53.5	1.2
B202	in-cyl	0.633	9.9	2.7	11.2	1.7	0.5	2.6	39.7	31.1	78.5	0.7
B205	in-cyl	0.882	9.9	1.3	6.0	1.8	0.5	1.3	38.6	33.8	87.8	0.3
ULSD 3	in-cyl	0.638	22.2	2.3	27.5	2.8	1.1	2.3	43.8	18.5	42.3	1.6
ULSD 4	in-cyl	0.763	18.5	2.6	20.8	2.8	0.9	2.5	47.0	28.7	61.0	1.2
ULSD 5	in-cyl	0.735	24.3	3.6	20.1	2.9	1.1	3.4	45.1	28.4	62.9	1.2
ULSD 6	exhaust	0.739	18.3	2.7	17.8	3.0	0.8	2.6	45.7	30.5	66.8	1.0
B206	exhaust	0.690	12.9	1.4	10.6	1.9	0.9	1.3	42.8	33.5	78.2	0.6
B204	in-cyl	0.687	17.8	2.7	15.0	1.9	0.9	2.5	44.3	31.8	71.8	0.9
B101	in-cyl	0.730	15.1	2.6	13.9	2.2	0.7	2.5	46.1	34.7	75.3	0.8
B102	in-cyl	0.898	17.4	2.2	13.0	2.2	0.8	2.2	43.8	32.9	75.2	0.8
B103	in-cyl	0.743	11.2	1.7	15.0	2.2	0.6	1.7	40.6	27.3	67.2	0.9
ULSD 1	exhaust	0.819	26.9	2.7	18.5	3.4	1.3	2.6	48.9	33.0	67.5	1.1
ULSD 8	in-cyl	0.744	22.5	3.0	44.0	3.0	1.0	2.9	85.2	44.0	51.7	2.6
ULSD 9	in-cyl	0.899	21.9	2.5	19.0	3.2	1.0	2.4	71.4	54.9	76.8	1.1
B104	in-cyl	0.896	15.7	1.5	14.9	2.3	0.7	1.5	43.8	30.5	69.5	0.9
ULSD 7R	in-cyl	0.830	25.9	2.9	14.1	2.9	1.2	2.8	48.4	37.1	76.7	0.8
ULSD 2R	in-cyl	1.056	19.8	0.8	10.1	3.1	0.9	0.8	48.3	39.0	80.7	0.6
ULSD 10	in-cyl	0.785	13.0	2.0	11.0	1.8	0.6	2.0	41.8	32.8	78.5	0.6

Table K4: Stage 3 Loading CPF Mass Balance

Variable	Time	Engine Speed	Engine Load	DOC Inlet Temp.	CPF Inlet Temp.	Exhaust Volumetric Flow Rate	Exhaust Mass Flow Rate	Engine Out PM Conc.	Engine Out PM mass	PM Mass Retained in CPF	PM Mass added	CPF Weight	Mass Oxidized	Percent PM Oxidized	CPF Loading
Abbreviation	Minutes	RPM	N-m	°C	°C	scm/sec	kg/min	Cin	g	g	g	g	g	%	mgcf-S3
Test/Units				TD0C IN-S3	TCPF IN-S3	Qexh-S3	mldot-exh-S3	mg/scm	mE.O.-S3	mRet-S3	madd-S3	mS3	mOxd-S3	PM% oxd-S3	g/L
B20 1	29.6	2100	195	264	268	0.187	13.2	13.3	4.4	24.4	4.2	17809.6	0.1	2.2	1.4
B20 2	29.4	2100	195	265	268	0.186	13.2	13.7	4.5	14.9	3.8	17797.9	0.6	14.3	0.9
B20 5	28.9	2100	195	263	266	0.185	13.1	13.8	4.4	9.8	3.9	17783.3	0.4	9.9	0.6
ULSD 3	29.3	2100	195	267	271	0.180	12.8	27.3	8.6	32.5	4.9	17805.9	3.4	39.7	1.9
ULSD 4	29.6	2100	195	268	272	0.179	12.7	21.6	6.9	25.7	4.9	17799.2	1.7	24.9	1.5
ULSD 5	29.4	2100	195	276	279	0.182	12.9	27.5	8.8	25.7	5.6	17799.2	2.8	32.1	1.5
ULSD 6	29.2	2100	195	275	277	0.180	13.0	23.4	7.4	23.7	5.9	17798.2	1.3	17.4	1.4
B20 6	29.3	2100	195	266	268	0.184	13.0	15.9	5.1	14.7	4.1	17790.5	0.7	13.6	0.9
B20 4	29.1	2100	195	266	268	0.184	13.0	21.7	7.0	19.0	4.0	17798.1	2.5	36.4	1.1
B10 1	27.3	2100	195	269	271	0.182	12.9	16.6	4.9	18.3	4.4	17800.8	0.4	8.8	1.1
B10 2	29.5	2100	195	269	273	0.183	13.0	18.0	5.8	17.8	4.8	17800.5	0.9	15.6	1.0
B10 3	29.6	2100	195	272	276	0.183	13.0	15.1	4.9	19.5	4.5	17799.4	0.2	5.1	1.1
ULSD 1	29.8	2100	195	278	282	0.181	12.8	26.4	8.5	25.1	6.6	17806.8	1.7	20.3	1.5
ULSD 8	29.5	2100	195	278	280	0.176	12.5	24.7	7.7	50.7	6.7	17838.4	0.8	10.8	3.0
ULSD 9	29.8	2100	195	276	279	0.178	12.6	24.5	7.8	25.8	6.8	17809.1	0.8	10.5	1.5
B10 4	29.4	2100	195	270	273	0.180	12.7	19.5	6.2	19.5	4.7	17808.3	1.3	21.4	1.1
ULSD 7R	29.4	2100	195	271	274	0.175	12.4	28.3	8.7	20.2	6.1	17808.3	2.4	27.3	1.2
ULSD 2R	29.4	2100	195	264	267	0.175	12.4	23.8	7.3	16.0	5.9	17803.6	1.3	17.8	0.9
ULSD 10	29.8	2090	255	272	278	0.185	13.1	9.4	3.1	14.6	3.6	17817.4	-0.6	-20.4	0.9

Table K5: Stage 4 Loading CPF Mass Balance

Variable	Time	Engine Speed	Engine Load	DOC Inlet Temp.	CPF Inlet Temp.	Exhaust Volumetric Flow Rate	Exhaust Mass Flow Rate	Engine Out PM Conc.	Engine Out PM mass	PM Mass Retained in CPF	PM Mass added	CPF Weight	Mass Oxidized	Percent PM Oxidized	CPF Loading
Abbreviation Test/Units	ts4 Minutes	RPM	N-m	°C	°C	Qexh-S4 scm/sec	mldot-exh-S4 kg/min	Cin mg/scm	mE.O.-S4 g	mRet-S4 g	madd-S4 g	mS4 g	mOxd-S4 g	PM% oxd-S4 %	mcpf-S4 g/L
B20 1	59.9	2100	195	259	262	0.186	13.2	13.3	8.9	32.9	8.5	17818.1	0.1	1.7	1.9
B20 2	60	2100	195	262	264	0.186	13.2	13.7	9.2	22.6	7.7	17805.6	1.3	14.3	1.3
B20 5	59.9	2100	195	258	266	0.184	13.0	13.9	9.2	17.8	8.0	17791.3	0.9	10.0	1.0
ULSD 3	59.9	2100	195	265	269	0.183	13.0	29.8	19.6	42.6	10.1	17816	8.9	45.3	2.5
ULSD 4	59.9	2100	195	257	259	0.177	12.5	21.6	13.7	35.7	10.0	17809.2	3.3	24.0	2.1
ULSD 5	60	2100	195	272	273	0.182	12.9	27.6	18.1	37.1	11.4	17810.6	5.9	32.4	2.2
ULSD 6	60	2100	195	273	275	0.183	13.0	22.8	15.0	35.8	12.1	17810.3	2.5	16.7	2.1
B20 6	59.9	2100	195	263	265	0.184	13.0	16.5	10.9	23.1	8.4	17798.9	1.8	16.5	1.4
B20 4	59.9	2100	195	266	269	0.184	13.0	21.4	14.2	27.3	8.3	17806.4	5.0	35.6	1.6
B10 1	59.7	2100	195	263	265	0.181	12.9	17.1	11.1	27.9	9.6	17810.4	1.2	11.0	1.6
B10 2	59.9	2100	195	265	267	0.182	12.9	17.9	11.7	27.5	9.7	17810.2	1.7	14.7	1.6
B10 3	60	2100	195	268	271	0.182	12.9	15.8	10.4	28.7	9.2	17808.6	0.9	8.7	1.7
ULSD 1	59.9	2100	195	276	279	0.160	11.3	26.5	15.2	38.3	13.2	17820	1.6	10.6	2.2
ULSD 8	60	2100	195	274	274	0.177	12.5	24.2	15.4	64.3	13.6	17852	1.5	9.5	3.8
ULSD 9	59.9	2100	195	272	284	0.178	12.6	24.9	15.9	39.5	13.7	17822.8	1.9	11.9	2.3
B10 4	59.9	2100	195	265	268	0.179	12.7	19.5	12.6	29.0	9.5	17817.8	2.6	20.9	1.7
ULSD 7R	60	2100	195	266	269	0.174	12.3	28.9	18.1	32.7	12.5	17820.8	5.2	28.5	1.9
ULSD 2R	60	2100	195	263	266	0.175	12.4	22.3	14.0	28.0	12.0	17815.6	1.7	12.4	1.6

Appendix L Doser Flow Rate Comparison

Differences in the doser flow rates were noticed throughout some of the tests conducted in this study. For example, the doser flow rates between tests B10-1 and B10-2, which were run under the same experimental conditions (same target CPF inlet temperature, dosing method, and CPF PM loading), but test B10-2 required 0.168 g/sec more fuel than what was required during B10-1 to maintain the same desired CPF inlet temperature. Other tests showed differences in the doser flow rate as well, therefore, a DOC energy balance was carried out using the methods described in reference [17] in order to estimate the upstream DOC HC concentrations and doser flow rate. The energy balance used the experimentally measured downstream DOC HC concentrations and the measured temperature rise across the DOC to estimate the concentration of HC required at the DOC inlet to produce the observed temperature change. The estimated DOC inlet HC concentrations can then be converted back to dosing flow rate in the same manner that is used to calculate upstream DOC hydrocarbon concentrations from the experimental dosing rate. Table L1 shows the results from the energy balance carried out for all tests. The 'Difference' column is the percent difference between the experimentally determined and estimated doser flow rates using the estimated values as the reference.

It can be seen that the tests which were conducted at similar experimental conditions have similar estimated doser flow rate values as well. This suggests that there is some variability in the experimental doser flow rate. The variability could be the result of the method used to determine the fuel flow rate during an experiment. During the pre-test and pre-active regeneration ramp phases of the experiment, the engine may be consuming different amounts of fuel based on differences in CPF PM loading. If the no-dosing AVL time was recorded during the pre-test portion of the experiment, the experimental dosing flow rate could potentially be in error. The dosing flow rate is calculated by taking the difference in measured fuel flow rate between the pre-test or pre-active regeneration ramp phases and the active regeneration phase. The difference in the fuel flow rate between these two phases is the doser flow rate. Error may also be compounded by the fact that the AVL time can only be recorded to the nearest second. The estimated doser flow rates are thought to be more accurate and are presented in Table 4.1 of the report.

Table L1: DOC Energy Balance Results

Run	Estimated Doser Flow Rate	Experimental Doser Flow Rate	Difference	CPF Inlet Temperature
	[g/sec]	[g/sec]	[%]	[°C]
B20 1	0.517	0.431	16.6	477
B20 2	0.608	0.633	-4.1	501
B20 5	0.695	0.832	-19.8	527
ULSD 3	-	0.638	-	524
ULSD 4	0.648	0.763	-17.8	526
ULSD 5	0.636	0.735	-15.5	525
ULSD 6	0.667	0.739	-10.7	524
B20 6	0.749	0.690	7.9	528
B20 4	0.594	0.687	-15.7	504
B10 1	0.654	0.730	-11.7	526
B10 2	0.646	0.898	-39.0	525
B10 3	0.648	0.743	-14.6	526
ULSD 1	0.759	0.819	-7.8	553
ULSD 8	0.635	0.744	-17.1	526
ULSD 9	0.727	0.899	-23.5	550
B10 4	0.738	0.896	-21.4	550
ULSD 7R	0.709	0.830	-17.0	550
ULSD 2R	0.893	1.056	-18.3	604
ULSD 10	0.663	0.785	-18.4	530

Appendix M Gaseous Emissions Summary

Table M1: Pre-test Preparation Phase Gaseous Emissions

Test Location	HC [ppm CI]			NOx [ppm]			NO [ppm]			NO2 [ppm]			CO [ppm]			CO2 [%]			O2 [%]		
	UDOC	DDOC	DCPF	UDOC	DDOC	DCPF	UDOC	DDOC	DCPF	UDOC	DDOC	DCPF	UDOC	DDOC	DCPF	UDOC	DDOC	DCPF	UDOC	DDOC	DCPF
B201	49	10	3	152	151	143	136	79	59	16	72	84	71	0	0	11.1	11.4	12.2	10.2	10.1	10.1
B202	49	10	8	138	125	116	121	58	50	17	67	66	76	0	0	7.9	7.6	6.9	10.0	10.4	11.3
B205	67	15	10	141	131	121	116	62	52	24	69	69	85	0	0	8.0	8.0	7.7	9.7	9.7	10.1
ULSD3	-	-	-	123	118	109	107	54	39	15	65	70	93	0	0	8.3	8.3	7.7	9.5	9.6	10.3
ULSD4	66	11	3	127	118	115	114	58	52	13	60	64	89	0	0	8.3	7.9	8.1	9.6	10.2	9.9
ULSD5	69	7	4	131	119	101	119	58	47	12	62	54	97	0	0	8.4	8.2	7.4	9.5	9.7	10.9
ULSD6	66	8	6	131	116	111	115	58	53	15	58	58	98	0	0	8.5	8.1	7.9	9.5	10.1	10.3
B206	57	9	7	123	116	102	111	55	46	13	61	56	84	0	0	8.1	8.1	7.4	9.8	9.8	10.8
B204	43	5	5	130	118	101	114	57	40	16	61	61	82	0	0	8.1	8.2	7.0	9.9	9.9	11.5
B101	48	4	2	118	107	90	103	52	40	16	55	50	90	0	0	8.2	7.8	7.2	9.7	10.3	11.1
B102	66	13	4	110	100	102	99	55	48	11	45	53	90	0	0	7.8	7.5	7.8	10.1	10.5	10.2
B103	62	7	4	111	109	108	100	59	45	11	50	63	96	0	0	8.3	8.3	8.3	9.6	9.6	9.6
ULSD1	49	6	5	106	98	95	96	54	36	10	44	59	108	0	0	8.6	8.6	8.6	9.1	9.1	9.1
ULSD8	69	7	4	136	121	123	122	68	58	13	52	65	102	0	0	8.5	8.5	8.6	9.3	9.3	9.3
ULSD9	93	19	4	114	108	111	103	64	56	11	44	55	108	0	0	8.5	8.6	8.5	9.2	9.2	9.3
B104	77	13	1	124	119	116	109	67	55	15	53	61	92	0	0	8.3	8.3	8.3	9.4	9.4	9.5
ULSD7R	81	10	4	137	131	127	122	64	58	15	66	69	97	0	0	8.5	8.5	8.5	9.4	9.4	9.4
ULSD2R	83	15	5	141	135	126	130	93	61	11	42	65	102	0	0	8.4	8.5	8.5	9.4	9.4	9.4
ULSD10	44	5	1	186	181	167	176	90	67	10	92	100	63	0	0	7.1	7.0	6.7	11.3	11.5	11.9

Table M2: Stage 1 Loading Gaseous Emissions

Test Location	HC [ppm CI]			NOx [ppm]			NO [ppm]			NO2 [ppm]			CO [ppm]			CO2 [%]			O2 [%]		
	UDOC	DDOC	DCPF	UDOC	DDOC	DCPF	UDOC	DDOC	DCPF	UDOC	DDOC	DCPF	UDOC	DDOC	DCPF	UDOC	DDOC	DCPF	UDOC	DDOC	DCPF
B201	72	20	6	85	84	81	56	59	34	29	47	130	47	0	7.5	7.6	7.8	14.0	14.3	14.0	
B202	68	20	8	83	83	72	54	56	33	29	27	39	128	0	5.0	5.0	4.6	14.0	14.0	14.0	
B205	70	21	9	83	82	74	56	61	28	27	21	46	126	0	5.0	4.9	4.9	13.8	13.9	14.0	
ULSD3	-	-	-	78	79	67	52	58	33	26	21	34	138	0	5.3	5.2	4.8	13.7	13.7	14.3	
ULSD4	87	18	3	86	83	83	63	58	38	23	25	45	131	0	5.1	5.0	5.0	13.8	14.1	14.0	
ULSD5	89	18	4	86	86	75	64	58	33	22	28	42	132	0	5.1	5.3	4.7	13.9	13.7	14.5	
ULSD6	103	18	6	81	79	73	60	56	33	21	23	40	138	0	5.3	5.3	5.0	13.8	13.8	14.2	
B206	-	-	-	76	76	66	50	53	32	26	23	34	135	0	5.1	5.2	4.7	13.9	13.8	14.5	
B204	72	15	7	80	80	64	53	57	32	27	23	32	129	0	5.1	5.2	4.5	14.1	14.0	14.9	
B101	60	10	1	81	78	68	56	52	33	25	26	35	124	0	5.1	5.1	4.5	13.9	13.9	14.7	
B102	91	4	0	84	83	72	59	55	36	25	28	36	121	0	5.1	4.9	4.9	13.9	14.1	14.1	
B103	83	16	4	84	83	74	63	62	37	21	37	130	0	5.2	5.2	5.2	14.0	14.0	14.0		
ULSD1	42	7	0	79	77	73	56	57	29	23	20	44	129	0	5.3	5.3	5.3	13.5	13.5	13.5	
ULSD8	86	14	2	96	93	82	76	63	41	20	30	41	122	0	5.2	5.3	5.2	13.7	13.7	13.6	
ULSD9	111	25	4	87	86	82	63	60	39	24	26	43	129	0	5.3	5.3	5.3	13.6	13.6	13.6	
B104	102	24	2	93	91	87	65	63	42	28	28	45	121	0	5.1	5.1	5.1	13.7	13.7	13.7	
ULSD7R	46	22	4	96	95	91	69	67	38	27	28	53	123	0	5.2	5.2	5.2	13.8	13.8	13.8	
ULSD2R	96	25	6	97	95	90	71	67	41	26	28	49	124	0	5.3	5.3	5.3	13.6	13.6	13.7	
ULSD10	79	17	7	217	197	175	182	131	126	35	66	49	81	0	5.1	4.6	4.4	13.9	14.6	14.9	

Table M3: Stage 2 Loading Gaseous Emissions

Test	HC (ppm Cl)			NOx (ppm)			NO (ppm)			NO2 (ppm)			CO (ppm)			CO2 [%]			O2 [%]		
	UDOC	DDOC	DCPF	UDOC	DDOC	DCPF	UDOC	DDOC	DCPF	UDOC	DDOC	DCPF	UDOC	DDOC	DCPF	UDOC	DDOC	DCPF	UDOC	DDOC	DCPF
B20 1	72	24	8	88	86	83	57	57	44	30	29	38	127	1	5.9	5.9	6.1	13.9	13.9	13.9	13.9
B20 2	54	14	3	88	87	76	59	63	40	29	24	36	123	0	5.0	5.0	4.6	14.0	14.0	14.6	14.6
B20 5	70	17	3	87	84	80	59	61	42	27	22	37	122	0	5.0	4.9	4.9	13.6	13.8	13.8	13.8
ULSD 3	-	-	-	84	81	74	57	58	38	27	23	36	134	0	5.3	5.3	4.9	13.6	13.7	14.2	14.2
ULSD 4	92	21	4	92	90	80	64	64	43	27	26	36	124	0	5.1	5.2	4.8	13.8	13.8	14.2	14.2
ULSD 5	92	22	5	90	86	77	66	61	41	24	25	36	125	0	5.3	5.3	4.7	13.6	13.7	14.4	14.4
ULSD 6	92	25	7	85	79	74	63	59	40	22	19	34	124	0	5.4	5.3	5.0	13.6	13.8	14.1	14.1
B20 6	90	25	18	78	76	65	54	55	36	24	21	29	130	0	5.1	5.2	4.8	13.9	13.9	14.4	14.4
B20 4	62	18	3	80	80	78	63	56	35	24	22	28	125	0	5.2	5.2	4.4	13.9	14.0	15.0	15.0
B10 1	66	16	0	82	79	70	58	58	37	25	22	33	124	0	5.2	5.1	4.7	13.8	13.9	14.6	14.6
B10 2	76	19	5	83	77	74	59	58	41	24	19	33	124	0	5.2	5.0	4.9	13.7	14.0	14.0	14.0
B10 3	91	28	5	84	83	78	62	62	44	22	21	34	127	0	5.3	5.2	5.3	13.8	14.0	13.9	13.9
ULSD 1	86	52	4	77	78	72	58	58	41	19	20	31	133	0	5.4	5.4	5.4	13.3	13.6	13.4	13.4
ULSD 8	108	24	5	95	91	85	73	69	51	23	22	35	122	0	5.3	5.2	5.3	13.9	13.9	13.8	13.8
ULSD 9	113	29	7	89	86	85	65	64	47	25	22	38	128	0	5.4	5.4	5.3	13.4	13.6	13.6	13.6
B10 4	104	28	5	93	90	87	65	66	47	27	24	40	121	0	5.2	5.1	5.2	13.9	13.9	13.9	13.9
ULSD 7R	101	28	6	98	96	93	70	69	52	28	27	41	122	0	5.2	5.2	5.2	13.8	13.8	13.8	13.8
ULSD 2R	102	28	7	98	96	93	72	66	49	25	30	43	124	0	5.3	5.3	5.3	13.5	13.6	13.6	13.6
ULSD 10	84	30	7	220	194	188	185	133	121	35	61	67	79	0	5.0	4.6	4.3	14.0	14.6	14.9	14.9

Table M4: Active Regeneration Gaseous Emissions

Test	HC (ppm Cl)			NOx (ppm)			NO (ppm)			NO2 (ppm)			CO (ppm)			CO2 [%]			O2 [%]		
	UDOC	DDOC	DCPF	UDOC	DDOC	DCPF	UDOC	DDOC	DCPF	UDOC	DDOC	DCPF	UDOC	DDOC	DCPF	UDOC	DDOC	DCPF	UDOC	DDOC	DCPF
B20 1	6941	226	5	152	150	147	136	142	105	16	8	42	71	7	11.1	4.0	3.9	10.2	8.8	8.6	8.6
B20 2	9277	374	16	138	142	126	121	138	102	17	4	24	76	23	7.9	9.0	8.0	10.0	8.0	10.0	10.0
B20 5	12340	355	19	141	135	126	116	133	108	24	2	17	85	24	8.0	9.0	9.1	9.7	8.2	8.1	8.1
ULSD 3	9850	-	-	123	122	110	107	118	92	15	5	18	93	4	8.3	9.8	8.8	9.5	7.6	8.8	8.8
ULSD 4	11927	289	35	123	134	119	107	126	99	15	8	19	93	9	8.3	9.8	9.1	9.5	7.6	8.5	8.5
ULSD 5	11346	346	39	131	136	119	119	130	101	12	6	18	97	11	8.4	9.7	8.9	9.5	7.7	8.8	8.8
ULSD 6	11408	571	64	131	131	115	115	126	98	15	4	17	98	13	8.5	9.9	9.2	9.5	7.7	8.6	8.6
B20 6	10075	644	87	123	139	126	111	129	108	13	10	17	84	19	8.1	9.4	9.3	9.8	8.2	8.3	8.3
B20 4	10229	300	32	130	133	107	114	128	87	16	5	20	82	14	8.1	9.4	7.8	9.9	8.3	10.5	10.5
B10 1	11276	430	33	118	118	110	103	115	90	16	3	20	90	16	8.2	9.7	9.2	9.7	7.8	8.4	8.4
B10 2	13695	342	46	110	127	110	99	120	94	11	7	16	90	15	7.8	9.7	8.9	10.1	7.7	8.7	8.7
ULSD 1	12639	585	55	106	116	110	96	112	99	10	4	11	108	18	8.6	10.0	10.1	9.1	7.2	6.9	6.9
ULSD 8	11863	698	52	136	139	132	122	133	115	13	6	17	102	29	8.5	9.8	10.0	9.3	7.6	7.6	7.6
ULSD 9	14044	894	43	114	128	122	103	122	111	11	6	11	108	33	8.5	9.9	10.1	9.2	7.3	7.0	7.0
B10 4	13840	600	23	124	131	125	109	128	115	15	3	10	92	26	8.3	9.9	10.0	9.4	7.5	7.3	7.3
ULSD 7R	13269	560	28	137	133	129	122	129	115	15	4	14	71	24	8.5	10.0	10.1	9.4	7.3	7.1	7.1
ULSD 2R	16904	513	45	141	131	129	130	134	122	11	-3	7	102	48	8.4	10.4	10.7	9.4	6.9	6.5	6.5
ULSD 10	11714	365	11	118	126	187	103	213	159	16	23	28	90	20	8.2	9.2	8.4	9.7	8.5	9.5	9.5

Table M5: Stage 3 Loading Gaseous Emissions

Test Location	HC (ppm Cl)			NOx (ppm)			NO (ppm)			NO2 (ppm)			CO (ppm)			CO2 [%]			O2 [%]		
	UDOC	DDOC	DCPF	UDOC	DDOC	DCPF	UDOC	DDOC	DCPF	UDOC	DDOC	DCPF	UDOC	DDOC	DCPF	UDOC	DDOC	DCPF	UDOC	DDOC	DCPF
B20 1	72	22	7	90	90	86	61	57	31	29	33	55	123	0	0	3.7	3.7	3.8	13.8	13.9	13.9
B20 2	57	20	8	91	89	77	62	61	36	29	28	41	121	0	0	5.0	5.0	5.0	13.9	14.0	14.7
B20 5	57	18	8	87	84	81	61	60	33	26	24	48	122	0	0	5.0	4.9	4.9	13.6	13.7	13.8
ULSD 3	-	-	-	86	85	72	60	58	29	26	27	43	130	0	0	5.3	5.3	4.8	13.7	13.6	14.3
ULSD 4	86	28	16	92	92	84	66	63	38	26	29	46	125	0	0	5.2	5.2	4.9	13.7	13.8	14.2
ULSD 5	92	30	15	92	91	80	68	61	36	24	30	44	126	0	0	5.3	5.3	4.9	13.5	13.5	14.1
ULSD 6	94	40	27	85	84	73	61	60	35	24	24	38	128	0	0	5.5	5.5	5.0	13.5	13.5	14.1
B20 6	95	48	40	81	80	74	55	57	36	26	23	38	129	0	0	5.2	5.3	5.1	13.8	13.8	14.0
B20 4	77	27	19	83	81	62	58	58	31	25	23	31	124	0	0	5.2	5.3	4.4	14.0	13.9	15.2
B10 1	91	32	19	84	81	73	59	57	35	25	24	38	126	0	0	5.3	5.2	5.0	13.8	13.9	14.2
B10 2	101	35	24	85	85	73	60	59	35	25	26	38	127	0	0	5.2	5.2	4.7	13.7	13.7	14.4
B10 3	99	36	20	84	82	74	63	64	38	21	18	36	127	0	0	5.3	5.3	5.2	13.8	13.8	13.9
ULSD 1	89	42	24	75	75	67	55	58	34	20	17	33	136	0	0	5.4	5.5	5.4	13.2	13.2	13.2
ULSD 8	99	48	21	99	97	88	77	77	48	22	20	40	123	2	0	5.3	5.3	5.3	14.0	14.0	14.0
ULSD 9	111	53	15	86	85	81	62	66	41	24	19	40	130	0	0	5.4	5.4	5.4	13.5	13.4	13.5
B10 4	97	37	8	94	92	88	68	68	42	26	24	46	125	0	0	5.2	5.2	5.2	13.8	13.8	13.9
ULSD 7R	97	45	9	96	95	89	70	70	44	26	25	45	124	0	0	5.2	5.2	5.2	13.7	13.7	13.7
ULSD 2R	97	35	11	98	96	91	70	72	48	28	24	43	122	0	0	5.3	5.3	5.2	13.8	13.8	13.8
ULSD 10	80	26	2	222	214	198	186	132	133	36	82	65	80	0	0	5.0	5.0	4.6	14.1	14.1	14.6

Table M6: Stage 4 Loading Gaseous Emissions

Test Location	HC (ppm Cl)			NOx (ppm)			NO (ppm)			NO2 (ppm)			CO (ppm)			CO2 [%]			O2 [%]		
	UDOC	DDOC	DCPF	UDOC	DDOC	DCPF	UDOC	DDOC	DCPF	UDOC	DDOC	DCPF	UDOC	DDOC	DCPF	UDOC	DDOC	DCPF	UDOC	DDOC	DCPF
B20 1	72	22	7	90	90	86	61	57	31	29	33	55	123	0	0	3.7	3.7	3.8	13.8	13.9	13.9
B20 2	64	26	9	89	88	76	61	62	42	28	26	34	123	0	0	5.1	5.1	4.5	13.9	13.9	14.7
B20 5	57	23	7	86	82	79	61	60	43	25	22	36	123	0	0	5.0	4.9	4.9	13.5	13.7	13.7
ULSD 3	-	-	-	86	84	76	61	57	41	25	27	43	130	0	0	5.3	5.3	4.9	13.6	13.7	14.2
ULSD 4	91	23	10	95	93	82	67	63	44	28	31	38	121	0	0	5.1	5.1	4.8	13.8	13.8	14.2
ULSD 5	95	29	10	90	87	80	66	65	46	23	23	33	127	0	0	5.3	5.4	5.0	13.6	13.5	14.0
ULSD 6	93	33	15	86	83	75	64	63	43	22	20	31	127	0	0	5.4	5.5	5.0	13.5	13.5	14.1
B20 6	90	38	20	79	77	71	56	56	39	23	22	33	127	0	0	5.2	5.2	5.0	13.9	14.2	14.2
B20 4	78	28	13	81	81	64	58	57	37	23	24	27	125	0	0	5.3	5.3	4.4	13.9	14.0	15.1
B10 1	94	41	21	84	79	75	59	58	41	25	21	34	124	0	0	5.3	5.1	5.0	13.8	14.0	14.2
B10 2	78	32	10	85	82	73	60	61	41	25	22	32	123	0	0	5.2	5.2	4.8	13.7	13.7	14.3
B10 3	99	34	14	83	81	77	63	62	46	20	19	31	127	0	0	5.3	5.3	5.3	13.7	13.8	13.8
ULSD 1	87	41	13	74	72	69	56	58	40	19	15	28	138	0	0	5.4	5.5	5.5	13.1	13.1	13.1
ULSD 8	100	42	13	97	95	90	75	76	57	22	19	33	126	3	0	5.4	5.3	5.3	13.9	14.0	13.9
ULSD 9	112	41	6	86	81	82	66	66	47	23	16	35	131	1	0	5.4	5.4	5.4	13.5	13.5	13.5
B10 4	106	36	8	88	88	84	62	68	49	26	20	36	127	0	0	5.2	5.2	5.2	13.8	13.8	13.7
ULSD 7R	96	37	10	98	92	93	71	71	52	27	21	41	123	0	0	5.2	5.2	5.3	13.7	13.7	13.7
ULSD 2R	95	35	10	99	96	95	72	69	53	27	27	42	122	0	0	5.3	5.3	5.3	13.7	13.7	13.7
ULSD 10	-	-	-	-	-	-	-	-	-	-	-	-	-	-	-	-	-	-	-	-	-

Appendix N Engine Air Flow Rate and CPF Pressure Drop Profile

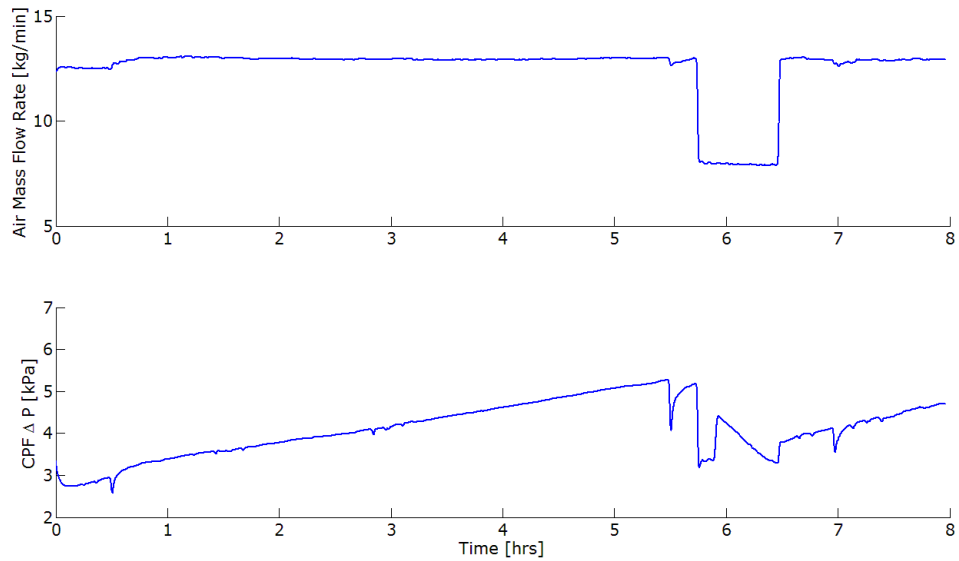


Figure N1: B20-1 Air Flow Rate (top) and CPF Pressure Drop Profile (bottom)

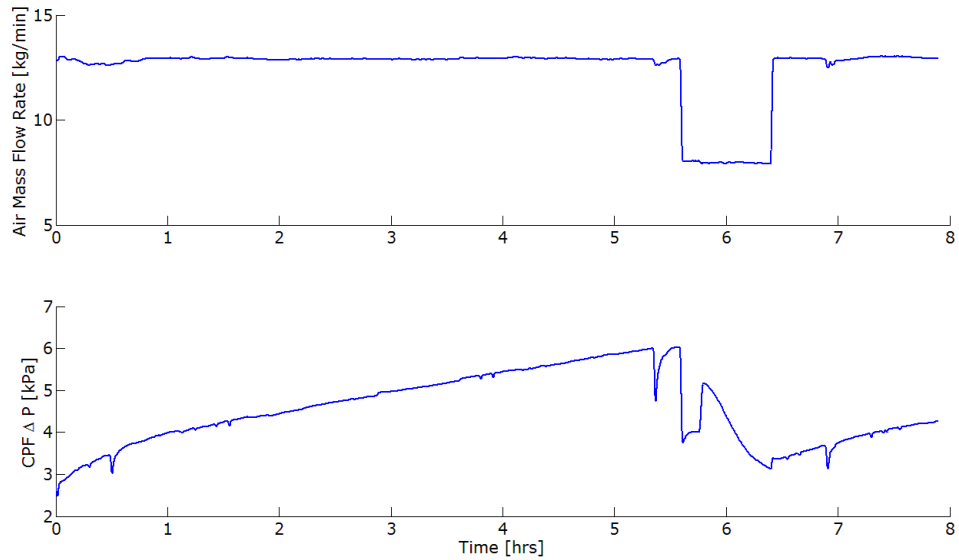


Figure N2: B20-2 Air Flow Rate (top) and CPF Pressure Drop Profile (bottom)

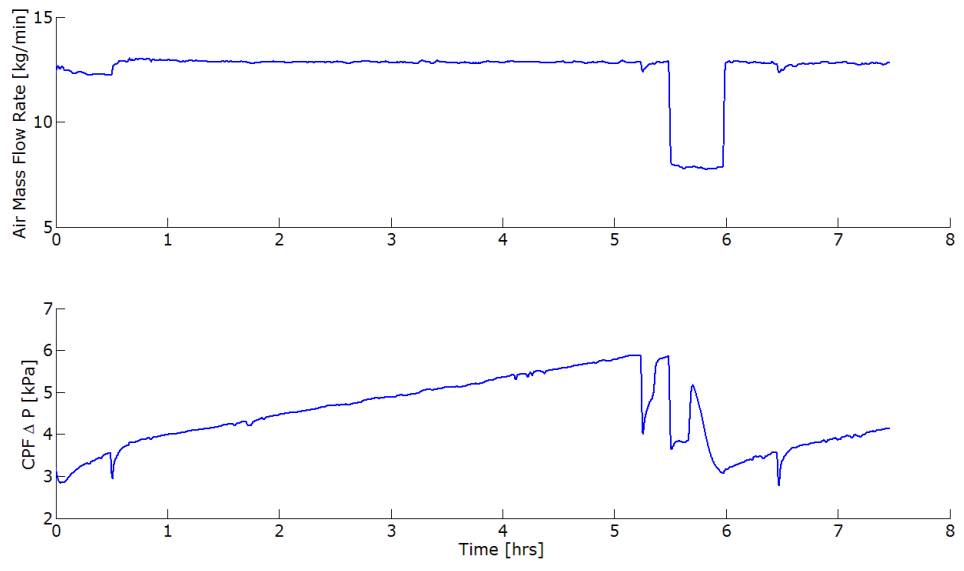


Figure N3: B20-5 Air Flow Rate (top) and CPF Pressure Drop Profile (bottom)

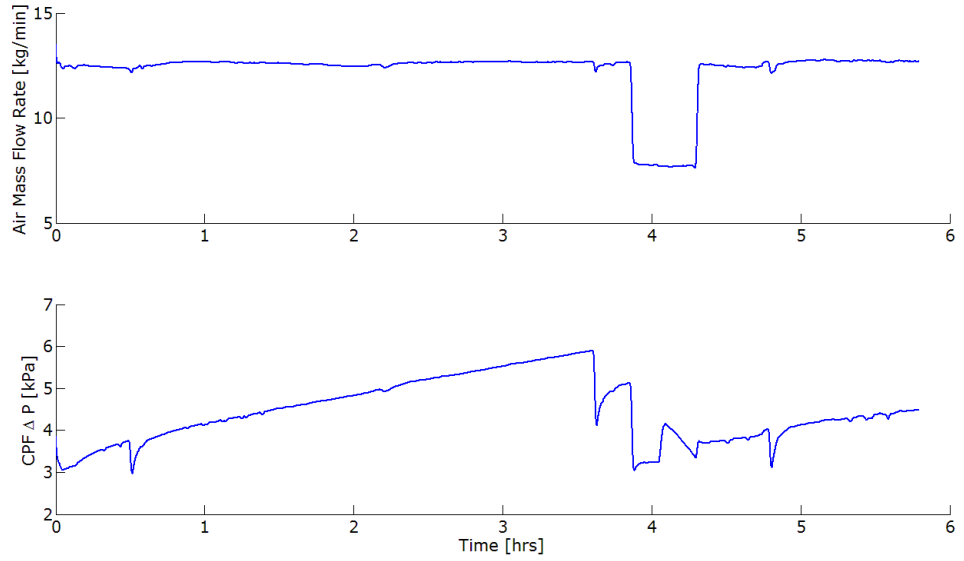


Figure N4: ULSD-3 Air Flow Rate (top) and CPF Pressure Drop Profile (bottom)

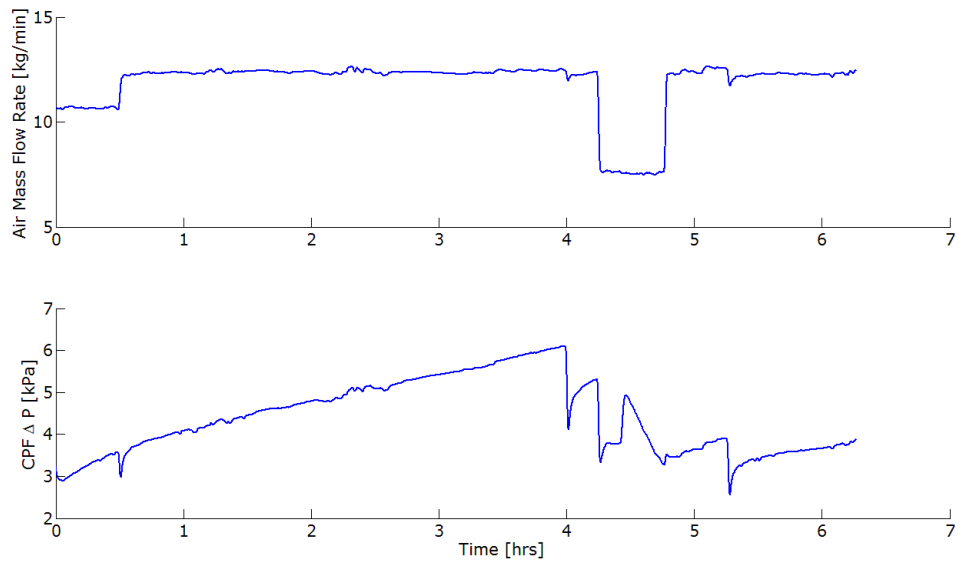


Figure N5: ULSD-4 Air Flow Rate (top) and CPF Pressure Drop Profile (bottom)

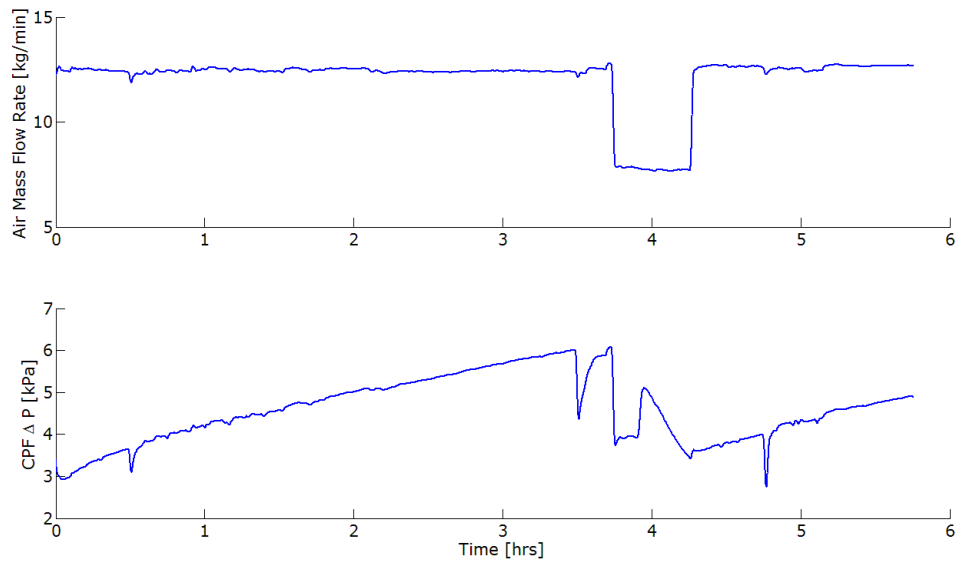


Figure N6: ULSD-5 Air Flow Rate (top) and CPF Pressure Drop Profile (bottom)

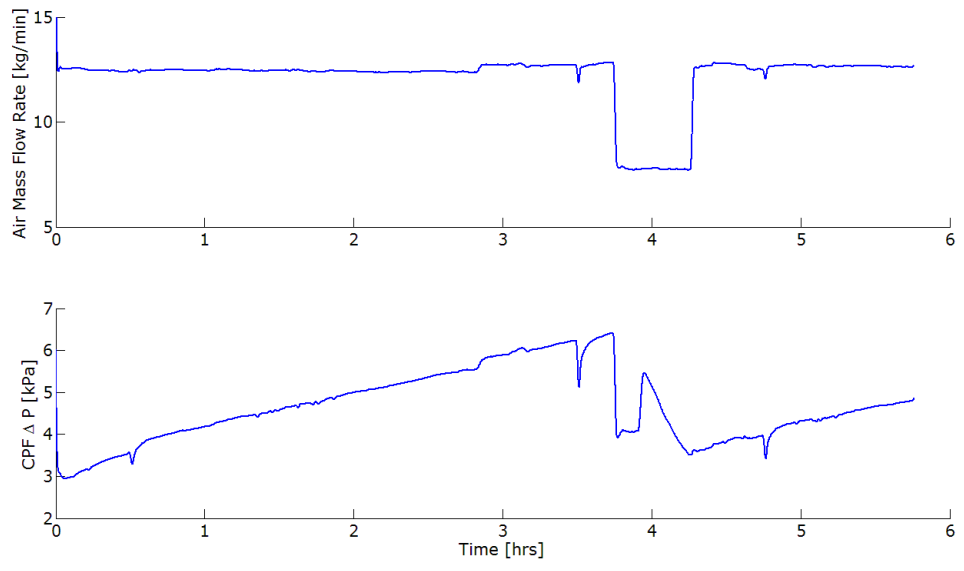


Figure N7: ULSD-6 Air Flow Rate (top) and CPF Pressure Drop Profile (bottom)

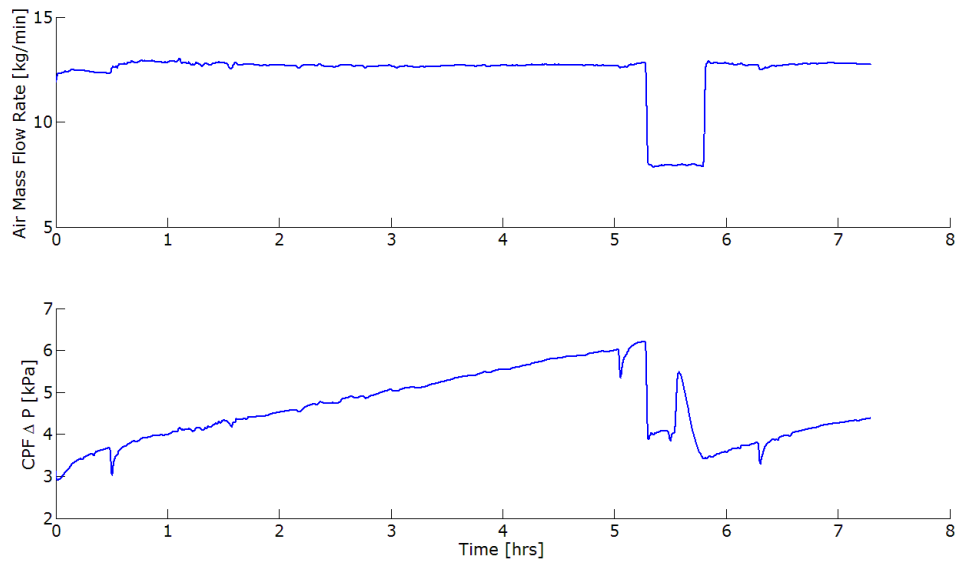


Figure N8: B20-6 Air Flow Rate (top) and CPF Pressure Drop Profile (bottom)

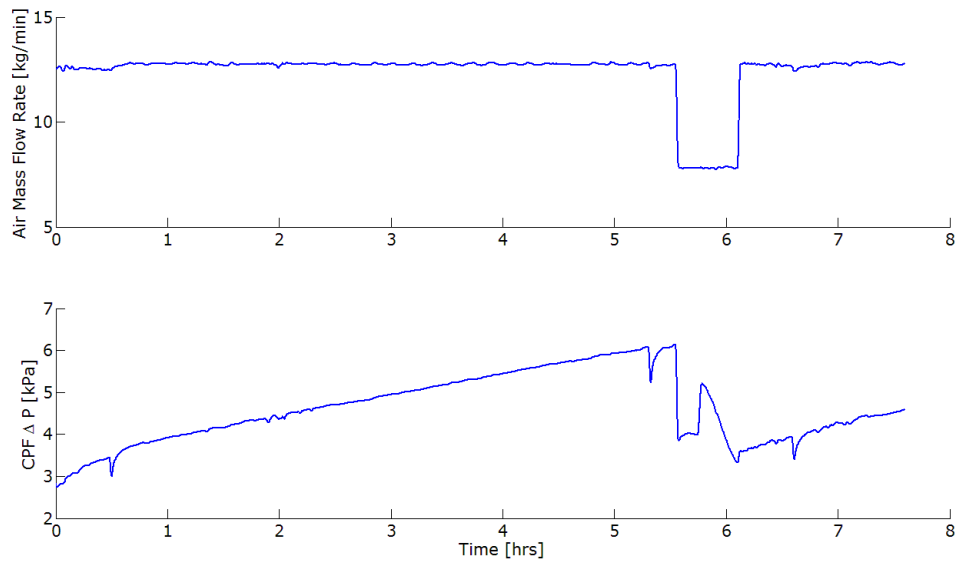


Figure N9: B20-4 Air Flow Rate (top) and CPF Pressure Drop Profile (bottom)

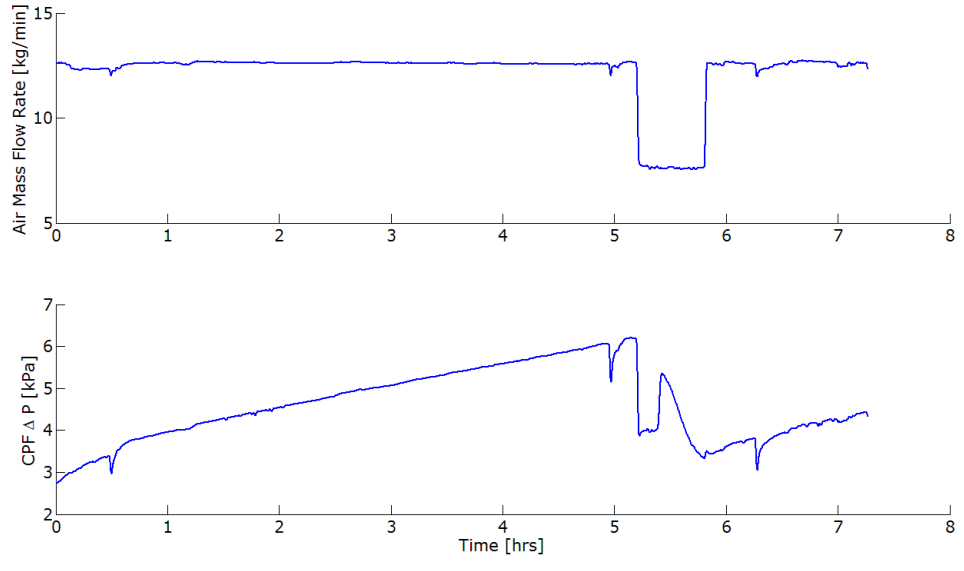


Figure N10: B10-1 Air Flow Rate (top) and CPF Pressure Drop Profile (bottom)

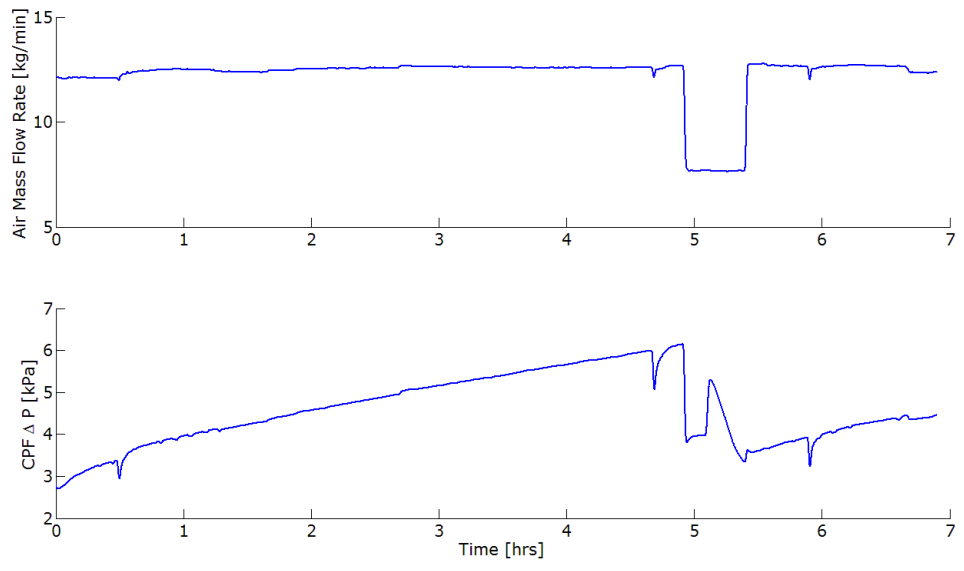


Figure N11: B10-2 Air Flow Rate (top) and CPF Pressure Drop Profile (bottom)

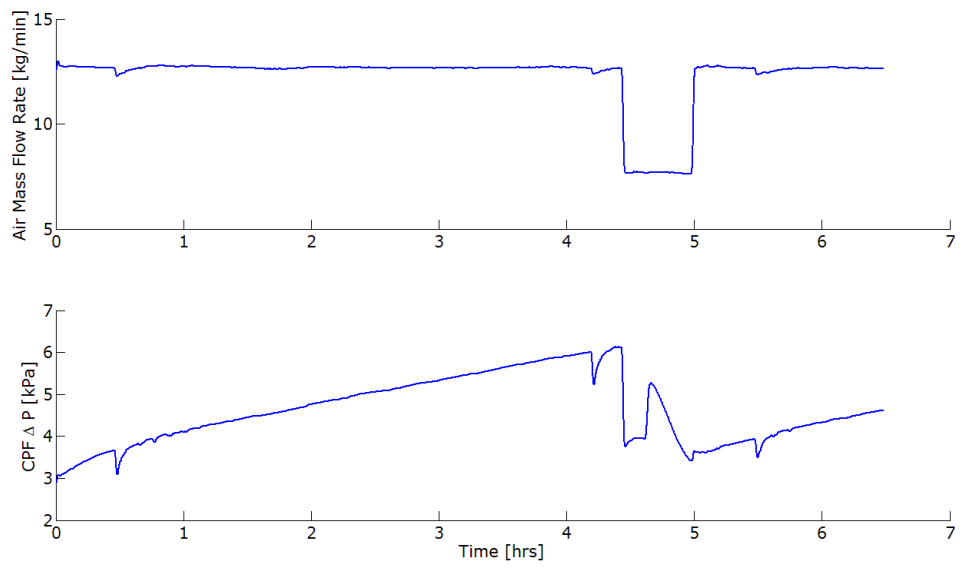


Figure N12: B10-3 Air Flow Rate (top) and CPF Pressure Drop Profile (bottom)

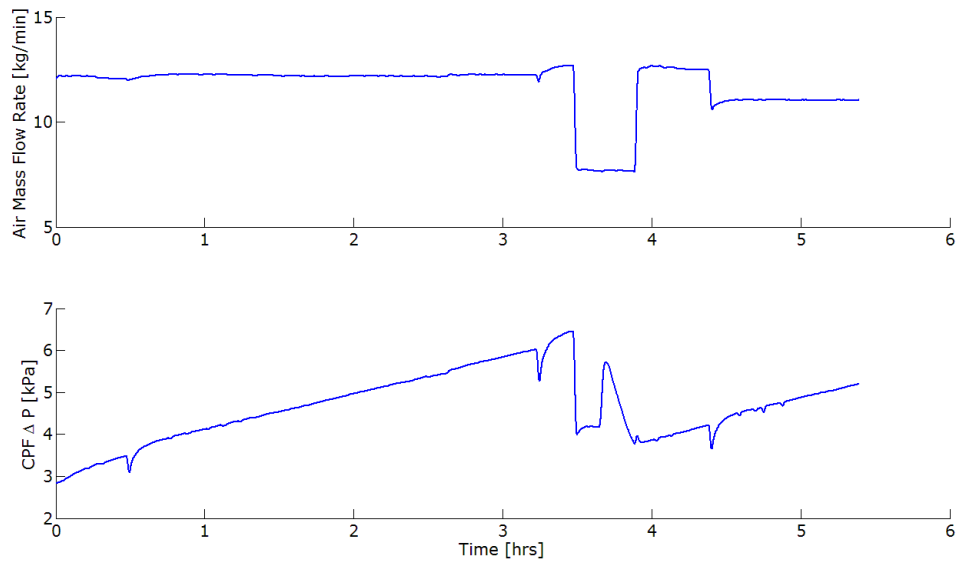


Figure N13: ULSD-1 Air Flow Rate (top) and CPF Pressure Drop Profile (bottom)

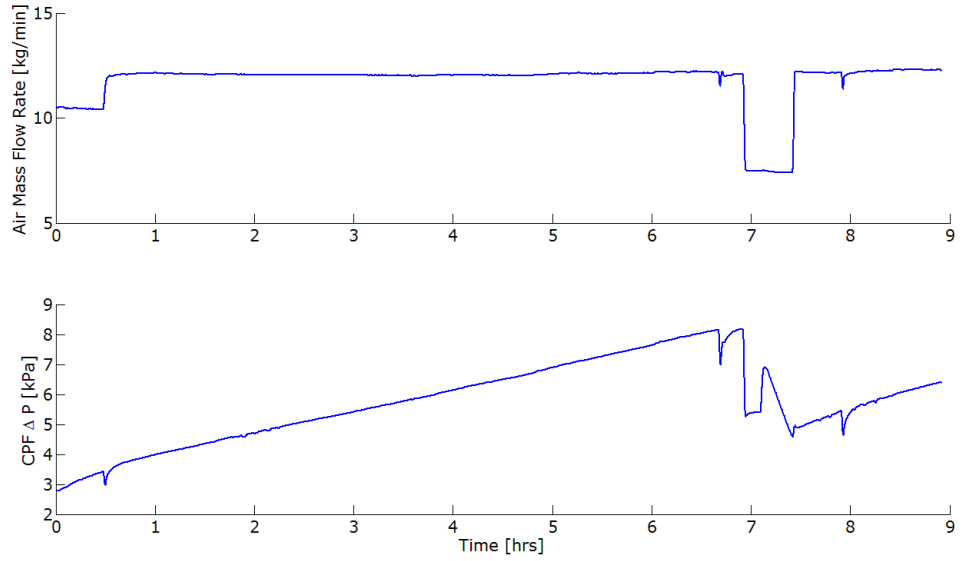


Figure N14: ULSD-8 Air Flow Rate (top) and CPF Pressure Drop Profile (bottom)

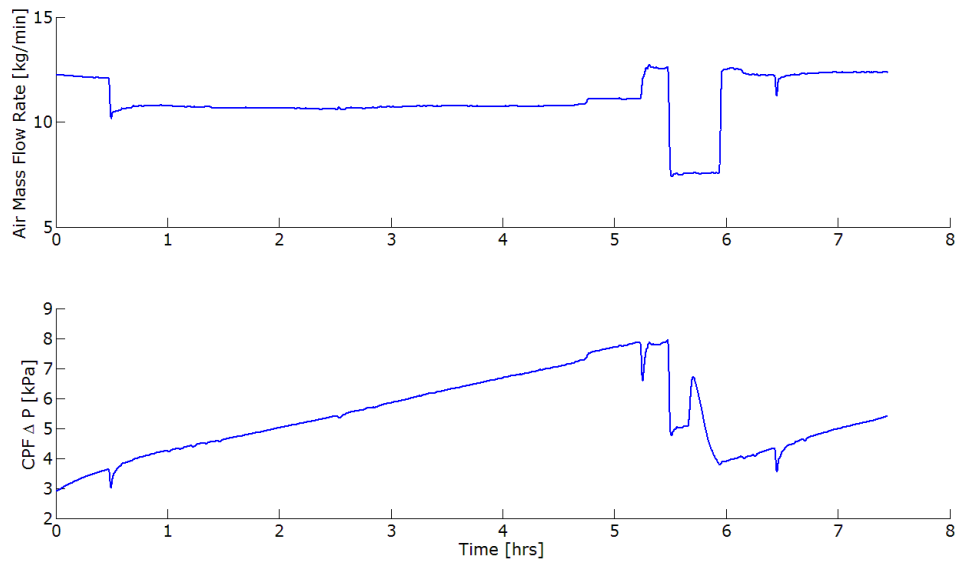


Figure N15: ULSD-9 Air Flow Rate (top) and CPF Pressure Drop Profile (bottom)

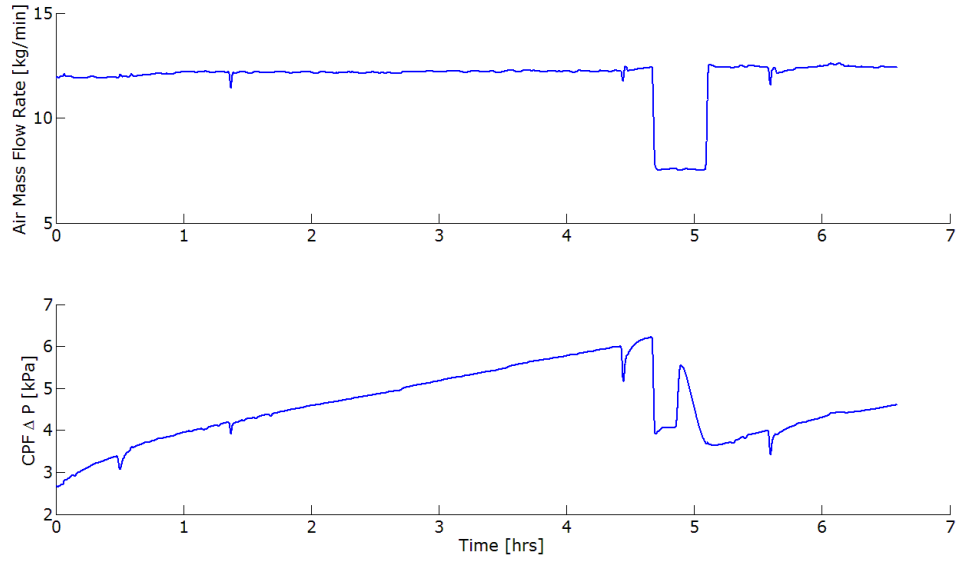


Figure N16: B10-4 Air Flow Rate (top) and CPF Pressure Drop Profile (bottom)

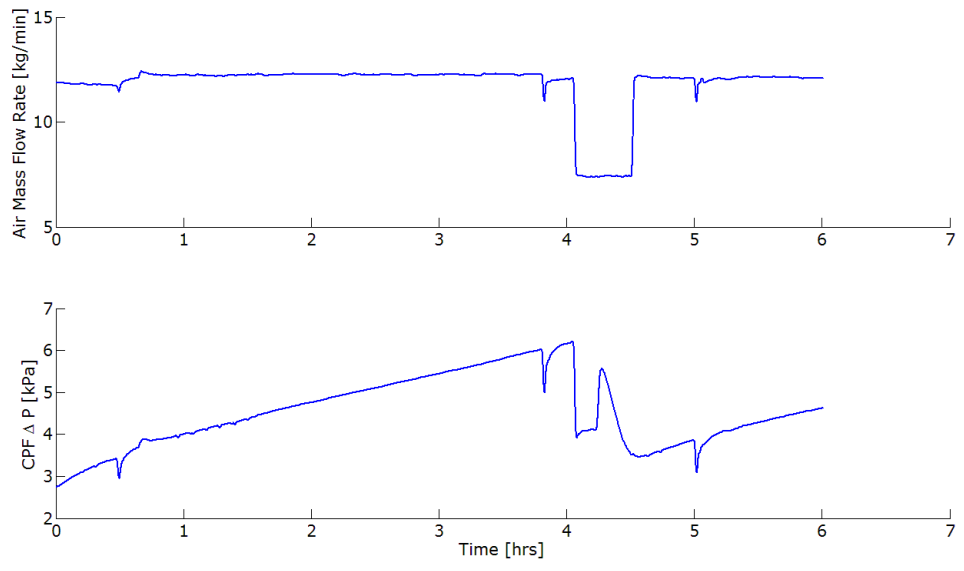


Figure N17: ULSD-7R Air Flow Rate (top) and CPF Pressure Drop Profile (bottom)

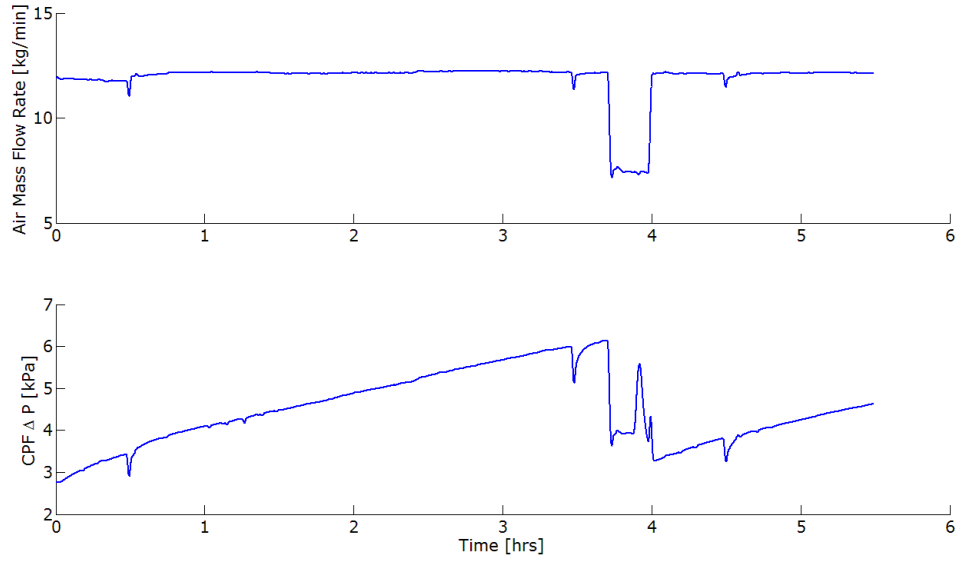


Figure N18: ULSD-2R Air Flow Rate (top) and CPF Pressure Drop Profile (bottom)

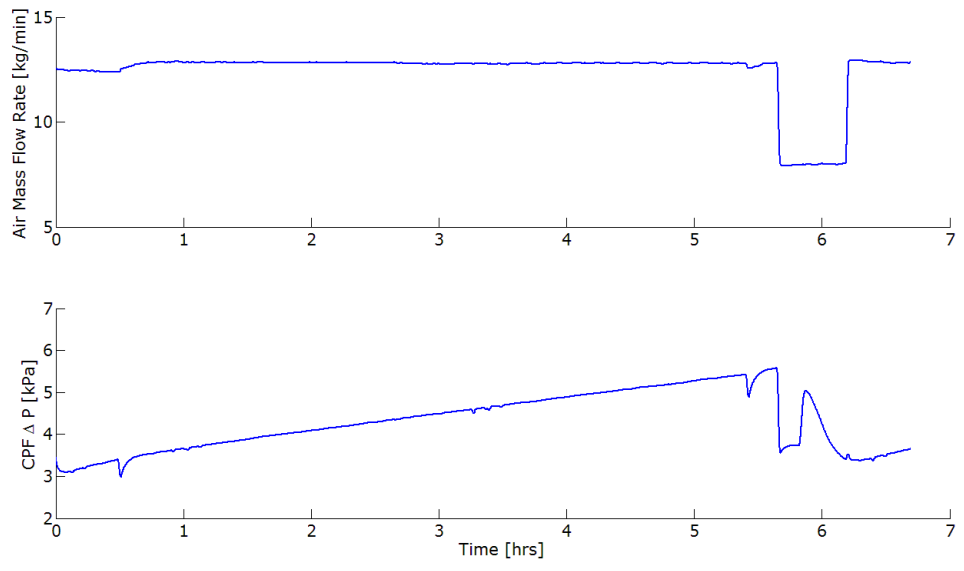


Figure N19: ULSD-10 Air Flow Rate (top) and CPF Pressure Drop Profile (bottom)

Appendix O Regeneration Efficiency of Fuel Dosing Calculation Method

In order to properly correlate grams of PM oxidized per gallon of dosing fuel injected, the experimental data must be normalized to the same initial and final PM mass inside the CPF. The initial PM mass needs to be constant because the initial PM loading of the CPF affects the PM oxidation rate. The final PM mass needs to be constant because as the PM concentration in the CPF decreases, more fuel is required to oxidize the remaining PM.

The average of the CPF PM loading at the start of active regeneration over all tests was used as the initial PM loading value. Experimentally determined pre-exponential factors were also averaged, although they were averaged by fuel. Using the average values for the pre-exponential factor, the reaction rate for each experiment can be calculated using Eqn. O1 and the average CPF temperature for each individual active regeneration. A MATLAB® model was produced which calculates the PM mass retained in the CPF over a 2 hour active regeneration simulation using Eqn. O2

$$RRo = A \cdot e^{[-E_a/(R \cdot T)]} \quad \text{Eqn. O1}$$

RRo = Reaction rate [1/s]

Ea = Activation energy [145 kJ/gmol]

R = Universal gas constant, 8.315 [J/(mol*K)]

T = CPF average temperature for entire active regeneration [K]

$$m_R(i) = [\eta_{\text{filt}} \cdot C_{\text{in}} \cdot Q - m_R(i-1) \cdot A \cdot RRo] \cdot dt + m_R(i-1) \quad \text{Eqn. O2}$$

i = Incremental point in time during active regeneration [-]

$m_R(i)$ = PM mass in CPF at time i during active regeneration [g]

$m_R(i-1)$ = PM mass in CPF calculated at time i - 1 [g]

η_{filt} = CPF filtration efficiency [-]

C_{in} = Engine out PM concentration [g/scm]

Q = Exhaust volumetric flow rate [scm/sec]

RRo = Reaction rate [1/s]

dt = Time step through active regeneration, 1 [sec]

Using the MATLAB® model, PM mass retained in the CPF throughout the entire simulated regeneration is plotted as seen in Figure O1. Also displayed on Figure O1

is the time it takes to reach 70% PM oxidation for ULSD-5 conditions, which is the final PM loading that the experimental data was normalized to since 70% PM oxidation was the target for all tests.

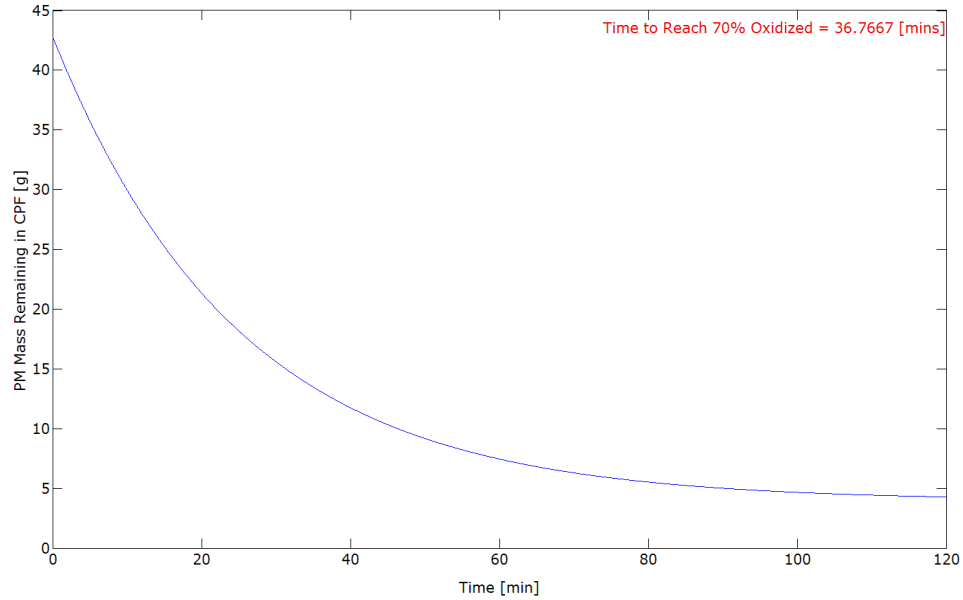


Figure O1: Modeled CPF PM Mass Retained in the CPF during Active Regeneration for Test ULSD-5

Using the model provided time to reach 70% PM oxidation within the CPF, the amount of fuel injected during dosing is calculated using Eqn. O3.

$$\text{gal}_{\text{dosed}} = \dot{m}_{\text{doser}} \cdot t_{\text{AR}} \cdot 1/\rho_{\text{fuel}} \cdot 15.85 \quad \text{Eqn. O3}$$

$\text{gal}_{\text{dosed}}$ = Fuel dosed during active regeneration [gal]

\dot{m}_{doser} = Dosing flow rate [g/sec]

t_{AR} = Active regeneration time [min]

ρ_{fuel} = Fuel density [kg/m³]

15.85 = Constant associated with converting min to sec, kg to g, and m³ to gal

Using the amount of fuel injected during dosing, dividing the PM oxidized by the amount of fuel injected during dosing yields the grams of PM oxidized per gallon of dosed fuel. Table O1 below displays the normalized data from the calculations

discussed above. The modeled PM oxidized is the same for all tests because 70% of the 42.8 g PM mass in the CPF at the start of active regeneration is 30.0 g.

Table O1: Normalized Experimental Data

Variable	Average CPF Temp	Modeled 70% Oxidized Time Requirement	AVL Dosing Rate	PM Concentration	Fuel Dosed	PM Oxidized/Gallon Fuel Dosed
Test/Units	°C	min	g/sec	mg/scm	gal	g/gal
B20 1	474	67.9	0.431	8.3	0.548	54.7
B20 2	508	26.3	0.633	9.9	0.311	96.3
B20 5	534	12.5	0.832	9.9	0.194	154.6
ULSD 3	526	40.3	0.638	22.2	0.475	63.1
ULSD 4	531	33.3	0.763	18.5	0.469	63.8
ULSD 5	529	36.8	0.735	24.3	0.500	60.0
ULSD 6	540	25.2	0.739	18.3	0.344	87.1
B20 6	540	10.7	0.690	12.9	0.138	216.7
B20 4	506	28.3	0.687	17.8	0.364	82.3
B10 1	534	22.7	0.730	15.1	0.312	96.0
B10 2	531	25.5	0.898	17.4	0.430	69.7
B10 3	531	24.1	0.743	11.2	0.337	88.8
ULSD 1	567	13.6	0.819	26.9	0.206	145.7
ULSD 8	539	26.3	0.744	22.5	0.361	83.0
ULSD 9	563	14.6	0.899	21.9	0.242	123.6
B10 4	563	11.1	0.896	15.7	0.187	160.6
ULSD 7R	562	15.0	0.830	25.9	0.230	130.4
ULSD 2R	616	4.4	1.056	19.8	0.086	346.8

Appendix P CPF Pressure Drop Comparison between National Instruments (NI) LabVIEW and CalTerm

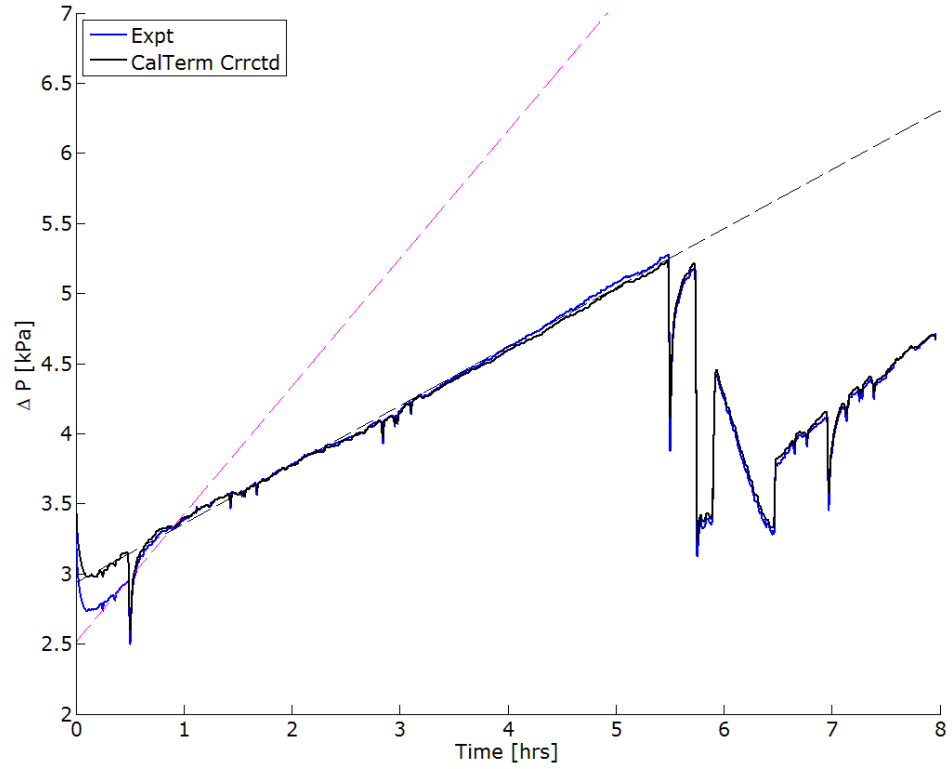


Figure P1: B20-1 CPF Pressure Drop

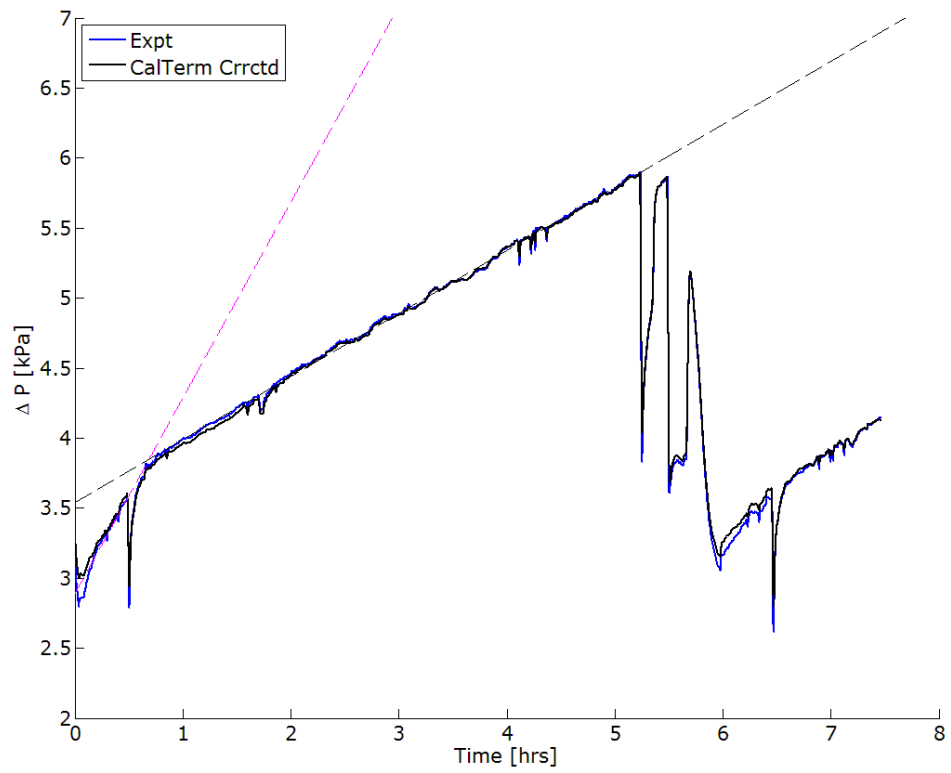


Figure P2: B20-5 CPF Pressure Drop

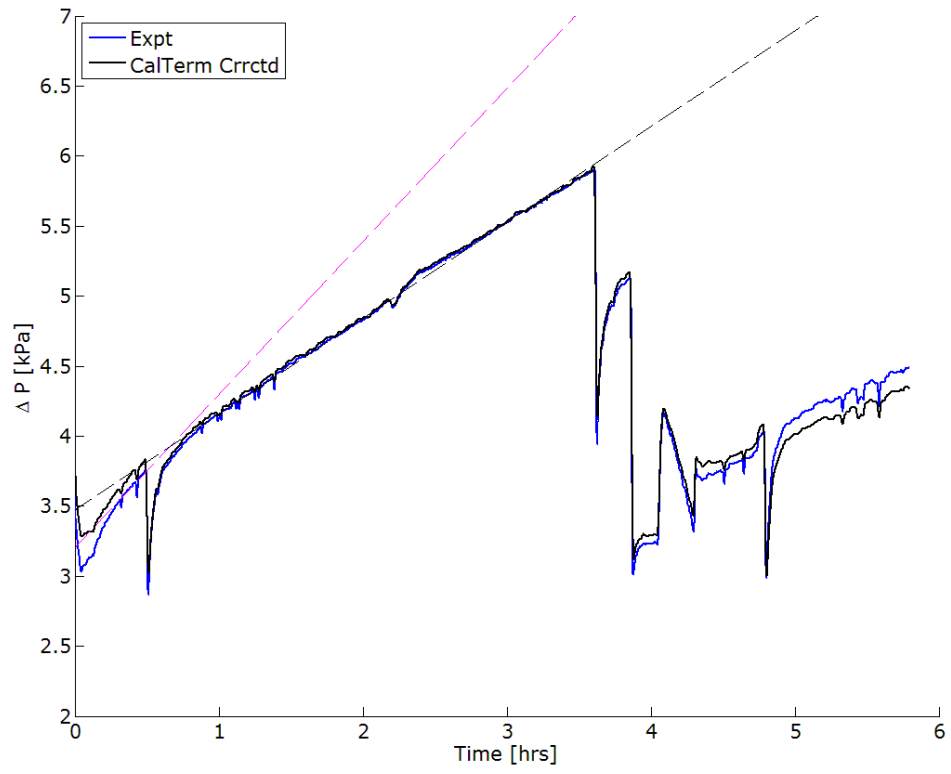


Figure P3: ULSD-3 CPF Pressure Drop

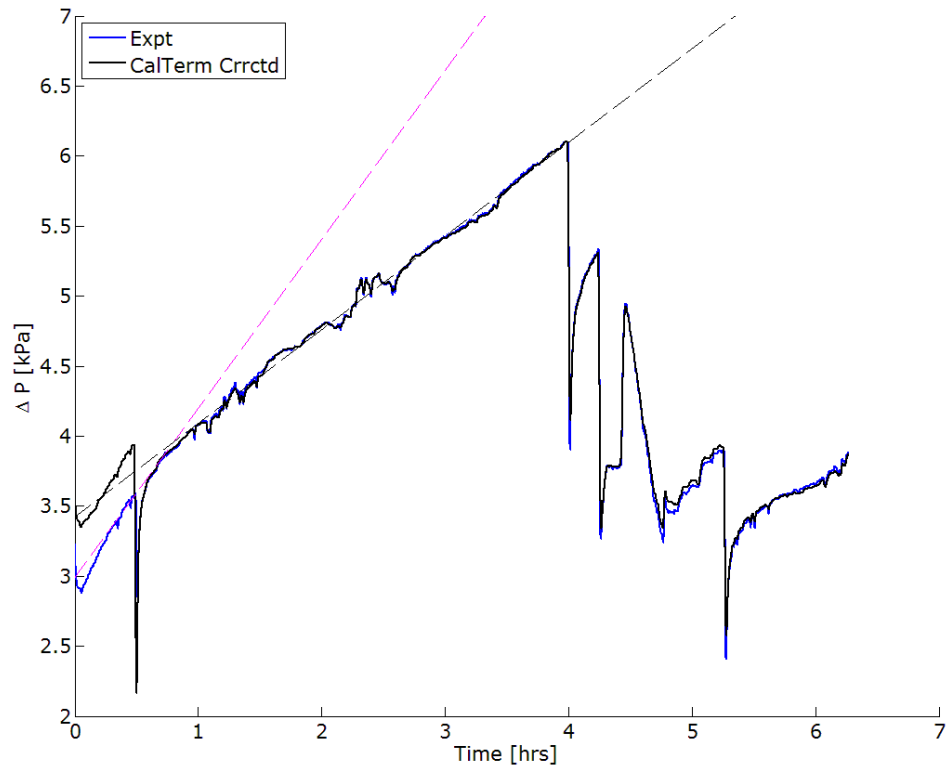


Figure P4: ULSD-4 CPF Pressure Drop

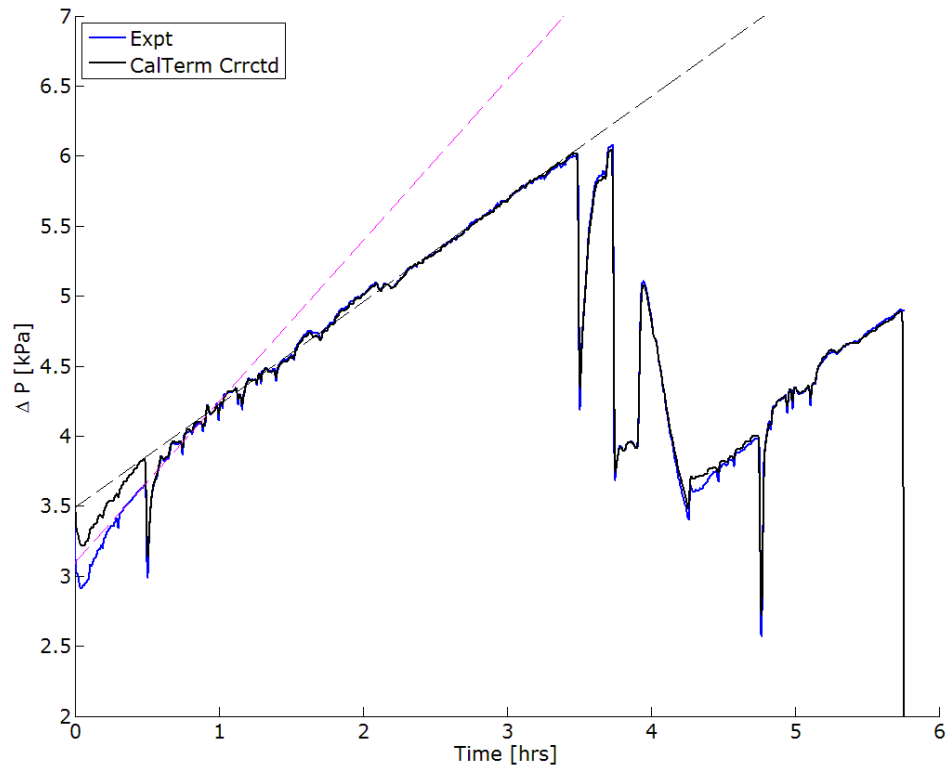


Figure P5: ULSD-5 CPF Pressure Drop

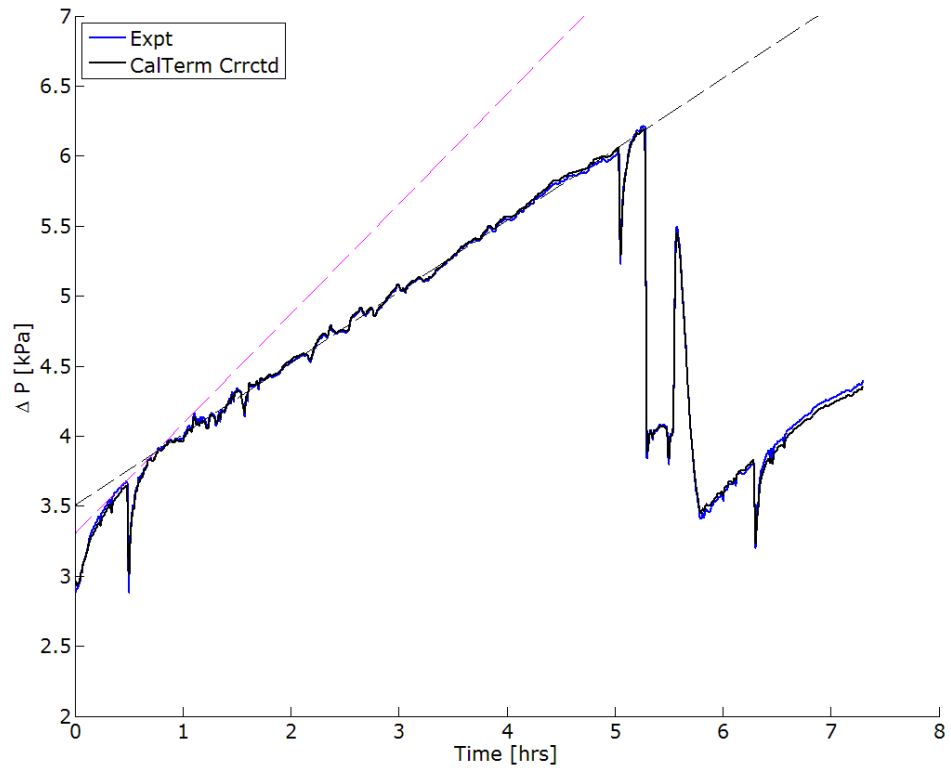


Figure P6: B20-6 CPF Pressure Drop

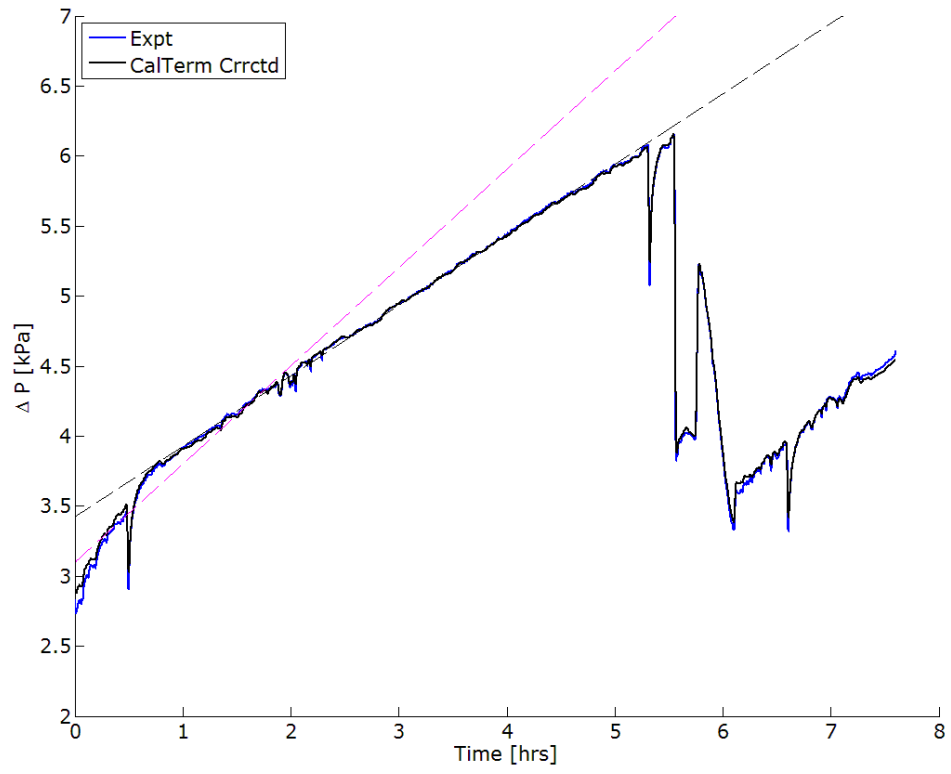


Figure P7: B20-4 CPF Pressure Drop

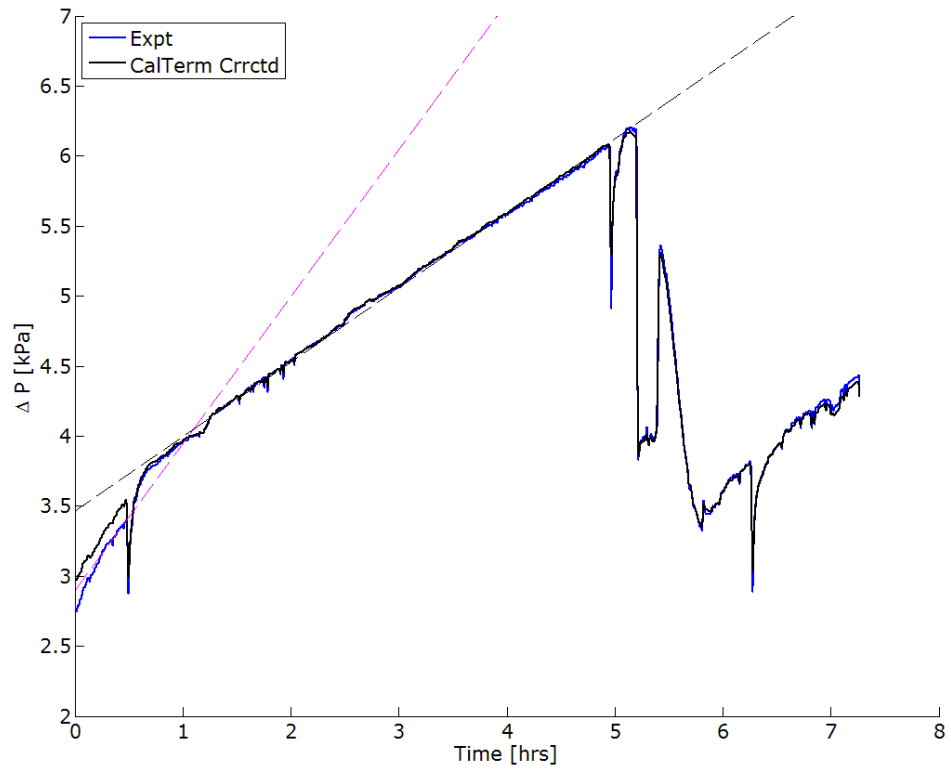


Figure P8: B10-1 CPF Pressure Drop

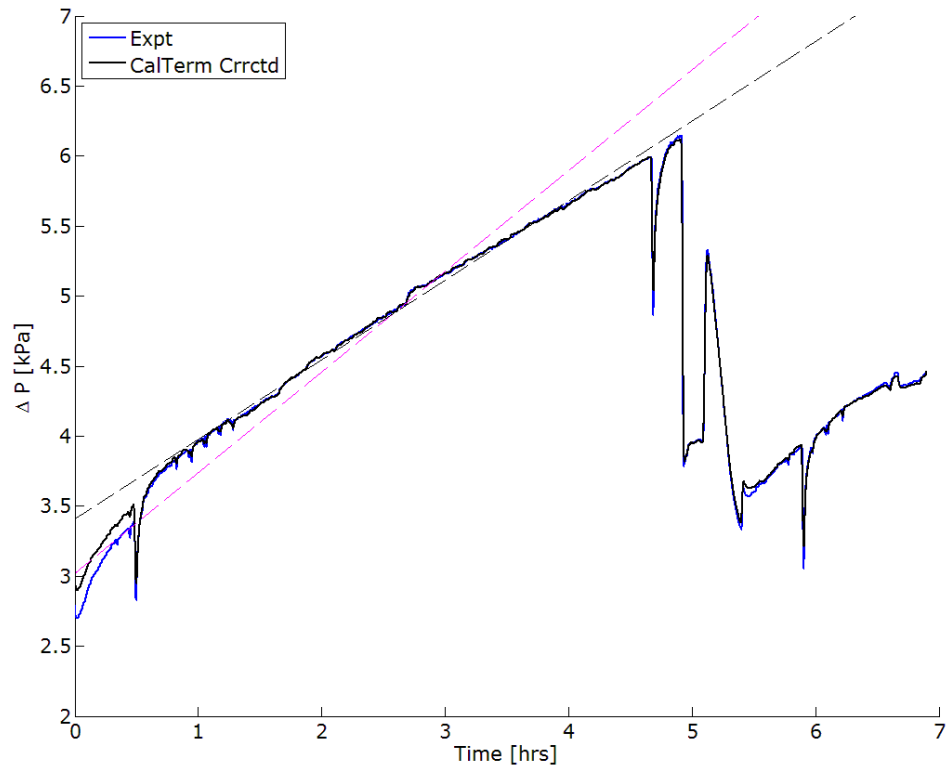


Figure P9: B10-2 CPF Pressure Drop

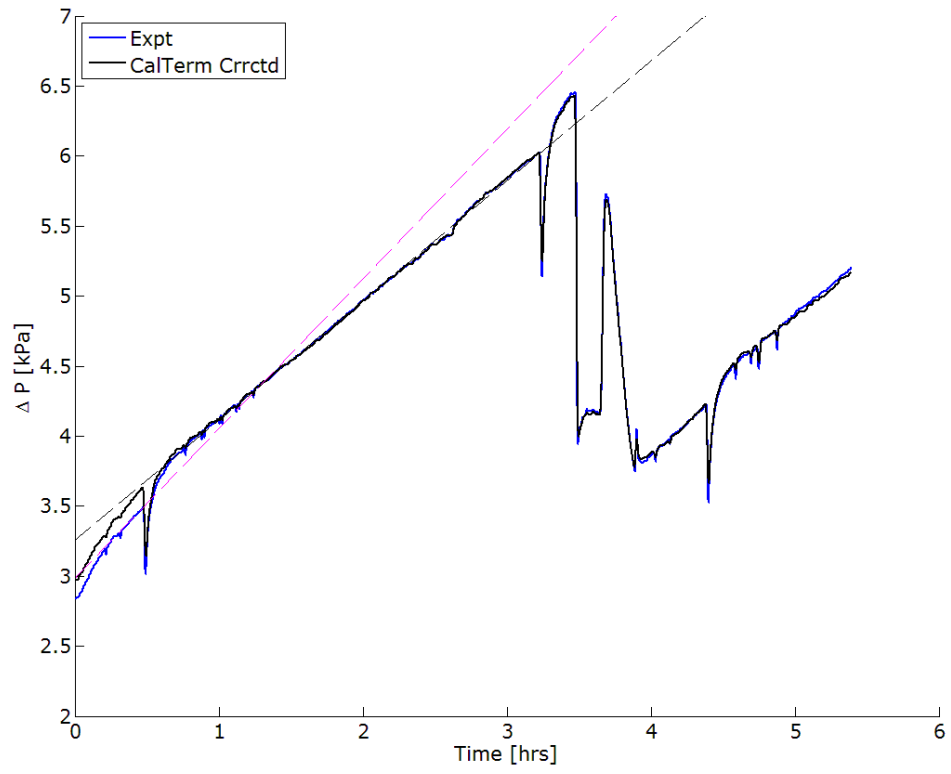


Figure P10: ULSD-1 CPF Pressure Drop

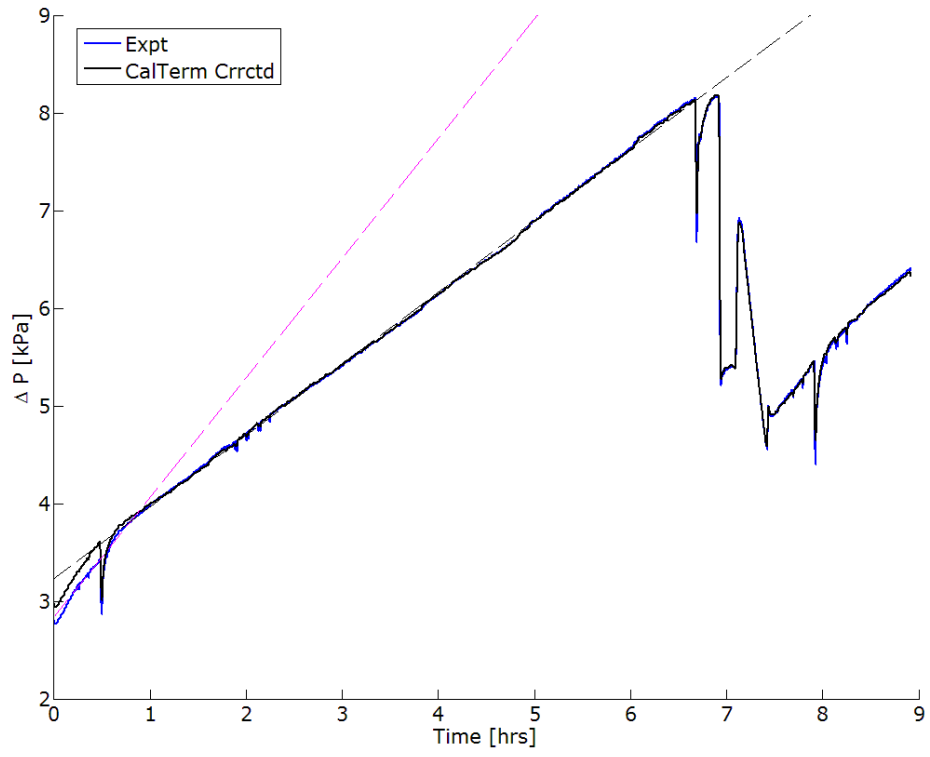


Figure P11: ULSD-8 CPF Pressure Drop

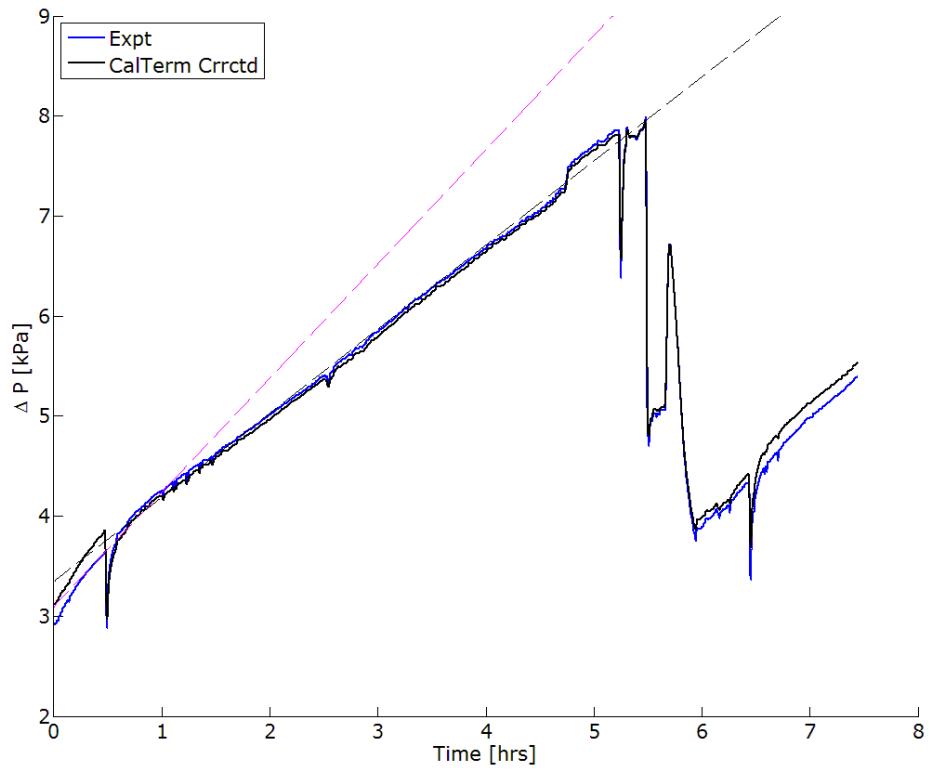


Figure P12: ULSD-9 CPF Pressure Drop

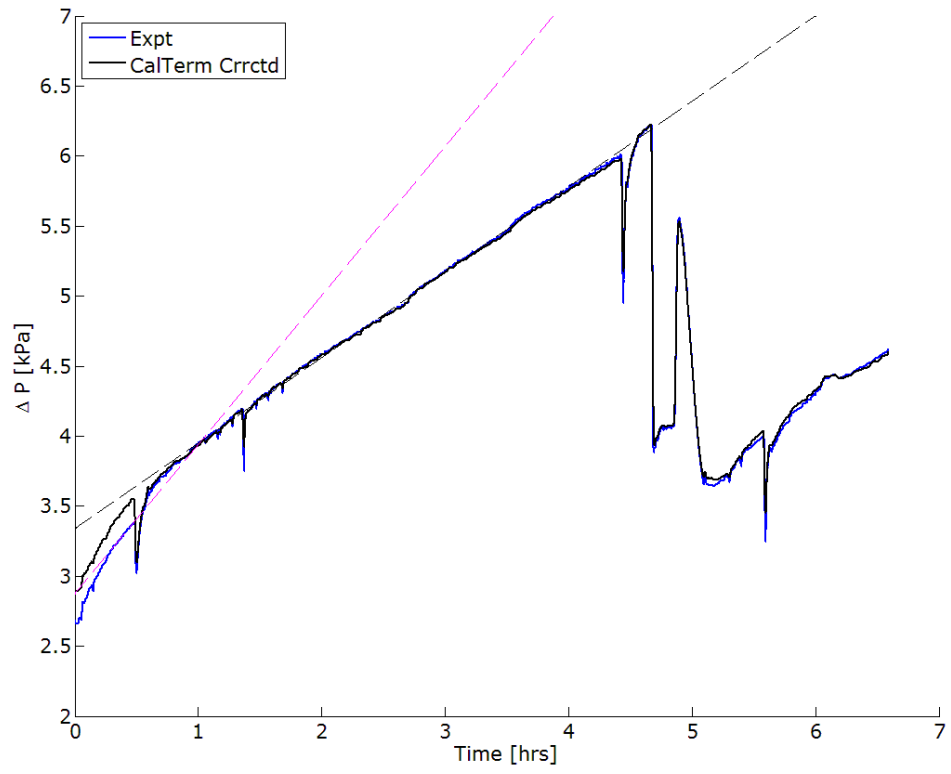


Figure P13: B10-4 CPF Pressure Drop

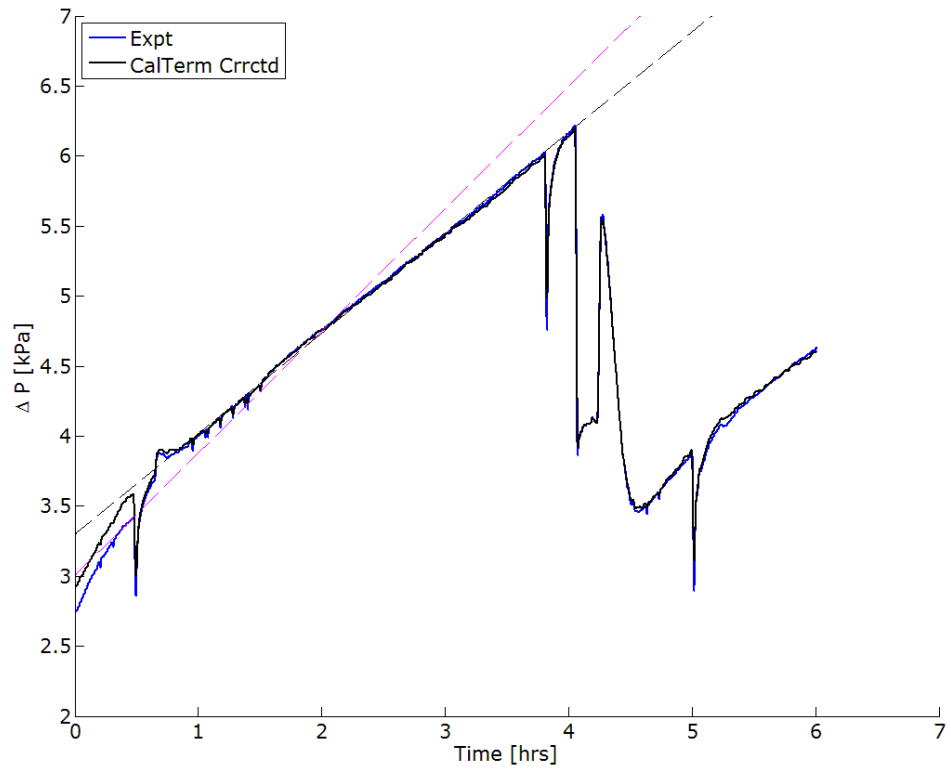


Figure P14: ULSD-7R CPF Pressure Drop

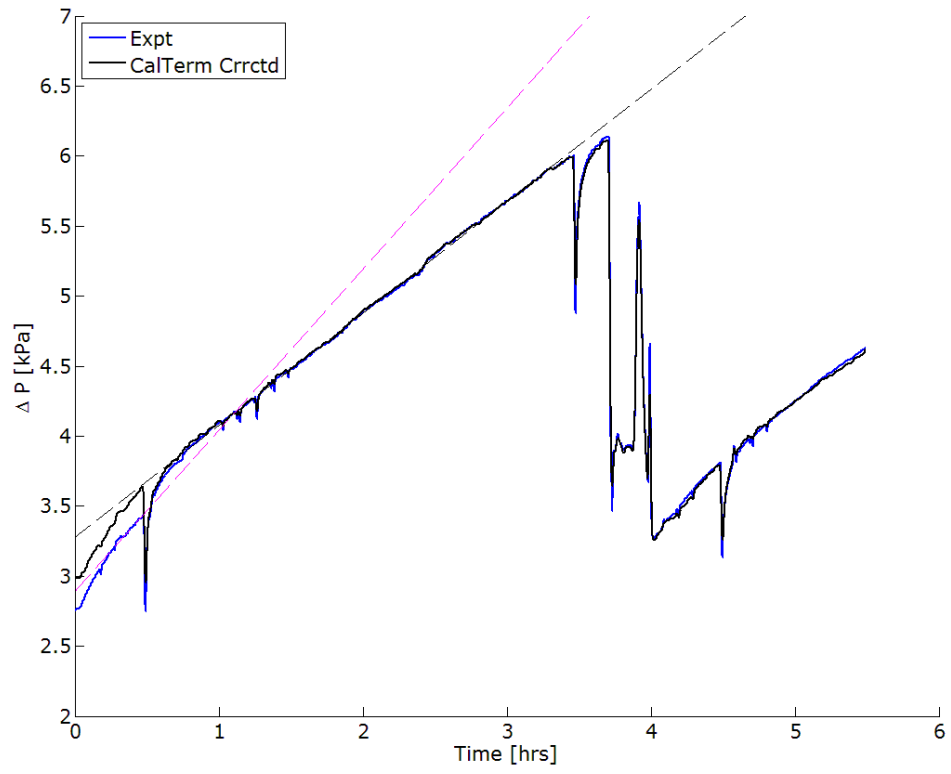


Figure P15: ULSD-2R CPF Pressure Drop

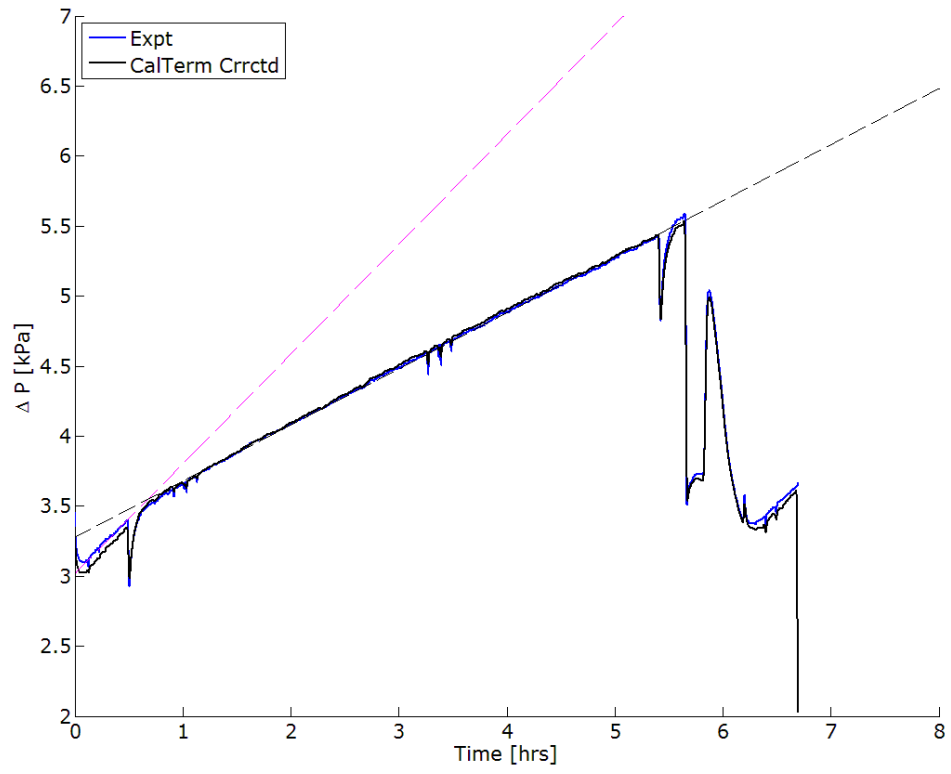


Figure P16: ULSD-10 CPF Pressure Drop

Appendix Q Permission to Use Copyrighted Material



James Pidgeon <jmpidgeo@mtu.edu>

Request for permission to use copyrighted figures

copyright <copyright@sae.org>
To: James Pidgeon <jmpidgeo@mtu.edu>

Thu, Sep 13, 2012 at 12:24 PM

Dear James,

Thank you for your correspondence requesting permission to include figures from SAE papers (noted below) in your thesis for a MS Mechanical Engineering degree at MTU.

Permission to reprint the figures from papers 2003-01-0833 and 2010-01-0307 is hereby granted, and is subject to the following conditions:

- Permission is granted for non-exclusive world English language rights, for this one-time single use.
- Permission is required for new requests, subsequent editions, for reprints or excerpts, or further use of the material.
 - The following copyright statement must appear directly below the figures: "Copyright © SAE International. Reprinted with permission." We also request that you credit the original source (author, paper number and SAE) in the reference section.
 - This permission does not cover any third party copyrighted work which may appear in the material requested. If this material originated from another source, you must contact the original copyright holder for this permission.

Permission to reprint the figures from paper [2012-01-1313](#) cannot be granted by SAE. This is a Government paper (Canadian) and SAE does not hold the copyright. You need to contact the authors, or Environment Canada, for this permission.

Please feel free to contact me if you need further assistance.

Best regards,

Terri Kelly

Intellectual Property Rights Administrator

SAE International | 400 Commonwealth Drive | Warrendale, PA 15096-0001 | USA

Office: +01 [724-772-4095](tel:724-772-4095) | Fax: +01 [724-776-9765](tel:724-776-9765)

terri@sae.org | www.sae.org

From: James Pidgeon [mailto:jmpidgeo@mtu.edu]

Sent: Wednesday, August 01, 2012 10:59 AM

To: copyright

Subject: Request for permission to use copyrighted figures

To whom it may concern,

My name is James Pidgeon and I am currently writing my MS thesis for graduation from Michigan Technological University this upcoming December. I am emailing to request for permission to use a number of figures from a number of SAE papers that I would like to include in my thesis. The SAE paper number and corresponding figure numbers are listed below.

[2012-01-1313](#): Figures 2 and 11

[2003-01-0833](#): Figure 6

[2010-01-0307](#): Figure 3

The title of my thesis is: An Experimental Investigation into the Effects of Biodiesel Blends on Particulate Matter Oxidation in a Catalyzed Particulate Filter during Active Regeneration

This thesis is being written for completion of the partial requirements for the MS Mechanical Engineering degree

The thesis will be distributed electronically throughout various individuals/departments at MTU and will be printed upon completion with an expected publication date of early (January to April) 2013.

If any other information is necessary, let me know. Thank you.

--

James Pidgeon
Mechanical Engineering
Cell: [\(715\) 781-5421](tel:7157815421)

Nothing in this message is intended to constitute an electronic signature unless a specific statement to the contrary is included in this message. Confidentiality Note: This message is intended only for the person or entity to which it is addressed. It may contain confidential and/or proprietary material. Any review, transmission, dissemination or other use, or taking of any action in reliance upon this message by persons or entities other than the intended recipient is prohibited. If you received this message in error, please contact the sender and delete it from your computer.

This letter is for Figure 2.8